



UNIVERSITY OF STRATHCLYDE  
Strathclyde Institute of Pharmacy and Biomedical Sciences  
CMAC  
Glasgow, UK

# **Predictive Design of Stable Polymer-based Amorphous Solid Dispersions**

A thesis submitted in accordance with the requirements for the  
degree of Doctor of Philosophy

**Ecaterina Bordos**

2023

## **Declaration of Author Rights**

This thesis is the result of the author's original research. It has been composed by the author and has not been previously submitted for examination which has led to the award of a degree.

The copyright of this thesis belongs to the author under the terms of the United Kingdom Copyright Acts as qualified by University of Strathclyde regulation 3.50. Due acknowledgement must be made of the use of any material contained in, or derived from this thesis.

Glasgow, UK, 2023

---

Ecaterina Bordos

*A scientist in his laboratory is not a mere technician: he is also a child confronting natural phenomena that impress him as though they were fairy tales.*

- Marie Curie

## **Abstract**

The potential of amorphous solid dispersions (ASDs) solving current aqueous solubility challenges within the pharmaceutical industry has been extensively reported. Nonetheless, the difficulty of ensuring long-term physical stability has limited its translation into commercial drug products. One of the main factors that determines ASD physical stability is the solubility of the API in the polymeric carrier. However, there is a scarcity of reliable methods available for its determination. In this thesis, this was directly addressed by developing a novel empirical method to determine the saturated solubility of crystalline API in polymer matrices. Hot melt extrusion and low-frequency Raman (LFR) spectroscopy were combined for the first time for real-time API-polymer solubility determination. This approach enabled construction of solubility phase diagrams that inform safe processing windows to avoid residual API crystallinity, inform maximum drug loadings and aid polymer selection for maximum API solubility and ASD physical stability. The solid-liquid equilibrium depicting the API solubility curve was also compared to state of the art DSC-based methods, including the Flory-Huggins and Kyeremateng modelling approaches, among others. Equilibrium assumptions and potential shortfalls leading to under or overestimations were discussed. In addition, the impact of drug loading and processing temperature on the ASD internal microstructure was investigated by means of synchrotron phase-contrast micro-tomography (Sync-PC- $\mu$ CT). Furthermore, the local distribution evolution of the API and polymer on the ASD surface was investigated through time-of-flight secondary ion mass spectrometry (ToF-SIMS) chemical mapping. Surface phase-separation and crystallisation kinetics were determined and compared to bulk crystallisation phenomena. A close link was established between the coordinates of the solubility phase diagram and ASD properties such as the degree of structural heterogeneity and the crystallisation induction time and rate. Overall, these results suggest the API saturated solubility determined by the LFR method could be used as a physical stability predictor for the design, development and manufacture of stable polymer-based ASDs with desired structure and performance.

## **Acknowledgements**

My PhD experience has been a long and rewarding journey, full of challenges and incredible people. First and foremost, I would like to express my deepest gratitude to my supervisors, Dr. John Robertson and Prof. Gavin Halbert, for all the patience, support and continuous encouragement throughout my PhD study. Your insights, expertise and guidance have enriched my experience as a researcher and as a person.

A very special thanks to Dr. Tariq Islam, Dr. Michael Devlin and Dr. Eleonora Paladino. Collaborating and doing science with you was a true privilege. I would also like to thank Dr. Carlota Torrecillas for all the help with image analysis. A special remark goes to all past and present members of the CMAC team that are always ready to help with a smile on their face.

I would also like to thank all my friends that have contributed to these marvellous years in Glasgow (Carlota, Georgia, Moulham, Russel, Michael, Martin, Eleonora, Sofia, Mariana, Patricia, Rita, Paquito, Claudia and Hugo). In a way or another, in one country or the other, our laughter, tears and joys have brought a special meaning to this journey.

Finally, I would like to extend my sincere gratitude to my family, in particular to my parents for their unconditional love and support. And last, but by no means least, to Arthur and Daisy, your love and affection mean the world to me.

## Contents

Declaration of Author Rights .....	i
Abstract .....	iii
Acknowledgements .....	iv
List of Figures .....	xi
List of Tables.....	xxi
List of abbreviations and symbols.....	xxii
Research outputs.....	xxvi
Chapter 1 Fundamentals of Amorphous Solid Dispersions: A Literature Review .....	1
1.1 Introduction .....	1
1.2 Poor aqueous solubility .....	1
1.3 Amorphous solid dispersions and the amorphous state.....	4
1.4 Classification of amorphous solid dispersions .....	6
1.5 Manufacturing methods.....	9
1.6 Factors affecting ASD physical stability.....	11
1.6.1 Thermodynamic aspects .....	13
1.6.1.1 API-polymer solubility .....	13
1.6.1.1.1 Flory – Huggins theory .....	16
1.6.1.2 API-polymer miscibility .....	17
1.6.1.2.1 Solubility parameter approach .....	18
1.6.2 Kinetic aspects .....	19
1.6.2.1 Glass transition temperature and molecular mobility .....	19
1.6.2.2 API-polymer interactions.....	21
1.6.2.3 Glass forming ability.....	22
1.6.3 Environmental aspects .....	23
1.7 Temperature-composition phase diagrams.....	25
1.8 Characterisation of Amorphous Solid Dispersions .....	27

1.8.1 Thermal methods .....	29
1.8.2 Spectroscopic methods .....	31
1.8.3 X-ray based methods .....	33
1.8.4 Microscopic methods .....	33
1.9 Translational limitations – current gaps .....	34
1.10 Aims and objectives .....	37
Chapter 2 Use of Low-frequency Raman Spectroscopy to Determine Solubility of Crystalline API in Polymeric Matrices .....	38
2.1 Introduction .....	39
2.2 Materials and Methods .....	40
2.2.1 Materials .....	40
2.2.2 Methods .....	41
2.2.2.1 Preparation of amorphous solid dispersions by hot melt extrusion (HME)...	41
2.2.2.4 Off-line Terahertz-Raman spectroscopy .....	46
2.2.2.5. Hot stage microscopy .....	46
2.2.2.6 Differential Scanning Calorimetry .....	47
2.2.2.7. X-ray powder diffraction .....	47
2.3 Results and discussion .....	48
2.3.1 Saturated solution temperature ( $T_S$ ) determination .....	48
2.3.2. Temperature-composition phase diagrams .....	51
2.3.2.1 Paracetamol-Affinisol system .....	52
2.3.2.2. Paracetamol-Plasdone system .....	53
2.3.3. Polymorphic phase identification .....	55
2.2.4 Crystal dissolution behaviour observed by hot stage microscopy .....	56
2.3.5 Predictive value of the critical concentration .....	58
2.4 Conclusions .....	61

Chapter 3 Comparative Study of Different Methods for the Prediction of Drug-Polymer Solubility .....	62
3.1 Introduction .....	62
3.2 Materials and Methods .....	63
3.2.1 Materials .....	63
3.2.2 Methods .....	64
3.2.2.1 Ball-milling .....	64
3.2.2.2 Differential Scanning Calorimetry .....	64
3.2.2.3 Helium pycnometry – density measurement.....	65
3.2.3 Theoretical considerations .....	66
3.2.3.1 Calculation of the solubility curves.....	66
3.2.3.1.1 Flory-Huggins model .....	66
3.2.3.1.2 Empirical equation .....	68
3.2.3.2 Calculation of the glass transition temperature .....	68
3.2.3.3 Calculation of the Hansen solubility parameters .....	69
3.3 Results and discussion.....	71
3.3.1 Glass transition temperature (T <sub>g</sub> ) prediction .....	71
3.3.2 Melting point depression and $\chi$ interaction parameter .....	74
3.3.3 Hansen solubility parameters.....	74
3.3.3 Gibb’s free energy .....	75
3.3.4 Temperature-composition phase diagram.....	78
3.3.4.1 The solid-liquid equilibrium .....	78
3.3.4.2 The spinodal curve.....	82
3.3.5 The zero enthalpy approach.....	82
3.4. Conclusion.....	86
Chapter 4 Linking API-polymer Solubility to Amorphous Solid Dispersion Microstructure Formation .....	87
4.1 Introduction .....	88

4.2 Materials and methods.....	90
4.2.1 Materials .....	90
4.2.2 Methods .....	90
4.2.2.1 Blending.....	90
4.2.2.2 Preparation of amorphous solid dispersions by hot melt extrusion (HME) ...	91
4.2.2.3 API-polymer solubility determination .....	93
4.2.2.4 Differential Scanning Calorimetry (DSC) .....	94
4.2.2.5 X-ray diffraction (XRD) .....	94
4.2.2.6 Synchrotron phase-contrast micro computed tomography (Sync-PC- $\mu$ CT)..	94
4.2.2.6 Tomographic reconstruction .....	95
4.2.2.7 Image analysis.....	96
4.2.2.8 N <sub>2</sub> Physisorption .....	99
4.3 Results and discussion.....	101
4.3.1 Effect of HME processing regime on the API physical state .....	101
4.3.2 XRD and DSC analysis .....	104
4.3.3 Structural characterisation of ASDs by phase contrast tomography .....	106
4.3.4 Analysis of the API-rich crystalline clusters .....	108
4.3.5 Impurity distribution .....	110
4.3.6 Polymer phase homogeneity .....	112
4.3.7 Pore fraction analysis.....	114
4.3.7.1 Porosity quantification .....	115
4.3.7.2 Pore size and shape .....	117
4.3.7.3 Pore orientation.....	119
4.3.8 Surface area measurements by N <sub>2</sub> physisorption.....	121
4.4 Conclusions .....	123
Chapter 5 ASD Surface Crystallisation as a Strategy for Early-Stage Physical Stability Assessment.....	125
5.1 Introduction .....	126
5.2 Materials and methods.....	127

5.2.1 Materials .....	127
5.2.2 Methods .....	127
5.2.2.1 Preparation of amorphous solid dispersions by hot melt extrusion (HME) .	127
5.2.2.3 Differential Scanning Calorimetry (DSC) .....	127
5.2.2.4 X-ray diffraction (XRD) .....	128
5.2.2.5 Time-of-flight secondary ion mass spectroscopy (ToF-SIMS).....	128
5.2.2.6 Kinetics of surface crystallisation .....	129
5.2.2.7 Scanning electron microscopy (SEM) .....	130
5.2.2.8 Optical microscopy .....	130
5.3. Results and discussion.....	132
5.3.1. ASD surface stability .....	132
5.3.1.1 Drug-rich clusters surface coverage.....	132
5.3.1.2 Crystal morphology.....	141
5.3.2 Bulk crystallinity.....	144
5.3.2.1 DSC crystallinity quantification.....	144
5.3.2.2 XRD crystallinity .....	145
5.4. Conclusions .....	148
Chapter 6 Application of the Low-frequency Raman Solubility Method to a Commercially Relevant Model Compound .....	149
6.1 Introduction .....	149
6.2. Materials and methods.....	150
6.2.1 Materials .....	150
6.2.2 Methods .....	151
6.2.2.1 Blending.....	151
6.2.2.2 Hot melt extrusion (HME) .....	151
6.2.2.3 API-polymer solubility determination .....	153
6.2.2.4 Differential Scanning Calorimetry (DSC) .....	153
6.2.2.5 X-ray diffraction (XRD) .....	153
6.2.2.6 Selected Ion Flow Tube - Mass Spectrometry (SIFT-MS) .....	153
6.2.2.7 Time-resolved X-ray Diffraction .....	154

6.3 Results and discussion.....	156
6.3.1 Low-frequency Raman solubility determination.....	156
6.3.2 DSC and XRD analysis .....	162
6.3.3 Accelerated stability study – rapid screening tool.....	163
6.3.4 Volatiles emitted during extrusion.....	165
6.4 Conclusions .....	170
Chapter 7 General Conclusions and Future Work .....	171
7.1 General conclusions .....	171
7.2 Future work .....	174
7.2.1 Equilibrium assumption validation.....	174
7.2.2 Refine and validate stability prediction .....	175
7.2.3 Explore the mechanisms of phase separation on the ASD surface.....	175
7.2.4 Investigate spectral features in the low-frequency Raman region.....	175
Bibliography .....	176
APPENDIX A – Additional data for Chapter 2 .....	197
APPENDIX B – Additional data for Chapter 3 .....	199
APPENDIX C – Additional data for Chapter 4 .....	202
APPENDIX D – Additional data for Chapter 5 .....	214
APPENDIX E – Additional data for Chapter 6 .....	220

## List of Figures

Figure 1.1. Biopharmaceutics classification system. ....	3
Figure 1.2, Energy pyramid of the crystalline form, amorphous solid dispersion and amorphous API form. $\mu$ is the chemical potential. Reconstructed from Baghel <i>et al.</i> , 2017.....	5
Figure 1.3. Generations of amorphous solid dispersions with exemplary carrier matrix. ....	8
Figure 1.4. ASD preparation methods. ....	10
Figure 1.5. Schematic representation of ASD failure modes from a (a) molecularly dispersed system to (b) amorphous phase separation and (c) crystallisation.....	12
Figure 1.6. Comparison of the (a) melting point depression, (b) recrystallisation and (c) melting enthalpy methods for approximating equilibrium solubility. ....	15
Figure 1.7. Specific volume variation as a function of temperature for a drug substance in the crystalline, liquid, supercooled liquid and glass states.....	20
Figure 1.8. Schematic phase diagram of the thermodynamic phase behaviour of an API-polymer system displaying the solubility curve (blue line), the miscibility curve (yellow line) and the glass transition temperature (dashed black line). Adapted from Tian <i>et al.</i> , 2013. ....	25
Figure 1.9. EMA and FDA approved ASD-based commercial products from 1985 to 2022. Compiled with data from Bhujbal <i>et al.</i> , 2021, Bennet-Lenane <i>et al.</i> , 2020 and by consulting the FDA drug database and the European Summary of Pharmaceutical Characteristics (SPC). For any drug substance only the year of approval of the first ASD dosage form was considered, independently of the approving regulatory body. ....	35
Figure 1.10. Publications in Scopus database under the term “amorphous solid dispersion” from 1985 to 2023.....	36
Figure 2.1. Chemical structure of A) paracetamol, B) Affinisol15LV and C) Plasdone S630. “n” and “m” represent the structural unit for both polymers. Plasdone S630 is a linear copolymer where $n/m = 6/4$ mass ratio. ....	41
Figure 2.2. Schematic representation of the HME experimental set-up and screw configuration. ....	45

Figure 2.3. THz-Raman spectra of PLSD (green), AFF (blue), amorphous PCM (red) and crystalline PCM (black). .....	49
Figure 2.4. THz-Raman spectral evolution of A-B) PCM-AFF 30-70wt% and C-D) PCM-PLSD 45-55wt% at different processing temperatures. In Figures B) and D) spectra are spatial averages of 20 spectra at each temperature. ....	50
Figure 2.5. THz-Raman spectra of A) PCM-AFF 20 wt% and B) PCM-PLSD 40 wt%. .....	51
Figure 2.6. Phase behaviour of the PCM-PLSD system during extrusion: A) HME processing temperatures and API physical state; B) Estimated equilibrium solubility curve. $C_c$ denotes the critical concentration up to which no crystallinity was found. ....	52
Figure 2.7. Phase behaviour of the PCM-PLSD system during extrusion: A) HME processing temperatures and API physical state; B) Estimated equilibrium solubility curve. $C_c$ denotes the critical concentration up to which no crystallinity was found; * denotes compositions expected to be crystalline at 140°C based on crystallinity of adjacent compositions; ** denotes the composition range where the API amorphous character is not a direct reflection of the polymer solubilisation capacity due to the proximity to the API $T_M$ . ....	54
Figure 2.8. THz-Raman spectra of amorphous PCM and crystalline forms III, II and I with respective recrystallisation temperatures from the amorphous glass .....	55
Figure 2.9. Hot stage microscopy images of A) pure AFF; B) and C) PCM-AFF 20-80 wt% during heating and cooling cycles, respectively; D) pure PLSD upon heating cycle; E) and F) PCM-PLSD 30-70 wt% during heating and cooling cycles, respectively. The scale bar is as indicated for all images. ....	57
Figure 2.10. A) DSC thermographs and B) XRPD diffractograms of PCM, AFF and PCM-AFF extrudates with different API contents. ....	58
Figure 2.11. A) DSC thermographs and B) XRPD diffractograms of PCM, PLSD and PCM-PLSD extrudates with different API contents. ....	60
Figure 3.1. DSC melting point depression method. ....	65
Figure 3.2. Glass transition temperature prediction for: a) PCM-AFF, b) PCM-PVA), c) PCM-EPO, d) PCM-SOL and e) PCM-PLSD. $Kwei$ prediction is depicted by the blue line, whilst the Gordon-Taylor ( $G - T$ ) model is depicted by the red	

line. The DSC experimental $T_g$ values are represented by the black triangles. The $T_g$ error bar represents the standard deviation ( $n = 3$ ). The associated $r^2$ values of the fitted $T_g$ models with respect to the experimental data is showed for each system.....	73
Figure 3.3. Bagley plot of the Hansen solubility parameters. ....	75
Figure 3.4. Plot of $\Delta G_{mix}/RT$ vs drug volume fraction for a) PCM-AFF, b) PCM-PVA, c) PCM-EPO, d) PCM-SOL and e) PCM-PLSD. ....	77
Figure 3.5. Binary temperature-composition phase diagrams for a) PCM-AFF and b) PCM-PLSD with the solubility curves modelled using Flory-Huggins ( $F - H$ ) theory and the empirical method ( $E - M$ ). ....	80
Figure 3.6. Binary temperature-composition phase diagrams for a) PCM-EPO, b) PCM-PVA and c) PCM-SOL with solubility curves modelled using $F - H$ theory and the $E - M$ approach. ....	81
Figure 3.7. Graphical representation of the depressed $\Delta HM$ as a function of drug loading. The extrapolated linear relationship of $\Delta HM$ is based upon least square regression of the experimental data.....	83
Figure 4.1. Experimental set-up at the beamline I13-2. a) Sample preparation schematics and b) sample presentation geometry. ....	95
Figure 4.2. 2D Image processing sequence from a) Raw unprocessed image; b) cropped image defining the region of interest inside the Kapton tube; c) to d) gray-scale images after histogram equalization and intensity adjustment, respectively; e) binary image after thresholding and binarisation: white - foreground (pellets), black – background/noise (empty space inside the Kapton tube); f) binary images after partial background noise removal; g) to h) contrast-inverted images and foreground noise removal; i) image after foreground noise removal; j) “clean” final binary images after the second background noise removal step; k) pellet outer and inner perimeter; l) pellet inner perimeter delimiting the pores; m) “filled” pore area; n) isolated NaCl particles; o) overlay of isolated NaCl clusters, pores and amorphous matrix (AM).....	97
Figure 4.3. Example of 3D segmentation of a 4000 x 4000 x 4000 $\mu\text{m}$ section. a) Unprocessed image, b) segmented solid fraction and c) segmented pores and NaCl. ....	100

Figure 4.4. API-polymer solubility determination: a) example low-frequency Raman spectral data with b) respective PCA outputs for the 50 wt % system. ....	102
Figure 4.5. PCA score plot of all drug loadings and processing temperatures. ....	103
Figure 4.6. Temperature composition phase diagram determined by PCA. ....	103
Figure 4.7. a) XRD and b) DSC analysis of the 50 wt% system processed under all extruding regimes. As a reference, the data of the raw unprocessed materials is also shown. ....	105
Figure 4.8. 3D volume renderings and 2D cross-sections of the 6-months aged pellets. In figures b) to f) the ASD outer surface and the homogenous solid fraction corresponding to the amorphous matrix were made transparent to enable visualisation of existing bulk heterogeneities. ....	107
Figure 4.9. API-rich crystalline clusters present in the aged samples extracted from the morphological-based segmentation. a) To c) overlay of segmented pores and crystalline API clusters superimposed to the raw unprocessed images, with respective crystallite size. d) Quantification of total porosity, fracture regions, API-rich crystalline clusters and amorphous matrix area (average $\pm$ standard deviation, n = 200 cross-sections). ....	109
Figure 4.10. a) Exemplary ToF-SIMS and optical microscopy images acquired on the surface of the 50wt% extrudate. ....	110
Figure 4.11. Representative 3D volume renderings of a) to c) 50 wt% drug loading system extruded at 180°C and d) to f) 10 wt% drug loading system 180°C. In images b), e) and f) the amorphous matrix was made transparent to highlight the NaCl clusters (denoted by the yellow arrows). ....	111
Figure 4.12. Size analysis of the NaCl clusters present in the a) 50 wt%, b) 35 wt%, c) 20 wt% and d) 10 wt % extrudates (calculated as the circle equivalent diameter, CED). ....	112
Figure 4.13. Impact of HME processing temperature and drug loading on the polymer phase homogeneity. a) 2D Cross-sections of all compositions and b) representative 3D volume rendering of the 50 wt% system extruded at 145°C. The black arrows denote the PRH clusters. ....	114

Figure 4.14. Pore size analysis of the a) 50 wt%, b) 35 wt%, c) 20 wt% and d) 10 wt% drug loading systems. Calculated as the length of the major eigenvector of the ellipsoid fitting the pores in 3D) .....	118
Figure 4.15. Shape analysis extracted from the flatness and elongation ratios for the 50wt% drug loading system extruded at a) 180°C), b) 155°C), c) 150°C and d) 145°C. Each point represents an individual pore. The same colour bar scale applies to all processing temperatures. ....	119
Figure 4.16. Pore orientation along the x, y and z axis.....	120
Figure 4.17. Impact of HME processing temperature and drug loading on the N <sub>2</sub> physisorption behaviour and surface area. a) and c) 50wt% solid dispersions extruded at different processing temperatures and b) and d) solid dispersions with varying drug loadings extruded at 180°C (meting regime). ....	122
Figure 5.1. Representative ToF-SIMS images of all drug loadings processed at the respective lowest temperature: 130°C for the 10 wt% and 20 wt% systems, 140°C for the 35 wt% system and 145°C for the 50 wt% drug loading system. The molecular ions/fragments corresponding to the drug are displayed in red, the polymer in green and Na in blue .....	133
Figure 5.2. a) Drug surface coverage quantification over 150 days. The error bar denotes the standard deviation of various ToF-SIMS images acquired on individual pellets (n > 3). Individual data points denote experimental values, which were fitted to the Avrami model. b) Drug enrichment rate on the surface of the solid dispersions.....	136
Figure 5.3. a) ToF SIMS images acquired on the surface of 50 wt% pellets from day 1 to day 28 of storage. The yellow arrows at 14 days of storage denote the appearance of secondary/late-stage nucleation of PCM-rich domains. b) Enlarged ToF SIMS image at 28 days of storage with b) high resolution inset (yellow frame) displaying drug terraced circular crystallites. ....	137
Figure 5.4. Logarithm plot of the crystallisation rate constant (k) as a function of polymer content. High temperature corresponds to 170°C for all drug loadings, middle temperature corresponds to 150°C for the 20 wt% and 30 wt% drug loading systems and 155°C for the 50 wt% system. Low temperature	

corresponds to 130°C for the 20 wt% system, 140°C for 35 wt% system and 145°C for the 50 wt% system.....	138
Figure 5.5. Impact of processing temperature on the ASD surface of the 35 wt% drug loading system. a), b) and c) ToF SIMS images showing residual crystallinity at 135°C and 140°C and newly formed surface crystals at <1 and 28 days of ageing. d) and e) Optical microscopy images taken on the cross-Sectional surface displaying the presence of residual crystallinity at 140°C and circular crystallites across all processing temperatures at 2 and 30 days of ageing, respectively. ....	140
Figure 5.6. Crystal morphology captured by ToF-SIMS. a) and b) Agglomerates of crystallites, c) plate-like crystallites, d) and e) spiral-growth forms growing laterally and towards the bulk, f) spiral-growth forms growing laterally and upwards. The black arrows denote the lateral growth direction. ....	141
Figure 5.7. Growth schematics of the terraced forms. ....	142
Figure 5.8. SEM images of the 50 wt% system processed at 145°C after 30 days of storage. The yellow arrows point to the circular terraced growth forms and black one to the plate-like crystallites.....	143
Figure 5.9. DSC crystallinity quantification at 0, 7, 30 and 150 days of storage. The error bar denotes the standard deviation for different pellets (n=3). ....	145
Figure 5.10. XRPD analysis results at different time points for a) 10wt%, b) 20wt%, c) 35wt% and d) 50wt% drug loading system. ....	147
Figure 6.1. a) SIFT-MS set-up for online VOC analysis. b) sampling position. ....	154
Figure 6.2. Time-resolved X-ray diffraction set-up. a) Device overview displaying the sampling arm and the short sample-to-detector distance. b) Sample holder unit. ....	155
Figure 6.3. Low-frequency Raman results at 20 wt% drug loading. a) Individual component reference spectra. b) Spectra obtained upon extrusion from 180°C to 140°C. c) Rayleigh and Stokes peak intensity plot. d) Principal component analysis score plot. ....	157
Figure 6.4. Low-frequency Raman spectra at 15 wt% drug loading. a) Spectra obtained upon extrusion from 180°C to 140°C with b) the respective Rayleigh and Stokes peak intensity plot. c) Spectra obtained upon extrusion at 100 rpm,	

300 rpm and 500 rpm at 140°C with d) the respective Rayleigh /Stokes intensity plot. ....	160
Figure 6.5. Accelerated stability study. a) Extrudates before and after 30 minutes of water exposure, b) XRD result for the 20 wt% system, c) and d) time-resolved XRD results for the 20 wt% and 25 wt% drug loadings, respectively.....	164
Figure 6.6. Impact of processing temperature on pure polymer. a) SIFT mass spectra upon extrusion from 200°C to 150°C at 100 rpm and b) the respective PCA score plot.....	165
Figure 6.7. Impact of screw speed on the volatile components emitted during extrusion of pure Soluplus. a) SIFT-MS spectra of Soluplus extruded at 200°C and variable screw speed. b) Principal component analysis of SIFT-MS spectra. c) Extrudate appearance showing increasing browning above 300 rpm. ....	166
Figure 6.8. Impact of screw speed on the volatile components emitted during extrusion of pure Soluplus. a) SIFT-MS spectra of Soluplus extruded at 200°C and variable screw speed. b) Principal component analysis of SIFT-MS spectra. c) Extrudate appearance showing increasing browning above 300 rpm. ....	167
Figure 6.9. a) SIFT mass spectra at 50 wt% drug loading with b) the respective PCA score plot. ....	168
Figure 6.10. a) SIFT mass spectra at 10 wt% drug loading upon variable temperature extrusion with b) the respective PCA score plot. c) SIFT mass spectra at 180°C and variable screw speed with d) the respective PCA .....	169
A 1. A) XRPD patterns and B) DSC thermograms of amorphous PCM and crystalline forms III, II and I with respective recrystallisation temperatures from the amorphous glass .....	197
A 2. Hot stage microscopy images showing thermally induced recrystallisation from the amorphous glass. PCM form III (identified by the characteristic spherulitic morphology) recrystallised at 50°C and experienced a solid-state transition to form II at 120°C, which was followed by polymorphic transition to form at 150°C, prior to melting at 170°C.....	198

B 1. XRPD of ball milled physical mixtures.....	199
B 2. Physico-chemical properties used in the F-H and E-M calculations.....	200
B 3. Hansen solubility parameters. ....	201
C 1. Schematic representation of the HME set-up and screw configuration. ....	202
C 2. Example of the sample-to-detector distance optimisation: A) tomograms acquired at a distance of 51 mm from the sample, B) at 21 mm and C) at 11 mm for the 50wt% drug-loading system extruded at 180°C.....	203
C 3. Loading plot of the PCA results showing that the principal component 1 (PC1) describes the broad amorphous shoulder with peak maxima at 12cm <sup>-1</sup> , while the principal component 2 (PC2) mainly captures the API's crystalline lattice vibration modes at 32, 51, 85 cm <sup>-1</sup> .....	204
C 4. THz-Raman spectral data and PCA outputs of a) 10wt%, b) 20wt%, c) 35wt% and d) 70wt% drug loading systems extruded at different temperatures. The black arrow denotes the API crystallinity onset temperature. For the 10wt% and 20wt% systems there was no crystalline API detected at any extruding temperatures.....	205
C 5. XRD and DSC analysis of the a) 10wt%, b) 20wt%, c) 35wt% and d) 70wt% drug loading systems extruded at different temperatures. ....	206
C 6. Image processing sequence for the segmentation of the API-rich crystalline clusters in (1) 2D and (2) 3D of the 6-months aged 50wt% drug-loading system. .....	207
C 7. Processing torque (a) and pressure (b) values at all HME experimental conditions. The HME device has a maximum torque and pressure of 12 Nm and 100 bar respectively. ....	208
C 8. Statistical analysis of the impact of processing temperature on porosity.....	209
C 9. Games-Howell pairwise statistical analysis of the impact of processing temperature on porosity.....	209
C 10. Impact of drug loading on porosity: Welch ANOVA statistical analysis. ....	210
C 11. Impact of porosity quantification method on total porosity: Welch ANOVA statistical analysis.....	210

C 12. Shape analysis of the 35wt% drug loading systems extruded at a) 180°C, b) 145°C, c) 140°C and d) 135°C. ....	211
C 13. Shape analysis of the 20wt% drug loading systems extruded at a) 180°C, b) 150°C and c) 130°C.....	212
C 14. Shape analysis of the 10wt% drug loading systems extruded at a) 180°C, b) 150°C and c) 130°C.....	213
D 1. ToF-SIMS images of the 35wt% drug loading system extruded at 150°C acquired over a period of 150 days. The yellow circles denote the initial drug-rich clusters that constitute active nucleation sites for surface crystallisation upon ageing. ....	214
D 2. Optical microscopy images acquired at 2 and 30 days of storage for the 20wt% drug loading system displaying the appearance of birefringent circular defects that are congruent with surface crystallisation at 30days.....	215
D 3. Optical microscopy images acquired at 2 and 30 days of storage for the 10wt% drug loading system. Despite formation of sharkskin defects there is no evidence of surface crystallisation events. ....	215
D 4. Optical microscopy images acquired at 2 and 30 days of storage for the 35wt% drug loading system displaying the appearance of birefringent circular defects that are congruent with surface crystallisation at 30days.....	216
D 5. Optical microscopy images acquired at 2days (under a polarised light) and 30days (under a bright field OM) of storage for the 50wt% drug loading system. Appearance of crystallites and their further growth is evident. ....	217
D 6. SEM images of the 10wt% system processed at 145°C after 30 days of storage. The yellow arrows point to the circular terraced growth forms and black one to the plate-like crystallites .....	217
D 7. SEM images of the 20wt% system processed at 145°C after 30 days of storage. The yellow arrows point to the circular terraced growth forms and black one to the plate-like crystallites .....	218

D 8. SEM images of the 35wt% system processed at 145°C after 30 days of storage. The yellow arrows point to the circular terraced growth forms and black one to the plate-like crystallites .....	219
E 1. LFR spectra with respective PCA score plot from 7.5wt% to 15wt% drug loadings. ....	220
E 2. LFR spectra with respective PCA score plot from 17.5wt% to 25wt% drug loadings. ....	221
E 3. LFR spectra with respective PCA score plot from 27.5wt% to 50wt% drug loadings. ....	222
E 4. Rayleigh and Stokes peak intensity variation from 12.5wt% to 30wt% drug loading.....	223
E 5. Rayleigh and Stokes peak intensity variation at 40wt% and 50wt% drug loading .....	224
E 6. XRD and DSC analysis of extrudates produced at variable temperatures from 7.5wt% to 15wt% drug loading.....	225
E 7. XRD and DSC analysis of extrudates produced at variable temperatures from 17.5wt% to 25wt% drug loading.....	226
E 8. XRD and DSC analysis of extrudates produced at variable temperatures from 27.5wt% to 50wt% drug loading.....	227

## List of Tables

Table 1.1. Nomenclature and classification of solid dispersions. ....	7
Table 1.2. General factors that influence stability of amorphous solid dispersions. Modified and extended from Bhujbal <i>et al</i> .....	24
Table 1.3. ASD solid-state characterisation techniques with respective length scales, limit of detection (LOD) or limit of quantification (LOQ). ....	28
Table 2.1. Hot melt extrusion experimental conditions for the PCM-AFF system. ..	43
Table 2.2. Hot melt extrusion experimental conditions for the PCM-PLSD system.	44
Table 3.1. Solubility and miscibility values at 25°C. ....	83
Table 3.2. DSC melting point data and Flory-Huggins solubilisation temperatures. DSC T <sub>M</sub> corresponds to the average T <sub>M</sub> values and the error represents the standard deviation (n=3). ....	84
Table 3.3. DSC melting point data (n=3) and E-M solubilisation temperatures with respective r <sup>2</sup> values. ....	85
Table 4.1. HME processing conditions. ....	93
Table 5.1. HME processing conditions. ....	127
Table 5.2. Avrami fitting parameters and mean squared error (MSE). ....	138
Table 6.1. Hot melt extrusion operating conditions. ....	152

## List of abbreviations and symbols

Abbreviation	Meaning
AFF	Affinisol 15 LV
AFM	Atomic force microscopy
API	Active pharmaceutical ingredient
APS	Amorphous phase separation
ASD	Amorphous solid dispersion
BCS	Biopharmaceutics classification system
$C_c$	Critical API concentration
CED	Circle equivalent diameter
DCS	Developability classification system
DEA	Dielectric analysis
DSC	Differential Scanning Calorimetry
DL	Drug loading
DMA	Dynamic Mechanical Analysis
DVS	Dynamic Vapor Sorption
E-M	Empirical Method, variation of Kyeremateng's method
EMA	European Medicines Agency
EPO	Eudragit EPO
FDA	Food and Drug Administration
F-H	Flory-Huggins
$\Phi_{drug}$	Drug volume fraction

$\Phi_{polymer}$	Polymer volume fraction
GI	Gastrointestinal
$\Delta G_{mix}$	Gibb's free energy of mixing
GFA	Glass forming ability
G-T	Gordon-Taylor
ICH	International Council for Harmonisation
$\Delta H$	Melting enthalpy
HSP	Hansen solubility parameters
HME	Hot melt extrusion
HPMC	Hydroxypropylmethyl cellulose
$k$	Crystallisation constant
L/D	Length to Diameter ratio
LFR	Low-frequency Raman
$\lambda_1$	Smallest eigenvalue
$\lambda_2$	Intermediate eigenvalue
$\lambda_3$	Largest eigenvalue
MSE	Mean Square Error
$M_w$	Molecular weight
NaCl	Sodium chlorate
NLDFT	Non local density functional theory
PCA	Principal Component Analysis

PCM	Paracetamol
PDF	X-ray pair distribution function
PLM	Polarised-light microscopy
PLSD	Plasdone
PRH	Polymer-related heterogeneities
PVA	Polyvinyl alcohol
PVP	Polyvinylpyrrolidone
PVP-VA	Polyvinylpyrrolidone vinyl acetate
$R$	Universal gas constant
ROI	Region of interest
SAXS	Small angle X-ray scattering
SEM	Scanning electron microscopy
SIFT-MS	Selected ion flow tube mass spectrometry
SMILES	Simplified Molecular Input Line Entry System
SNV	Standard normal variate
SOL	Soluplus
$S_p$	Pore surface area
ssNMR	Solid-state nuclear magnetic resonance
Sync-PC- $\mu$ CT	Synchrotron phase contrast micro-computed tomography
$T_{extrusion}$	Hot-melt extrusion temperature
TEM	Transmission electron microscopy

$T_g$	Glass transition temperature
TGA	Thermogravimetric analysis
THz-Raman	Terahertz-Raman spectroscopy
$T_M$	Melting temperature
ToF-SIMS	Time of flight secondary ion mass spectrometry
$T_S$	Saturated solubility temperature
$T_{spinodal}$	Spinodal miscibility temperature
UV-VIS	Ultraviolet-visible spectroscopy
VOCs	Volatile organic components
$V_P$	Pore volume
XPS	X-ray photoelectron spectroscopy
XRPD	X-ray powder diffraction
$\chi$	Flory-Huggins interaction parameter
WAXS	Wide angle X-ray scattering

---

## Research outputs

### Publications

1. **Bordos, E.**, Islam, M. T., Florence, A. J., Halbert, G. W. and Robertson, J. Use of Terahertz-Raman Spectroscopy to Determine Solubility of the Crystalline Active Pharmaceutical Ingredient in Polymeric Matrices during Hot Melt Extrusion. *Mol. Pharm.* 16, 4361–4371 (2019).
2. Paladino, E., Doerr, F., **Bordos, E.**, Onyemelukwe, I., Lamprou, D., Florence, A., Gilmore, I. and Halbert, G. W. High spatial resolution ToF-SIMS imaging and image analysis strategies to monitor and quantify early phase separation in amorphous solid dispersions. *Int. J. Pharm.* 628, 122191 (2022).
3. **Bordos, E.**, Das, G., Schroeder, S. L. M., Florence, A. J., Halbert, G. W. and Robertson, J. Probing the interplay between drug saturation, processing temperature and microstructure of amorphous solid dispersions with synchrotron X-ray phase-contrast tomography. *Int. J. Pharm.* 669, 125018 (2025).
4. **Bordos, E.**, Paladino, E., Florence, A. J., Halbert, G. W. and Robertson, J. ASD Surface Crystallisation as a Strategy for Early-Stage Physical Stability Assessment. *Mol. Pharm.* (2023, under construction).

## Conference contributions

1. **Bordos, E.,** Islam, M. T., Florence, A. J., Halbert, G. W. and Robertson, J. Novel Method for API-Polymer Solubility Determination Using Hot Melt Extrusion and THz-Raman Spectroscopy. APS 10<sup>th</sup> International PharmSci Conference, September 2019. Greenwich, UK.

**Poster presentation.**

2. **Bordos, E.,** Islam, M. T., Florence, A. J., Halbert, G. W. and Robertson, J. Novel Method for Solubility Determination of Crystalline Drugs in Polymeric Matrices Using Hot Melt Extrusion and Terahertz-Raman Spectroscopy. FACSS SciX, October 2019. Palms Springs, US.

**Oral presentation, invited speaker.**

3. **Bordos, E.,** Halbert, G. W. and Robertson, J. Real-time analysis of volatiles emitted during hot-melt extrusion in support of continuous manufacturing. Anatune webinar: Rapid, Simplified Residual Solvent and Volatile Impurity Analysis Using SIFT-MS, November 2021. Online.

**Oral presentation.**

4. **Bordos, E.,** Halbert, G. W. and Robertson, J. Emerging continuous manufacturing applications for the pharmaceutical industry. Syft European User Days, May 2022. Online.

**Oral presentation.**

# Chapter 1

## Fundamentals of Amorphous Solid Dispersions: A Literature Review

### 1.1 Introduction

The potential of amorphous solid dispersions (ASD) solving current aqueous solubility challenges within the pharmaceutical industry has been extensively demonstrated, both *in vitro* and *in vivo*. However, poor understanding of the multiple aspects governing their solid-state physical stability and the subsequent difficulty of ensuring long-term product stability has hindered their implementation in commercial drug products. In order to shift the ASD development from trial and error to science-driven, continued efforts are required to develop further understanding of the complex interplay between material properties, processing parameters and ASD physical stability. This Chapter aims to provide a comprehensive literature review on the ASD topic and the main factors determining ASD physical stability.

### 1.2 Poor aqueous solubility

Poor aqueous solubility poses significant hurdles to drug product development of oral solid dosage forms in the pharmaceutical industry. It can reduce the amount of drug

available for absorption, lead to low bioavailability and diminish the drug's inherent therapeutic efficacy.<sup>1</sup> From the multiple factors known to affect the rate and extent of absorption from the gastrointestinal (GI) tract, the solubility of the drug in the available GI fluid volume is of prime importance. If the drug is not in the solution form at the absorption site, it cannot reach the systemic circulation and will not have a therapeutic effect. A well-known example is ritonavir, which is an HIV protease inhibitor drug with an aqueous solubility at pH 6.8 of  $\sim 1 \mu\text{g/ml}$ .<sup>2</sup> With a daily therapeutic dose of 100-200 mg, the volume intake required to dissolve this drug would be about 100-200 L, which is not feasible *in vivo*. Despite this limitation, the percentage of drug candidates having poor aqueous solubility has steadily increased in recent years, as predicted by Lipinski *et al.* two decades ago.<sup>3</sup> It is expected that around 90% of the drugs under development and about 40% of the marketed drugs possess poor aqueous solubility.<sup>4</sup> High throughput screening and computational drug design have largely contributed to this paradigm shift, as they often prioritise hydrophobicity for drug-receptor binding affinity. Recent drug discovery trends also indicate a greater number of drugs emerging beyond "Lipinski's rule of 5" chemical space, especially in terms of molecular weight and number of hydrogen bond acceptors.<sup>5,6</sup> This increasingly diverse and complex molecular pipeline portfolio challenges the classic "drugability" concept and creates the need for new formulation approaches to reduce the risk of compound failure due to low oral bioavailability.

Poorly soluble drugs encompass class II and IV of the Biopharmaceutics Classification System (BCS). The BCS was developed in 1995 by Amidon *et al.* to provide a regulatory framework for *in vivo-in vitro* correlations for immediate release oral dosage forms.<sup>7</sup> It outlines four classes of active pharmaceutical ingredients (APIs) based on their aqueous solubility and intestinal permeability, as indicated in Figure 1.1. An API is deemed poorly soluble if the highest single dose strength is not soluble in 250 ml of aqueous media over the entire GI pH range (1.2 to 6.8 at  $37 \pm 1^\circ\text{C}$ , as per the European Medicine Agency guidelines on BCS).<sup>8</sup> This often results in solubility values below  $10 \mu\text{g/ml}$ , which is defined as practically insoluble according to the United States Pharmacopeia (USP) and British Pharmacopeia (BP) solubility criteria.<sup>9</sup> Differentiation between class II and class IV drugs is based on the intestinal membrane permeability that is another barrier to drug absorption. Although this classification

system considers solubility and permeability as two distinct aspects, the solubility-permeability interplay should be considered as suggested by Miller *et al.*<sup>10</sup> A trade-off between solubility increase and permeability decrease has been reported when using surfactant- and cyclodextrin-based approaches to increase solubility.<sup>10,11</sup>

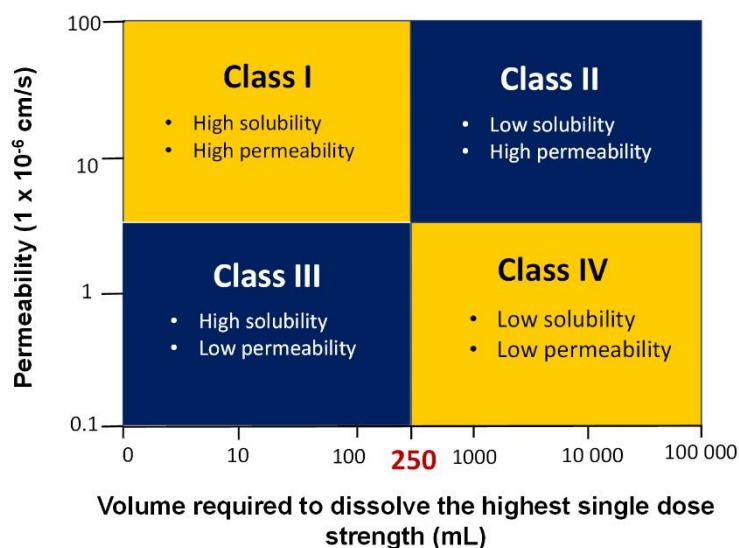


Figure 1.1. Biopharmaceutics classification system.

Because of BCS' regulatory focus on assurance of bioequivalence and patient safety, an alternative classification system was introduced by Butler *et al.* in 2010 to improve guidance for formulation development of new drug candidates for oral delivery, the Developability Classification System (DCS).<sup>12</sup> Key differences between BCS and DCS is that the latter considers compound solubility under small intestinal conditions using fasted-state simulated intestinal fluid (FaSSIF) and assumes higher GI fluid volume (500 ml instead of 250 ml). Consequently, many drug substances with pH-dependent solubility classified as class II drugs within BCS have been reclassified as class I drugs in the DCS (e.g., Ibuprofen and Ketoprofen). BCS class II drugs were further divided into subclasses IIa (dissolution rate limited) and IIb (solubility limited). Distinction between these subclasses is given by the solubility limited absorbable dose, introduced to account for the fact that low solubility of class II drugs may be compensated by high permeability.

For any drug substance, poor aqueous solubility can be derived from the drug's lipophilicity and strength of the intermolecular forces within the crystal lattice.<sup>13</sup> Thus,

several solubility enhancement techniques have been developed to address these two properties separately. For highly lipophilic drugs (“grease ball compounds”), approaches such as solubilisation in co-solvents or surfactant addition, formulation of micro- or nano-emulsions and complexation with cyclodextrins are frequently employed. However, their utility is limited as the achievable drug loading is typically low.<sup>14</sup> When poor aqueous solubility results from strong intermolecular forces within the crystal lattice (“brick dust compounds”), various solid-state engineering approaches are available. These include but are not limited to formation of salts, co-crystals and solvates, particle size reduction and amorphous solid dispersions (ASDs). There is no universally applicable method and each one has advantages and potential limitations. The reader is referred to relevant literature for additional details.<sup>15</sup> Among the aforementioned methods, amorphous solid dispersions comprise one of the most successful formulation approaches. Compared to methods that preserve the crystalline drug form, ASDs can induce a 1.1 to 1000 fold solubility increase.<sup>16</sup> An ASD is a solid dispersion in which the active pharmaceutical ingredient is dispersed in the amorphous state within a polymeric carrier matrix.

### **1.3 Amorphous solid dispersions and the amorphous state**

The crystalline to amorphous conversion of a compound is characterised by loss of long-range three dimensional order and increase in free energy, entropy, enthalpy and chemical potential as depicted in Figure 1.2.<sup>17</sup> The absence of a crystal lattice and the disordered structure reduce the energy penalty required to dissociate the molecules and generally, the amorphous drug has better apparent solubility properties than its crystalline counterpart.<sup>18,19</sup> However, this advantage comes with inherent stability liabilities. As a result of the higher free energy, the amorphous state is metastable and thermodynamically driven for phase separation and crystallisation. Incorporating the amorphous drug in a polymer matrix can improve physical stability whilst retaining the solubility advantage. Stability enhancement conferred by polymer-based ASDs has been attributed to various mechanisms, including presenting a physical barrier for API diffusion, increasing the glass transition temperature (anti-plasticisation effect), reducing molecular mobility, increasing configurational entropy, reducing chemical potential, and establishing drug-polymer molecular interactions.<sup>20-22</sup> ASDs enhance the

API dissolution rate and increase its apparent solubility not only as a result of the absence of lattice energy barrier but also due to increased surface area, increased wettability, maintenance of a supersaturated environment upon dissolution and higher GI membrane flux.<sup>23,24</sup>

Despite the stabilising effects presented by the polymer matrix, the manufacture of stable ASDs remains challenging and often requires optimisation of formulation, manufacturing routes and processing parameters to attain reliable drug product quality. The lack of control over the potential risk of phase separation and crystallisation during

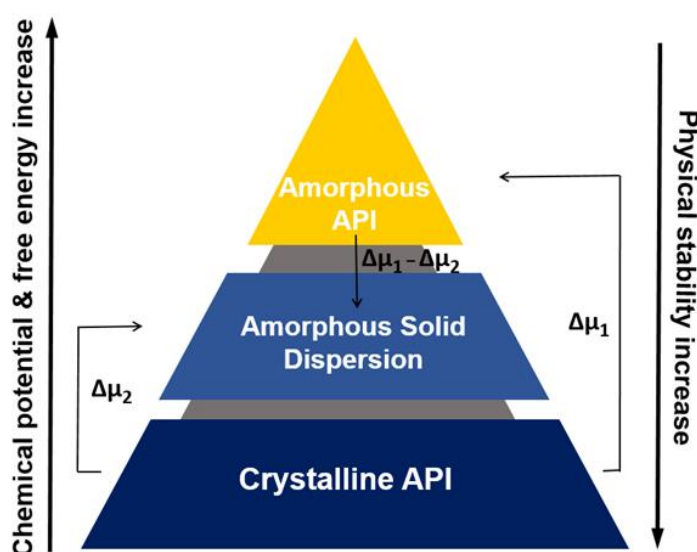


Figure 1.2, Energy pyramid of the crystalline form, amorphous solid dispersion and amorphous API form.  $\mu$  is the chemical potential. Reconstructed from Baghel *et al.*, 2017.

manufacturing, storage, transportation and dissolution is the main factor restricting a wider adoption of ASD formulation approaches in modern medicine manufacturing.<sup>25-27</sup> Crystallisation of the API during any of these stages may compromise the physical integrity of the solid dosage form and reduce the potential solubility advantage, limiting product shelf-life and therapeutic efficacy. Thus, a mechanistic understanding of the factors determining physical stability of amorphous solid dispersions is paramount to assure quality, safety, and efficacy of this class of pharmaceutical drug product. Furthermore, as the cost of bringing a drug compound from discovery to market is expected to exceed 1 billion U.S. dollars<sup>28</sup> and with the average investment in research and development (R&D) phases representing around 20% of this value,<sup>29</sup>

the need for cost saving is evident. The physical stability aspects will be further discussed in Section 1.5.

#### **1.4 Classification of amorphous solid dispersions**

The term solid dispersion was first introduced by Chiou and Riegelman as “the dispersion of one or more active ingredients in an inert carrier matrix at solid-state prepared by melting (fusion), solvent, or melting– solvent method.”<sup>30</sup> This broad definition encompasses many types of solid dispersions, such as eutectic mixtures, crystalline and amorphous solid solutions, and suspensions. The various types of solid dispersions are distinguished based on the molecular arrangement of the individual components, as indicated in Table 1.1. The most relevant solid dispersions in current pharmaceutical practice are amorphous solid solutions, amorphous solid suspensions and crystalline solid suspensions.

Table 1.1. Nomenclature and classification of solid dispersions.

	Type of solid dispersion	Polymer	API*	Number of phases
I	Eutectic mixture	C	C	2
II	Crystalline solid solution	C	M or C	1 or 2
III	Crystalline solid suspension	A	C	2
IV	Amorphous solid solution	A	M	1
V	Amorphous solid suspension	A	A	2

\*A: amorphous, C: crystalline, M: molecularly dispersed.

The term amorphous solid dispersion is an umbrella concept that evolved from the classic solid dispersion definition. Presently, it refers to systems where the API is molecularly dispersed in an amorphous polymeric matrix, although it covers both amorphous solid solutions and amorphous solid suspensions. Amorphous solid solutions, also known as amorphous glass solutions, comprise a pharmaceutically desirable single-phase system where the API is homogeneously dispersed in the polymer at a molecular level.<sup>27</sup> This is the ideal conformation as it is likely to have better long-term physical stability. In amorphous solid suspensions, the API is not molecularly dispersed, but consists of small amorphous domains dispersed throughout the polymeric matrix. Amorphous suspensions are not frequently intentionally designed but result from partial API-polymer miscibility or limited mixing during manufacturing. Lastly, crystalline solid suspensions are the most stable type of solid dispersion, wherein the API is in its thermodynamically stable crystalline configuration. As a consequence of the crystalline drug state, such systems provide only a moderate improvement of the apparent solubility mainly via particle size reduction and increased wettability.<sup>31</sup> Despite the archetypal ASD classification, heterogeneous ASDs where the API is only partially dissolved and the excess fraction is suspended in the amorphous and crystalline states (which may involve one or more polymorphic forms) are frequently formed because of limited control and understanding of API-polymer solubility and miscibility.

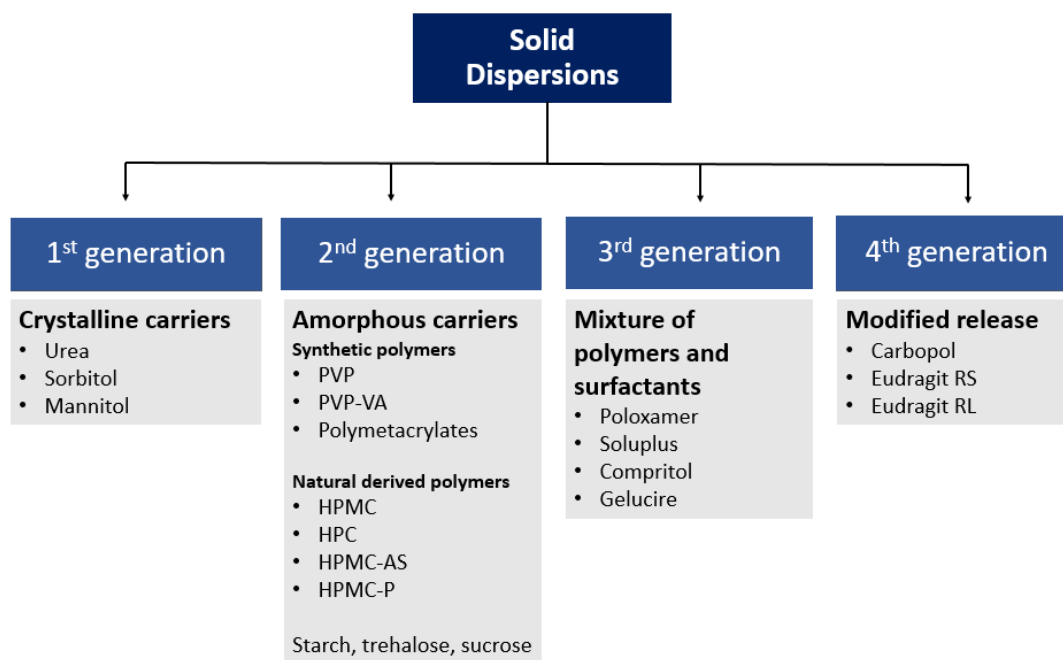


Figure 1.3. Generations of amorphous solid dispersions with exemplary carrier matrix.

According to the type of carrier matrix, solid dispersions are further classified as first, second, third or fourth generation, as indicated in Figure 1.3. First generation solid dispersions were prepared using crystalline carriers, like urea, sorbitol and mannitol.<sup>32,33</sup> These tend to present the slowest drug release rates.<sup>34</sup> ASDs consisting of an amorphous drug in combination with an amorphous polymeric carrier constitute the second generation. Amorphous polymeric carriers can be divided into synthetic polymers such as vinyl polymers (e.g., polyvinylpyrrolidone (PVP) and polyvinylpyrrolidone-co-vinyl-acetate (PVP-VA)) and natural/cellulose derived polymers such as hydroxypropyl methylcellulose (HMPC). Further polymer classifications are possible based on the type of constituent monomer, physical state, relative hydrophilicity and ionisation potential.<sup>35,36</sup> Independently of the classification criteria, the most ubiquitous polymers in contemporary ASD formulation are PVP, PVP-VA, HMPC, HMPC-AS (hydroxypropyl methylcellulose acetyl succinate) and Soluplus (a graft copolymer comprising of polyvinyl caprolactam–polyvinyl acetate–polyethylene glycol).<sup>35</sup> ASD formulations that contain more than one polymer or additional excipients such as surfactants comprise the third ASD generation. These are usually added to enhance drug release and facilitate processability. The fourth

generation is intended for controlled release of drug substances with short biological half-lives.

## **1.5 Manufacturing methods**

Various manufacturing techniques are used to prepare ASDs, which can be broadly classified into solvent- and fusion-based methods. Each group encompasses many technologies, as schematically shown in Figure 1.3. Other processes based on mechanical activation (e.g., ball milling or cryo-milling) can disrupt the crystalline lattice and render the drug amorphous. However, the degree of amorphisation and the level of robustness are generally low and hence, these methods are of limited usefulness beyond lab-scale manufacturing.<sup>37,38</sup>

Solvent-based methods involve the dissolution of the API compound and polymer carrier in a solvent system that is rapidly evaporated to precipitate the amorphous product. The fusion-based methods promote the dissolution of the API in a molten/softened polymer. Traditionally, this requires heating the drug-polymer mixture to temperatures close to the drug's melting point and above the polymer's glass transition temperature in order to dissolve the drug in the polymer matrix. This can be followed by rapid cooling to kinetically trap the amorphous form. Examining the main manufacturing methods of marketed ASD formulations, spray drying (SD) and hot-melt extrusion (HME) emerge as the most frequently used methods in industrial settings.<sup>39</sup> Therefore, the main reasons underpinning the choice of each technique will be discussed in more detail in the Section below.

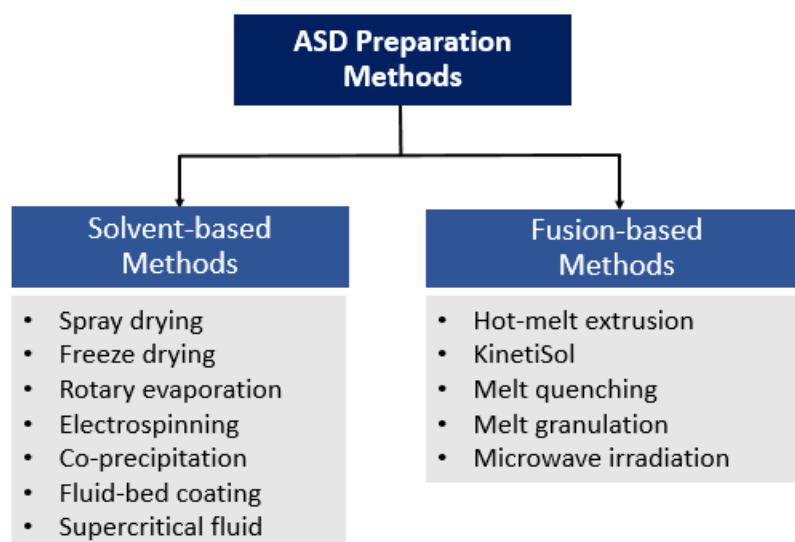


Figure 1.4. ASD preparation methods.

The selection of the appropriate manufacturing technique is based on the physicochemical properties of the drug substance and polymer, and the intended use. Thermostable compounds with low melting points are usually processed with HME, whilst high melting points in combination with high solubility in volatile solvents favours SD. Although there is evidence to suggest that these two methods have the potential to produce amorphous materials with different solid-state properties, there is a paucity of studies performing a direct head-to-head comparison. An interesting study by Agrawal *et al.*, that reported the impact of HME and SD on the physical stability, manufacturability and physicochemical properties of ASDs of compound X and PVP-VA.<sup>40</sup> The authors reported differences in material properties such as surface area, morphological structure, powder densities and flow characteristics. Compared to HME, SD solid dispersions were physically less stable under accelerated stability conditions. Similar results were reported by Haser *et al.* for a Naproxen-PVP K25 system.<sup>41</sup> In this study, SD materials were more susceptible to recrystallisation during processing and storage. A larger number of nucleation sites and higher surface area made SD materials more prone to physical instability. This trend is reflected in the increasing number of HME patents, highlighting the growing importance of this processing technique in the ASD manufacturing landscape. The main advantages over other ASD technologies are the absence of solvents, continuous processing, high

throughput, highly scalable, amenability for process analytical technology (PAT) implementation, and suitability for coupling downstream processing operations like tableting and 3D printing.<sup>42</sup> Despite these advantages, many challenges still exist, particularly for thermally labile compounds and polymers with limited thermoplasticity. Avoidance of thermal degradation and absence of residual crystallinity are two critical quality attributes of HME-based ASDs that must be monitored to ensure consistent drug product quality. It should be noted that as there is a dual energy input from heat transfer from the barrel and heat generated from shear between screws and material (viscous dissipation), modelling of temperatures and API-polymer mixing within the HME device becomes quite complex.<sup>43</sup>

Thermal stability for SD processes is not as important as the exposure time to high temperatures is relatively short. For spray drying, the choice of the solvent system is crucial. Both polymer and API should fully dissolve to ensure an efficient and economical process. The solvent(s) used should be volatile and residual amounts must be carefully controlled within the ICH limits. The inclusion of residual solvents or water in the final formulation may decrease the system's glass transition temperature and induce amorphous phase separation and/or crystallisation phenomena.<sup>44,45</sup>

## **1.6 Factors affecting ASD physical stability**

The physicochemical aspects governing the solid-state physical stability of amorphous solid dispersion formulations can be largely categorised into thermodynamic, kinetic and environmental factors.<sup>46</sup> The thermodynamic aspects dictate the drive for phase separation and crystallisation, while the kinetic factors determine the rate and extent thereof. The environmental aspects include temperature, humidity and mechanical stress exposure, which can affect both thermodynamic and kinetic stability aspects.

According to classic nucleation theory, crystallisation of an amorphous drug in an ASD system is a two-step process involving nucleation and crystal growth.<sup>24</sup> Nucleation involves formation of minute molecular clusters/nuclei capable of independent existence. This step is followed by nuclei growth until a complete crystalline lattice is built. As nucleation requires a certain amount of energy to overcome the high interfacial tension between small particles (i.e., activation energy),

crystallisation will not start until a certain degree of supersaturation is reached. As a result, ASD destabilisation via non-classical nucleation pathways is also possible. For example, an intermediate metastable structure may form in which amorphous drug-rich and polymer-rich aggregates are formed. However, the precise relationship between the resultant amorphous phase separation (APS), physical stability and product performance has not been fully established yet. The general belief is that API-rich domains can trigger crystallisation and act as precursors for the crystalline phase.<sup>47</sup> Nonetheless, various studies have reported minimal to no impact of amorphous phase separation on the *in vitro* and *in vivo* dissolution performance.<sup>48</sup> In some cases, APS has been deliberately induced to enhance the API dissolution rate and increase the degree of supersaturation reached (without promoting crystallisation), as reported by Li and Taylor for a Lopinavir-HPMC system.<sup>49</sup> This apparent paradox can be explained by various factors, including surface area increase and formation of fast dissolving polymer-rich domains that promote the disintegration of the API-rich domains upon dissolution. Other studies suggest that the formation of API-rich amorphous phases may also improve the drug's oral absorption by enhancing its GI membrane permeability.<sup>50,51</sup>

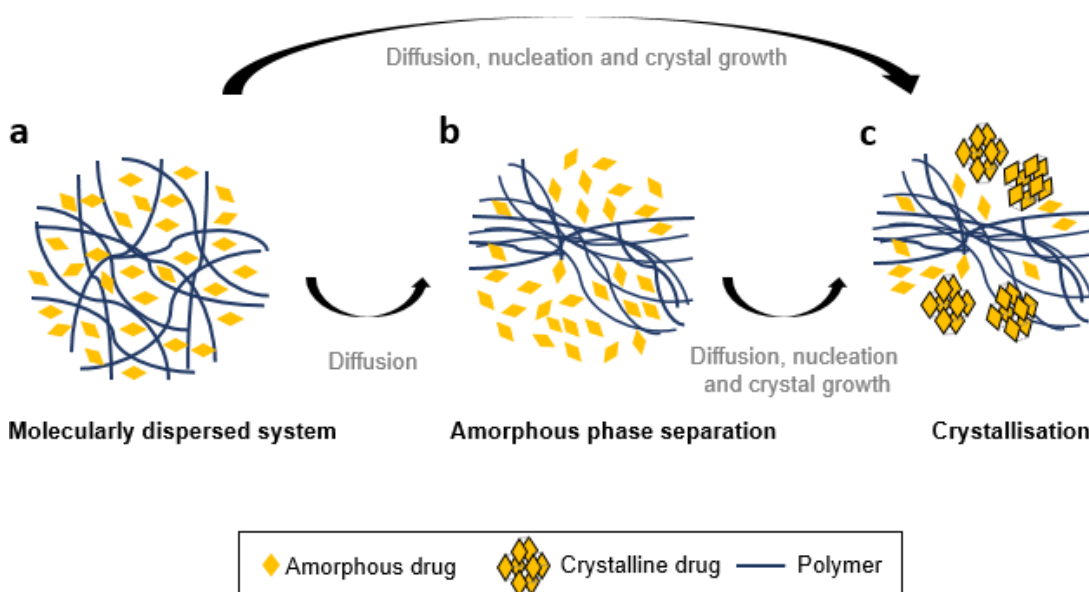


Figure 1.5. Schematic representation of ASD failure modes from a (a) molecularly dispersed system to (b) amorphous phase separation and (c) crystallisation.

## **1.6.1 Thermodynamic aspects**

The thermodynamic perspective on ASD physical stability comes from regular solution theory, where miscibility and solubility are applied to describe mixing solutions and dissolving solutes into solvents. Within the ASD context, the API is generally defined as the solute and the polymer as the solvent because it is often present in a higher mass fraction than the API. Although these two concepts are used interchangeably in the literature, the term “solubility” describes the solubility of crystalline API into soften/liquefied polymer and the term “miscibility” refers to the mixing process of both amorphous API and polymer. Even though this is an oversimplified view, it provides a theoretical framework to understand and investigate ASD physical stability.

### **1.6.1.1 API-polymer solubility**

The solubility of API in the polymer matrix is one of the critical factors determining ASD solid-state physical stability. If the API concentration in the ASD is below its saturation concentration in the polymer matrix, the system is thermodynamically stable. Conversely, if the API exceeds the saturated solution concentration, the ASD will be prone to crystallisation and phase separation. However, experimental determination of the solubility of an API in a polymer matrix is difficult because both materials are usually in the solid-state at room/storage temperatures, and due to high viscosity and low molecular mobility in the glass state, equilibrium solubility is difficult to reach and test.<sup>52,53</sup> Apart from API solubility measurement in a low molecular weight liquid monomer or oligomer (when feasible), currently, there is no established experimental method to assess API-polymer solubility at ambient temperatures. Various thermal methods based on differential scanning calorimetry (DSC) have been proposed to determine API-polymer solubility at elevated temperatures and extrapolate it to storage temperatures. These include the melting point depression method, the recrystallisation method, the melting enthalpy approach and thereof variations.<sup>52,54,55</sup>

The melting point depression approach was introduced to the ASD context by Marsac *et al.* and exploits the API chemical potential reduction in the presence of a miscible polymer.<sup>56</sup> In this method, API–polymer physical mixtures of known compositions are prepared by geometric mixing, ball milling or cryo-milling and analysed by DSC at low heating rates (0.1°C/min to 5°C/min) to promote the dissolution of the drug in the polymer matrix. The introduction of milling steps before DSC analysis aims to compensate for the slow dissolution kinetics by reducing particle size to allow for diffusive mixing.<sup>53</sup> The plot of the depressed melting points as a function of composition provides the solubility curve. The main disadvantages of this approach are that (1) solubility data cannot be obtained close or below T<sub>g</sub> since the drug dissolution kinetics becomes much slower than the time scale of the measurement and (2) observation of the melting point is restricted to high drug loadings. Despite these limitations, this is still the most frequently used methodology to determine drug–polymer solubility.

The recrystallisation method by Mahieu *et al.* postulates that the ASD demixing process is considerably faster than the dissolution of the API in the polymer matrix.<sup>55</sup> Thus, the saturated solubility state is reached by demixing. In this protocol, supersaturated ASDs prepared by cryo-milling are annealed at different temperatures below the drug’s melting point for 2-3 h to crystallise the excess drug and reach equilibrium solubility. After annealing, the sample is subjected to a cooling-heating cycle to determine the T<sub>g</sub> of the material. The amount of the drug remaining in the amorphous state is then derived from the T<sub>g</sub> of the annealed material using pre-determined calibration curves or the Gordon-Taylor Equation.

Lastly, the enthalpy approach is based on the premise that the fraction of the dissolved API does not contribute to the melting endotherm. As a result, linear regression is applied to estimate the relationship between experimental values of melting enthalpy and API concentrations in a series of API-polymer physical mixtures. The solubility of the API in the polymer at any given annealing temperature is estimated as the x-intercept from the regression Equation. This corresponds to the composition where no residual API crystallinity would be observed. Schematic representation of these three methods is shown in Figure 1.6.

Overall, these methods involve long exposure times to elevated temperatures and risk thermal degradation, chemical instability and solubility under- or overestimations because of mixing or demixing restrictions imposed by the melt rheological properties. Furthermore, they require equilibrium assumptions, which limits their wider application.

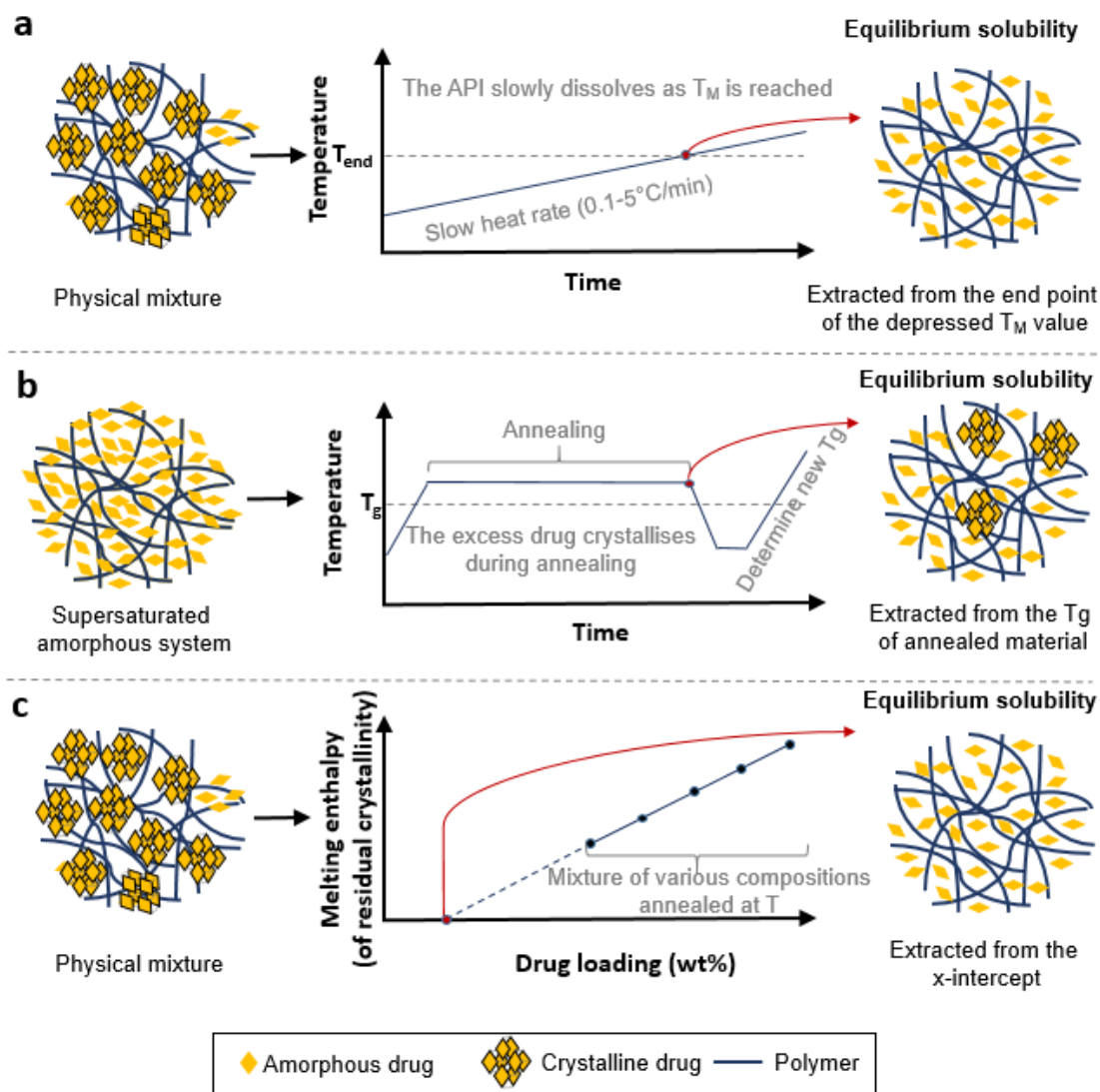


Figure 1.6. Comparison of the (a) melting point depression, (b) recrystallisation and (c) melting enthalpy methods for approximating equilibrium solubility.

### 1.6.1.1.1 Flory – Huggins theory

Experimental solubility data obtained from the DSC methods can be fitted with the Flory-Huggins (F-H) model to predict solubility at storage temperatures by extrapolation. The F-H theory is a well-known lattice-based solution model developed to describe polymer-polymer and polymer-solvent mixing based on the Gibb's free energy change.<sup>56</sup> According to this model, the free energy of mixing ( $\Delta G_{mix}$ ) of an API-polymer system can be described by Equation 1.1:

$$\frac{\Delta G_{mix}}{RT} = \phi_{drug} \ln \phi_{drug} + \frac{\phi_{polymer}}{m} \ln \phi_{polymer} + \phi_{drug} \phi_{polymer} \chi \quad (1.1)$$

Above,  $\phi_{drug}$  and  $\phi_{polymer}$  are the drug and polymer volume fractions, respectively,  $m$  is the ratio of the polymer volume to that of the drug,  $R$  is the molar the gas constant,  $T$  is the absolute temperature and  $\chi$  is the F-H interaction parameter. The first two terms on the right side of Equation 1.1 represent the entropic contribution, which favours API solubilisation and the last term acknowledges the enthalpic contribution. Hence, the enthalpic component described by the  $\chi$  interaction parameter determines whether solubilisation may be spontaneous. Negative  $\chi$  values indicate attractive forces between the API and the polymer, which favours solubilisation. On the contrary, positive  $\chi$  values suggest repulsive forces and describe API-polymer systems with limited solubility. The use of the DSC data to calculate the  $\chi$  value can be obtained from the application of the Nishi-Wang modified F-H Equation:<sup>57</sup>

$$\frac{1}{T_m^{mix}} - \frac{1}{T_m^{pure}} = \frac{-R}{\Delta H_{fus}} \left[ \ln \phi_{drug} + \left(1 + \frac{1}{m}\right) \phi_{polymer} + \chi \phi_{polymer}^2 \right] \quad (1.2)$$

Above  $T_m^{mix}$  and  $T_m^{pure}$  are the melting points of the drug-polymer physical mixture and pure drug, respectively, and  $\Delta H_{fus}$  is the melting enthalpy of the drug. To develop temperature-composition phase diagrams that accommodate variations in temperature, the temperature dependence of the API-polymer interaction parameter is determined according to:

$$\chi = A + \frac{B}{T} \quad (1.3)$$

Through the application of this Equation, a plot of  $\chi$  vs  $1/T$  enables the calculation of constants A and B. Once these have been determined, it is possible to estimate solubility at any temperature value. Although the F-H theory cannot account for the impact of specific molecular interactions such as hydrogen bonding, it has been effectively applied to several API-polymer systems.<sup>58-60</sup> Nonetheless, examples of inaccurate predictions using this approach have also been reported.<sup>53,61</sup> Alternative methods include the empirical model by Kyeremateng et al.,<sup>62</sup> and the Perturbed-Chain Statistical Associating Fluid Theory (PC-SAFT) developed by Gross and Sadowski.<sup>63-</sup>

65

### 1.6.1.2 API-polymer miscibility

ASD phase homogeneity is the prime miscibility indicator. Thus, the glass transition temperature ( $T_g$ ) of the ASD is frequently used to assess miscibility. A single  $T_g$  value intermediate of the pure polymer and API is often taken as the leading qualitative indicator of phase homogeneity. However, calorimetric  $T_g$  measurements via DSC analysis require a minimum 10°C difference and a minimum domain size 30-100 nm range for accurate determination. Moreover, it should be noted that the presence of single  $T_g$  event is a measure of the state of dispersion at the point of analysis and that miscibility is only inferred rather than unambiguously demonstrated.

Alternatively, the glass transition temperature of the mixture ( $T_g^{mix}$ ) can also be predicted based on the weight fraction contributions of each component. Although there are other approaches available, such as the Fox and the Couchman-Karasz thermodynamic models, the most widely used model for the  $T_g^{mix}$  estimation is the Gordon-Taylor Equation:<sup>66</sup>

$$T_g^{mix} = \frac{w_1 T_{g1} + K w_2 T_{g2}}{w_1 + K w_2} \quad (1.4)$$

Above,  $w$  and  $T_g$  are the weight fraction and glass transition temperature of each component, while subscripts 1 and 2 represent components with the lowest and highest  $T_g$ , respectively. Constant K depends on the thermal expansion coefficient of the

components upon their transformation from the glassy to the rubbery state and it can be calculated using the Simha-Boyer rule:<sup>67</sup>

$$K = \frac{\rho_1 T_{g1}}{\rho_2 T_{g2}} \quad (1.5)$$

where  $\rho_1$  and  $T_{g1}$  are the density and glass transition temperature of the amorphous component with the lowest  $T_g$ , and  $\rho_2$  and  $T_{g2}$  are the density and glass transition temperature of the amorphous component with the highest  $T_g$ , respectively. Deviations from the theoretical  $T_g$  values can determine the mixing behaviour and reflect potential interactions between the drug and the polymer. If strong drug-polymer intermolecular interactions are present, positive  $T_g$  deviations will occur. Conversely, if strong drug-drug or polymer-polymer interactions are present, negative  $T_g$  deviations are seen.

#### 1.6.1.2.1 Solubility parameter approach

Another qualitative estimation of drug-polymer miscibility is obtained from the Hildebrand and Hansen Solubility Parameter (HSP) approach. Hildebrand defined the solubility parameter ( $\delta$ ) as the square root of the cohesive energy density that can also be expressed as:<sup>68</sup>

$$\delta = \sqrt{\frac{\Delta E_v}{V_m}} \quad (1.6)$$

Where  $E_v$  is the energy of vaporisation and  $V_m$  is the molar volume. For a given pair of materials, the closer are the  $\delta$  values, the greater is their similarity, and thus their affinity is stronger. The Hansen solubility parameters represent a step forward from Hildebrand as it splits the total cohesive energy into contributions from atomic dispersion forces ( $\delta_d$ ), dipole-dipole/ polar contributions ( $\delta_p$ ) and hydrogen bonding ( $\delta_h$ ). This approach examines the molecular structure of both components and ascribes values to each of them based on the total contributions of the functional groups. The Equation for determining the total HSP value ( $\delta_{\text{Total}}$ ) of a substance is shown below:

$$\delta_{\text{Total}} = (\delta_d^2 + \delta_p^2 + \delta_h^2)^{0.5} \quad (1.7)$$

The difference in the magnitude of the solubility parameters of materials is used to make rough predictions about their miscibility. Systems with  $\Delta\delta < 7\text{MPa}^{1/2}$  are likely to be miscible, whereas  $\Delta\delta > 10\text{MPa}^{1/2}$  are likely to be immiscible.<sup>69</sup> Solubility parameters are widely used for rapid screening and ranking potential polymer carriers, however, inadequacies in the theory require extensive experimental validation. The major limitations of this approach is that (1) cohesive energy density is not a defined concept for molecules that cannot be vaporised like polymers and (2) it fails to account for factors such as temperature, concentration and viscosity that are known to affect mixing dynamics.<sup>70,71</sup> Furthermore, its application is also constrained by limited data for many relevant structural groups.

## 1.6.2 Kinetic aspects

### 1.6.2.1 Glass transition temperature and molecular mobility

The glass transition temperature is a defining feature of all amorphous glasses. The molecular phenomena occurring at the  $T_g$  can be more easily understood by analysing the free volume variations of a substance as a function of temperature, as depicted in Figure 1.5. For a crystalline compound (blue line), the specific volume increases linearly with increasing temperature until the melting point ( $T_M$ ) is reached. At  $T_M$ , a discontinuous increase in free volume is observed representing a first-order thermodynamic transition from the crystalline solid-state to the liquid (amorphous) state. If the molten material is rapidly cooled (i.e., melt quenching), it may attain a supercooled liquid or rubbery state without crystallising (black line). Upon further cooling, a change in the specific volume slope is observed at  $T_g$  as the material solidifies and changes from the flexible rubbery state into a brittle glass state. Melt quenching into the glassy state introduces a non-equilibrium structure that tends to approach an equilibrium state via small-scale relaxation processes also known as physical ageing, causing volume contraction and densification of the sample.<sup>72</sup> The ageing process can also be detected through the time evolution of other thermodynamic



cooperative movement of multiple neighbouring molecules. Below  $T_{g\alpha}$ , the molecules are less free to rotate and only secondary or  $\beta$ -relaxation processes occur (i.e., local mobility). These involve rotations around chemical bonds or motions of entire molecules in isolated glass regions, as reported by Johari and Goldstein for completely rigid molecules.<sup>77</sup>

Hancock *et al.* provided the longstanding rule of thumb of ASD storage temperature of 50°C below  $T_g$ .<sup>78</sup> The authors observed that molecular mobility at temperatures 50°C below the  $T_g$  of three amorphous materials (indomethacin, PVP and sucrose) was sufficiently low to be considered kinetically “frozen” over the expected lifetime of a pharmaceutical product. Thus, the scientific consensus was that an amorphous product should be stored at least 50°C below its  $T_g$  to reduce molecular mobility and ensure solid-state physical stability. Nonetheless, multiple exceptions to this principle have been reported.<sup>79–82</sup>

For many years, the potential role of local motions as precursors of nucleation and crystallisation was poorly understood. As a result, selection of storage temperature has been only based on the overall  $T_g$  value depicting global mobility. More recently, Kissi *et al.* reported an empirical correlation between the temperature at which  $\beta$ -relaxation processes occur ( $T_{g\beta}$ ) and the API recrystallisation onset temperature for nine compounds.<sup>83</sup> The authors demonstrated that if storage temperature is below  $T_{g\beta}$ , no API crystallinity is observed, whereas if storage temperature is above  $T_{g\beta}$ , molecular mobility is sufficiently high to enable API crystallisation. Although further research is necessary to validate these findings for binary ASD systems, these results suggest  $T_{g\beta}$  is a potential predictor of physical stability and could be exploited to develop stability testing protocols.

### **1.6.2.2 API-polymer interactions**

Most pervasive API-polymer interactions in the ASD context comprise hydrogen bonding, however ionic, dipole-dipole and van der Waals interactions have also been reported to occur.<sup>84–87</sup> The mechanisms by which they enhance ASD physical stability is primarily via kinetic stabilisation by reducing molecular mobility and inhibiting API

nucleation. Several authors have reported the role of hydrogen bonding between PVP polymers and a variety of drugs, like nifedipine, itraconazole, bicalutamide and probucol, which has been reported to result in physically stable ASDs, contrary to correspondent systems with polymers with weaker or no hydrogen bond propensity.<sup>86,88-90</sup> Hydrogen bond formation has also been reported to inhibit nucleation and prevent drug crystallisation during dissolution.<sup>91,92</sup> In a different study by Doreth *et al.*, the role of Eudragit EPO (a cationic copolymer) was reported to stabilise two APIs, naproxen and ibuprofen, through ionic interactions.<sup>93</sup> Marsac *et al.* demonstrated the role of dipole-dipole interactions between polar molecules such ketoconazole and PVP in obtaining stable ASDs.<sup>94</sup>

API-polymer intermolecular interactions may also improve manufacturability for fusion-based processes such as HME by reducing processing temperature through melting point depression phenomena.<sup>60,95-97</sup> This has also been known to minimise thermal degradation of heat-sensitive drugs during HME processing.<sup>98,99</sup>

### **1.6.2.3 Glass forming ability**

The glass forming ability (GFA) of a material provides a qualitative estimation of its ability to convert to the amorphous solid-state (glass form). This ability is usually determined by DSC analysis based on the crystallisation behaviour from the melt in relation to the cooling/heating rate employed. Baird *et al.* proposed the first GFA classification system whereby drugs that crystallise upon cooling from the melt (at 20°C/min) are classified as GFA class I, whilst drugs that crystallise upon heating (at 10°C/min) comprise GFA class II and drugs do not crystallise either upon cooling or heating are termed GFA class III.<sup>100</sup> The classification criteria were improved by Blaabjerg *et al.*, who solved the problem associated with the arbitrary nature of the chosen cooling and heating rates by introducing the critical cooling rate concept.<sup>101</sup> In this case, GFA class I drugs usually require cooling rates faster than 750°C/min to form the amorphous glass. GFA Class II drugs require cooling rates larger than 10°C/min and class III drugs have a critical cooling rate of about 2°C/min.

Wytttenbach *et al.* reported that the vast majority of the amorphous compounds in marketed drug products belongs to GFA class III.<sup>102</sup> However, GFA class III drugs do

not necessarily guarantee formation of stable single-phase ASDs. Recent investigation on the impact of the GFA class on the physical stability of the resultant ASD study revealed that GFA class III drugs, on average, have better physical stability than GFA class II and I drugs but are not devoid of the crystallisation risk.<sup>103</sup> At a level of 25 wt% above the saturated solubility in the polymer, even GFA class III drugs crystallised when stored 20°C below T<sub>g</sub>. Similar results were reported by Panini *et al.*, that studied the impact of GFA class III drugs on the physical stability of ASDs prepared by spray drying and film casting.<sup>104</sup> The authors stated that only half of the APIs under study formed homogeneous crystal-free ASD after the preparation and drying process. All ASDs in this study were prepared at 40 wt% drug loading without considering the solubility of the API in the polymer matrix or the subsequent degree of supersaturation. Although there are other factors to be considered, such as the impact of the solvent system or the manufacturing method, it could be argued that even for good glass formers, the primary crystallisation driving force within a binary ASD system is determined by the solubility of the API in the polymer.

### **1.6.3 Environmental aspects**

Exposure of ASDs to environmental humidity, thermal and mechanical stress is another source of physical instability. As temperature increases, molecular mobility increases, which can promote phase separation and enhance the API crystallisation propensity.<sup>46</sup> In addition, thermal expansion of the ASD matrix may also reduce the degree of interaction between the components and thereby decreasing the miscibility limit.<sup>105,106</sup> As a consequence of the plasticising effect of water, ambient humidity can increase molecular mobility.<sup>107</sup> Absorbed moisture can also compete for hydrogen bond formation and disrupt API-polymer interactions.<sup>108</sup> Furthermore, upon contact with an aqueous dissolution medium, certain ASD systems undergo crystallisation and reduce the solubility advantage at the final drug delivery stage.<sup>109,110</sup> Mechanical stress induced by downstream processing steps, such as milling, pelletisation or compression, has been reported to create defects with increased surface energy that promote deformation-induced molecular mobility and increase the API nucleation rate.<sup>111–113</sup>

Table 1.2. General factors that influence stability of amorphous solid dispersions. Modified and extended from Bhujbal *et al.*

<b>Factors</b>	<b>Impact on stability</b>
Drug-polymer miscibility	Fully miscible components originate a single-phase amorphous systems that are less prone to crystallisation.
Drug-polymer solubility	A system is stable when the API content is below the thermodynamic equilibrium solubility.
Drug-polymer interactions	Drug-polymer intermolecular interactions reduce molecular mobility and increase the kinetic barrier to crystallisation.
Gibbs free energy	Lower Gibbs free energy systems tend to be more stable due to a reduced crystallisation driving force.
Glass forming ability	The API's glass-forming ability describes the intrinsic API propensity to convert to the amorphous phase.
Glass transition temperature	Stability increases with increasing T <sub>g</sub> . Polymers increase the kinetic stability of amorphous drugs because of the anti-plasticisation effect.
Molecular mobility	Restriction of molecular mobility decreases the API crystallisation rate and improves ASD stability.
Manufacturing technique	Different preparation methods induce different degrees of API-polymer mixing, level of amorphisation and originate different thermal and mechanical histories. This may result in variable solid-state stability.
Preparation conditions	Processing temperature, screw speed and feed rate in an HME process can affect the amount of dissolved drug, leading to impaired ASD stability.
Supersaturation	The degree of supersaturation can affect the rate and extent of recrystallisation.
Temperature, humidity and mechanical stress	Temperature affects molecular mobility and moisture may plasticise the ASD, decreasing crystallisation temperature and increasing the crystallisation rate. Mechanical stress also causes significant differences

## 1.7 Temperature-composition phase diagrams

A general introduction has been given above to the role of API-polymer solubility and miscibility in the context of ASD physical stability. The academic and industrial communities have widely recognised their importance in the development of amorphous solid dispersions. It is useful to address these concepts by examining the thermodynamic phase behaviour schematically depicted in the temperature-composition phase diagram shown in Figure 1.7 and that is most frequently obtained by employing the Flory-Huggins theory discussed in the Sections above.

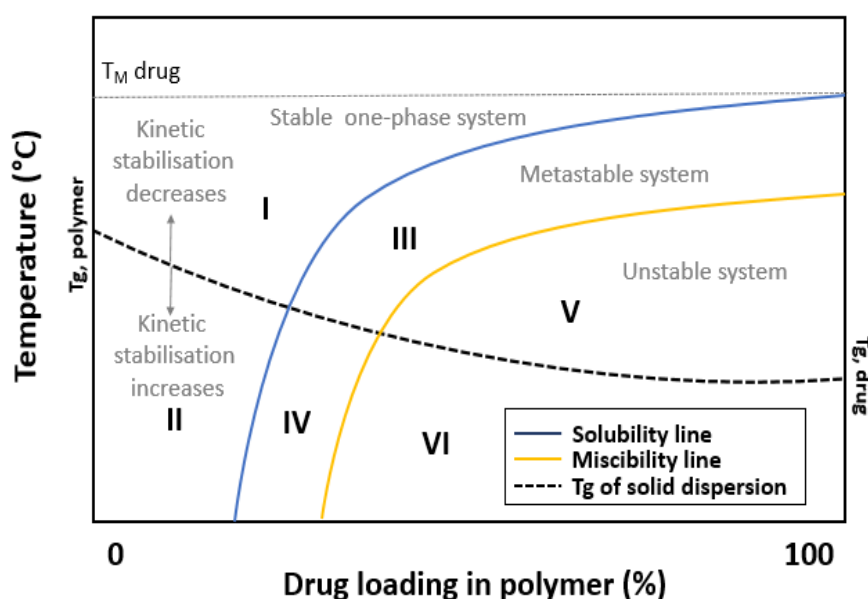


Figure 1.8. Schematic phase diagram of the thermodynamic phase behaviour of an API-polymer system displaying the solubility curve (blue line), the miscibility curve (yellow line) and the glass transition temperature (dashed black line). Adapted from Tian et al., 2013.

The solubility line (blue line) describes the solid-liquid equilibrium that defines the maximum amount of crystalline API that can be dissolved into a polymeric carrier at a certain temperature and pressure. Above the solubility line, the ASD is thermodynamically stable against crystallisation. This is the case at low drug loadings and high temperatures (regions I and II). Below the solubility line, ASDs are supersaturated and prone to recrystallisation. However, this may not occur at the

thermodynamic solubility line, as crystallisation is kinetically hindered due to the high viscosity conferred by the polymer. This originates metastable solid dispersions that crystallise at much lower temperatures or after prolonged storage periods (regions III and IV). An adequately formulated system could provide a sufficiently high kinetic barrier in this metastable region to prevent crystallisation during pharmaceutically relevant periods, especially if stored at temperatures below  $T_g$ . For example, Theil *et al.* showed that amorphous nifedipine in a ternary nifedipine-PVPVA-Eudragit RS system produced by HME remained stable for as long as 25 years when stored under at  $\sim 30^\circ\text{C}$  below the ASD  $T_g$ .<sup>114</sup>

The miscibility line (yellow curve) demarks the liquid-liquid equilibrium of amorphous API and polymer. The area below this line corresponds to compositions and temperatures where formation of two amorphous phases is expected (region V and VI). The shape of the miscibility line may vary between convex or concave, depending on if phase separation occurs below an upper critical solution temperature (UCST) or above a lower critical solution temperature (LCST), respectively. However, for most of the API-polymer phase diagrams published to date, UCST behaviour has been reported.<sup>59</sup> The glass-transition temperature (dashed black line) depicts the transition temperature from the supercooled liquid to the glass state. Above  $T_g$ , molecular mobility is high and the system may reach equilibrium relatively quickly. Conversely, below  $T_g$  the system falls in the “frozen” kinetic state characterised by low molecular mobility and long relaxation times. Consequently, even thermodynamically unstable regions can be kinetically stabilised below  $T_g$  (regions IV and VI).

The construction of temperature-composition phase diagrams separates the formulation design space into stable, metastable and unstable regions and aids selection of appropriate drug loadings and processing conditions during ASD preparation. However, these are seldom developed due to a paucity of reliable experimental and predictive methods to determine solubility and miscibility. ASDs are still mainly developed by trial and error, with multiple drug-polymer combinations and conditions being screened. This significantly increases development costs and time to the market. In most cases, stability data is gathered through long-term stability studies on the material after manufacturing is complete. Therefore, there is a pressing need for

reliable methods to determine the solubility of the API in the polymeric carrier. Ideally, such methods would be coupled with PAT tools to monitor and control the manufacturing process to avoid the risk of residual crystallinity and assure formation homogeneously dispersed amorphous drug products.

## **1.8 Characterisation of Amorphous Solid Dispersions**

Given the metastable nature of ASDs, in-depth characterisation is critical in all stages of product development. Proper characterisation and understanding of behaviour allow the rational selection of the suitable polymeric carrier, maximum drug loading, manufacturing method, processing parameters and storage conditions for optimum solid-state stability. There is no single technique capable of providing all the information required. Thus, an orthogonal approach with complementary characterisation techniques must be taken to obtain comprehensive physical stability information. A brief selection of the available literature will be discussed here. This section is divided into four main groups: thermal, spectroscopic, X-ray based and microscopic analytical methods. Table 1.3 summarises the most frequently employed techniques and emerging new ones with respective sensitivity values (when available).

Table 1.3. ASD solid-state characterisation techniques with respective length scales, limit of detection (LOD) or limit of quantification (LOQ).

<b>Method</b>	<b>Derived information</b>	<b>Length scale, LOD/LOQ</b>
<b>Thermal</b>		
DSC	Tg, Tm, heat capacity, phase composition, API-polymer solubility and miscibility	30 -100 nm; <sup>115,116</sup> ~5 wt% <sup>117</sup>
TGA	Mass loss, chemical degradation	
DMA	Tg, viscosity, relaxation time, molecular mobility	2 wt% <sup>118</sup>
DEA	Tg, molecular mobility, relaxation times	
TSDC	Tg, molecular mobility, relaxation times,	
Rheology	Complex viscosity, loss and storage moduli	
<b>Spectral</b>		
Raman	Phase composition, molecular interactions, surface mapping	0.03–0.05 wt% <sup>119</sup>
IR	Phase composition, molecular interactions, surface mapping	1-2 wt% <sup>120</sup>
UV-VIS	Phase composition, molecular interaction <sup>121,122</sup>	
TPS	Crystallinity, polymorphs, surface mapping,	1.5 wt% <sup>123</sup>
ssNMR	Phase composition, relaxation time, domain size, API-polymer miscibility	0.1 -1 wt% <sup>124</sup>
<b>X-ray based</b>		
XRPD	Crystallinity quant./ kinetics, polymorphic identification	1-5 wt% <sup>110,125,126</sup>
X-ray CT	2D and 3D visualisation of internal structures	
SAXS	Growth kinetics, polymer mesophases	

PDF	API-polymer miscibility, short-range structure	
<hr/> Microscopic/surface-based <hr/>		
SEM	Morphology, particle size	
TEM	Crystallinity, API-polymer miscibility	0.2 nm; 0.1 wt%
PLM	Morphology, crystallinity (birefringence)	
AFM	Surface topography	0.2 nm
XPS	Elemental composition	200 $\mu\text{m}$ (lateral); 1-10 nm (depth); 1 wt%
SEM-EDS	Morphology, elemental composition	100 nm (lateral); 0.1-3 $\mu\text{m}$ (depth); 0.01-1 wt% <sup>127</sup>
ToF-SIMS	Surface chemical mapping and depth profiling	50 nm (lateral); 1 nm (depth); <sup>128</sup>

DSC – differential scanning calorimetry, TGA – thermogravimetric analysis, DMA – dynamic mechanical analysis, DEA – dielectric analysis, TSDC - thermally stimulated depolarisation current analysis, IR – infra-red spectroscopy, UV-Vis – ultraviolet-visible spectroscopy, TPS – terahertz-pulsed spectroscopy, ssNMR – solid state nuclear magnetic resonance, XRPD – x-ray powder diffraction, X-ray CT – x-ray computed tomography, SAXS – small angle x-ray scattering, PDF – x-ray pair distribution function analysis, SEM – scanning electron microscopy, TEM – transmission electron microscopy, PLM – polarised light microscopy, AFM – atomic force microscopy, XPS – x-ray photoelectron spectroscopy, SEM-EDS – scanning electron microscopy energy dispersive spectroscopy and ToF-SIMS – time-of-flight secondary ion mass spectrometry.

### 1.8.1 Thermal methods

Disappearance of the melting endotherm and presence of a glass transition temperature are two of the gold standard properties used to confirm the amorphous conversion of a crystalline drug. As a result, differential scanning calorimetry (DSC) and thermogravimetric analysis (TGA) are two of the most frequently employed thermal

tools in ASD characterisation. Multiple molecular-level events can be assessed, including glass transition, molecular mobility, relaxation times, API crystallisation, polymorphic phase transitions, mass loss/chemical degradation (exclusive of TGA), as well as API-polymer miscibility and solubility. However, DSC exhibits several limitations for the characterisation of solid dispersions, as partially discussed in Section 1.5. The potential drug-polymer mixing and the subsequent drug dissolution resulting from the DSC heating scan can cause diminution or disappearance of the drug-specific endothermic melting peak(s), which may be erroneously considered to indicate solid-state material properties. Furthermore, DSC's ability to differentiate between two glass transition temperatures requires a minimum 10°C temperature difference, which is aggravated by other simultaneous events occurring in a multicomponent system. This becomes particularly relevant considering that  $T_g$  expands over a range of temperature values and is strongly dependent on the employed heating rate and the material's thermal history.<sup>129</sup> Likewise, the generally assumed limit of detection of ~30 nm has various limitations. It is based on a study from 1977<sup>115</sup> that assesses phase separation in a styrene block copolymer system and requires further validation before direct extrapolation to binary ASD systems. Despite widespread use, there is little experimental data available to accurately evaluate the DSC detectable domain size to assess mixing homogeneity and phase separation in amorphous solid dispersions. Qian *et al.* reported that even when phase separation is at the scale of tens of microns, it is still undetectable by DSC.<sup>130</sup> Therefore, a single  $T_g$  value and the absence of a melting endotherm (especially at low drug loadings) obtained from DSC analysis could be unreliable for the assessment of physical stability of solid dispersions. Modulated DSC (MDSC) and high sensitivity DSC (hyper-DSC) could be used to deconvolute overlapping thermal events and improve resolution for phase transitions by employing faster heating rates.

Other thermal techniques are gaining increased expression for ASD analysis due to higher sensitivity to glass transition events, molecular mobility and relaxation times. These methods include dynamic mechanical analysis (DMA), dielectric analysis (DEA) and thermally stimulated depolarisation current (TSDC) analysis. DMA measures the mechanical properties of a material (stiffness, strain and damping) as a function of temperature, time and frequency by applying an oscillatory mechanical

stress to the sample.<sup>131</sup> DMA can be used to measure the  $T_g$  of an amorphous system because there are marked discontinuities in elasticity and viscosity (storage and loss moduli, respectively) around this transition point. Gupta *et al.* compared DSC and DMA to study the devitrification of amorphous celecoxib under several stress conditions (temperature, humidity and pressure).<sup>132</sup> The authors reported higher robustness and sensitivity of DMA to glass transition-related events, which is reported to be around 10 to 100x more sensitive.<sup>133</sup> Several other authors have described the use of this technique to study phase separation and secondary relaxation processes in polymeric amorphous glasses.<sup>134–136</sup> Another study by Yang *et al.*, investigated the solubility of paracetamol in poly-ethylene oxide (PEO) using DMA viscosity variations as a function of drug load and temperature.<sup>137</sup> The authors reported a solubility increase from 14 wt% at 80°C to 41 wt% at 140°C. DMA's ability to determine the viscoelastic properties of a material is of great interest to rheological investigations and could provide useful information to determine the initial processing window for HME processing, as pointed out by Ojo and Lee.<sup>131</sup>

DEA and TSDC use a similar principle to that of DMA, with the exception that they employ an electrical perturbation instead of mechanical stress to probe molecular mobility. They promote the reorientation of dipoles under the influence of an electric field of variable frequency. Apart from being applied to assess  $T_g$ , relaxation times and recrystallisation events in neat amorphous compounds and polymers, DEA has also been used to study the anti-plasticising effect of polymers and plasticisers in binary and ternary ASD systems.<sup>138–141</sup> Compared to DEA, TSDC has higher sensitivity and can provide better differentiation between overlapping relaxation events but requires specialised expertise for data analysis and interpretation.<sup>82,142</sup>

## 1.8.2 Spectroscopic methods

Spectroscopic methods include all methods that capture the interaction of electromagnetic radiation with matter. Raman and infrared (IR) spectroscopies are the most frequently employed vibrational spectroscopic methods. They have been used for multiple applications, including detection of drug-polymer intermolecular interactions, polymorph identification, phase transitions, amorphous phase separation and

quantification of amorphous and crystalline content in ASD systems.<sup>143–148</sup> These techniques yield structural and molecular conformation information by probing typical band vibrations at frequencies between  $10^{14}$  -  $10^{13}$  Hz ( $4000$  to  $400$   $\text{cm}^{-1}$ ). The signal in the Raman spectrum results from polarisability changes, whereas the IR spectrum originates from molecular dipole moment variations. Raman spectroscopy has the advantage of covering the classic “fingerprint” region and the lower frequency region ( $< 400$   $\text{cm}^{-1}$ ) that provides information about the crystal lattice vibration modes.<sup>149</sup> Recent technological advances enable the use of ultra-narrow-band notch filters to suppress Rayleigh scattering and extend the accessible Raman range down to  $10$   $\text{cm}^{-1}$ .<sup>150</sup> This enhances the signal-to-noise ratio and improves differentiation between different packing arrangements. Larkin *et al.* reported a tenfold increase in the Raman intensity in the low-frequency region compared to the mid-frequency region when monitoring the amorphous to the crystalline conversion of indomethacin-based systems over time.<sup>151</sup> Ibrahim *et al.* reported the use of low-frequency Raman (also known as Terahertz-Raman) as a mapping technique to distinguish between the amorphous and crystalline forms of paracetamol in paracetamol-HPMC ASDs produced by HME.<sup>152</sup> Tres *et al.* also reported the use of this technique to study the API recrystallisation pathways upon dissolution of a bicalutamide-PVPVA system.<sup>153</sup> Terahertz pulsed spectroscopy (TPS) is an alternative spectroscopic technique that probes the terahertz range in the far-IR region ( $10^{10}$  –  $10^{12}$  Hz/  $2$ - $130$   $\text{cm}^{-1}$ ).<sup>154</sup> TPS has been used to differentiate between multiple polymorphic phases and determine Tg and  $\beta$ -relaxation processes in neat amorphous compounds.<sup>155–157</sup> Despite promising potential application in crystallisation and amorphisation processes, low-frequency Raman and terahertz spectroscopies are still relatively underexplored in the ASD context. For this thesis work, focus is given to low-frequency Raman (LFR) spectroscopy as a process analytical technology (PAT) tool due to its great ability to differentiate between amorphous and crystalline materials.

Solid-state nuclear magnetic resonance (ssNMR) is another valuable analytical tool that has been used to assess relaxation times, miscibility and phase separation on the nanometre scale in ASD systems. By correlating the proton relaxation times (spin-lattice and spin-spin relaxation times) with the length scale of the spin diffusion,

inferences can be made about the size of the API- or polymer-rich phases within the 5-100 nm range.<sup>158</sup>

### 1.8.3 X-ray based methods

X-ray powder diffraction (XRPD) is considered the gold standard for crystallinity detection.. Crystalline materials display sharp Bragg diffraction peaks as a result of constructive interference, whilst amorphous materials display the characteristic amorphous “halo” conferred by diffuse scattering. It should be noted that X-ray diffraction techniques can only detect molecular order and that disorder is only implied. This technique is limited by mass fraction and dilution effects, crystal quality (e.g., variations in lattice strain, preferred orientation and crystallite size) and acquisition parameters.<sup>120,159</sup> Its sensitivity is insufficient to detect nanocrystalline domains or crystalline content below 1-5 wt%.<sup>125</sup> Zhu *et al.*, have used time-resolved small angle X-ray scattering/wide angle scattering (SAXS/WAXS) to investigate the phase behaviour and microstructural evolution of several APIs in PEG-based solid dispersions.<sup>160</sup> Furthermore, X-ray pair distribution function analysis (PDF) has been gaining importance to study short range order beyond the amorphous “halo” provided by XRPD. Billinge *et al.*, have used PDF to study amorphous and nanocrystalline carbamazepine and indomethacin.<sup>161</sup> Terban *et al.*, have also used PDF to understand local structure of disordered materials produced by different processes.<sup>162</sup>

### 1.8.4 Microscopic methods

Methods for the visual analysis of solid dispersions are also crucial for the characterisation of ASDs because surface properties may reflect early stages of physical instability. In general, the microscopic methods employed in ASD characterisation include polarised light microscopy (PLM), scanning electron microscopy (SEM), transmission electron microscopy (TEM), atomic force microscopy (AFM), time-of-flight secondary ion mass spectrometry (ToF SIMS) and X-ray photoelectron spectroscopy (XPS). They have been used for particle size analysis, particle morphology, crystallinity detection, phase homogeneity, elemental composition and study surface mechanical properties.<sup>163-166</sup>

## 1.9 Translational limitations – current gaps

As seen throughout the previous Sections, there are conflicting schools of thought regarding the frameworks by which solid-state physical stability of ASDs can be understood, with many contradictory results reported in the literature. For instance, Mahieu *et al.* have suggested that de-mixing of supersaturated ASDs occurs faster than the dissolution of the API in the polymer matrix during the ASD formation process.<sup>55</sup> This provided the basis for the recrystallisation API-polymer solubility method discussed in the sections above. However, for the same API-polymer system (indomethacin-PVP 12), Mathers *et al.* have demonstrated that de-mixing is markedly slower than the dissolution process, resulting in solubility overestimations.<sup>167</sup> Another important example refers to the recrystallisation driving forces in neat amorphous compounds. Zhou *et al.* suggested that compounds with high entropic barrier and low mobility were more difficult to crystallise, regardless of the thermodynamic driving forces.<sup>168</sup> Contrary to that, Graeser *et al.* reported no direct correlation between relaxation time (i.e., molecular mobility) and physical stability, especially below T<sub>g</sub>.<sup>169</sup>

These two examples illustrate the complex nature of ASDs and the lack of fundamental understanding of the multiple aspects governing their solid-state physical stability. This has led to significant discrepancies between research and market access. From 1985, when the first ASD product was introduced (Cesamet), to 2022 only 47 ASD-based commercial products were cumulatively approved by the EMA and FDA (Figure 1.9).<sup>170,171</sup> This number is substantially inferior to the number of publications on the ASD topic that is actively researched (Figure 1.10). Shah *et al.* provided a more elaborate discussion regarding the main reasons for the lack of exploitation of ASD formulations in commercial dosage forms.<sup>117</sup> Therefore, the following enumeration was adapted and extended from Shah *et al.*:

- Limited knowledge regarding the physicochemical properties of the APIs, polymers and their interactions.
- Limited API availability during early stages of product development.
- Lack of available techniques/models for predicting physical stability.

- Limited availability of small-scale (or miniaturised) processing techniques for formulation screening during early-stage development.
- Lack of structured development.
- Lack of reliable methods to determine the solubility of the API in the polymer.

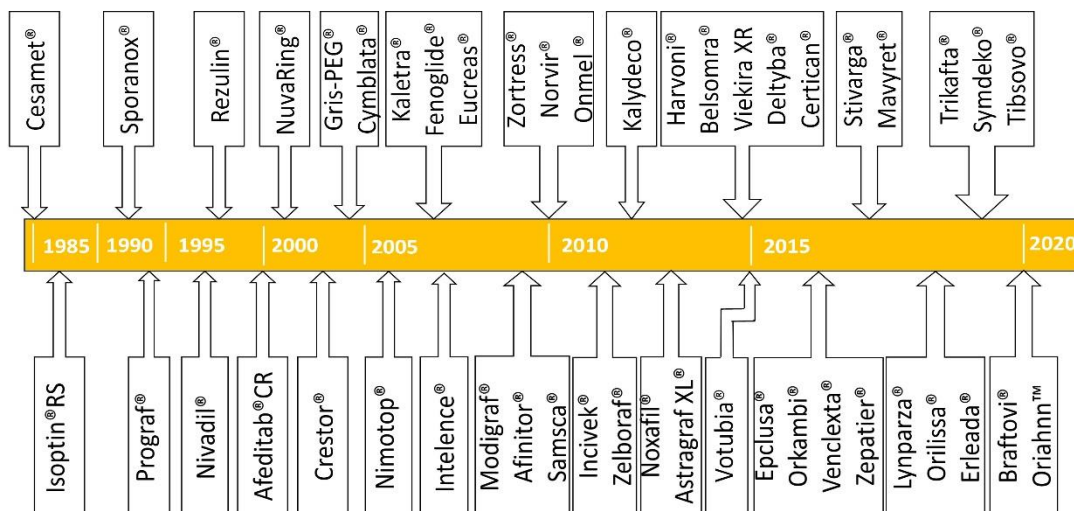


Figure 1.9. EMA and FDA approved ASD-based commercial products from 1985 to 2022. Compiled with data from Bhujbal et al., 2021, Bennet-Lenane et al., 2020 and by consulting the FDA drug database and the European Summary of Pharmaceutical Characteristics (SPC). For any drug substance only the year of approval of the first ASD dosage form was considered, independently of the approving regulatory body.

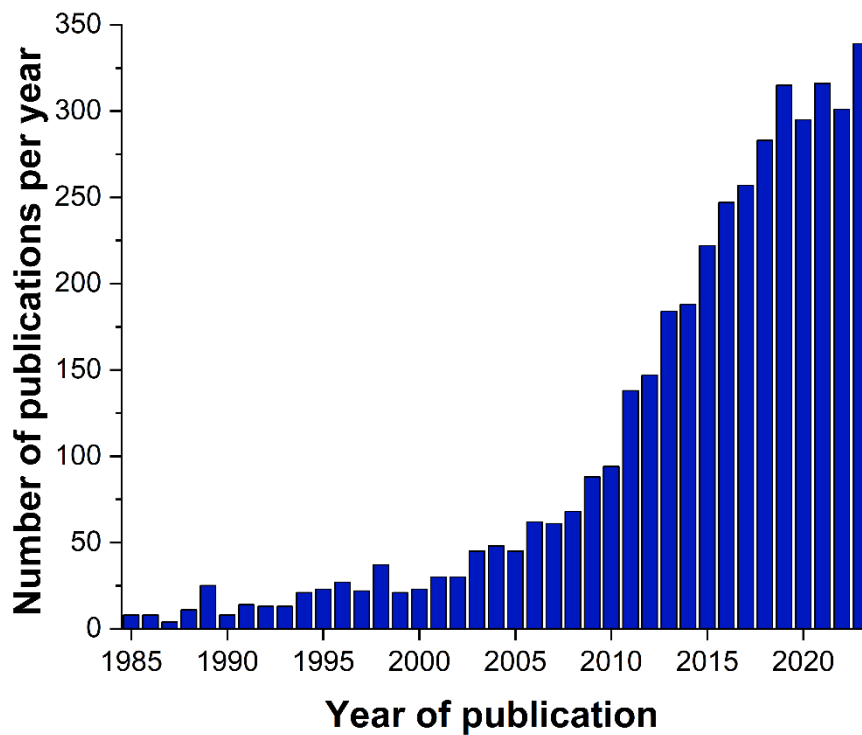


Figure 1.10. Publications in Scopus database under the term “amorphous solid dispersion” from 1985 to 2023.

## **1.10 Aims and objectives**

The main aims and objectives of this thesis are to:

- Identify, develop, and apply new characterisation tools to link structure-process properties for a targeted design of stable amorphous solid dispersions.
- Increase the understanding of the impact of API-polymer solubility on ASD physical stability.
- Develop new experimental methods to determine the solubility of crystalline API in polymeric matrices and build solubility phase diagrams.
- Investigate the impact of the API saturation level and processing temperature on the internal microstructure of ASDs produced by hot-melt extrusion.
- Study the impact of API-polymer solubility on the ASD surface phase distribution homogeneity and compare the kinetics of surface-mediated instability with bulk-mediated instability.

# **Chapter 2**

## **Use of Low-frequency Raman Spectroscopy to Determine Solubility of Crystalline API in Polymeric Matrices**

**The work carried out in this Chapter was fully published in a peer-reviewed journal.**

**Bordos, E.,** Islam, M. T., Florence, A. J., Halbert, G. W. and Robertson, J. Use of Terahertz-Raman Spectroscopy to Determine Solubility of the Crystalline Active Pharmaceutical Ingredient in Polymeric Matrices during Hot Melt Extrusion. *Mol. Pharm.* 16, 4361–4371 (2019).

## 2.1 Introduction

The solubility of the API in the carrier polymer is one of the major factors determining ASD physical stability.<sup>54,112,172</sup> Its determination is of paramount importance in the manufacture of crystal-free, stable ASDs and is therefore of considerable commercial importance with regards to shelf life of this class of pharmaceutical drug product. If the amount of API in the formulation (i.e., the chosen drug loading) is below the equilibrium solubility of the API in the polymer matrix, the ASD will be thermodynamically stable and will not recrystallise. When the API content exceeds its thermodynamic solubility, the ASD becomes supersaturated and API phase separation and recrystallisation are likely to occur.<sup>173</sup> However, if the system is kinetically stabilised at storage conditions, molecular mobility may be slowed enough to retain the amorphous configuration and inhibit recrystallisation during pharmaceutically relevant time periods.<sup>114</sup>

However, experimental determination of the solubility of an API in a polymer matrix is an analytically challenging task as both components are normally in the solid-state at room temperature and due to the high viscosity of the polymeric carrier, equilibrium solubility is difficult to reach and test.<sup>52,53</sup> In fact, the current pack of “industry standard” analytical techniques is limited in that it is often based on differential scanning calorimetry (DSC) analysis or inferred based on post-production analysis, providing an account of the material state after manufacturing is complete. The DSC methods include the melting point depression method, the recrystallisation method and the enthalpy approach amongst others.<sup>52,54,174,175</sup> Aside from thermal degradation and chemical instability these methods generally risk solubility under or overestimations due to low molecular mobility in a viscous polymer (*i.e.*, no mixing is applied) and require equilibrium assumptions which limits their wider application.

There is a growing body of evidence suggesting that the apparent solubility of an API in polymer system may vary according to the processing method used.<sup>176–178</sup> This may be driven by differences in mixing rather than a true thermodynamic equilibrium being

reached. Within this study, a co-rotating twin screw extruder is used as the mixing device. This type of unit provides intense mixing and has the potential to overcome kinetic limitations and reach true equilibrium. Therefore, the objective of this study is to determine API solubility directly during hot melt extrusion (HME). This is achieved by monitoring the low-frequency Raman region covering the API crystalline to amorphous structural phase transitions as it dissolves in the polymer matrix. For this purpose, paracetamol (whilst not presenting *in vivo* solubility constraints) was selected as model compound and two commercially relevant polymer systems, Affinisol 15LV (hydroxypropyl methylcellulose) and Plasdone S630 (Copovidone) as polymeric carriers, to assess the above application of THz-Raman spectroscopy. Extrusion is performed at different API-polymer ratios and for each composition, different processing temperatures are explored to allow phase-equilibria inferences and construction of temperature-composition phase diagrams.

## **2.2 Materials and Methods**

### **2.2.1 Materials**

Pharmaceutical grade special granular paracetamol (PCM) was purchased from Mallinckrodt Inc. (Raleigh, USA). Hydroxypropyl methylcellulose (HPMC) grade Affinisol 15LV (AFF) and Copovidone (PVP:VA 6:4) grade Plasdone S630 (PLSD) were kindly donated by Dow Inc. (The Dow Chemical Company, Michigan, USA) and Ashland Inc. (Columbus, OH, USA), respectively. The chemical structure of all

materials is displayed in Figure 2.1. All compounds were used as obtained, without further purification.

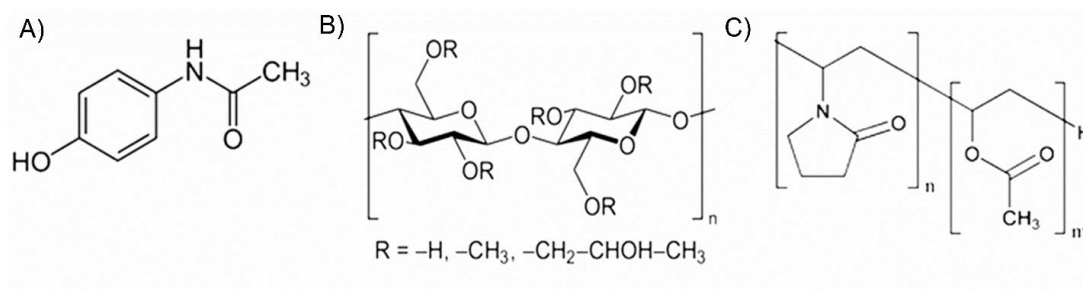


Figure 2.1. Chemical structure of A) paracetamol, B) Affinisol15LV and C) Plasdane S630. “n” and “m” represent the structural unit for both polymers. Plasdane S630 is a linear copolymer where  $n/m = 6/4$  mass ratio.

## 2.2.2 Methods

### 2.2.2.1 Preparation of amorphous solid dispersions by hot melt extrusion (HME)

HME was performed with a Eurolab 16 twin-screw extruder (Thermo Scientific, Karlsruhe, Germany) equipped with two DDW-M FW20 feeders (Brabender Technologie, Duisburg, Germany) operating in gravimetric mode with a vertical crammer hopper (Brabender Technologie, Duisburg, Germany) set to 100 rpm. The experimental set-up was as illustrated in Figure 2.2. API and polymers were separately fed at different feeding rates to reach the desired API-polymer ratio. A combined feeding rate of 1kg/h was used. For all experiments, barrel zone 1 was operated at 20°C and barrel zones 2 and 3 were controlled at temperature set points of 50°C and 100°C, respectively, to prevent powder melting and blockage of the feeding zone. The processing temperature limits of the remaining barrel zones were constrained by the polymer glass transition temperature (Affinisol 15LV - 115°C and Plasdane S630 - 109°C) and the drug melting point (170°C). This was required to assure the soften/liquefied state of the polymer (i.e. act as a “liquid solvent”) to mix and dissolve the API, while keeping the API below its melting point to enable detection of excess

crystalline API. Barrel sections 4 to 10 and die zone were controlled to the same temperature set point values, which are reported in Tables 2.1 and 2.2. Product melt temperature was monitored with a pressure-temperature probe (Terwin Instruments Ltd., Bottesford, UK) immersed in the polymer-API mixture within the confines of the die section. The temperature measured values monitored in barrel sections 4-10, the die and the product melt probe varied from reported set point values less than  $\pm 3^{\circ}\text{C}$ . Therefore, within the present work temperature is denoted as the set-point temperature values. Collected extrudates were pelletised and stored at  $25^{\circ}\text{C}/60\% \text{ RH}$  until further analysis.

Table 2.1. Hot melt extrusion experimental conditions for the PCM-AFF system.

<b>API feeding rate (kg/h)</b>	<b>Polymer feeding rate (kg/h)</b>	<b>Processing temperature (°C) (Barrel sections 4 to 10 and die zone )*</b>	<b>Screw speed (rpm)</b>
0.1	0.9	115, 130, 150, 170	200
0.2	0.8	115, 120, 125, 130, 140, 150	200
0.25	0.75	115, 120, 125, 130, 140, 150,160, 170	200
0.275	0.725	115, 120, 125, 130, 140, 150	200
0.3	0.7	115, 120, 125, 130, 140	200
0.325	0.675	115, 120, 125, 130, 135,140	200
0.35	0.65	115, 120, 125, 130,135, 140,145,150	200

\*Each value in this column represents a distinct experimental condition and denotes the cumulative set-point barrel temperature of sections 4 to 10 and die (i.e. zones 4-10 and the die were operated isothermally).

Table 2.2. Hot melt extrusion experimental conditions for the PCM-PLSD system.

<b>API feeding rate (kg/h)</b>	<b>Polymer feeding rate (kg/h)</b>	<b>Processing temperature (°C) (Barrel sections 4 to 10 and die zone )*</b>	<b>Screw speed (rpm)</b>
0.3	0.7	110,120,130,150	200
0.35	0.65	110	200
0.375	0.625	110,120	200
0.4	0.6	110, 120, 130	200
0.425	0.575	110, 120, 130, 140	200
0.45	0.55	110, 120, 130, 140, 150	200
0.475	0.525	110, 120, 130, 140, 150	200
0.50	0.5	110, 120, 140, 150	200
0.525	0.475	150	200
0.55	0.45	150	200
0.575	0.425	150	200
0.6	0.4	150, 160	200
0.625	0.375	150, 160	200
0.65	0.35	150, 160, 170	200
0.675	0.325	150, 160, 170	200
0.70	0.3	150, 160,170	200

\* Each value in this column represents a distinct experimental condition and denotes the cumulative set-point barrel temperature of sections 4 to 10 and die (i.e. zones 4-10 and the die were operated isothermally).

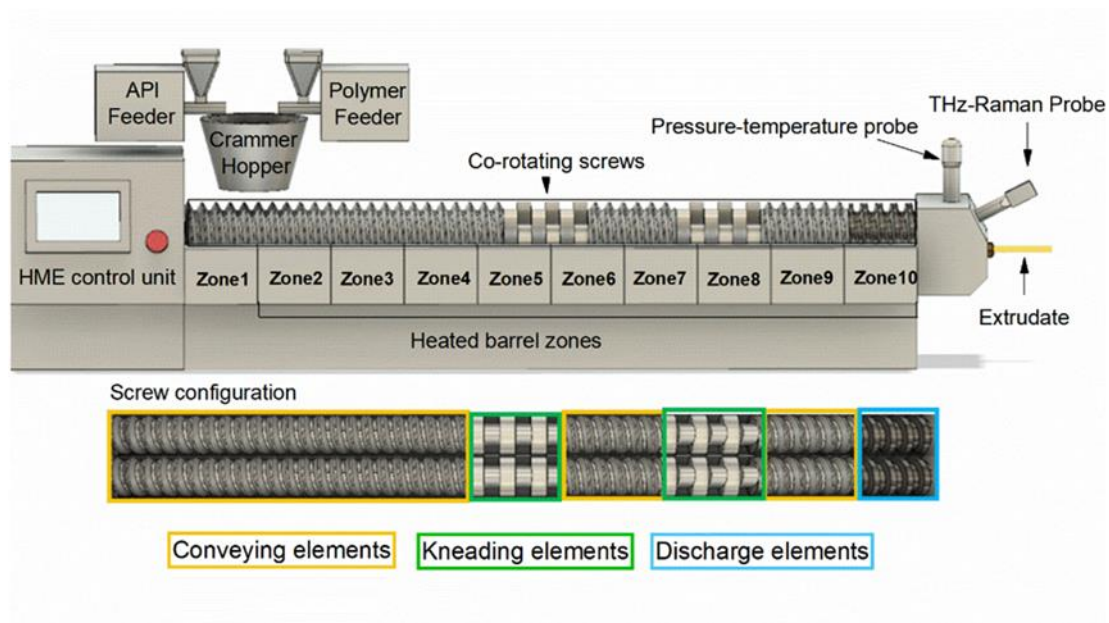


Figure 2.2. Schematic representation of the HME experimental set-up and screw configuration.

### 2.2.2.3 API-polymer solubility measurements

A Terahertz-Raman probe (Ondax Inc., USA) coupled with a RNX1 Raman spectrometer unit (Kaiser Optical Systems Inc., USA) was immersed in the polymer API-mixture in an adjacent port immediately beside the pressure temperature probe to monitor the API structural phase transitions occurring during extrusion. Data was collected with a 785 nm laser excitation source operating at 70 mW power. An exposure time of two seconds and three spectral accumulations were used. Spectra were acquired with Holograms software (version 4.1) over the  $-20\text{ cm}^{-1}$ – $1800\text{ cm}^{-1}$  spectral range and integrated into PharmaMV RealTime software (version 5.2, Perceptive Engineering Ltd., Daresbury, UK) for real-time visualisation. Spectral pre-processing was performed with PharmaMV Development software (version 5.2) applying Whittaker smoothing and standard normal variate (SNV) for baseline effect removal and normalisation, respectively. Thermally induced transitions in the low frequency Raman region ( $5\text{ cm}^{-1}$ – $200\text{ cm}^{-1}$ /0.15 – 6.0 THz) were used to distinguish between the crystalline and amorphous states of the API. Transition temperatures from crystalline-to-amorphous and amorphous-to-crystalline were used to determine the

temperature-composition coordinates at each API-polymer ratio and construct the solubility phase diagram for both systems.

#### **2.2.2.4 Off-line Terahertz-Raman spectroscopy**

Off-line variable-temperature THz-Raman analysis was performed to obtain the reference spectra of each PCM polymorph as well as amorphous paracetamol. Data was collected with the Terahertz-Raman probe (coupled with a RNX1 spectrometer unit) attached to a Linkam LTS420 hot stage. To prepare the amorphous paracetamol and the three polymorphs, the temperature cycling method outlined by Nanubolu and Burley was adopted.<sup>179</sup> PCM samples of 3-5 mg were confined between a microscope glass and a cover slip and heated to 180°C at a rate of 20°C/min and held at that temperature for 2 min. Subsequent melt quenching to 0°C was performed at a cooling rate of 20°C/min to obtain the amorphous glass form. To obtain the paracetamol polymorphs, the amorphous glass from these steps was then allowed to equilibrate at 0°C for 5 min prior to a second heating cycle to 180°C using a heating rate of 1°C/min. As the temperature rises at this slow heating rate, the glass transforms to PCM form III, then form II then form I before melting at ~ 170°C. Therefore the reference spectra for the amorphous and three polymorphs was gathered through this cycle. At the specific transition temperatures identified (80°C for form III, 120°C for form II and 150°C for form I) the heating rate was paused and the spectra was acquired using an exposure time of two seconds and three spectral accumulations.

#### **2.2.2.5. Hot stage microscopy**

Hot-stage microscopy (HSM) experiments were conducted using a Leica DM2700 transmission optical microscope (Leica Microsystems, Milton Keynes, UK) under a cross-polarized light. The apparatus was equipped with a Leica DF320 digital camera (Leica Microsystems, Milton Keynes, UK) and a Linkam LTS420 T95 temperature control stage. Samples of 3-5 mg were placed into the hot-stage chamber and heated to 180°C at a heating rate of 1°C/min. Pure polymers and API-polymer physical mixtures were subjected to isothermal steps of 3 min at every 10°C above 100°C to equilibrate. Cooling cycle to 0°C was performed at a rate of 1°C/min. Birefringence

properties of crystalline materials were used to distinguish the crystalline API from amorphous API-polymer mixtures. Pure PCM samples were confined between a microscope glass and a cover slip and subjected to an additional heat cycle to assess recrystallisation behaviour from the amorphous glass.

### **2.2.2.6 Differential Scanning Calorimetry**

All experiments were performed on a DSC 214 Polyma differential scanning calorimeter (Netzsch-Geratebau GmbH, Germany) under a helium environment (purge 1=40 ml/min, purge 2=60 ml/min). Samples of 3-5 mg were accurately weighed and crimped in 25  $\mu$ L aluminium pans with pierced lids and subjected to heat-cool-heat cycles. Heating cycles were performed to 180°C at a heating rate of 20°C/min. Cooling was performed from 180°C to 0°C at 20°C/min.

### **2.2.2.7. X-ray powder diffraction**

Variable temperature powder diffraction data (VT-XRPD) was collected using a Bruker D8 Advance II diffractometer (Bruker Ltd, Coventry, UK) equipped with  $\theta/\theta$  geometry and primary monochromated radiation (Cu,  $\lambda = 1.54056 \text{ \AA}$ ). Data was collected in the 2 theta range of 4°–35° using a step size of 0.017° and 1 s/step speed. Operating voltage and current were 40 kV and 50 mA, respectively. Pure PCM samples were placed into 0.7 mm borosilicate glass capillaries and subjected to heat-cool-heat cycles to 180°C, 0°C and 180°C, respectively. Heating and cooling rates of 6°C/min were employed due to instrumental limitations. Identification of the crystalline form was made by comparison to CCSD crystalline forms I, II and III (HXACAN27, HXACAN31 and HXACAN29, respectively) using Mercury software (version 3.9).

HME extrudates were analysed at ambient temperature and data was collected on a Bruker AXS D8 Advance transmission diffractometer equipped with  $\theta/\theta$  geometry, primary monochromated radiation (Cu  $K\alpha_1$   $\lambda = 1.54056 \text{ \AA}$ ) and an automated multiposition x-y sample stage. Samples were mounted on a polyimide film (Kapton, 7.5  $\mu$ m thickness) and analysis was performed in the angular range of 4-35° 2 $\theta$  with a 0.017°2 $\theta$  step size and 2 s per step count time.

## 2.3 Results and discussion

### 2.3.1 Saturated solution temperature ( $T_s$ ) determination

The main premise required to construct an API-polymer solubility phase diagram is the determination of the temperature at which a given crystalline API content is soluble in the polymer matrix. Access to this temperature was directly obtained during hot melt extrusion by monitoring the API structural phase transitions from crystalline to amorphous as it dissolved in the polymeric carrier. These phase transitions were monitored in the low-frequency Raman spectral region that covers Stokes signal ( $5\text{ cm}^{-1} - 200\text{ cm}^{-1}$ ) and provides information about the crystal lattice vibration modes.<sup>180,181</sup> Such vibrations are sensitive to local order and disorder and enable the distinction between different crystal packing arrangements, as well as the amorphous and crystalline states.<sup>151,182</sup>

THz-Raman spectra of PLSD, AFF, amorphous and crystalline PCM are shown in Figure 2.3. Crystalline PCM has distinctive peaks at  $32\text{ cm}^{-1}$ ,  $56\text{ cm}^{-1}$  and  $89\text{ cm}^{-1}$  which are characteristic to form I.<sup>179</sup> Given the lack of long-range structural order in amorphous materials, these lattice modes are absent in the amorphous drug form and in both polymeric matrices and were used to differentiate between amorphous and crystalline PCM within the API-polymer mixtures. As the API dissolves in the polymer, the crystalline structure is disrupted and the drug is rendered amorphous. Therefore, to assure the robustness of the method, API solubility was determined by cycling extrusion temperature up, to induce dissolution and down, to force drug precipitation.

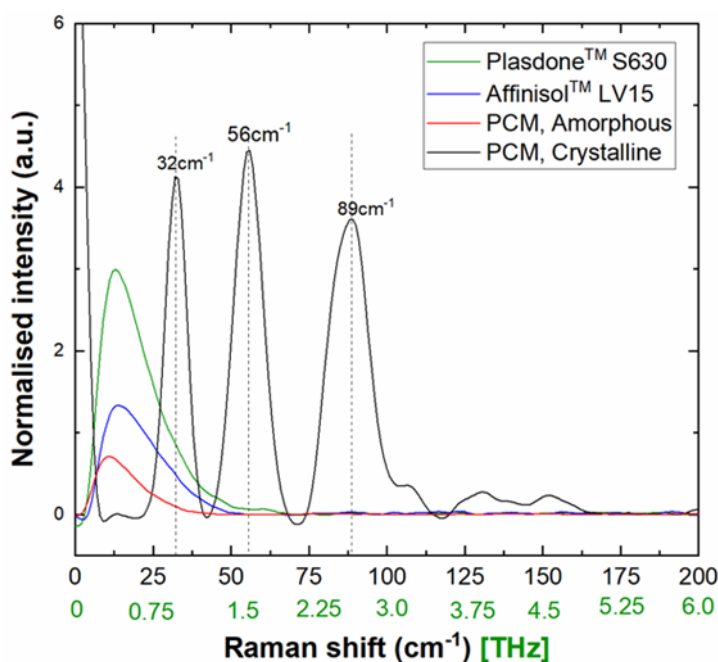


Figure 2.3. THz-Raman spectra of PLSD (green), AFF (blue), amorphous PCM (red) and crystalline PCM (black).

As an example, Figure 2.4 illustrates the spectra used to determine the saturated solution temperature ( $T_S$ ) for PCM-AFF 30-70 wt% (A-B) and PCM-PLSD 45-55 wt% (C-D). As  $T_{\text{EXTRUSION}}$  approaches  $T_S$ , the drug progressively dissolves in the polymer and the intensity of the lattice modes associated with crystalline PCM decreases until disappearing at 130°C for PCM-AFF 30-70 wt% (Figure 4B) and 150 °C for PCM-PLSD 45-55 wt% (Figure 4D), when no crystalline API is detected.  $T_S$  was then estimated at the intermediate temperature point between the API amorphous and crystalline phases, corresponding to 127.5°C for PCM-AFF 30-70 wt% and 145°C for PCM-PLSD 45-55 wt%. It should be noted that  $T_S$  was approached by varying extrusion temperature using relatively large steps of 5°C p/step for PCM-AFF and 10°C p/step for PCM-PLSD. Therefore, solubility estimation is associated with an error of at least  $\pm 2.5^\circ\text{C}$  for PCM-AFF and  $\pm 5^\circ\text{C}$  for PCM-PLSD.

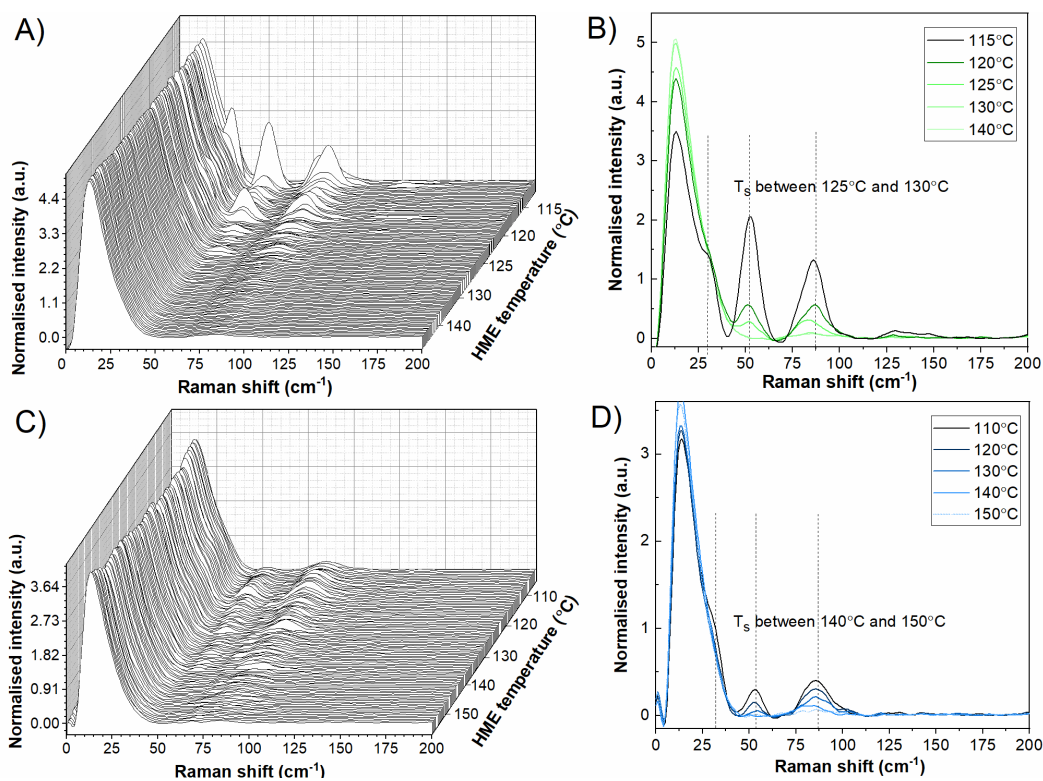


Figure 2.4. THz-Raman spectral evolution of A-B) PCM-AFF 30-70wt% and C-D) PCM-PLSD 45-55wt% at different processing temperatures. In Figures B) and D) spectra are spatial averages of 20 spectra at each temperature.

It is also noteworthy that the product melt temperature may differ from set point temperature values as a result of heat from the shear between the screws and material, so care should be taken with regards barrel zone temperature measurements and actual local material temperatures.<sup>43,183</sup> Within this work, product melt temperature was monitored at the die section and typical  $\pm$  variation did not exceed 3°C compared to the system set point value. In the upstream sections, the extent of heating and cooling required to maintain set-point temperatures was observed. This showed that there was no substantial cooling requirement to compensate for frictional heat. As a result, it was assumed that the reported temperature values are reflective of the local material temperature within the system.

Using the same approach,  $T_S$  was determined for all API-polymer compositions. For both systems, temperature-composition phase diagrams were generated by plotting the lowest temperature required for complete API amorphisation (API dissolution end temperature) and the highest temperature at which residual crystalline API could be

detected. Figure 2.5 and 2.6 show the amorphous and crystalline coordinates and the estimated equilibrium solubility curve as a function of the HME processing temperature for both systems.

### 2.3.2. Temperature-composition phase diagrams

The drug phase transition region demarks the boundary between the undersaturated region (region I in Figure 2.6.B and 2.7.B) where the API is fully amorphous and the supersaturated region (region II in Figure 2.6.B and 2.7.B), where crystalline API particulates are suspended in a supersaturated API-polymer matrix. At certain API-polymer ratios, API dissolution showed no temperature dependence and complete miscibility was observed at all processing temperatures, including the polymer glass transition temperature ( $T_g$ ). This was considered the critical concentration ( $C_c$ ) as it defined the maximum API concentration where no crystallinity was detected. The experimental limiting factor determining the lowest HME processing temperature for each system was the polymer  $T_g$  to avoid solidification of the polymer and subsequent equipment blockage. Figure 2.5 shows the THz-Raman spectra at the critical concentration for both systems.

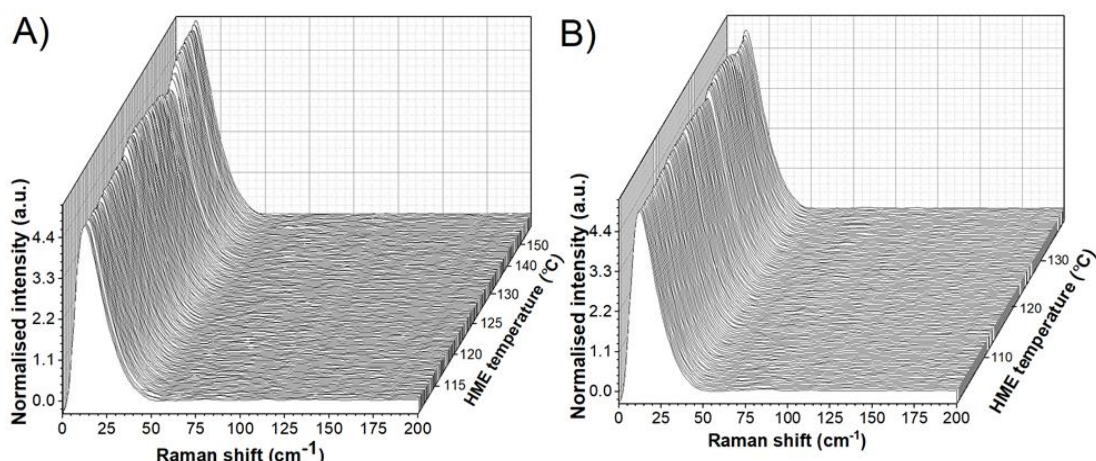


Figure 2.5. THz-Raman spectra of A) PCM-AFF 20 wt% and B) PCM-PLSD 40 wt%.

### 2.3.2.1 Paracetamol-HPMC system

For the HPMC-based compositions, the API critical concentration was 20 wt% (Figure 2.6). Upon further increase of the API mass fraction, equilibrium solubility is reached at higher temperatures and an almost linear temperature increment is observed for mixtures  $\geq 27.5$  wt% API-load. This observed trend is most likely to be a result of the relatively large temperature steps taken at the given compositions ( $5^{\circ}\text{C}$  per step). Reducing the temperature steps could improve the accuracy in determining the position of the equilibrium temperature and refine the shape of the curve.

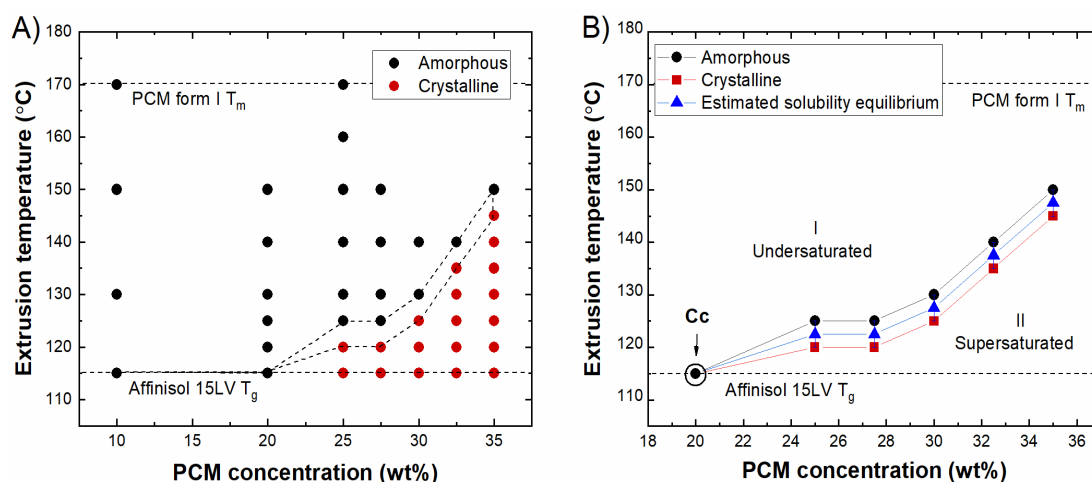


Figure 2.6. Phase behaviour of the PCM-PLSD system during extrusion: A) HME processing temperatures and API physical state; B) Estimated equilibrium solubility curve. Cc denotes the critical concentration up to which no crystallinity was found.

For all experimental compositions the API dissolved at temperatures well below its melting point (*e.g.*,  $55^{\circ}\text{C}$  lower at 20 wt% API-load), indicating good miscibility between both components and a marked reduction of its chemical potential in the presence of the polymer.<sup>56</sup> The reduction in the chemical potential is usually observed using DSC through detection of a depressed melting point.<sup>175,184</sup> However, these results show that spectroscopic methods can also be used to indirectly assess these phenomena. Moreover, this is a direct observation that extrusion can be performed at temperatures below the API melting point and attain complete drug solubilisation. Understanding the correlation between the HME processing temperature, drug

composition and residual crystallinity is of utmost importance to define HME processing boundaries and to identify the optimal processing window to promote formation of stable molecular dispersions whilst avoiding potential compound degradation.<sup>60,185</sup> This is particularly relevant for ASDs containing thermally labile drug substance.

### 2.3.2.2. Paracetamol-Copovidone system

Compared to HPMC, copovidone exhibited higher solubilisation capacity and the API critical concentration up to which there was no detected free API was 40 wt% (Figure 2.7). When increasing the API content from 45 wt% to 60 wt%,  $T_s$  appears to reach a plateau, remaining at 145°C despite the drug increase. Note that physical mixtures from 52.5 to 57.5 wt% API (identified by single asterisk in Figure 2.7.A) were only extruded at the dissolution end temperature (150°C). However, given the crystalline character of adjacent concentrations at 50 wt% and 60 wt% API at 140°C, it is reasonable to assume crystallinity of this intermediate concentration range at 140°C.

Apart from the impact of the temperature steps taken at each composition (10°C/step) the “plateau effect” is thought to be related to temperature-dependent structural changes of the polymer. It has been described that PVP-based polymers could assume a helical conformation under specific circumstances which potentially could also occur during extrusion.<sup>186</sup> This conformation would enable incorporation of additional drug molecules upon expansion, by reducing steric hindrance of API molecules already linked to the polymeric chain, and could explain the solubility increase despite the constant temperature. Further investigation is required to provide experimental support for this hypothesis, but this was out of the scope of the present work.

From 60 wt% to 62.5 wt% API,  $T_s$  experiences an abrupt temperature increment. Above 65 wt% API-load, as  $T_{extrusion}$  approaches the API melting point, the amorphous state of the drug is not a reflection of the polymer solubilisation capacity. This is one of the limitations of this approach since it requires (i) miscible API-polymer systems where the API  $T_M >$  polymer  $T_g$  and (ii) processing temperatures below the API  $T_M$  to enable detection of the excess crystalline API.

When comparing to PC-SAFT and F-H predictions performed by Lehmkemper and co-workers,<sup>64</sup> there are evident differences between predictions and experimental measurements performed in this study. PC-SAFT and FH predictions lack the plateau effect and solubility equilibrium is usually lower than the one determined by THz-Raman, especially at high polymer content. Even though the shape of the solubility curve and specific saturation temperatures differ, the magnitude of the values is of the same order. The work of Lehmkemper and co-workers shows that the maximum stable concentration of API in this polymer lies between 30 and 40%, which is comparable to the critical concentration determined during this work using LFR (i.e. 40 w %). This suggests that this critical concentration could indicate the solid solution capacity of the polymer after HME processing and thus, provide a concentration threshold that can differentiate stable amorphous systems from metastable/unstable systems. This correlation will be elaborated upon in more detail later on.

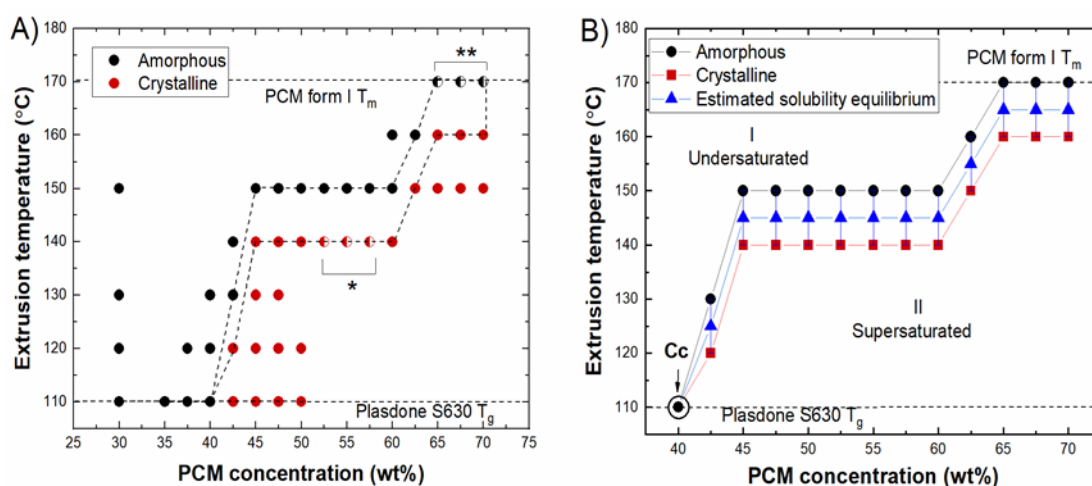


Figure 2.7. Phase behaviour of the PCM-PLSD system during extrusion: A) HME processing temperatures and API physical state; B) Estimated equilibrium solubility curve.  $C_c$  denotes the critical concentration up to which no crystallinity was found; \* denotes compositions expected to be crystalline at 140°C based on crystallinity of adjacent compositions; \*\* denotes the composition range where the API amorphous character is not a direct reflection of the polymer solubilisation capacity due to the proximity to the API  $T_M$ .

### 2.3.3. Polymorphic phase identification

In order to assess eventual polymorphism occurring during extrusion, variable-temperature off-line THz-Raman experiments were performed to obtain THz reference spectra of each polymorph. We used constrained crystallisation under a microscope slide and a cover glass to kinetically trap polymorphs via Ostwald rule of stages. paracetamol has three known polymorphs under normal pressure conditions: monoclinic (form I, stable), orthorhombic (metastable, form II) and form III, the most metastable of all.<sup>187,188</sup> Its recrystallisation behaviour from the amorphous glass is highly variable and dependent on both sample thermal history and presentation method.<sup>189</sup> Therefore HSM, DSC and variable-temperature XRPD experiments were performed as confirmatory techniques (results shown in Appendix A).

Collected THz-Raman spectra of polymorphs III, II and I, as well as the amorphous form are shown in Figure 2.8. The spectral features of each polymorph are in good agreement with literatures data. By comparing the THz-Raman spectra obtained during HME with the reference spectra of each polymorph, only PCM form I was identified for both systems. There were no metastable crystalline forms during the API solubilisation process nor recrystallisation from the amorphous form during extrusion. Hence, measured solubility depicts PCM form I solubility in both matrices. However, recrystallisation to different polymorphs could occur after HME for supersaturated systems.

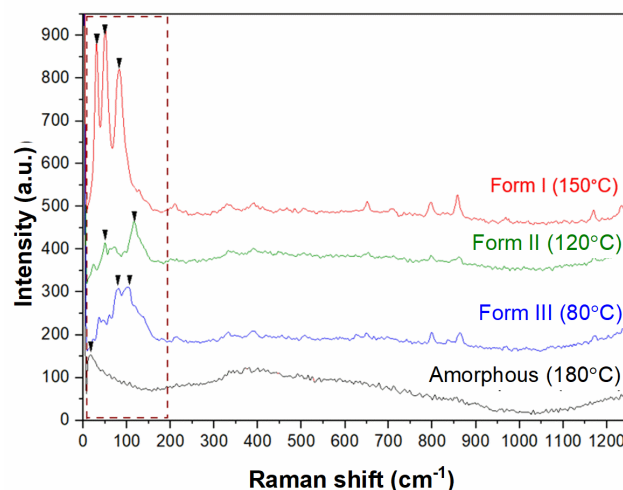


Figure 2.8. THz-Raman spectra of amorphous PCM and crystalline forms III, II and I with respective recrystallisation temperatures from the amorphous glass

## 2.2.4 Crystal dissolution behaviour observed by hot stage

### microscopy

It is interesting to note that at the  $T_g$  of pure polymer, thermal diffusion and molecular mobility – essential to the mixing of the two chemical entities – were sufficient to fully dissolve the API up to the  $C_c$  in both polymeric matrices during the short residence time in the extruder (~150 seconds for empty extruder conditions). Traditional DSC solubility protocols disregard solubility data near the  $T_g$ , since the drug dissolution kinetics becomes much slower than the time scale of the measurement.<sup>190</sup> However, the energy provided during extrusion via intensive mixing, shear and temperature input were sufficient to overcome this barrier and dissolve the API. Thus, as an alternative means of understanding the thermodynamic driving force for crystal dissolution, HSM experiments were carried to simulate the temperature conditions of the HME process by using isothermal steps of equal duration as the mean residence time within the extruder (empty barrel conditions).

Figure 2.9 shows the representative micrographs at the end of the isothermal steps in both polymeric matrices as well as sample behaviour during cooling cycles. Based on the birefringence properties, there is no observable API dissolution at the polymer  $T_g$ , as both systems comprise just physical mixtures. Apart from heat transfer variations, without the HME-induced distributive and dispersive mixing, API dissolution is only diffusion controlled (i.e., there is no mixing) and complete API dissolution occurs at higher temperatures, possibly due to kinetic constraints. However, upon complete dissolution a single phase system is obtained, corroborating THz-Raman indication of miscibility. For both polymer systems during HSM analysis, there was no API recrystallisation upon cooling, indicating that both polymers are capable of stabilising the amorphous drug. Although the absence of recrystallisation is also partially related to the intrinsic glass forming ability of the drug.<sup>191</sup> There is also evidence of a marked API-induced plasticising effect. When in a single component system, Plasdane S630 (Figure 2.9.D) experiences a drastic change in the viscoelastic properties with apparent liquefaction occurring at 160°C (~50°C above its  $T_g$ ), whereas pure Affinisol (Figure 2.9.A) has higher viscosity and no evident liquefaction is observed up to 180°C.

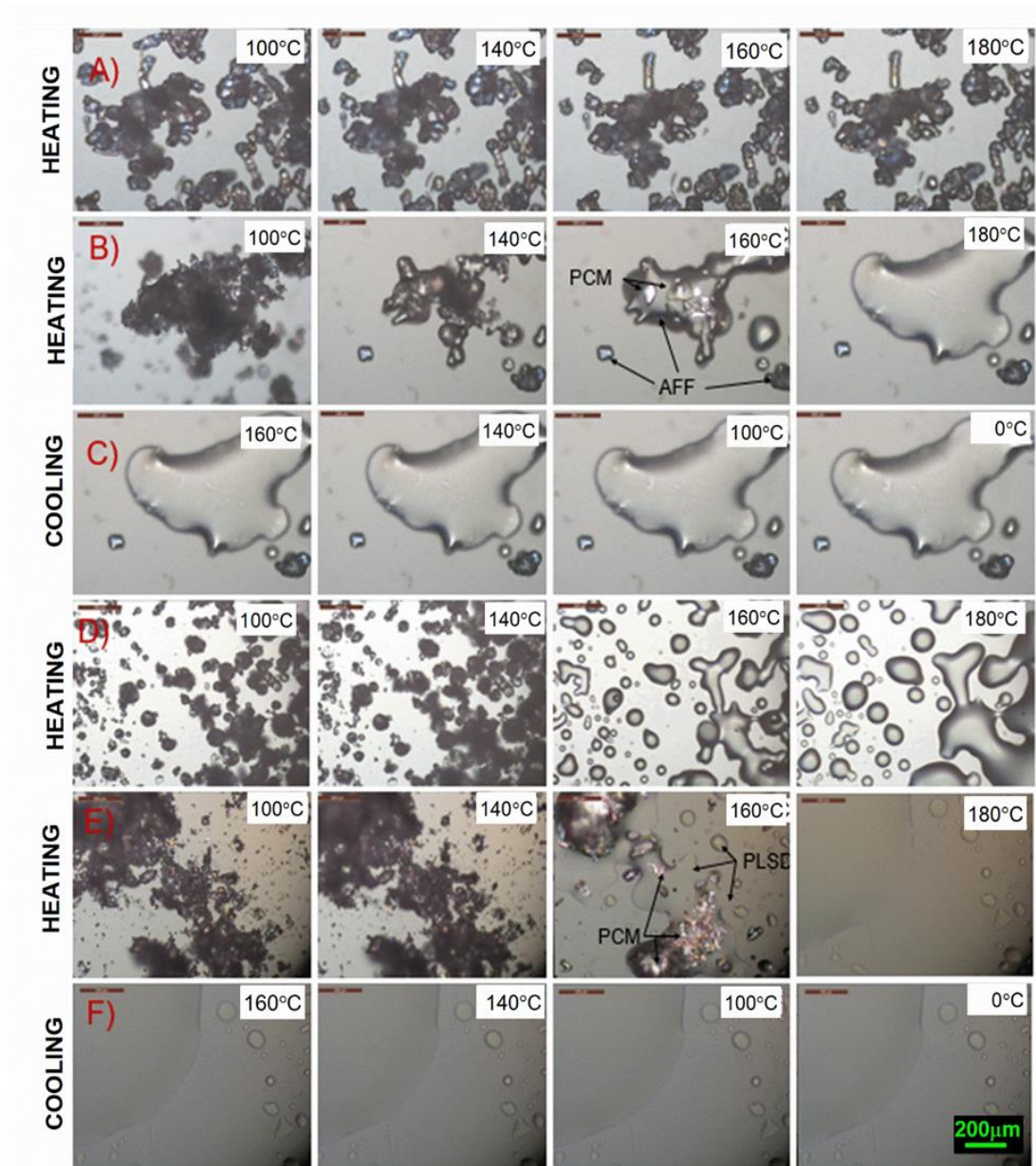


Figure 2.9. Hot stage microscopy images of A) pure AFF; B) and C) PCM-AFF 20-80 wt% during heating and cooling cycles, respectively; D) pure PLSD upon heating cycle; E) and F) PCM-PLSD 30-70 wt% during heating and cooling cycles, respectively. The scale bar is as indicated for all images.

### 2.3.5 Predictive value of the critical concentration

To validate our hypothesis with respect to the use of the critical concentration as a stability predictor, DSC and X-ray diffraction analysis were performed to assess the physical state of the extrudates after extrusion. For this purpose, only samples processed at the dissolution end temperature (i.e., lowest amorphisation temperature) were considered for each composition. DSC thermograms of PCM, AFF and PCM-AFF extrudates are displayed in Figure 2.10.A. Up to the critical concentration ( $C_c = 20$  wt %) there is no evidence of endothermic events due to melting of crystalline material. For drug loadings  $> 20$  wt%, there is an exotherm at 140-150°C depicting partial recrystallisation to form II, and two melting endotherms at  $\sim 155^\circ\text{C}$  and  $170^\circ\text{C}$ , ascribed to melting of forms II and I, respectively.

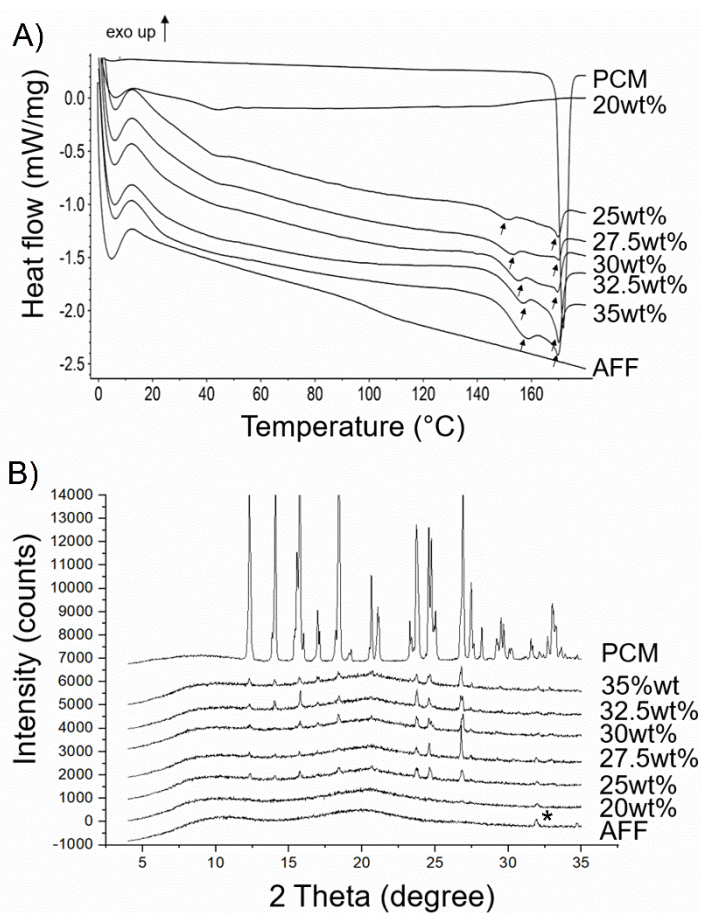


Figure 2.10. A) DSC thermograms and B) XRPD diffractograms of PCM, AFF and PCM-AFF extrudates with different API contents.

XRPD analysis (Figure 2.10.B) confirmed the lack of crystallinity up to 20 wt% drug loading, as indicated by the halo pattern characteristic of amorphous materials. In contrast, Bragg peaks corresponding to PCM form I were found for all concentrations above  $C_c$ . An additional diffraction peak with maxima at  $\sim 32^\circ$  ( $2\theta$ ) was observed in the diffractograms of pure Affinisol and all low API-loading extrudates. This peak is ascribed to NaCl that is used as a manufacturing additive for Affinisol 15LV up to 5 wt%. It should be noted that NaCl was not spectrally active in the THz-Raman region and therefore had no contribution to crystallinity detected during extrusion.

The same recrystallisation trend is observed for Plasdane-based extrudates. Up to the critical concentration ( $C_c = 40$  wt %) there is a single phase amorphous dispersion with no melting endotherms (Figure 2.11.A). At 42.5 wt%, 45 wt% and 50 wt% the small melting endotherm at  $169^\circ\text{C}$ , denotes melting of PCM form I. At higher drug loadings, there are two endotherms at *ca.*  $160^\circ\text{C}$  (melting of form II) and  $169^\circ\text{C}$  (melting of form I). X-ray diffraction analysis is depicted in Figure 2.11.B. It corroborated the amorphous character of the extrudates up to the  $C_c$ . For formulations  $\geq 42.5$  wt% crystalline peaks corresponding to form I were found and as expected, their intensity increased with increasing the API mass fraction. Given its absence in the XRPD patterns, form II is thought to be thermally induced by the DSC heating scan for both polymers.

Appearance of crystalline API following cooling of the extrudates suggests the solubility limit has been exceeded. This was evident for all API-polymer extrudates with drug-loadings above  $C_c$  (i.e.,  $> 20$  wt% for PCM-AFF and  $> 40$  wt% for PCM-PLSD). This offers compelling evidence that (i) THz-Raman identification of the saturated solution temperature is valid and (ii) that the critical concentration has the ability to differentiate ASD formulations that are truly unstable/metastable and those which are more likely to be stable at point of use. Based on the correlation between  $C_c$  and DSC and XRPD amorphicity, the maximum solubility of paracetamol at temperatures encountered post HME in Affinisol and Plasdane are  $\leq 20$  wt% and  $\leq 40$  wt% respectively. Thus,  $C_c$  appears to provide a maximum drug loading threshold that can be used to infer ASD physical stability at the point of developing the manufacturing process. This enables early identification of recrystallisation tendencies within an ASD and allows identification of the maximum API load that can

be molecularly dispersed in the polymer during extrusion and remain amorphous at the point of use.

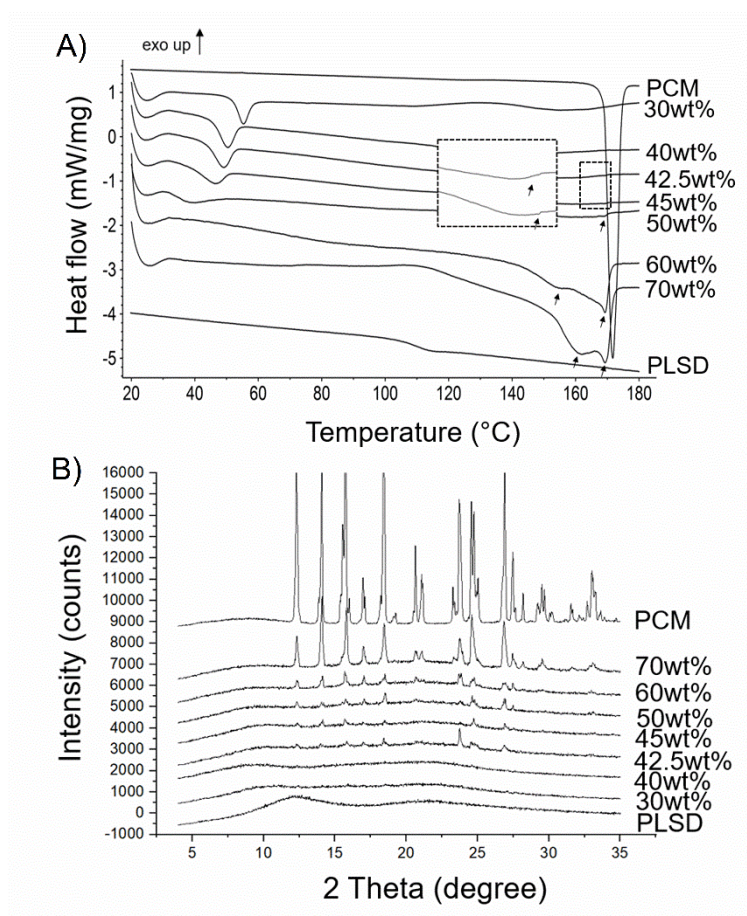


Figure 2.11. A) DSC thermographs and B) XRPD diffractograms of PCM, PLSD and PCM-PLSD extrudates with different API contents.

The THz-Raman method herein developed has allowed an insight into the likely equilibrium solubility range for these particular systems. Care was taken to allow extrusion to reach steady state at each experimental condition and THz-Raman data was only considered when steady state conditions were satisfied. This allied with the length of the 16 mm extrusion unit ( $HME \text{ Length } (L) / \text{Diameter } (D) = 40$ ) and the intensive mixing provided offers sufficient confidence to assume true equilibrium was reached and that observed solubility data is not constrained by kinetic limitations.

Furthermore, by enabling in-line drug-polymer solubility determination, this method also provides a valuable process analytical technology (PAT) tool for process

optimisation during the development of new ASDs systems by hot melt extrusion. It has the potential to correlate product critical quality attributes, such as residual crystallinity, to HME critical process parameters such as residence time, screw speed, feed rate, screw configuration and processing temperature, as promoted by the International Conference on Harmonization (ICH) Q8 (R2) and quality by design (QbD) frameworks advised by the major regulatory authorities, namely FDA and EMA.

## **2.4 Conclusions**

The objective of this Chapter was to develop a new empirical method to determine the solubility of crystalline API in polymeric matrices directly during hot melt extrusion processing. For the first time, low-frequency Raman spectroscopy was coupled with HME to monitor the amorphous-crystalline phase transitions of the API as a means of providing real-time API solubility. As a proof of concept, the solubility of paracetamol in HPMC, grade Affinisol 15LV and PVP-VA, grade Plasdone S630 was determined. Successful identification of the saturated solution temperature enabled construction of solubility phase diagrams for the binary systems. From the phase diagrams generated in this manner a critical API concentration was identified, 20 wt% for Affinisol 15LV and 40 wt% for Plasdone S630. This critical concentration was found to reveal the maximum API load that can be molecularly dispersed in the polymer during extrusion and remain in the amorphous state at storage conditions after HME processing. DSC and XRPD analysis supported this inference and showed that this critical concentration could be used as a stability predictor.

Overall, solubility data generated by this approach provides a more accurate reflection of the likely solubility equilibrium for optimum HME processing at temperatures below the API  $T_M$  and a reliable alternative solubility measurement for determining stable amorphous solid dispersions. This approach also offers an important in-line process control tool for process optimisation and QbD implementation in the manufacture of HME-based ASDs.

# **Chapter 3**

## **Comparative Study of Different Methods for the Prediction of Drug-Polymer Solubility**

### **3.1 Introduction**

To accommodate the needs of emerging pharmaceutical formulations, there is a continuous requirement for simultaneous innovation in process development and quality control. In response, the ICH and FDA released the quality by design (QbD) frameworks to guide the implementation of digital innovation within the pharmaceutical industry.<sup>192</sup> QbD allows quality to be included into the formulation and process design stages in a predictive manner. In order to successfully implement the QbD framework within the ASD field, API-polymer solubility and miscibility must be integrated into the design space.<sup>193</sup> Their prediction in advance of processing could assist formulation development to aid polymer selection and expedite the identification of stable drug loadings. Several publications have reported the phase behaviour of

binary API-polymer systems from a thermodynamic perspective using classic Flory-Huggins (F-H) modelling of melting point depression data.<sup>195–198</sup> A typical F-H phase diagram depicts six zones divided by three curves: the solid-liquid curve depicting the API-polymer solubility, the spinodal decomposition curve representing the metastability boundary between a single-phase amorphous system and an amorphous-amorphous phase separated one, and finally, the  $T_g$  curve as previously discussed in Section 1.6. However, full validation of these phase diagrams has been limited, with only a few points across the temperature-composition space being tested.<sup>60,198</sup> This Chapter aims to compare different methods for the API-polymer solubility determination and prediction. In particular, temperature composition phase diagrams will be developed via the Flory-Huggins and the Kyeremateng modelling approaches, and the solid-liquid equilibrium will be compared with the one provided by the low-frequency Raman method developed in Chapter 2. Additionally, the predictive potential of the Hansen solubility parameters and the zero enthalpy approach will also be assessed.

## **3.2 Materials and Methods**

### **3.2.1 Materials**

Soluplus (SOL), a polyvinyl caprolactam-polyvinyl acetate-polyethylene glycol graft co-polymer (at a ratio of 57/30/15, respectively) was kindly donated by BASF Chemical Co. (Ludwigshafen, Germany). Eudragit EPO (EPO), a cationic copolymer composed of methyl and butyl methacrylic acid esters and dimethylaminoethyl methacrylate monomers was provided as a free sample by Evonik Industries (Darmstadt, Germany). Polyvinyl alcohol (PVA) grade Emprove Parteck MXP was purchased from Merck (Merck, Germany). The remaining polymers (Affinisol and Plasdone) and the API (powdered paracetamol) were the same as described in Chapter 2 Section 2.2.1. The polymer choice criteria aimed to include 5 of the most ubiquitous polymers in current pharmaceutical processing.

## **3.2.2 Methods**

### **3.2.2.1 Ball-milling**

For each system, physical mixtures (~20 g) were first prepared by geometric mixing using a mortar and pestle at the following drug-polymer ratios: 10-90 wt%, 20-80 wt%, 30-70 wt%, 40-60 wt%, 50-50 wt%, 60-40 wt%, 65-35 wt%, 70-30 wt%, 75-25 wt%, 80-20 wt%, 85-15 wt% and 90-10 wt%. Subsequent ball-milling was performed to reduce particle size and to allow for diffusive mixing during the DSC heat exposure cycle. Ball milling was carried out on a Retsch GmbH ball mill (Haan, Germany). Powdered samples (~1 g) were placed in 25 ml stainless steel milling containers with two stainless steel balls (7 mm in diameter) and milled at 30 Hz. A predefined milling time of 2 min was chosen, which was followed by 2 min cooling time to reduce API amorphisation. A total of 4 milling-cooling cycles were used for all samples (8 min total milling time). The number of milling-cooling cycles was determined by measuring the melting point temperature of the mixture beyond which no further melting point decrease was observed. Care was also taken to assure no polymorphic phase transition occurred and that crystalline API was still present at the end of milling (confirmed by XRPD). Appendix B 1 shows the corresponding data.

### **3.2.2.2 Differential Scanning Calorimetry**

Melting point depression experiments were performed on a DSC 214 Polyma differential scanning calorimeter (Netzsch-Geratebau GmbH, Germany) under a helium environment (purge 1=40 ml/min, purge 2=60 ml/min). Samples of 3-5 mg were accurately weighed and crimped in 25  $\mu$ L aluminium pans with pierced lids (to allow the moisture to escape) and subjected to two heat-cool cycles as shown in Figure 3.1. The first heating cycle comprises 3 phases: (1) heating from 0°C to 100°C at 20°C/min, (2) an isothermal step for 30 min at 100°C for the formulations containing EPO, PVA and SOL and at 110°C for the AFF- and PLSD-based systems – this is an intermediate temperature between the polymer's  $T_g$  and the API's  $T_M$  and (3) heating from 100°C to 180°C at 1°C/min to allow for diffusive mixing and provide sufficient

time to solubilise the API. There is a continuous debate in the literature as to whether to use the onset, peak top, or offset temperature of the API melting endotherm as the solubilisation temperature ( $T_S$ ). Here the recommendation of Höhne *et al.*,<sup>199</sup> was followed and the peak top of the melting endotherm was taken as the correct  $T_S$  value. All cooling cycles were performed from 180°C to 0°C at 20°C/min to quench cool the samples. The second heating cycle was performed from 0°C to 180°C at 20°C/min to obtain the  $T_g$  related to the API loading. The midpoint of the glass transition event was evaluated as  $T_g$ . For each drug-polymer system, measurements were performed in triplicate at all drug-polymer ratios.

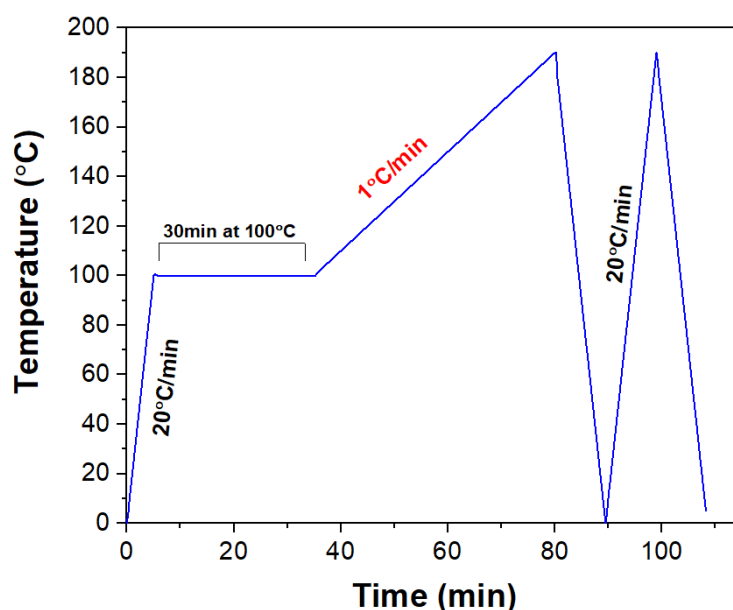


Figure 3.1. DSC melting point depression method.

### 3.2.2.3 Helium pycnometry – density measurement

True density measurements were performed on a Quantachrome MicroUltracyc 1200e gas pycnometer (Anton Paar, UK) using Nitrogen gas purge (0.684 bar gas pressure). The system was equilibrated and calibrated before use. System performance was verified using two standard stainless balls with known volume (2.145cm<sup>3</sup>) before testing materials, to ensure accuracy. Measurements were performed in duplicate for each material. For each replicate, the measurement was made in triplicate (n=6 for each material).

## 3.2.3 Theoretical considerations

### 3.2.3.1 Calculation of the solubility curves

#### 3.2.3.1.1 Flory-Huggins model

The use of Flory-Huggins lattice theory to construct a temperature-composition phase diagram depicting the drug-polymer solubility as a function of temperature has been well established in the literature. Accordingly, the Gibb's free energy of mixing  $\Delta G_{mix}$  may be expressed as:

$$\Delta G_{mix} = RT \left( \frac{\phi_{drug}}{N_A} \ln \phi_{drug} + \frac{\phi_{poly}}{N_B} \ln \phi_{poly} + \chi \phi_{drug} \phi_{poly} \right) \quad (3.1)$$

where  $\phi$  is the volume fraction,  $N$  is the molecular volume of the drug or polymer,  $\chi$  is the F–H interaction parameter,  $R$  is the molar gas constant, and  $T$  is the temperature. In a drug–polymer mixture,  $N_A$  is defined as the molecular size of the drug. Thus,  $N_B = mN_A$ , where  $m$  is the ratio of the volume of a polymer chain to drug molecular volume (Eq. 3.2):

$$m = \frac{\frac{Mw_{poly}}{\rho_{poly}}}{\frac{Mw_{drug}}{\rho_{drug}}} \quad (3.2)$$

where the  $Mw_{poly}$  and  $Mw_{drug}$  are the molecular weight of polymer and drug, respectively, and the  $\rho_{poly}$  and  $\rho_{drug}$  are the density of polymer and drug, respectively. The free energy of mixing for a drug–polymer binary system may therefore be written alternatively as:

$$\Delta G_{mix} = RT \left( \phi_{drug} \ln \phi_{drug} + \frac{\phi_{poly}}{m} \ln \phi_{poly} + \chi \phi_{drug} \phi_{poly} \right) \quad (3.3)$$

The free energy of mixing may be calculated at a specified temperature with respect to the corresponding interaction parameter. Furthermore, the melting point depression data collected from the DSC may be used to predict the drug–polymer interaction parameter using the following the approach developed by Nishi and Wang<sup>57</sup>:

$$\frac{1}{T_M} - \frac{1}{T_{M0}} = -\frac{R}{\Delta H} \left[ \ln \phi_{drug} + \left( 1 - \frac{1}{m} \right) \phi_{poly} + \chi \phi_{poly}^2 \right] \quad (3.4)$$

where  $\phi$  is the volume fraction of the drug,  $T_M$  and  $T_{M0}$  are the melting points of the drug crystal in the drug-polymer mixture and the pure drug, respectively,  $R$  is the gas constant, and  $\Delta H$  is the heat of fusion of the drug. For estimating the interaction parameter  $\chi$  from the melting point depression, Eq. 3.4 required rearrangement, which yields Eq. 3.5:

$$\left(\frac{1}{T_M} - \frac{1}{T_{M0}}\right) * \frac{\Delta H}{-R} - \ln \phi_{drug} - \left(1 - \frac{1}{m}\right) \phi_{poly} = \chi \phi_{poly}^2 \quad (3.5)$$

The slope of the line obtained from plotting Eq. 3.5 provides the  $\chi$  value. It should be noted that the interaction parameter is not constant but temperature and composition dependent.<sup>200</sup> The temperature dependence of  $\chi$  is defined as shown in Eq. 3.6:

$$\chi = A + \frac{B}{T} + C_1\phi + C_1\phi^2 \quad (3.6)$$

where  $A$  is the value of the temperature-independent term (entropic contribution),  $B$  is the value of the temperature-dependent term (enthalpic contribution), and  $C_1$  and  $C_2$  are fitting constants of  $\chi$  with respect to volume fraction.<sup>201</sup> This relationship subsequently has been simplified to Eq. 3.7, which has proven to be sufficient in many polymer systems.<sup>202</sup>

$$\chi = A + \frac{B}{T} \quad (3.7)$$

This first order relationship between  $\chi$  and temperature is an additional assumption of F–H polymer solution theory, which summarises the nontrivial dependencies of  $\chi$  on polymer composition, chain length and temperature. The variation of the relationship between  $\chi$  and temperature has been previously reported and it has been used to extrapolate the value of  $\chi$  for drug–polymer binary systems outside experimental temperatures.<sup>201,203</sup> Herein, Eq. 3.7 was employed to relate  $\chi$  to temperature and to identify constants  $A$  and  $B$ .

Furthermore, the spinodal curve, which provides the boundary between the metastable and unstable region beyond which amorphous phase separation occurs, can be plotted by equalising the second derivation of  $\Delta G_{mix}$  to zero, hence:

$$T_{spinodal} = \frac{2B}{\frac{1}{\phi_{drug}} + \left(\frac{1}{m\phi_{poly}}\right) - 2A} \quad (3.8)$$

Where  $T_{spinodal}$  is the spinodal miscibility temperature.

### 3.2.3.1.2 Empirical equation

Alternatively, the solubility curve of an API–polymer binary system can be modelled by the empirical approach developed by Kyeremateng *et al.*<sup>62</sup> according to the following:

$$T_s = Ae^{bx} + T_M + C \quad (3.9)$$

In Eq. 3.8,  $T_s$  is the API's solubility temperature,  $T_M$  is the API melting temperature,  $x$  is the API content (wt%) and  $A$ ,  $b$  and  $C$  are the fitting parameters. According to the authors<sup>62</sup>, the  $C$  parameter represents the magnitude of the API-polymer interaction and can take only zero or integer values (i.e.,  $C = 0$  for systems exhibiting repulsive or non-existent API-polymer interaction and  $C = 1, 2, 3$  etc... for systems exhibiting attractive API-polymer interactions). In this study, the approach developed by Mathers *et al.*<sup>204</sup> was adopted and the experimental solubility data was fitted to Eq.3.8 with no constraint to the  $C$  parameter after optimisation of  $A$  and  $b$ , with  $C$  set to zero. These parameters were obtained with a nonlinear fitting procedure by minimising the residual sum of squares. Given that this approach is a combination of the methods developed by Kyeremateng *et al.*, and Mathers *et al.*, it will be referred to as the empirical method (E-M) from here on to avoid misrepresentation.

### 3.2.3.2 Calculation of the glass transition temperature

Multiple approaches have been developed for estimating the  $T_g$  curve of API-polymer mixtures from a knowledge of their pure component physicochemical properties.<sup>205</sup> The Gordon-Taylor ( $G - T$ ) equation is commonly used for binary systems according to:

$$T_g = \frac{W_{drug}Tg_{drug} + K_{G-T}W_{poly}Tg_{poly}}{W_{drug} + K_{G-T}W_{poly}} \quad (3.10)$$

In Eq. 3.9,  $W_{drug}$  and  $W_{poly}$  is the weight fraction of the drug and polymer, respectively.  $T_{gdrug}$  and  $T_{gpoly}$  is the glass transition temperature (in Kelvin) of the drug and the polymer, respectively. The  $K_{G-T}$  parameter can be estimated from the Simha-Boyer rule<sup>67</sup>:

$$K_{G-T} = \frac{\rho_{drug} T_{gdrug}}{\rho_{poly} T_{gpoly}} \quad (3.11)$$

where,  $\rho_{drug}$  and  $\rho_{poly}$  is the density of the drug and polymer, respectively.

Alternatively, Kwei<sup>206</sup> reported that several systems demonstrated a  $T_g$  behaviour that differed from the results obtained employing the  $G - T$  equation. To account for this deviation, a second parameter,  $q$ , was included as shown in Equation 3.12 below. This parameter is used to model the effects of specific interactions between components on the  $T_g$  of the binary system.<sup>167</sup>

$$T_g = \frac{W_{drug} T_{gdrug} + K W_{poly} T_{gpoly}}{W_{drug} + K W_{poly}} + q W_{drug} W_{poly} \quad (3.12)$$

Parameters  $K$  and  $q$  were determined by fitting them simultaneously to the experimental values following the approach suggested by Iemtsev *et al.*<sup>207</sup>

### 3.2.3.3 Calculation of the Hansen solubility parameters

The Hansen solubility ( $\delta$ ) parameters were calculated with the Hansen Solubility Parameters in Practice (HSPiP) software (version 5.1.08). The chemical structure of the API and polymers were drawn and the SMILES (Simplified Molecular Input Line Entry System) string was used to determine solubility parameters employing the Y-MB group contribution method according to the following Equation:

$$\delta_{Total} = (\delta_d^2 + \delta_p^2 + \delta_h^2)^{0.5} \quad (3.13)$$

Where  $\delta_{Total}$  is the total solubility parameter,  $\delta_d$  is the contribution from dispersion forces,  $\delta_p$  is the contribution from polar forces and  $\delta_h$  is the contribution from hydrogen bonding. The HSP difference ( $\Delta\delta_{Total}$ ) between the API and polymers were calculated.

Additionally the volume dependent solubility parameter ( $\delta_v$ ) was calculated according to:

$$\delta_v = (\delta_d^2 + \delta_p^2)^{0.5} \quad (3.14)$$

Apart from  $\Delta\delta_{\text{Total}}$ , the Bagley diagram was used to assess API-polymer pairs. The Bagley diagram is a two-dimensional plot of  $\delta_v$  against  $\delta_h$  that has been reported as one of the most efficient ways of representing polymer-polymer and polymer-solvent interactions with regards to HSP.<sup>208</sup>

### 3.3 Results and discussion

#### 3.3.1 Glass transition temperature ( $T_g$ ) prediction

The ASD  $T_g$  curve is an important component of the drug-polymer phase diagram, as it provides key kinetic information for guiding the ASD storage temperature.<sup>194</sup> In this study, two approaches for predicting the glass transition temperature were investigated, the Gordon-Taylor ( $G - T$ ) and the *Kwei* models. These models permit the theoretical calculation of the  $T_g$  values over the entire API-polymer composition range through the application of relevant pure component physicochemical properties (see Section 3.2.3.2). The modeled  $T_g$  curves along with the experimental  $T_g$  data obtained from DSC and the associated  $r^2$  values are illustrated in Figure 3.2. All systems exhibited a single  $T_g$  value between the  $T_{gs}$  of the individual components, which indicates potential homogeneous miscible systems. Both models provided a good fit to the experimental data ( $r^2 > 0.98$ ) with exception of PCM-AFF that showed a strong negative deviation from the  $G - T$  model ( $r^2 = 0.638$ ). It should be noted that the  $G - T$  model is based on volume additivity and assumes no interactions between drug and polymer.<sup>209</sup> Thus, deviations from ideal linear  $G - T$  behaviour are the result of entropy effects beyond combinatorial mixing, such as strong intermolecular interactions between the components.<sup>210</sup> In this case, the difference between the experimental and the predicted  $G - T$  values is most likely due to the stronger drug–drug interaction (i.e., self-association/dimer formations through the amide group), which would account for the observed negative  $G - T$  deviation. Such behaviour was not observed for any of the other polymer systems, suggesting better miscibility for the remaining ones. This is also supported by the (relatively) higher experimental  $T_g$  values compared to the PCM-AFF system.

Overall, and based on the  $r^2$  values, the *Kwei* model outperformed the  $G - T$  model and provided a better fit to the experimental data. The *Kwei* equation extends the  $G - T$  model by introducing the binary parameter  $q$ , which accounts for the effects of specific interactions between components.<sup>204</sup> Therefore only this model will be considered for the drug-polymer phase diagram construction. The physicochemical

properties of the pure components used in the modeling the  $T_g$ , as well as solubility and spinodal curves are summarized in Appendix B 2.

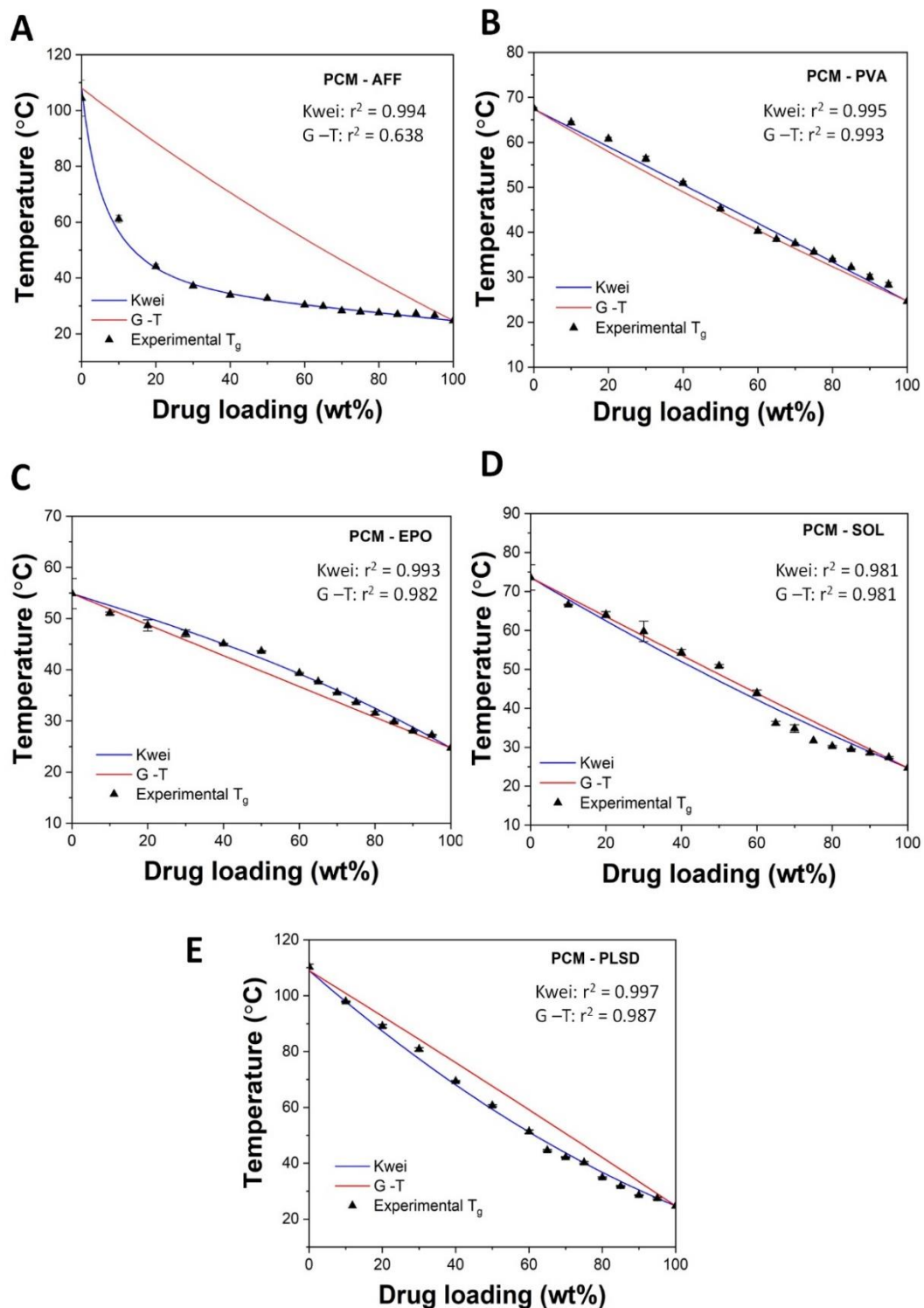


Figure 3.2. Glass transition temperature prediction for: a) PCM-AFF, b) PCM-PVA), c) PCM-EPO, d) PCM-SOL and e) PCM-PLSD. *Kwei* prediction is depicted by the blue line, whilst the Gordon-Taylor ( $G - T$ ) model is depicted by the red line. The DSC experimental  $T_g$  values are represented by the black triangles. The  $T_g$  error bar represents the standard deviation ( $n = 3$ ). The associated  $r^2$  values of the fitted  $T_g$  models with respect to the experimental data is showed for each system.

### 3.3.2 Melting point depression and $\chi$ interaction parameter

For a pure crystalline drug at the melting point temperature ( $T_M$ ), the chemical potential of both the solid-state and molten state is equal, and for drug-polymer mixtures, the melting point temperature of the drug could be reduced if the crystalline drug solubilises into the amorphous polymer.<sup>211</sup> Table 3.3 shows that the PCM melting point temperature decreased with increasing polymer concentrations for all systems. Based on the magnitude of the melting point depression (see Table 3.2), the polymers can be clustered in two groups: (I) PLSD and SOL and (II) EPO, PVA and AFF. The former group displayed greater melting point depression suggesting greater solubility, whilst the latter showed less significant  $T_M$  reduction. The experimental  $T_M$  data acquired using the DSC method were subsequently applied to the two methods described in Section 3.2.3 (i.e., the F-H model and the empirical equation) to model the solid-liquid equilibrium, the spinodal curve and the free energy of mixing that will be further discussed in the Section below. With regards to the  $F - H$  model, the interaction parameter  $\chi$  values for PCM-EPO, PCM-PVA, PCM-AFF, PCM-PLSD and PCM-SOL were 0.51, 0.12, -0.11, -0.85 and -1.85, respectively. Positive  $\chi$  values suggest immiscibility, whereas negative or close to zero values indicate miscibility.<sup>195</sup>

### 3.3.3 Hansen solubility parameters

The proximity of the Hansen solubility parameters (HSP) of the drug to that of the polymer ( $\leq 7 \text{ MPa}^{1/2}$ ) has been proposed to indicate miscibility between the compounds.<sup>71,212</sup> This could speed up the screening process by excluding underperforming polymers early in the screening process. With exception of PVA, a direct correlation between the HSP proximity values and drug-polymer solubility was found. Figure 3.3 displays the Bagley plot for the various drug-polymer systems. The raw HSP values calculated by the HSPiP software are shown in Appendix B 3. A similar grouping behaviour and polymer ranking was observed: group I (PLSD and SOL) displaying the smallest difference compared to group II (AFF and EPO). PVA did not follow the same trend and despite having the smallest HSP difference, it did not correlate well to the experimental data. This is most likely related to the high

hydrogen bonding count given by the PVA's hydroxyl groups. The existence of specific functional groups that hinder a direct translation of the Hansen solubility parameters has been previously reported in literature.<sup>71</sup>

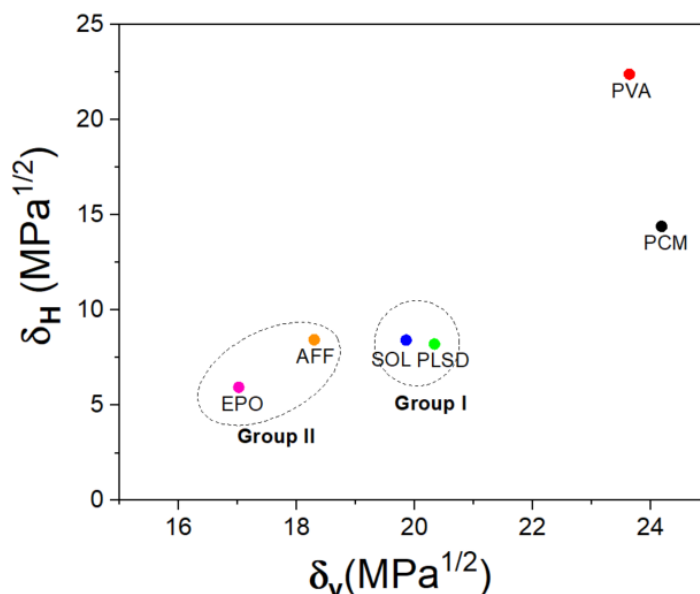


Figure 3.3. Bagley plot of the Hansen solubility parameters.

### 3.3.3 Gibb's free energy

To better understand miscibility between two components, consideration of the temperature effects on Gibb's free energy of mixing ( $\Delta G_{mix}$ ) is useful. In drug-polymer systems exhibiting negative  $\Delta G_{mix}$ , miscibility is thermodynamically favored, whereas positive  $\Delta G_{mix}$  values are typically observed for immiscible systems.<sup>201</sup> The Gibbs free energy variation as a function of composition and temperature was obtained by fitting the  $\chi$  values into Equation 3.3, and results are shown in Figure 3.4. The  $\Delta G_{mix}/RT$  for group I polymers (i.e., PLSD and SOL) is negative and convex as shown in Figures 3.4.d and 3.4.e, which suggests thermodynamically stable and homogeneous mixtures would be generated at all compositions. For group II polymers (i.e., AFF, PVA and EPO) a mixed  $\Delta G_{mix}$  behaviour was obtained. For this group, miscibility would be attained only at high temperatures and only for certain drug-polymer ratios (Figure 3.4.a, b and c). In particular, for the PCM-AFF system, temperatures  $\leq 100^\circ\text{C}$  resulted in a  $\Delta G_{mix}/RT$

that became positive at high drug loadings. The drug composition at which the Gibb's free energy became positive decreased as temperature decreased. For PCM-PVA, temperatures  $\geq 120^{\circ}\text{C}$  resulted in negative  $\Delta G_{mix}/RT$  at all compositions. As the temperature decreased ( $\leq 100^{\circ}\text{C}$ ), the Gibb's free energy became positive at drug volume fractions  $>0.3$ . Lastly, for the PCM-EPO system, negative  $\Delta G_{mix}/RT$  values were only obtained at  $140^{\circ}\text{C}$  for drug volume fractions  $<0.35$ . As temperature decreased  $\Delta G_{mix}/RT$  became positive at all compositions, suggesting extremely reduced miscibility.

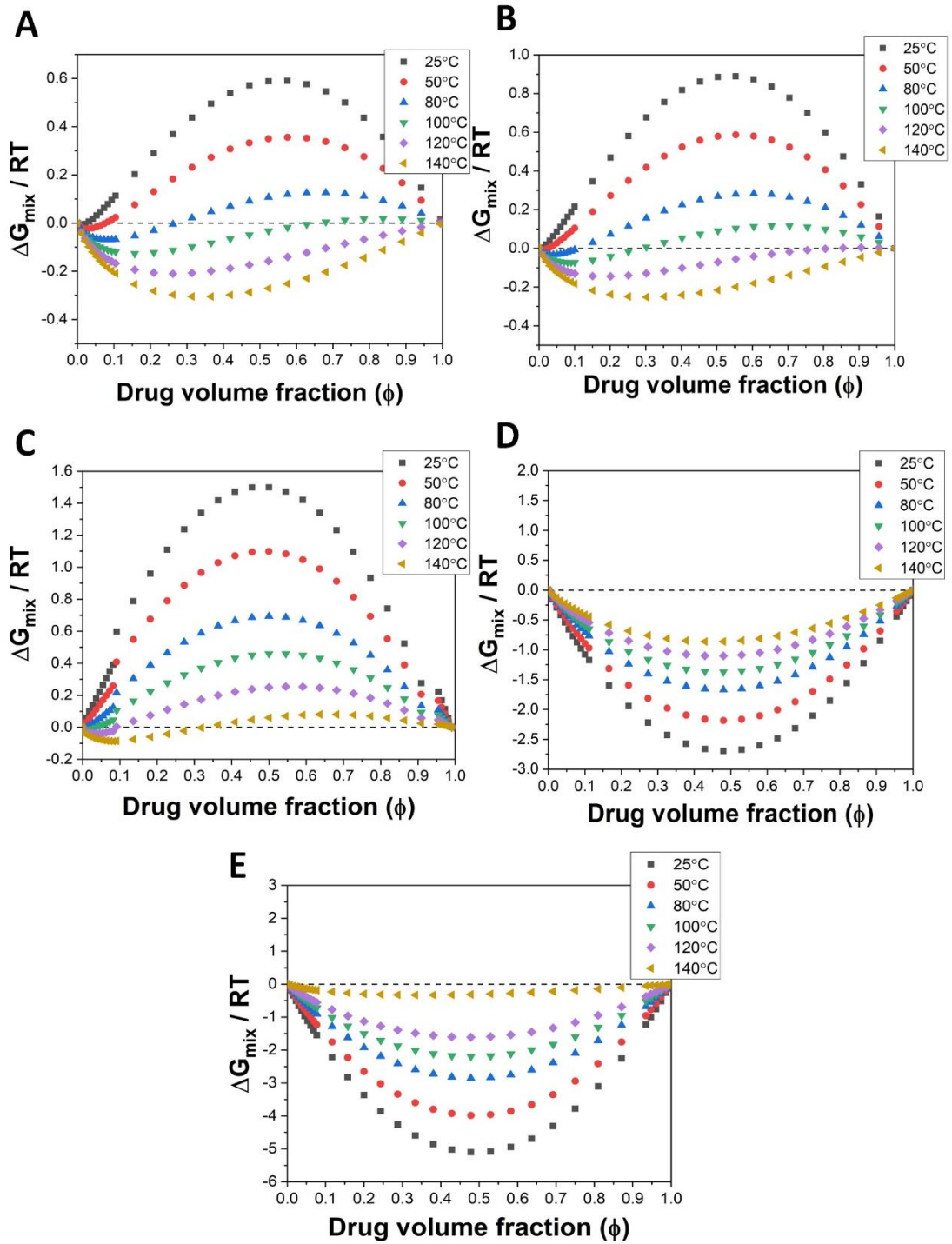


Figure 3.4. Plot of  $\Delta G_{mix}/RT$  vs drug volume fraction for a) PCM-AFF, b) PCM-PVA, c) PCM-EPO, d) PCM-SOL and e) PCM-PLSD.

### 3.3.4 Temperature-composition phase diagram

#### 3.3.4.1 The solid-liquid equilibrium

As discussed above, the  $F - H$  and the empirical methods were used to model the DSC melting point depression data in order to extrapolate API solubility at lower temperatures of interest (i.e., storage temperatures). Figures 3.5 and 3.6 display the temperature-composition phase diagrams containing the solid-liquid equilibrium, as well as the spinodal and  $T_g$  curves. To make a direct comparison with the solubility approach developed in Chapter 2, the saturated solubility temperature ( $T_S$ ) points obtained from the THz-Raman amorphous-crystalline transition were added to Figure 3.5.a and 3.5.b for AFF and PLSD, respectively.

While  $F - H$  and the empirical methods showed good correlation to the DSC depressed melting point data at high temperature ( $r^2$  values displayed in the Tables 3.3 and 3.4 respectively), there were considerable differences between the experimental low-frequency Raman solubilisation temperature values and the predicted ones. For both prediction methods, differences as high as 20°C for AFF and 50°C for PLSD were observed at the lower drug loadings where the pure polymer properties dominate the system. However, upon increasing the drug loading level  $\geq 35$  wt% for AFF and  $\geq 50$  wt% for PLSD, both measurements and predictions became comparable within a  $\pm 5^\circ\text{C}$  temperature interval. Such differences were expected to some extent, because the thermodynamic models do not include any viscosity considerations. Due to the *in situ* nature of the low-frequency Raman approach, viscosity and shear variations are directly translated into the experimental  $T_s$  values obtained. Further work is necessary to identify the drug-polymer composition associated with drastic viscosity changes that prevents true thermodynamic equilibrium from being reached during DSC and beyond which these models are no longer applicable for the drug-polymer solubility prediction.

The level of mixing of the components, the particle size and the polymer viscosity will affect the accuracy of the underlying DSC measurements as the drug dissolution requires transport of molecules into the polymer matrix. If the components are poorly

mixed, contain large particle and the system is highly viscous, mixing will require transport over longer distances and time, which will result in a diffusive and thermal lag. This may explain the higher solubilisation temperature values obtained from the DSC and can ultimately lead to an underestimation of the API solubility using only DSC-based methods. In this study, care was taken to mitigate these effects by (1) preparing physical mixtures by geometric mixing, (2) ball-milling the physical mixtures to further reduce particle size and increase the interaction surface area and (3) employing a slow-heating rate of 1°C/min above the polymer  $T_g$  to allow for diffusive mixing. Hence, it is reasonable to assume that at low drug loadings thermodynamic equilibrium was not reached during DSC and that due the intensive mixing provided by the twin-screw extruder, the  $T_S$  values obtained from the THz-Raman provide a more accurate reflection of the likely solubility equilibrium throughout the entire composition range.

The predicted solubility at 25°C provided by the  $F - H$  and  $E - M$  approaches was further compared to the critical concentration,  $C_c$ , (i.e., maximum stable composition) extracted from the THz-Raman approach (Table 3.2). The predicted solubilities from the empirical method correlated well with the THz-Raman solid solution capacity indication:  $E-M = 14\text{wt}\%$  vs  $C_c \sim 20\text{ wt}\%$  for AFF and  $E-M = 37\text{ wt}\%$  vs  $C_c \sim 40\text{ wt}\%$  for PLSD. Due to the compositional step change taken in Chapter 2, no drug loadings were tested between 10 wt% and 20 wt% for the PCM-AFF system. Thus, the  $E - M$  predicted solubility at 25°C not only corroborates the proposed  $C_c$  value but it refines it down to 14 wt%. On the other hand, the  $F - H$  predicted solubility values at 25°C were as low as 1 wt% for AFF and 3 wt% for PLSD. For PVA, EPO and SOL there was no THz-Raman data to compare with. Nonetheless, despite differences between the predicted solubility values at 25°C, both of these approaches suggested similar polymer ranking:  $SOL > PLSD > AFF > PVA > EPO$ . This suggests that the empirical method could be better suited for solubility screening, as it would provide a better indication of the maximum stable drug loading. In general, the  $F - H$  method predicted lower API solubility at storage temperature than the  $E - M$  approach. Overall, these results are in good agreement with literature data.<sup>64,213</sup>

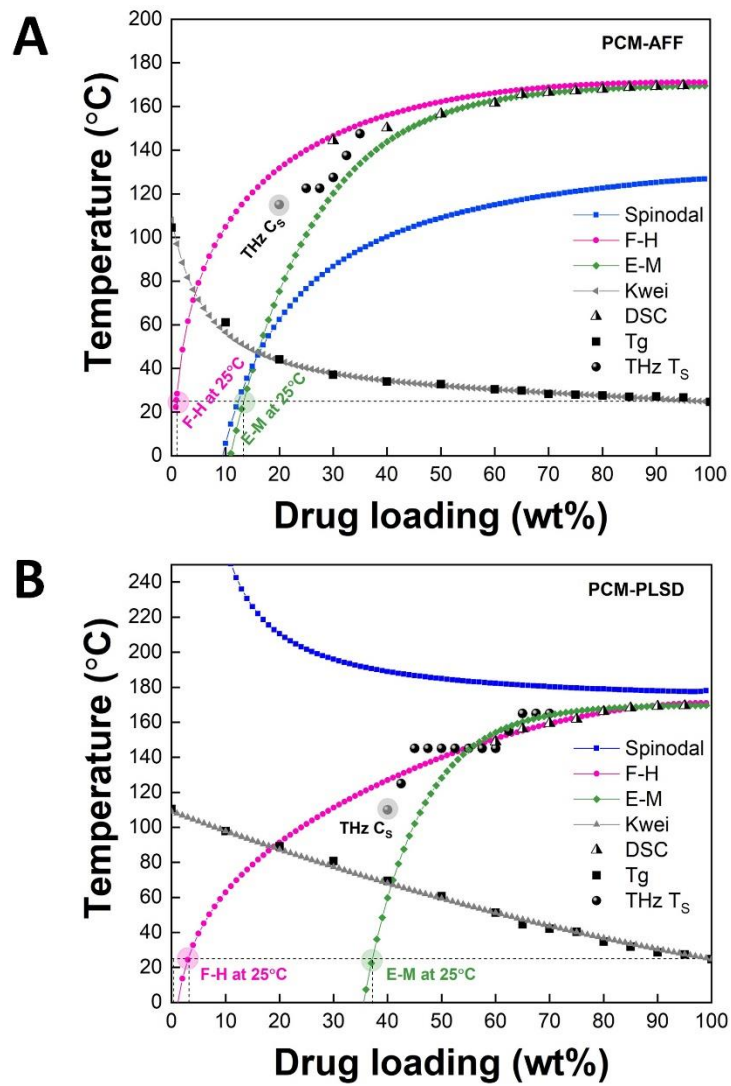


Figure 3.5. Binary temperature-composition phase diagrams for a) PCM-AFF and b) PCM-PLSD with the solubility curves modelled using Flory-Huggins ( $F - H$ ) theory and the empirical method ( $E - M$ ).

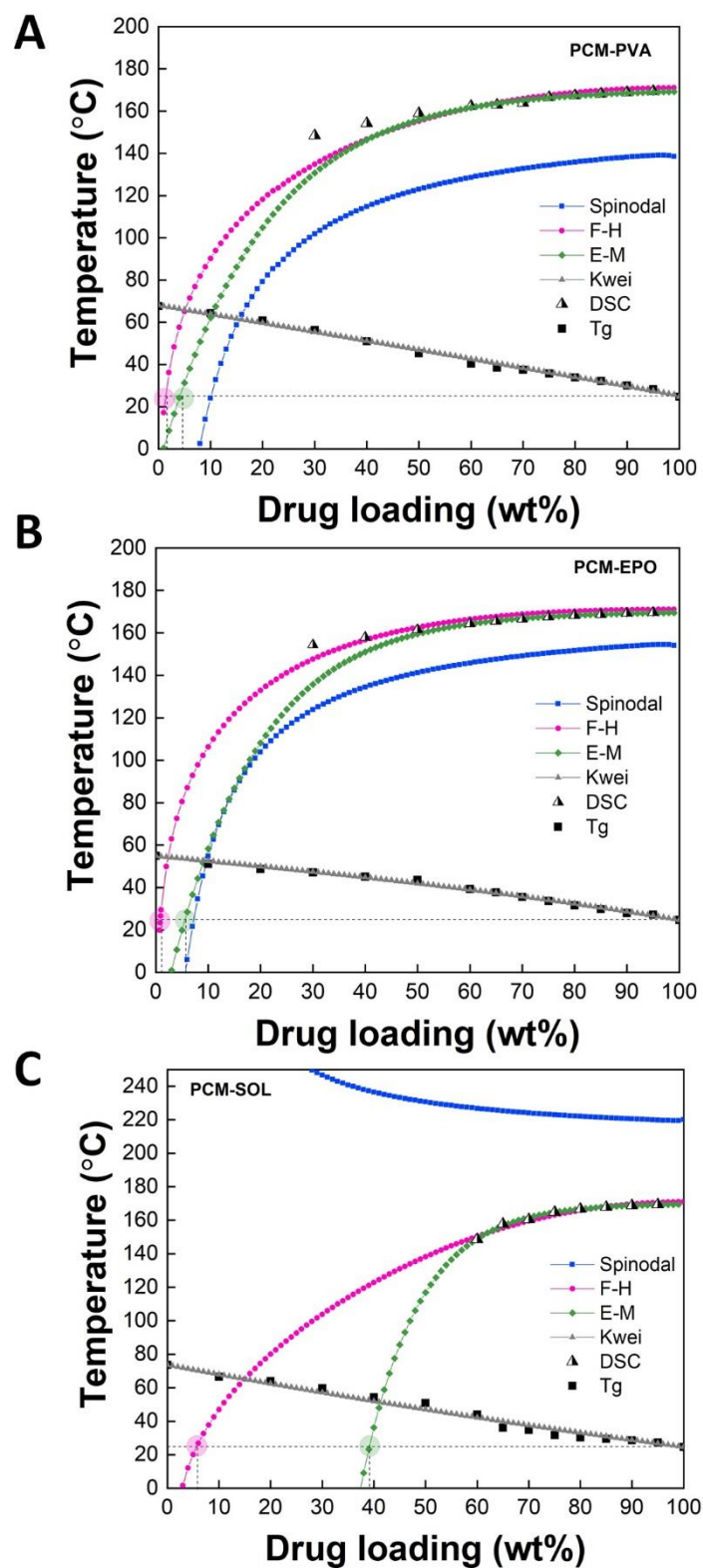


Figure 3.6. Binary temperature-composition phase diagrams for a) PCM-EPO, b) PCM-PVA and c) PCM-SOL with solubility curves modelled using  $F - H$  theory and the  $E - M$  approach.

### 3.3.4.2 The spinodal curve

The spinodal curve represents the boundary between the metastable and unstable regions, beyond which amorphous-amorphous phase separation is expected to occur.<sup>194</sup> For the vast majority of published drug-polymer phase-diagrams, an upper critical solution temperature (UCST) behaviour, with positive  $B$  and negative  $A$  values has been reported (refer to Eq. 3.7). Therefore, it is surprising to observe that a concave spinodal profile was obtained for group II polymers, with  $B < 0$  and  $A > 0$  indicating a lower critical solution temperature (LCST) behaviour (Figure 3.5.b and 3.6.c). This behaviour has been reported for temperature responsive polymer-water systems wherein the polymer solution transitions to a gel form as temperature increases.<sup>214</sup> Although not seldom observed for drug-polymer ASDs, this behaviour has been reported for indomethacin-, naproxen- and ibuprofen-Eudragit EPO systems, as well as for the carbamazepine-Affinisol system.<sup>59</sup> The position of the spinodal curve relative to the solubility curve can strongly affect the kinetics of amorphous phase separation. For any point located below the UCST spinodal curve or above the LCST curve, a single phase homogeneous system is expected to separate into two-phases, i.e., drug-rich and polymer-rich phases. Thus, due to the positioning of the spinodal curve, the two systems demonstrating LCST behaviour are deemed less prone to amorphous phase separation at usual storage temperatures post manufacture. For the group I polymers, an UCST behaviour was observed, which suggests phase separation could occur post manufacture.

### 3.3.5 The zero enthalpy approach

Alternatively, the solubility of the API in the polymer was also inferred by the zero enthalpy method.<sup>54</sup> The plot of the regression Equations and intercept values at zero enthalpy are shown in Figure 3.7 and Table 3.2, respectively. The intercept values provide an indication of the maximum drug concentration that can be solubilised in liquefied/molten polymer at zero enthalpy.<sup>204</sup> From these, the same polymer grouping behaviour was obtained and the following polymer solubility ranking was obtained: SOL~PLSD >> AFF > PVA > EPO. These results are in good agreement with the

solubility ranking provided by the  $F - H$ ,  $E - M$  and low-frequency Raman method (only AFF and PLSD for the latter).

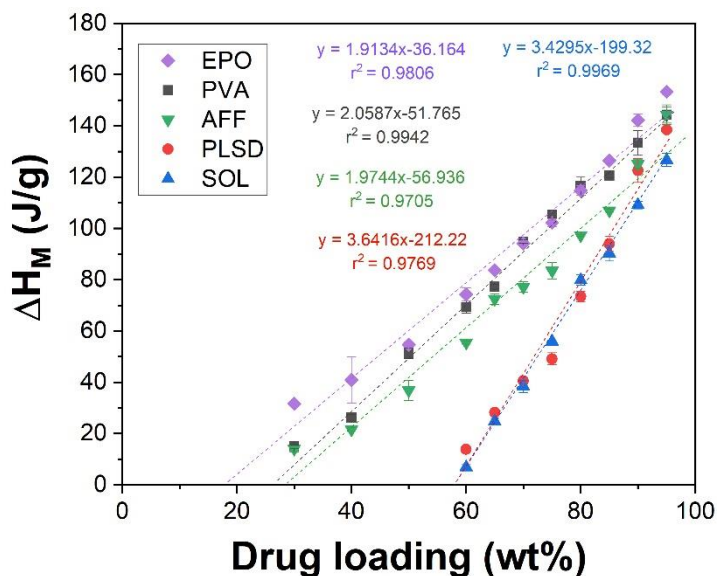


Figure 3.7. Graphical representation of the depressed  $\Delta H_M$  as a function of drug loading. The extrapolated linear relationship of  $\Delta H_M$  is based upon least square regression of the experimental data

Table 3.1. Solubility and miscibility values at 25°C.

Wt (%)	EPO	PVA	AFF	PLSD	SOL
F-H solubility at 25°C	0.6	0.7	1	3	5
E-M solubility at 25°C	4	6	<b>14</b>	<b>37</b>	39
Low-frequency Raman $C_c$	-	-	<b>20</b>	<b>40</b>	-
Solubility at $\Delta H = 0$	18.89	25.14	28.83	58.27	58.11
Miscibility at 25°C <sup>a</sup>	7	10	13	-	-

**a** – Obtained from the spinodal curve.

### Flory-Huggins

		<b>PCM:EPO</b> $r^2 = 0.839$ $\chi = 0.51$		<b>PCM:PVA</b> $r^2 = 0.950$ $\chi = 0.12$		<b>PCM:AFF</b> $r^2 = 0.977$ $\chi = -0.11$		<b>PCM:PLSD</b> $r^2 = 0.982$ $\chi = -0.85$		<b>PCM:SOL</b> $r^2 = 0.958$ $\chi = -1.81$	
Wt %	DSC $T_M$	F-H $T_S$	DSC $T_M$	F-H $T_S$	DSC $T_M$	F-H $T_S$	DSC $T_M$	F-H $T_S$	DSC $T_M$	F-H $T_S$	
95	$169.6 \pm 0.1$	167.74	$169.3 \pm 0.05$	168.94	$169.63 \pm 0.05$	171.19	$169.46 \pm 0.05$	170.66	$169.36 \pm 0.05$	170.75	
90	$169.2 \pm 0.1$	171.00	$168.8 \pm 0.15$	168.50	$169.23 \pm 0.05$	171.14	$169.13 \pm 0.5$	169.61	$168.83 \pm 0.05$	169.89	
85	$168.66 \pm 0.05$	170.95	$168.16 \pm 0.11$	167.94	$168.73 \pm 0.05$	170.86	$168.16 \pm 0.15$	167.90	$167.83 \pm 0.03$	168.42	
80	$168.23 \pm 0.05$	170.82	$167.36 \pm 0.11$	167.23	$167.9 \pm 0.11$	170.31	$166.06 \pm 0.11$	165.58	$166.66 \pm 0.05$	166.33	
75	$167.53 \pm 0.1$	170.60	$166.63 \pm 0.05$	166.30	$167.16 \pm 0.12$	169.48	$161.73 \pm 0.25$	162.66	$164.9 \pm 0.01$	163.58	
70	$166.5 \pm 0.11$	170.25	$163.9 \pm 0.36$	165.12	$166.5 \pm 0.264$	168.35	$159.4 \pm 0.2$	159.18	$160.43 \pm 0.20$	160.16	
65	$165.5 \pm 0.13$	169.72	$162.96 \pm 0.15$	163.59	$165.63 \pm 0.13$	166.86	$156.2 \pm 0.51$	155.16	$157.76 \pm 0.97$	156.03	
60	$164.4 \pm 0.09$	168.95	$162.43 \pm 0.15$	161.64	$161.5 \pm 0.69$	165.00	$148.83 \pm 0.60$	150.60	$148.56 \pm 1.15$	151.19	
50	$161.5 \pm 0.21$	166.47	$158.96 \pm 0.05$	155.89	$156.56 \pm 0.45$	159.90					
40	$157.93 \pm 0.56$	162.07	$154.2 \pm 0.45$	147.07	$150.2 \pm 0.23$	152.47					
30	$154.3 \pm 0.59$	154.50	$148.5 \pm 1.65$	135.02	$144.36 \pm 1.32$	141.70					

Table 3.2. DSC melting point data and Flory-Huggins solubilisation temperatures. DSC  $T_M$  corresponds to the average  $T_M$  values and the error represents the standard deviation (n = 3).

<b>Empirical Method</b>										
	<b>PCM:EPO</b> $r^2 = 0.988$		<b>PCM:PVA</b> $r^2 = 0.952$		<b>PCM:AFF</b> $r^2 = 0.92$		<b>PCM:PLSD</b> $r^2 = 0.971$		<b>PCM:SOL</b> $r^2 = 0.992$	
<b>Wt %</b>	<b>DSC T<sub>M</sub></b>	<b>E-M T<sub>S</sub></b>	<b>DSC T<sub>M</sub></b>	<b>E-M T<sub>S</sub></b>	<b>DSC T<sub>M</sub></b>	<b>E-M T<sub>S</sub></b>	<b>DSC T<sub>M</sub></b>	<b>E-M T<sub>S</sub></b>	<b>DSC T<sub>M</sub></b>	<b>E-M T<sub>S</sub></b>
95	169.6 ± 0.1	169.29	169.3 ± 0.05	168.94	169.63 ± 0.05	169.29	169.46 ± 0.05	169.46	169.36 ± 0.05	169.18
90	169.2 ± 0.1	169.04	168.8 ± 0.15	168.50	169.23 ± 0.05	169.00	169.13 ± 0.5	168.69	168.83 ± 0.05	168.69
85	168.66 ± 0.05	168.70	168.16 ± 0.11	167.94	168.73 ± 0.05	168.60	168.16 ± 0.15	167.91	167.83 ± 0.03	167.91
80	168.23 ± 0.05	168.24	167.36 ± 0.11	167.23	167.9 ± 0.11	168.05	166.06 ± 0.11	166.67	166.66 ± 0.05	166.67
75	167.53 ± 0.1	167.63	166.63 ± 0.05	166.30	167.16 ± 0.12	167.29	161.73 ± 0.25	164.72	164.9 ± 0.01	164.72
70	166.5 ± 0.11	166.80	163.9 ± 0.36	165.12	166.5 ± 0.264	166.24	159.4 ± 0.2	161.61	160.43 ± 0.20	161.61
65	165.5 ± 0.13	165.69	162.96 ± 0.15	163.59	165.63 ± 0.13	164.80	156.2 ± 0.51	156.68	157.76 ± 0.97	156.68
60	164.4 ± 0.09	164.20	162.43 ± 0.15	161.64	161.5 ± 0.69	162.80	148.83 ± 0.60	148.87	148.56 ± 1.15	148.87
50	161.5 ± 0.21	159.5	158.96 ± 0.05	155.36	156.56 ± 0.45	156.26				
40	157.93 ± 0.56	152.85	154.2 ± 0.45	146.40	150.2 ± 0.23	143.83				
30	154.3 ± 0.59	135.55	148.5 ± 1.65	130.74	144.36 ± 1.32	120.20				

Table 3.3. DSC melting point data (n = 3) and E-M solubilisation temperatures with respective  $r^2$  values.

### 3.4. Conclusion

The use of Flory-Huggins phase diagrams as a pre-formulation tool for the design and manufacture of stable ASDs has long been proposed. However, only a few API-polymer systems have been studied and in most cases, its validation has been insufficient and based on selected individual points across the phase diagram. In this study, the solid-liquid equilibrium depicting the thermodynamic API-polymer solubility curve was modelled with Flory-Huggins (F-H) and the Kyeremateng-based empirical Equations (E-M). Results were compared to the solubility curve obtained from the low-frequency Raman & HME approach. The Hansen solubility parameters and the zero enthalpy approach were also used as alternative screening methods. Both modelling approaches showed good correlation to the DSC data, but there were considerable differences between the LFR solubilisation temperature values and the predicted ones. For both prediction approaches, differences as high as 20°C for AFF and 50°C for PLSD were observed at the low drug loadings where the pure polymer properties dominate the system. At higher drug loading levels (i.e.,  $\geq 35$  wt% for AFF and  $\geq 50$  wt% for PLSD) both measurements and predictions became comparable within a  $\pm 5^\circ\text{C}$  temperature interval. This suggests that (1) at low drug loadings thermodynamic equilibrium was not reached during DSC and (2) due to the intensive mixing provided by the twin-screw extruder, the  $T_S$  values obtained from the THz-Raman provide a more accurate reflection of the likely solubility equilibrium across the entire composition range.

The E-M solubility extrapolation to typical storage temperature outperformed F-H. In fact, E-M was in excellent agreement with the critical concentration provided by the LFR method and physical stability data. Overall, these results further confirm the newly developed LFR method provides a reliable alternative solubility measurement for determining stable amorphous solid dispersions.

# **Chapter 4**

## **Linking API-polymer Solubility to Amorphous Solid Dispersion Microstructure Formation**

**The work carried out in this Chapter was fully published in a peer-reviewed journal.**

**Bordos, E., Das, G., Schroeder, S. L. M., Florence, A. J., Halbert, G. W. and Robertson, J.** Probing the interplay between drug saturation, processing temperature and microstructure of amorphous solid dispersions with synchrotron X-ray phase-contrast tomography. *Int. J. Pharm.* 669, 125018 (2025).

## 4.1 Introduction

Over the last decade, hot melt extrusion (HME) processing has been gaining growing importance as an oral drug delivery strategy to ensure adequate bioavailability of poorly soluble BCS class II drugs.<sup>215–218</sup> Within the extruding apparatus, the physical mixture of crystalline API and polymer is subjected to varying temperatures along the barrel to promote the solubilisation of the API in the polymer matrix. During this process the drug could be molecularly dispersed or exist as a suspended amorphous or crystalline phase. The degree of homogeneity and the number of phases present within the resultant ASD are primarily the result of the physico-chemical properties of the drug and polymer used in the formulation. These dictate the miscibility and solubility of the drug in the polymer matrix. However, equipment and process variables such as the screw configuration, barrel temperature, screw speed and feed rate have also been shown to impact the extent and rate of conversion of the crystalline drug into the amorphous form, as well as the degree of homogeneity within the final ASD product.<sup>183,219,220</sup>

Due to limited residence time in the extruding apparatus, it is critical to provide an adequate level of mixing and sufficient thermal input to promote the solubilisation of the API whilst avoiding thermal degradation. From an API-polymer solubility perspective (i.e., solubility of crystalline drug in molten/soften polymer) and based on kinetic and thermodynamic considerations, three processing regimes have been proposed to define the operating design space for miscible API-polymer systems during HME: (i) melting, (ii) dissolution and (iii) suspension.<sup>60</sup> Melting regime occurs at processing temperatures corresponding to and greater than the melting point of the drug species. For most polymer systems this occurs at temperatures values well above the glass transition temperature. Within this regime both drug and polymer have sufficient molecular mobility to reach a molecular level of mixing under a minimum mechanical input. Although assuring phase homogeneity and absence of residual drug crystallinity, this regime precludes extrusion of thermolabile substances that degrade upon or after melting. Therefore, processing under the dissolution/solubilisation

regime, at temperatures between the API's melting point and the saturated solution temperature ( $T_s$ ), is highly desirable. Under this regime ASDs can be obtained below the drug's melting point as a result of drug melting point depression phenomena. However, the determination of the API solubilisation end point during extrusion is challenging and not routinely performed. To address this aspect, in Chapter 2 it was demonstrated that the saturated solubility of a crystalline drug in a molten/softened polymeric matrix can be determined with in-situ THz-Raman spectroscopy. The aim of this Chapter is to further evaluate this approach by combining it with X-ray imaging analysis to assess the resultant ASD microstructure.

The internal structure of the ASD drug product is an important critical quality attribute that has a direct impact on downstream processing, as well as on the performance of the finished amorphous drug product.<sup>49,221</sup> Although it reflects the efficiency of the manufacturing process in producing a homogeneous amorphous product, it is a rather neglected aspect. To date, the great majority of studies has focused on the production process and performance of ASDs, but there has been limited data about the effect of material and process parameters on the interior ASD microstructure. Synchrotron phase-contrast micro-computed tomography (Sync-PC- $\mu$ CT) is an advanced imaging technique that can be used to circumvent this problem. It allows non-invasive imaging of specimens to depict cross-sectional and three-dimensional internal structures. Sync-PC- $\mu$ CT has been extensively used in material science<sup>222,223</sup> and biomedical research<sup>224-226</sup> fields to study weakly absorbing features in low-density objects or multiphase materials where the different components have similar X-ray attenuation coefficients. Whilst conventional X-ray imaging methods rely mainly on X-ray absorption differences across different materials as a mechanism of contrast formation, phase-contrast tomography is also sensitive to the refraction of X-rays in matter.<sup>227</sup> This provides enhanced contrast at the interface boundaries of existing structural domains within a specimen independently of their X-ray attenuation coefficients.<sup>228</sup> This aspect is particularly useful for low atomic number materials, such as the ones typically present in organic pharmaceutical ASDs.

The specific objectives of this Chapter are hence to investigate the internal structure of HME-based ASDs by means of Sync-PC- $\mu$ CT and to develop further understanding

of the impact of the drug saturation level and HME processing regimes on the ASD microstructure, as well as its potential implications on ASD stability. For this purpose, solid dispersions were produced under varying saturation conditions and the process was monitored with a low-frequency Raman probe combined with multivariate data analysis. The Sync-PC- $\mu$ CT investigation was coupled with a bespoke image analysis strategy to extract qualitative and quantitative morphological descriptors for a model binary system of Paracetamol and HPMC.

## **4.2 Materials and methods**

### **4.2.1 Materials**

Pharmaceutical grade paracetamol (PCM) powder form I was purchased from Mallinckrodt Inc., (Raleigh, USA). Hydroxypropyl methylcellulose (HPMC) grade Affinisol 15LV, a cellulose derivative amorphous polymer, was kindly donated by Dow Inc., (The Dow Chemical Company, now DuPont Inc., Michigan, USA).

### **4.2.2 Methods**

#### **4.2.2.1 Blending**

Binary mixtures of crystalline PCM and HPMC were prepared at mass ratios of 10-90 wt %, 20-80 wt %, 35-65 wt %, 50-50 wt % and 70-30 wt % using a bin blender (AgiBlend MB015AB Blender, Pharmatech, Warwickshire, UK) with a 1L vessel. Each formulation was blended for 20 minutes at a set blend speed and agitation of 25 rpm and 100 rpm, respectively. Prior to blending, materials were sieved through a 710  $\mu$ m mesh to remove powder agglomerates.

#### **4.2.2.2 Preparation of amorphous solid dispersions by hot melt extrusion (HME)**

HME was performed with an 11 mm co-rotating twin-screw extruder (Process 11, 40: 3/4 L/D Thermo Fisher Scientific, Karlsruhe, Germany) in combination with a loss-in-weight gravimetric feeder (Brabender Gravimetric feeder DDW-MD-MT, Brabender Technologie, Duisburg, Germany). A constant screw speed of 100 rpm and a feed rate of 0.1 kg/h were employed. The extruding apparatus is formed of 8 barrel sections and a die zone (refer to schematics in Appendix C 1). Barrel Section 1 was not heated, whilst Sections 2 and 3 were at set-point values of 50°C and 100°C, respectively, to prevent blockage of the feeding zone. Barrel Sections 4 to 8 and the die zone were operated at the same set-point temperature values, which varied according to the drug-polymer composition as reported in Table 4.1. The chosen temperature range was intended to create three distinct processing regimes: melting ( $T_{extrusion} < T_M$ ), dissolution ( $T_S \leq T_{extrusion} < T_M$ ) and suspension ( $T_{extrusion} < T_S$ ) to assess the effect of processing temperature on the ASD microstructure. Product melt temperature was monitored with a pressure-temperature probe (Terwin Instruments Ltd., Bottesford, UK) immersed in the API-polymer mixture in the die Section. Processing pressure, screw speed, barrel temperature and motor torque were recorded with Prismdde software (Omron Corporation, UK). The temperature values measured by the melt probe were constantly higher than the reported set-point values due to the heat generated from shear. However, within this work temperature values are denoted as the set-point temperature values to demark each processing regime and facilitate inter-sample comparison. For the actual product melt temperature refer to Table 4.1. Collected extrudates were allowed to cool to ambient temperature by natural convection prior to pelletisation (Thermo Scientific™ VariCut Pelletizer, Thermo Fisher Scientific, UK) and storage until further analysis.

Extruded materials obtained from the work developed in Chapter 2 were used for preliminary Sync-PC- $\mu$ CT tests. For this purpose the following compositions were used: 10 wt%, 20 wt%, %, 35 wt%, 50 wt% drug loading and pure polymer extrudates (i.e., no API incorporated). All samples were processed at a set-point barrel

temperature of 150°C, with exception of the pure polymer extrudates that were extruded at a set-point of 180°C. Samples were stored in sealed plastic bags at ambient conditions and aged for 6 months prior to the tomographic tests.

Drug loading (wt%)	Process set temperature (°C) <sup>a</sup>	Processing regime <sup>b</sup>	Measured product melt temperature (°C) <sup>c</sup>	Screw speed (rpm)	Feed rate (kg/hr)
10	180	M	193 ± 0.9	100	0.100
	150	D	158 ± 2.5	100	0.100
	130	D	136 ± 2.3	100	0.100
20	180	M	193.5 ± 0.34	100	0.100
	150	D	155 ± 3.5	100	0.100
	130	D	137.3 ± 2.7	100	0.100
35	180	M	192.5 ± 0.5	100	0.100
	145	D	153 ± 0.4	100	0.100
	140	S	147 ± 0.48	100	0.100
	135	S	142 ± 0.9	100	0.100
50	180	M	191.9 ± 0.2	100	0.100
	155	D	164.2 ± 0.4	100	0.100
	150	S	159.7 ± 0.46	100	0.100
	145	S	153 ± 0.98	100	0.100
70 <sup>d</sup>	180	M	190 ± 0.99	100	0.100
	160	D	169 ± 0.4	100	0.100
	155	S	163 ± 0.3	100	0.100
	150	S	158 ± 0.23	100	0.100

**a** - Refers to set-point temperature values of barrel Sections 4 to 8 and the die zone.

**b** - M: melting regime, D: dissolution regime and S: suspension regime.

**c** - Steady state temperature values (average ± standard deviation).

**d** - For this composition the lowest temperature where no API crystallinity was detected was very close to the API's  $T_M$ , therefore, it was excluded from the tomography study.

#### 4.2.2.3 API-polymer solubility determination

Table 4.1. HME processing conditions. THz-Raman spectroscopy was used to determine the API-polymer phase equilibria during extrusion by employing the methodology outlined in Chapter 2, Section 2.2.2.3. In addition, a principal component analysis (PCA) method based on the covariance matrix was applied to the low frequency region (0 – 200 cm<sup>-1</sup>) to interpret spectral variations using Origin Pro software (Origin Pro 2018b, OriginLab Corporation, USA).

#### **4.2.2.4 Differential scanning calorimetry (DSC)**

DSC analysis was performed from 0°C to 180°C at a heating rate of 20°C/min according to the methodology described in Section 2.2.2.6 in Chapter 2.

#### **4.2.2.5 X-ray diffraction (XRD)**

XRD data was collected as described in Section 2.2.2.7 in Chapter 2.

#### **4.2.2.6 Synchrotron phase-contrast micro computed tomography (Sync-PC- $\mu$ CT)**

X-ray tomography experiments were performed at the Diamond-Manchester Imaging Branchline I13-2 of the third generation synchrotron Diamond Light Source (DLS) (Didcot, UK). This beam line offers a small source size and a long distance between the source and the sample (250 m), which results in partially-coherent illumination at the sample position. In combination with the ample space available to adjust the propagation distance, it provides optimum conditions for generating in-line phase contrast for edge enhancement of weakly absorbing features.<sup>229</sup>

Experiments were conducted in a near-parallel geometry using a filtered polychromatic ‘pink’ beam with a peak energy of 23 keV. The process of generating the polychromatic ‘pink’ beam is described in detail elsewhere.<sup>228,230</sup> Pelletised materials were transferred to polyimide Kapton tubes (OD = 6.0 mm and ID = 5.85 mm) (GoodFellow Cambridge, UK) and attached to a manual goniometer mounted on perpendicular linear stages (Newport Corp., USA). For the preliminary tests, individual pellets were mounted on cellulose sample holders. In all cases, an Aerotech ABRT-260 rotation stage (Aerotech Inc., USA) was used to rotate the samples at equally-spaced angles over 180° of continuous rotation with an exposure time of 80 ms per projection. A total of 2158 projections were acquired for each sample. Raw projection data was collected by a pco.edge 5.5 (PCO AG, Germany) detector (sCMOS image sensor of 2560 × 2160 pixels and 6.5  $\mu$ m pixel size) mounted on a visual light microscope of variable magnification. Data was acquired with two

resolution levels: (1) a 1.25x objective coupled to a 500  $\mu\text{m}$   $\text{CdWO}_4$  scintillator provided an effective pixel size of 2.6  $\mu\text{m}$  and (2) a 4x objective coupled to a 100  $\mu\text{m}$   $\text{LuAg:S021}$  scintillator provided an effective pixel size of 0.81  $\mu\text{m}$ . Slits were used to restrict the beam outside the field of view to limit sample exposure and reduce noise arising from scintillator defects. The sample-to-detector distance was optimised to generate in-line phase-contrast while minimising edge blurring and the best absorption/propagation contrast ratio was obtained at a distance of 51 mm (Appendix C 2). The experimental set-up is displayed in Figure 4.1.

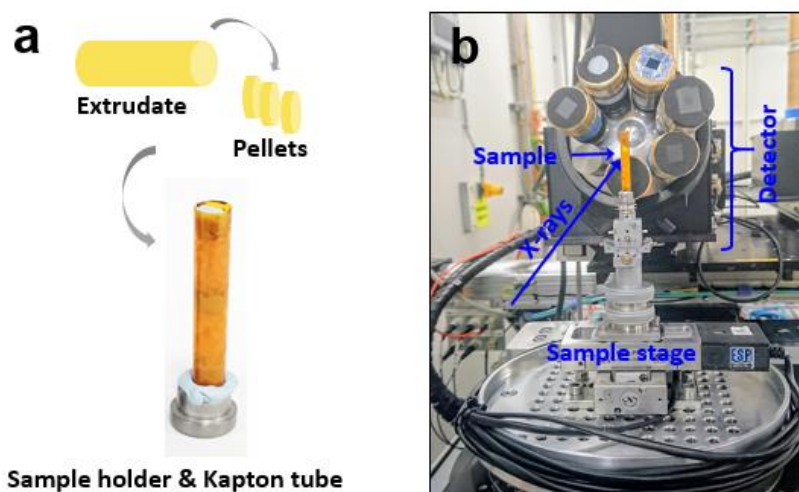


Figure 4.1. Experimental set-up at the beamline I13-2. a) Sample preparation schematics and b) sample presentation geometry.

#### 4.2.2.6 Tomographic reconstruction

Data was reconstructed using the filtered back projection algorithm implemented in the DLS software platform SAVU 2.2.10. All images were corrected for zingers and subjected to flat and dark-field corrections. An additional correction step was employed to reduce ring artefacts and correct the in-plane tilt of  $0.072^\circ$  that occurred during experimentation. A single distance propagation-based phase contrast filter was also applied with ANKPhase11 employing the Paganin algorithm with a  $\delta/\beta$  ratio of 85. This step helped improve the grey level of separation between sample and background despite partially enhancing the ring artefacts.

#### 4.2.2.7 Image analysis

Image processing and analysis strategies were implemented in MATLAB (2018b, MathWorks, USA) with a custom-made segmentation algorithm developed specifically for this data. This process aimed to partition the images into main regions of interest (ROIs) to enable extraction of quantitative and qualitative descriptors.

Images at each processing step are shown in Figure 4.2. To increase the discriminative efficiency of the segmentation algorithm, the polyimide Kapton tube and surrounding space were removed by defining a conservative ROI inside the tube (Figure 4.2.b). The contrast of the cropped images was enhanced using a contrast adjustment step which combined histogram equalization and image intensity adjustment (Figures 4.2.c and 4.2.d, respectively). Thresholding and binarisation (Figure 4.2.1.e) was performed with Otsu's automated global thresholding method to maximise inter-class variance between foreground and background pixel classes.<sup>231</sup> Background noise was iteratively removed with a series of area and image opening morphological operations. First, all connected components with fewer than 1000 pixels (value  $\ll$  to the pellet minimum area) were removed with area opening operations to discard major noise regions (Figure 4.2.f). Then, the small contaminant regions connected to the pellets' outer limits were eliminated with an image opening operation employing a 30 pixel 'disk' structuring element applied to Figure 4.2.i in order to obtain the "clean" final binary image (Figure 4.2.f). Foreground noise was removed with an intermediate step by inverting the contrast of the image and applying an area opening morphological operation to remove all blank regions under 3 pixels (Figures 4.2.g to 4.2.i). There is no standard quality indicator for image segmentation and the most widely used method to assess its effectiveness is a subjective visual inspection.<sup>232</sup> Hence, at each step the binarised images were superimposed to the reference unprocessed tomograms before further processing to assure the preservation of the delimitations of the pellets' borders and overall shape conservation.

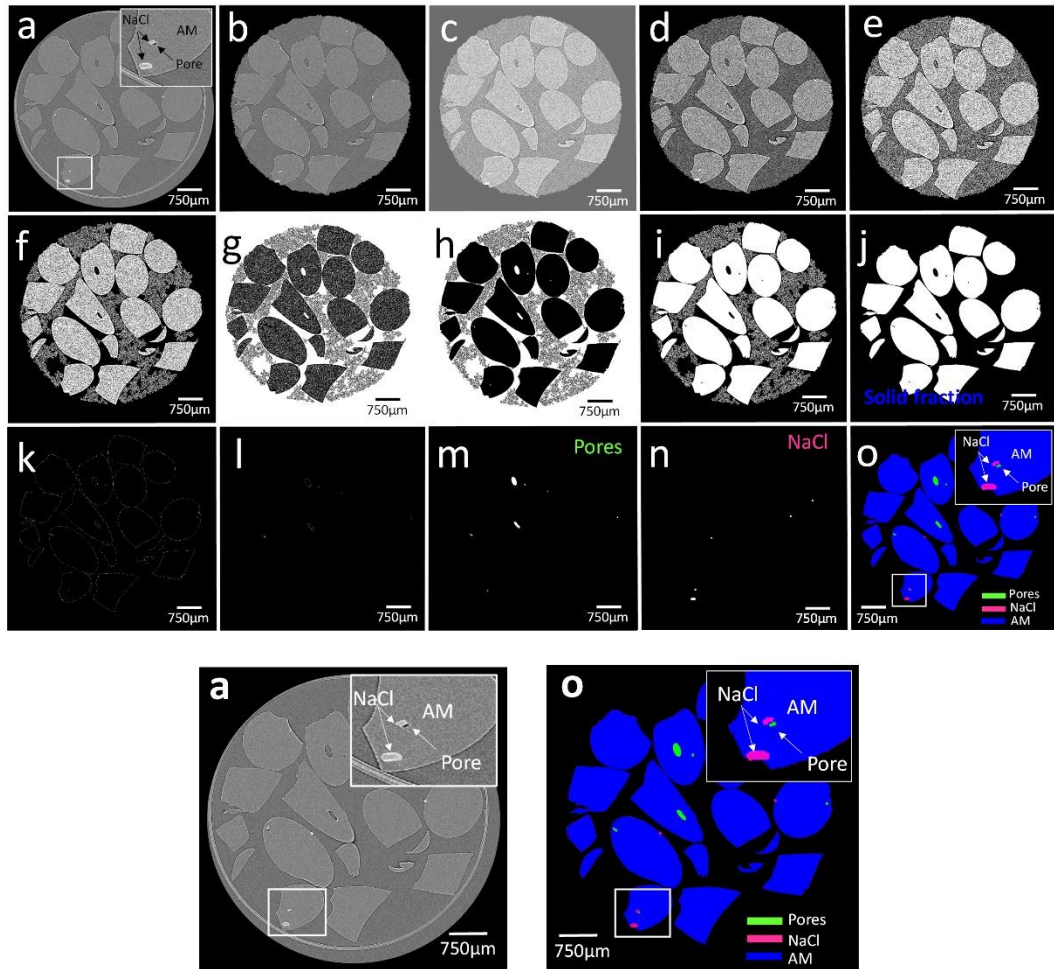


Figure 4.2. 2D Image processing sequence from a) Raw unprocessed image; b) cropped image defining the region of interest inside the Kapton tube; c) to d) gray-scale images after histogram equalization and intensity adjustment, respectively; e) binary image after thresholding and binarisation: white - foreground (pellets), black – background/noise (empty space inside the Kapton tube); f) binary images after partial background noise removal; g) to h) contrast-inverted images and foreground noise removal; i) image after foreground noise removal; j) “clean” final binary images after the second background noise removal step; k) pellet outer and inner perimeter; l) pellet inner perimeter delimiting the pores; m) “filled” pore area; n) isolated NaCl particles; o) overlay of isolated NaCl clusters, pores and amorphous matrix (AM).

To isolate the pores, a pixel-based arithmetic operation was applied to the clean binary images to subtract the solid fraction comprised between the pellets' outer perimeter (Figure 4.2.k.) and that of the inner perimeter delimiting the "holes"/ pores (Figure 4.2.l.) After applying a filling algorithm to the inner perimeter, the pore corresponding areas were obtained (Figure 4.2.m). The Euclidean distance transform and the watershed segmentation were applied to separate potential touching pore bodies and allow subsequent analysis on each individual pore. Extracted information comprised pore size and shape descriptors. Porosity was defined as the ratio of the total pore area to the whole nominal area of the pellets, including porosity. Calculations were made for a minimum of 750 successive images for each sample.

The NaCl particulates were isolated by partially opening the connected foreground components present in Figure 4.2.f with an 11x13 pixel matrix (Figure 4.2.n). Once extracted these were characterised in terms of total percentage and size distribution. Figure 4.2.o shows the overlay of the NaCl particulates, pores and API-polymer amorphous matrix.

To gain access to local voxel (cubic pixel) neighbourhood information and avoid directional bias resultant from a 2D 'slice-by-slice' segmentation, a 3D array of the segmented binary images was created and each connected object was identified and labelled. The watershed algorithm was reapplied to separate touching objects in 3D. Figure 4.3 shows the 3D volume renderings of the solid fraction, pores and NaCl clusters resultant from this approach. The eigenvectors, eigenvalues, Euler angles, volume and surface area of each pore were extracted employing the `regionprops3` functionality available in Matlab.<sup>233</sup> This data is obtained from the ellipsoid with matching image moments as the object. Porosity was recalculated as the volumetric percentage and results were compared to the area ratio measurements resultant from the 2D segmentation. The effect of the quantification method, drug loading and processing temperature on porosity was statistically analysed using one-way analysis of variance employing the Welch ANOVA test due to unequal variance. Individual differences within each group were identified using Games-Howell *post hoc* test at a significance level of 95% ( $\alpha = 0.05$ ). Pore sphericity (S) was further calculated as:

$$S = \quad (4.1)$$

where  $V_p$  and  $S_p$  are the pore volume and surface area, respectively. The pores were further characterised in terms of shape and orientation. The main orientation of a pore is given by the eigenvector with the highest eigenvalue and the ratios between the eigenvalues provide shape descriptors of the pore.<sup>234,235</sup> Hence, for shape analysis, the classification approach proposed by S. Blott and K. Pye<sup>236</sup> was adapted to assign particles to form classes based on the elongation (E) and flatness (F) ratios that are calculated as:

$$E = \frac{\lambda_2}{\lambda_1} \quad (4.2)$$

$$F = \frac{\lambda_3}{\lambda_1} \quad (4.3)$$

where  $\lambda_1$ ,  $\lambda_2$  and  $\lambda_3$  are the largest, second largest and smallest eigenvalues respectively. For 3D visualisation, image stacks were imported in CTvox (version 3.2.0, Bruker, Kontich, Belgium).

#### **4.2.2.8 N<sub>2</sub> Physisorption**

Characterisation of the surface of the pellets was performed by N<sub>2</sub> gas physisorption with an Autosorb IQ Model 6 (Quantachrome Instruments, Florida, US). Samples were transferred to 9 mm cells and degassed at 40°C for 48 hours prior to analysis. Measurements were conducted at 77.4 K employing an equilibration time setting of 3 min. A total of 41 data points were acquired for producing both adsorption and desorption isotherms. Data analysis was performed with the Non-Local Density Functional Theory (NLDFT) method employing the calculation model of N<sub>2</sub> at 77 K on carbon (slit pore).

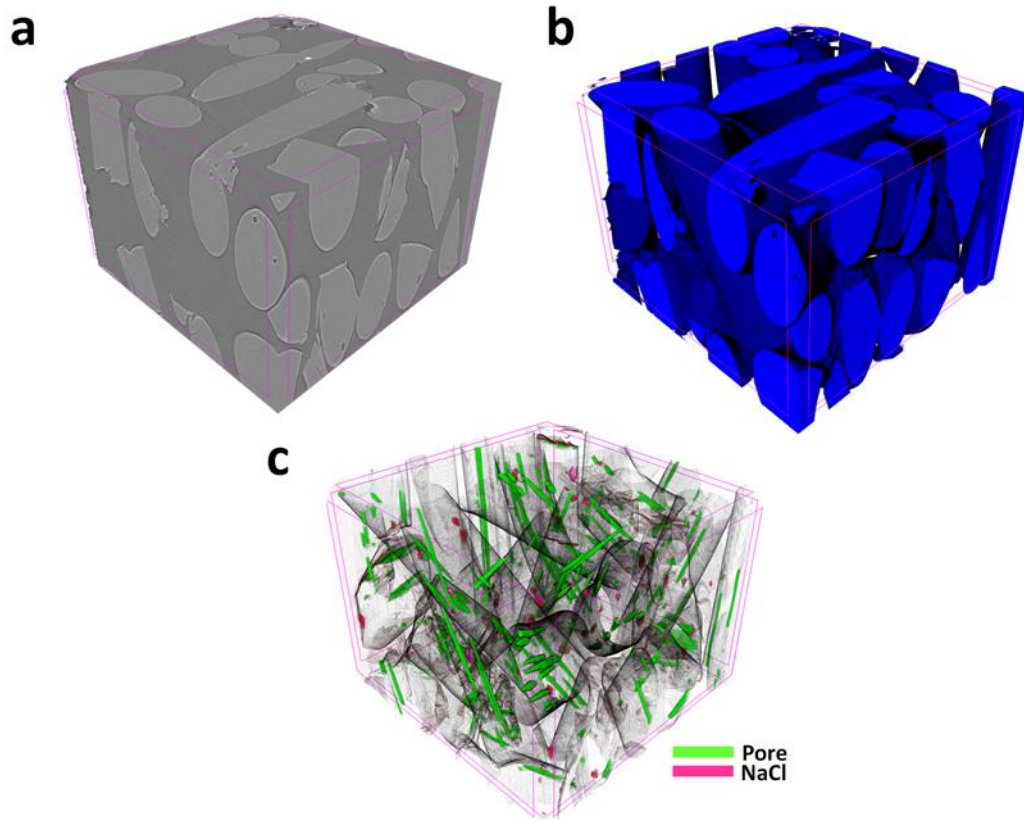


Figure 4.3. Example of 3D segmentation of a 4000 x 4000 x 4000  $\mu\text{m}$  section. a) Unprocessed image, b) segmented solid fraction and c) segmented pores and NaCl.

## 4.3 Results and discussion

### 4.3.1 Effect of HME processing regime on the API physical state

Extrusion was performed over a wide range of API-polymer compositions and several processing temperatures were employed to produce solid dispersions with different degrees of saturation and structural complexity with an 11 mm extruder. Three extruding regimes, melting, dissolution and suspension were applied to produce: (i) ASDs extruded above the drug's melting point, (ii) ASDs extruded below the drug's melting point and (iii) crystalline suspensions obtained by incomplete API dissolution, respectively. The low-frequency Raman data acquired during extruding conditions confirmed the amorphous state of the API in the ASDs produced under regimes(i) and (ii), whereas archetype (iii) was crystalline as a result of processing below the saturated solution temperature ( $T_S$ ). ASDs extruded within the suspension regime exhibited low-frequency Raman spectral bands characteristic of crystalline PCM form I at 32, 51 and 85  $\text{cm}^{-1}$ (179,237) that were absent upon temperature increase to the dissolution and melting regimes, indicating complete drug dissolution (Figure 4.4.a). Under these regimes only an amorphous broad shoulder with peak maxima at  $12\text{cm}^{-1}$  is seen.

Principal component analysis of the spectral data showed that two principal components (PCs) suffice to classify the data into distinct groups according to the processing temperature and to describe over 98% of data variance (Figure 4.4.b and 4.5). PC1 separated signals arising from the amorphous band at  $12\text{ cm}^{-1}$ , while PC2 described PCM's signals corresponding to the API's crystalline lattice vibration modes, which is supported by the PCA loading plot (Appendix C 3). Disappearance of the API's crystalline lattice vibration modes upon solubilisation resulted in a change in the PC2 scores from negative to positive values, which provided a rational basis to distinguish between amorphous and crystalline API.

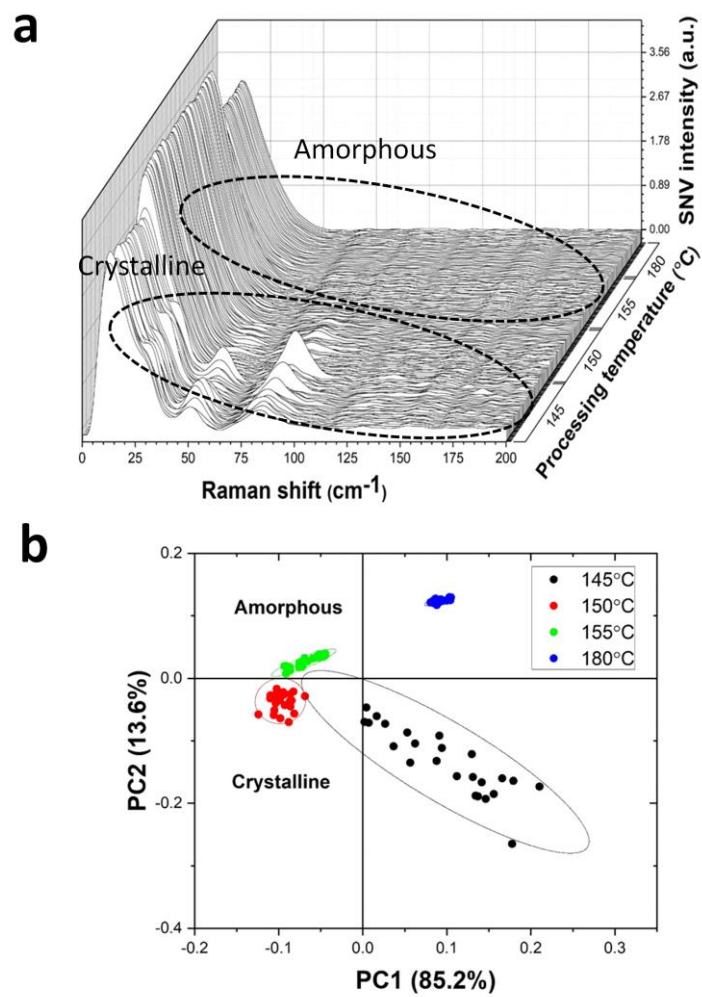


Figure 4.4. API-polymer solubility determination: a) example low-frequency Raman spectral data with b) respective PCA outputs for the 50 wt % system.

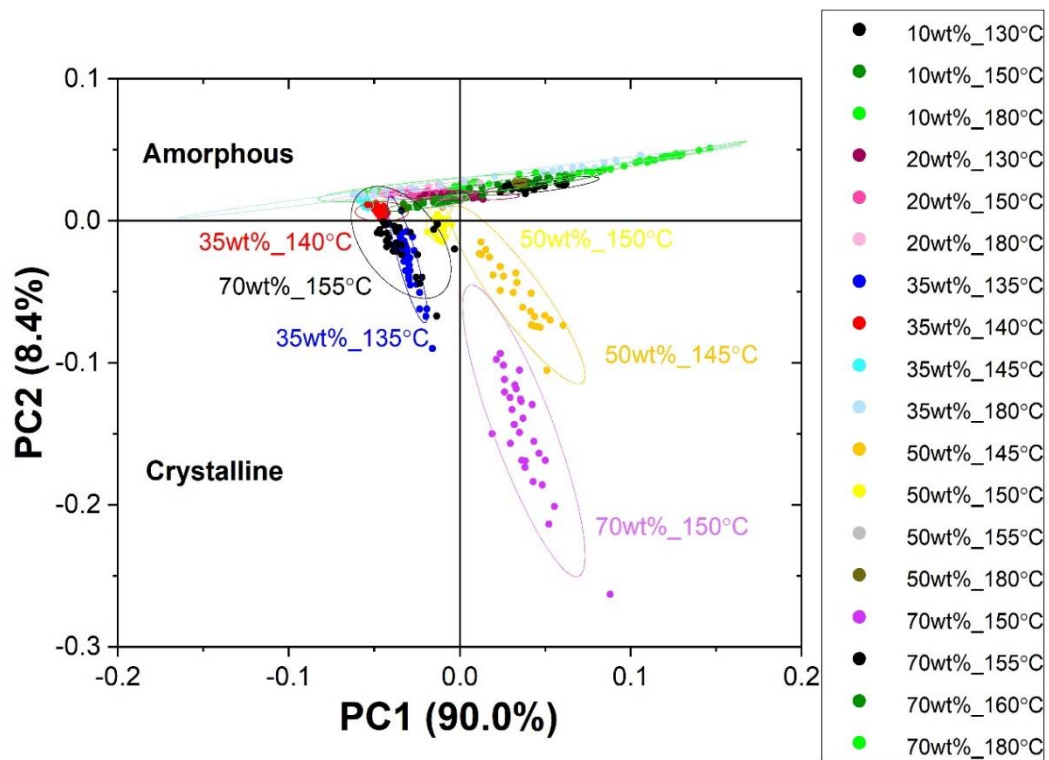


Figure 4.5. PCA score plot of all drug loadings and processing temperatures.

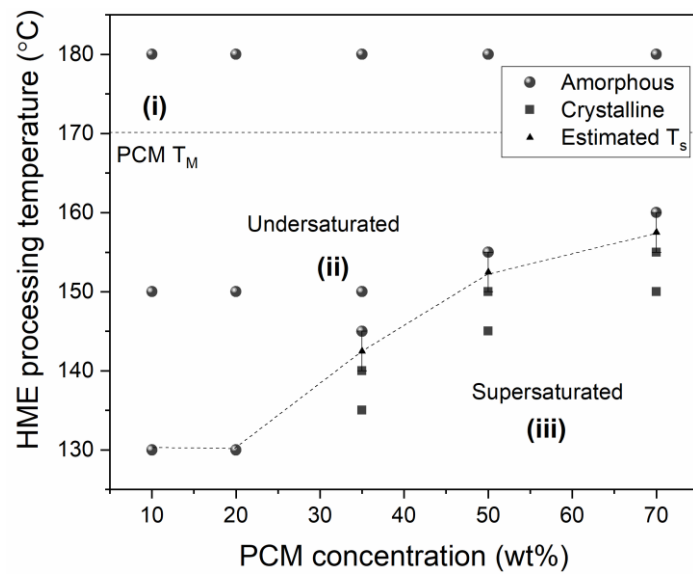


Figure 4.6. Temperature composition phase diagram determined by PCA.

The temperature-composition phase diagram displayed in Figure 4.6 was obtained from the PCA outputs of all compositions (Figure 4.5). It shows the API's amorphous and crystalline temperature coordinates, as well as the estimated equilibrium temperature with an error of at least  $\pm 2.5^{\circ}\text{C}$ . Drug loadings  $> 20$  wt % originated ASD archetypes (i), (ii) and (iii), whilst type (iii) did not occur at or below this threshold concentration (Appendix D). This is in good agreement with the work developed in Chapter 2 suggesting a solid solution capacity of  $\sim 20$  wt % for this drug-polymer system. However, despite the amorphous state of the drug in ASD archetypes (i) and (ii), these results do not assure formation of homogeneous dispersions nor preclude existence of amorphous API- or polymer-rich mesophases. Therefore there is an opportunity for Sync-PC- $\mu$ CT to probe the potential impact of drug saturation and processing temperature on the ASD inner structure.

### **4.3.2 XRD and DSC analysis**

XRD served as reference technique to compare the low-frequency Raman data. It confirmed the amorphous character of the drug in ASD archetypes (i) and (ii) after extrusion, as well as its crystalline state in archetype (iii). As an example, Figure 4.7.a shows the XRD results for the 50 wt% system. Diffraction peaks corresponding to crystalline PCM form I are seen at  $145^{\circ}\text{C}$  and  $150^{\circ}\text{C}$  (suspension regime), while amorphous halos are present at  $155^{\circ}\text{C}$  and  $180^{\circ}\text{C}$  (dissolution and melting regimes, respectively). The same trend was observed for the remaining compositions, as displayed in Appendix C 5. In the lower drug loading systems, an additional diffraction peak corresponding to NaCl (impurity present in the polymer) is seen at  $2\theta$  values of  $32^{\circ}$ .

DSC analysis displayed recrystallisation exotherms within the temperature range of  $109$ - $120.5^{\circ}\text{C}$  at all extruding temperatures as a result of exposure to heat during the measurement (Figure 4.7.b). This corresponded to a partial recrystallisation to PCM form II, as indicated by the respective melting endotherm at  $\sim 156.6$  -  $160.0^{\circ}\text{C}$ . For the compositions processed within the suspension regime an additional melting endotherm at  $\sim 168.8^{\circ}\text{C}$  confirmed residual crystallinity of PCM form I. The same recrystallisation trend was observed for all compositions above 20 wt% drug loading, suggesting these

systems are supersaturated and unstable upon exposure to heat (Appendix C 5). For the compositions at and below 20 wt% drug loading, no melting endotherms or recrystallisation exotherms were seen at any extruding temperatures, indicating these systems are stable. This provides further support to the 20 wt% drug loading as the critical threshold concentration dividing compositions between stable and metastable/unstable after extrusion. Additionally, the presence of a single glass transition temperature in the DSC thermograms indicates phase miscibility at the tested drug-loading levels.

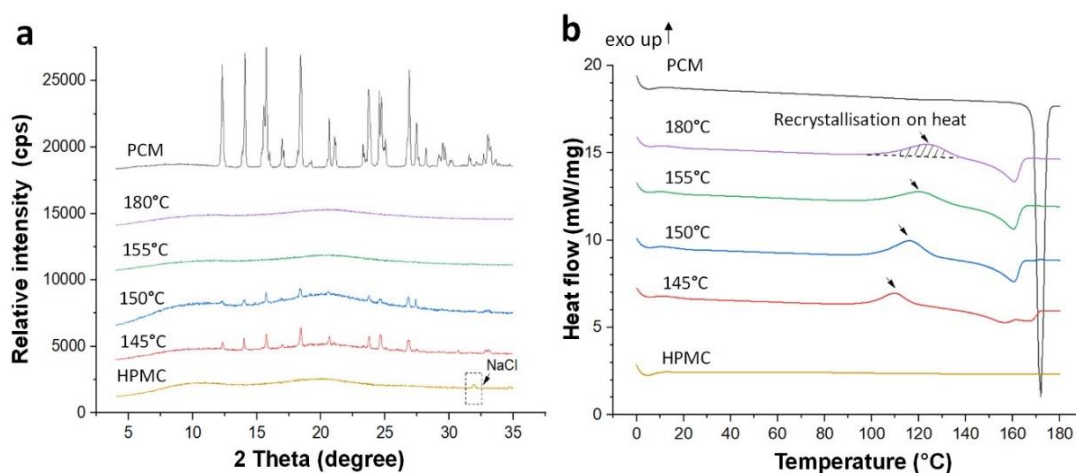


Figure 4.7. a) XRD and b) DSC analysis of the 50 wt% system processed under all extruding regimes. As a reference, the data of the raw unprocessed materials is also shown.

### 4.3.3 Structural characterisation of ASDs by phase contrast

#### tomography

The potential of using Sync-PC- $\mu$ CT to probe the inner structure of organic HME-based ASDs was first investigated in the preliminary study where 6 months-aged samples were analysed. Figure 4.8 shows 2D cross-Sections and 3D volume renderings of the reconstructed data. Despite the similar elemental composition of the drug and polymer used in the formulation, various structural domains were identified within the amorphous matrix of the pellets: drug-rich crystalline domains, impurities (NaCl), polymer-related heterogeneities (PRH) and void cavities/pores, which will be discussed separately in the following Sections. Surface related phenomena such as sharkskin defects and increased roughness at the cut cross-sectional surfaces were also observed in great detail (Figure 4.8.a). Drug loadings above the assumed solid solution capacity (i.e., supersaturated and metastable/unstable ASDs) were found to contain higher structural complexity and displayed highly defective API-rich crystalline domains and abundant pores (Figures 4.8.d to 4.8.f).

This was in stark contrast with the relatively homogeneous matrix almost devoid of pores of the undersaturated formulations (Figures 4.8.b and 4.8.c). The drug-rich crystalline clusters had a typical size range between 4 and 430  $\mu\text{m}$  in diameter and were found to be dispersed within the solid and the porous fractions of the amorphous matrix. They displayed a highly defective structure with multiple fracture planes and channels that could have both intrinsic (i.e., grain boundaries) and mechanical origins induced by the HME process. In the context of the API dissolution mechanism within a polymer matrix, this type of fragmented structure supports the defect site-driven dissolution and fragmentation model in addition to diffusion as proposed by Moseson et al.<sup>238</sup> Nevertheless, given the time elapsed between ASD manufacture and Sync-PC- $\mu$ CT analysis, the observed crystalline drug clusters could be the result of growth of residual nanocrystalline nuclei (i.e., undissolved API) and/or nucleation and growth from the supersaturated amorphous matrix upon ageing.

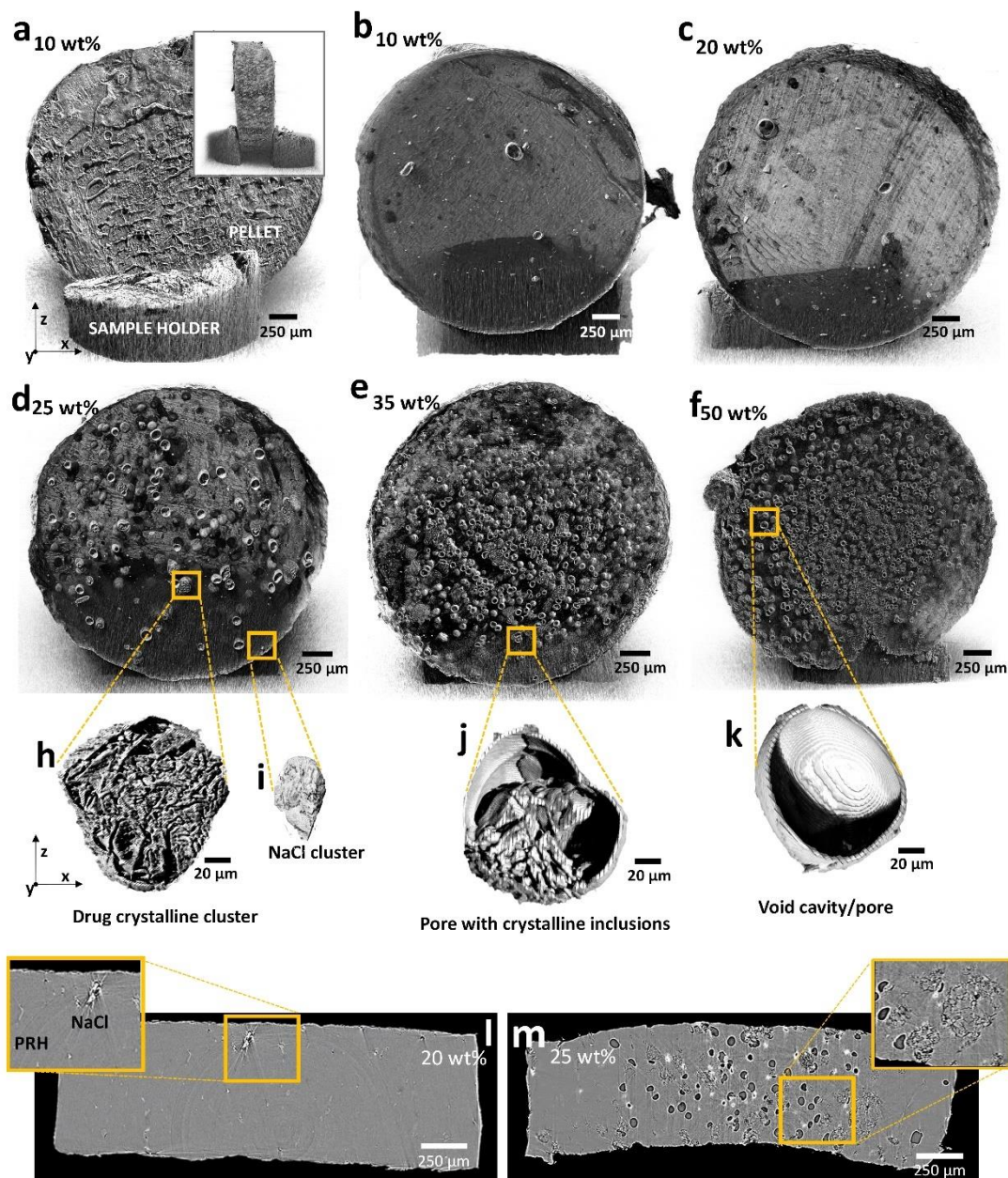
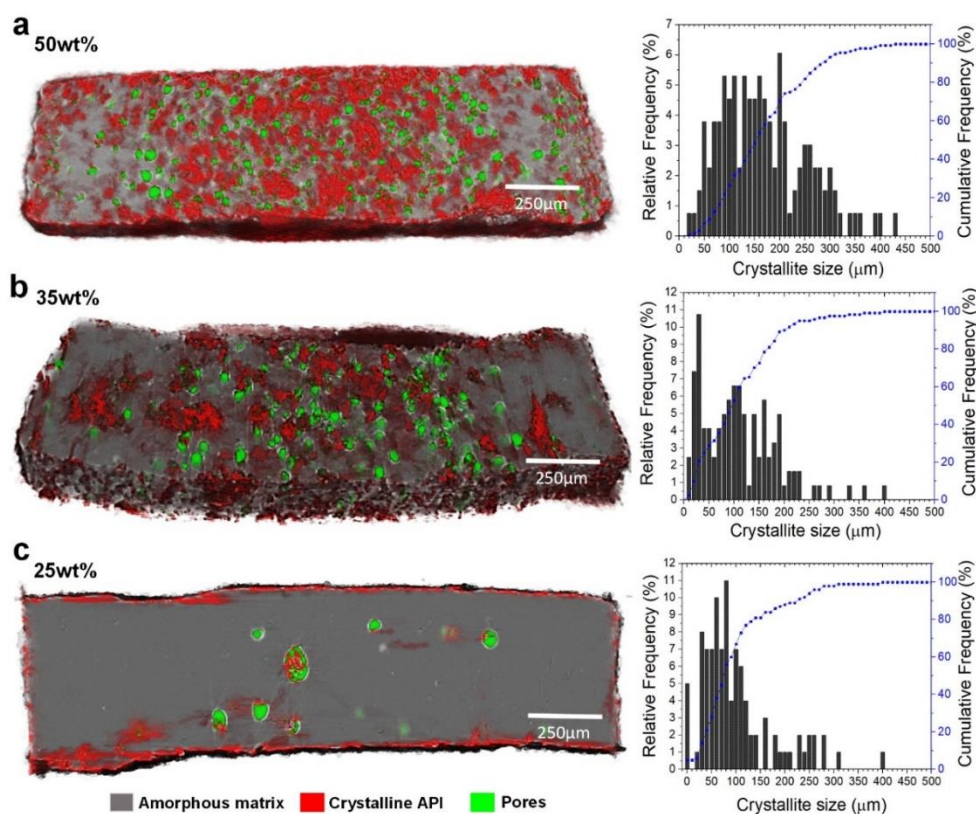


Figure 4.8. 3D volume renderings and 2D cross-sections of the 6-months aged pellets. In figures b) to f) the ASD outer surface and the homogenous solid fraction corresponding to the amorphous matrix were made transparent to enable visualisation of existing bulk heterogeneities.

#### 4.3.4 Analysis of the API-rich crystalline clusters

With exception of the NaCl clusters, there was little discernible difference between the grayscale values of the structural domains identified within the solid fraction. This hampered extraction and quantification of the crystalline API clusters based on intensity threshold strategies. As an alternative approach, the characteristic fracture planes present within the crystalline API domains were used as a morphological marker for segmentation for the samples where crystallinity was present. These were segregated from the remaining parts of the image by subtracting the isolated porous fraction from the binarised images. Considering that the drug-rich crystalline clusters extend around and between the breakage planes, a dilation operation was applied to add pixels to the boundaries of the fracture planes in order to illustrate the potential extension of the crystalline clusters. A dilation of 5 pixels was found sufficient to obtain objects representative of the crystalline drug clusters identified in the reference raw image data. Further details about this strategy are shown in Appendix C 6.

Figure 4.9 exhibits the evolution of the segmented crystalline regions as a function of the drug loading, as well as the main descriptors extracted. The size and total percentage of the segmented crystalline drug domains were found to increase with increasing drug loading levels, as expected from increasing levels of supersaturation. These were predominantly distributed within the core of the pellets and to a lesser extent in the peripheral Sections. This is comprehensible as shear stress decreases along the radius from the exterior towards the core of the screw cross-Section or die channel. The closer the melt is to the barrel/die wall, the more intensive the shear becomes and better drug-polymer mixing is achieved.<sup>194</sup>



**d**

Drug-loading (%)	Porosity (%)	Fracture area (%)	API-rich crystalline area (%) <sup>a</sup>	Amorphous matrix area (%) <sup>b</sup>
50	10.32 ± 0.38	9.51 ± 1.06	39.37 ± 3.29	50.30 ± 3.41
35	7.79 ± 1.06	7.34 ± 2.25	28.34 ± 6.47	63.85 ± 6.75
25	1.46 ± 0.25	1.9 ± 1.8	9.83 ± 6.39	88.83 ± 6.47
20	1.54	---	---	---
10	1.01	---	---	---

**a** - derived from the fracture regions after a 5 pixel dilation operation

**b** - obtained from the total area after porosity and API-rich crystalline area subtraction

Figure 4.9. API-rich crystalline clusters present in the aged samples extracted from the morphological-based segmentation. a) To c) overlay of segmented pores and crystalline API clusters superimposed to the raw unprocessed images, with respective crystallite size. d) Quantification of total porosity, fracture regions, API-rich crystalline clusters and amorphous matrix area (average ± standard deviation, n = 200 cross-sections).

Based on the segmentation analysis, the surface and sub-surface Sections of the pellets also displayed a considerable amount of API-rich crystalline clusters, indicating both surface and bulk-mediated API re-crystallisation upon ageing for the supersaturated compositions. The surface API enrichment and crystallisation were confirmed by ToF-SIMS analysis and optical microscopy under a polarized light as shown in Figure 4.10

(data acquired according to the methods described in Section 5.2.2.5 and 5.2.2.8 in Chapter 5, respectively).

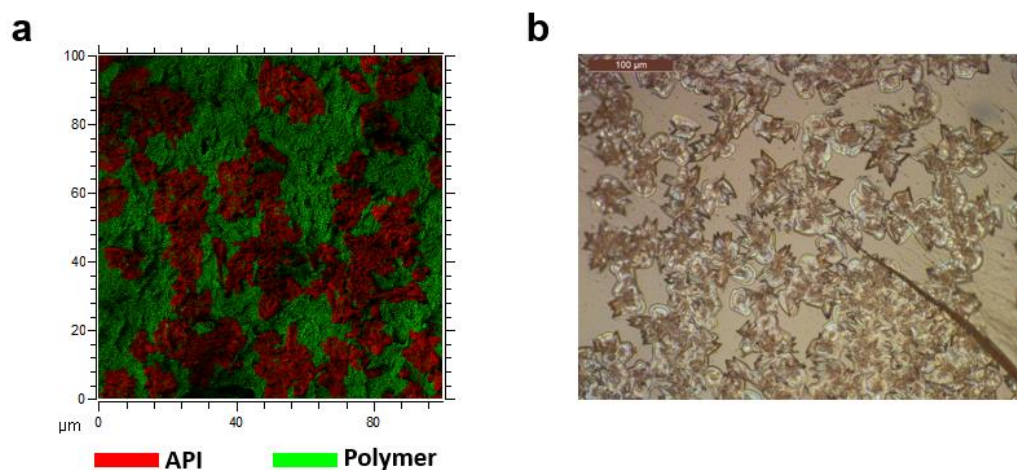


Figure 4.10. a) Exemplary ToF-SIMS and optical microscopy images acquired on the surface of the 50wt% extrudate.

Despite successful identification of the drug crystalline domains in the aged samples (preliminary tests), their detection with Sync-PC- $\mu$ CT in the freshly prepared samples was only possible in 50wt% dispersions processed at 145°C (where larger residual crystals are expected). This is attributed to detection limitations and size differences between the initial PCM particulates used in the two studies. For the preliminary study a granular grade PCM with a D50 of 378  $\mu$ m was used, whereas for preparation of the fresh extrudates a powder grade PCM with a D50 of 68  $\mu$ m was employed. Therefore, even if there is sufficient residual crystalline material to be detected by the other techniques used (i.e., low-frequency Raman, DSC and XRD), their individual particle size is below the lowest Sync-PC- $\mu$ CT detection limit when using powdered PCM (0.81  $\mu$ m/pixel under the present experimental setup). This did not occur for the aged samples because of the larger particle size of the initial material, which along with the time elapsed between ASD manufacture and X-ray imaging enabled further growth to detectable ranges.

#### 4.3.5 Impurity distribution

In addition to the drug crystalline structures, highly absorbing clusters of material were observed in all samples independently of the drug saturation level. These correspond

to clusters of NaCl salt that is a known impurity present in the polymer.<sup>185</sup> The NaCl content was found to be less than 1 wt%, which is in good agreement with the manufacturer's specifications (< 5 wt %). Figure 4.11 displays 3D images highlighting the distribution of this impurity within the pellets. ASDs extruded within the dissolution and suspension regimes were dominated by NaCl particulates with smaller diameters, whilst the systems extruded within the melting regime displayed larger NaCl particulates (Figure 4.12). This variation is likely to be caused by mechanical breakage of the initial NaCl particulates as a result of higher shear stress and product melt viscosity at lower processing temperatures. Nevertheless, partial NaCl solubilisation is also likely to occur, especially in the melting regime.

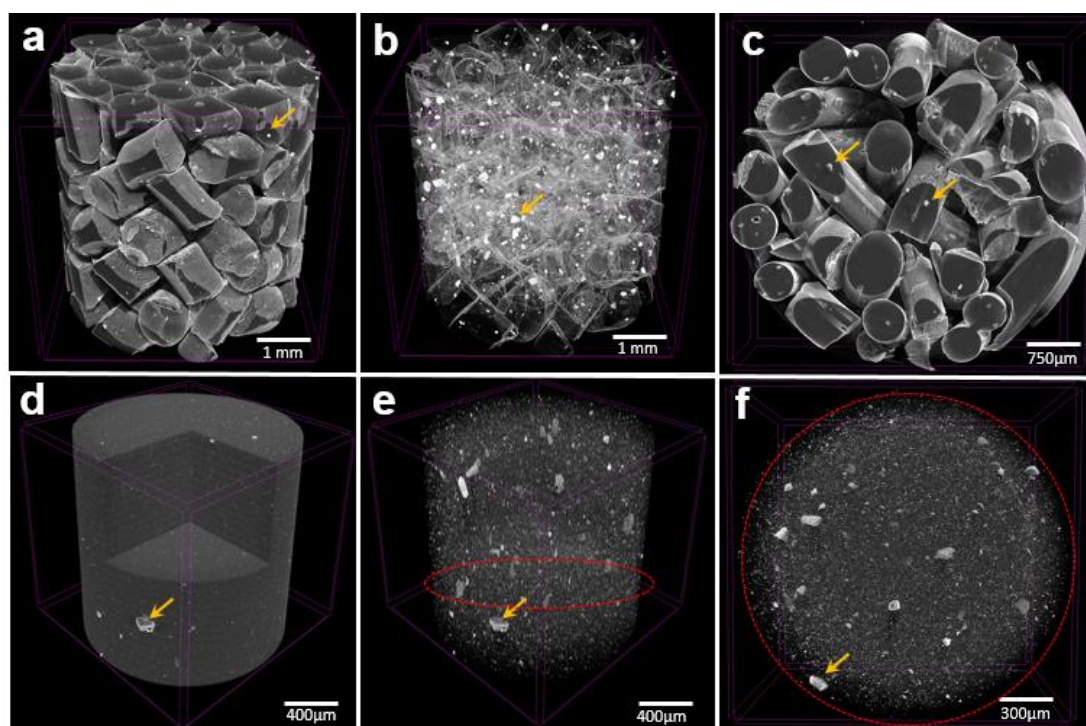


Figure 4.11. Representative 3D volume renderings of a) to c) 50 wt% drug loading system extruded at 180°C and d) to f) 10 wt% drug loading system 180°C. In images b), e) and f) the amorphous matrix was made transparent to highlight the NaCl clusters (denoted by the yellow arrows).

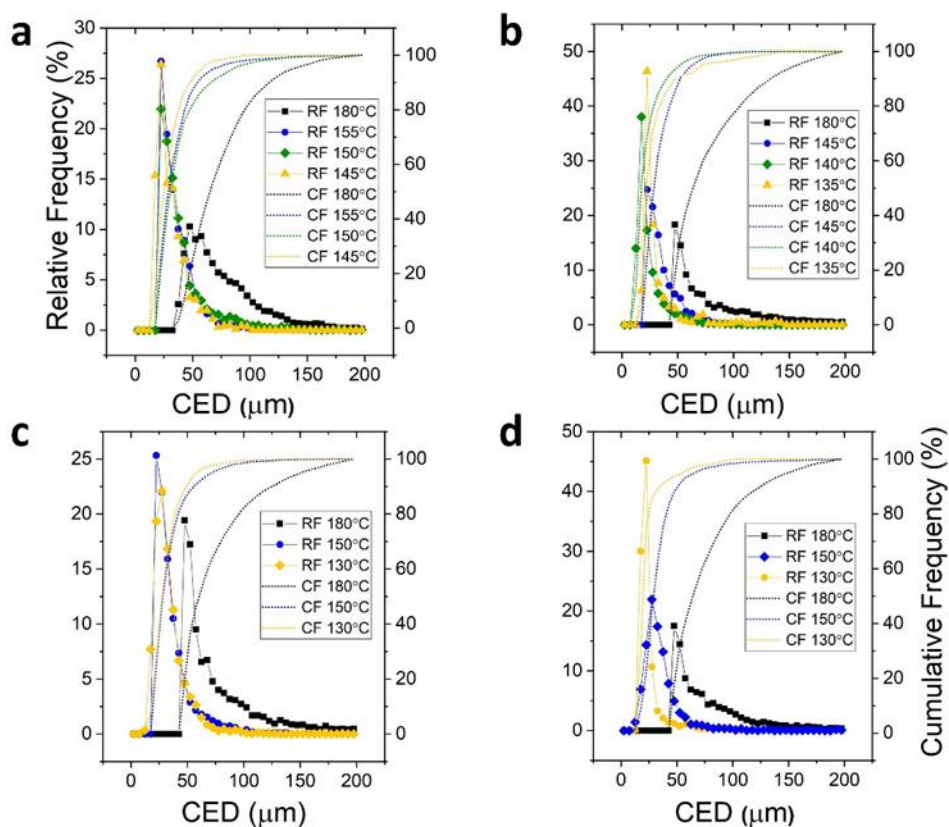


Figure 4.12. Size analysis of the NaCl clusters present in the a) 50 wt%, b) 35 wt%, c) 20 wt% and d) 10 wt % extrudates (calculated as the circle equivalent diameter, CED).

### 4.3.6 Polymer phase homogeneity

The most commonly reported phase separation behaviour in binary ASDs systems is the segregation of the incorporated drug from the carrier polymer as either amorphous or crystalline domains.<sup>158,173,239–242</sup> Nonetheless, within this study, polymer-related heterogeneities (PRH) were found across all systems extruded below the drug's melting point, as well as in the pure polymer extrudates, (i.e., extrudates with no API incorporated). Figure 4.13 shows 2D and 3D cross-sections highlighting droplet and string-shaped polymer-rich areas as a function of the processing temperature and drug loading. Given their presence in the pure-polymer extrudates, these structures are likely to form as a result of incomplete softening of the polymer particulates during extrusion. Cellulose derived materials have an intrinsic poor thermal conductivity<sup>243</sup> and the polymer grade used in this study has a high complex viscosity.<sup>244</sup> It

encompasses a wide range of molecular weights (50-70 kDa) and the heavier fractions make the system less plastic.<sup>245,246</sup> Thus, higher temperatures are required to completely soften/liquefy the polymer even if processed above polymer's glass transition.

Extrudates prepared under the melting regime lacked the polymer-rich domains and formed homogeneous ASDs, potentially true molecular dispersions. At this temperature, the drug is in the molten state and acts as a "liquid phase", plasticising and homogenising any unsoften polymer fractions. Upon temperature decrease to processing regimes (ii) and (iii), as well as drug loading increase, there is an apparent increase in the number and size of the polymer-rich domains (from ~30µm to ~250µm). Within the dissolution regime, there is no continuous liquid API phase and the polymer-related heterogeneities subsist. In the suspension regime, the presence of residual drug crystalline particulates is likely to exacerbate this tendency by further inhibiting heat propagation within the polymer matrix. Due to the lack of well-defined borders upon image binarisation, it was not possible to extract and quantify the PRH domains with the implemented image analysis algorithm.

M. Meere *et al.* have predicted similar behaviour in a cellulose-based binary system (Felodipine/HPMCAS) by developing a general multicomponent diffusion model for solid dispersions.<sup>247</sup> The authors simulated a simplified extrusion/thermal process and predicted formation of polymer-rich regions at  $T_{extrusion} < T_M$ , which is in good agreement with our findings. These results also suggest that further excipients, such as additional plasticisers, might be necessary to obtain single phase homogeneous ASDs under the dissolution regime, at least for highly viscous polymer systems as the one in this study.

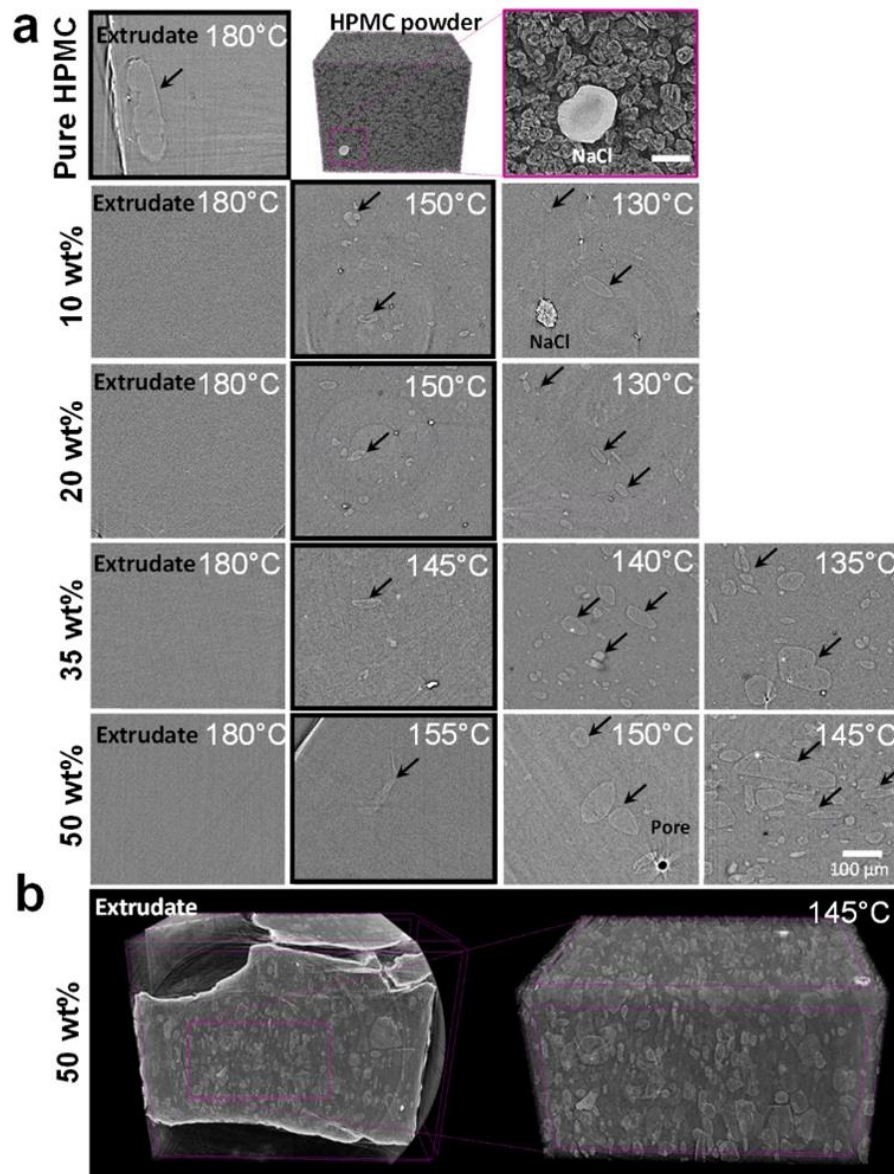


Figure 4.13. Impact of HME processing temperature and drug loading on the polymer phase homogeneity. a) 2D Cross-sections of all compositions and b) representative 3D volume rendering of the 50 wt% system extruded at 145°C. The black arrows denote the PRH clusters.

#### 4.3.7 Pore fraction analysis

For this type of HME-based ASDs, porosity is generally not created by design but a by-product of the extrusion process. Although it can be attributed to multiple factors,

including air incorporation from the feeding phase, residual humidity and presence of volatile components due to thermal/mechanical degradation or sublimation, its assessment is not routinely performed or reported for this type of drug product. Thus, an in depth qualitative and quantitative structural analysis of the isolated pore fraction was performed.

#### **4.3.7.1 Porosity quantification**

Porosity is usually determined in 3D as the pore volumetric percentage,<sup>248</sup> however it was aimed to investigate whether 2D porosity analysis as the area ratio could be equally used since it is readily obtained from the segmentation process. Results are shown in Figure 4.15. Overall, porosity was found to increase with increasing processing temperature and drug loading, with the 50 wt% system displaying the highest porosity across all processing regimes. It should be noted that the high standard deviation seen in the 2D measurements reflects pore and pellet area variations between successive tomographic slices rather than actual porosity variations. Statistical analysis across the temperature-composition space indicates that porosity differences between drug loadings and processing regimes are statistically significant at a significance level of 95% (Appendix C 8 to C 10). The equivalence of both quantification methods was also demonstrated in Appendix C 11 where no significant statistical difference was found between the two approaches.

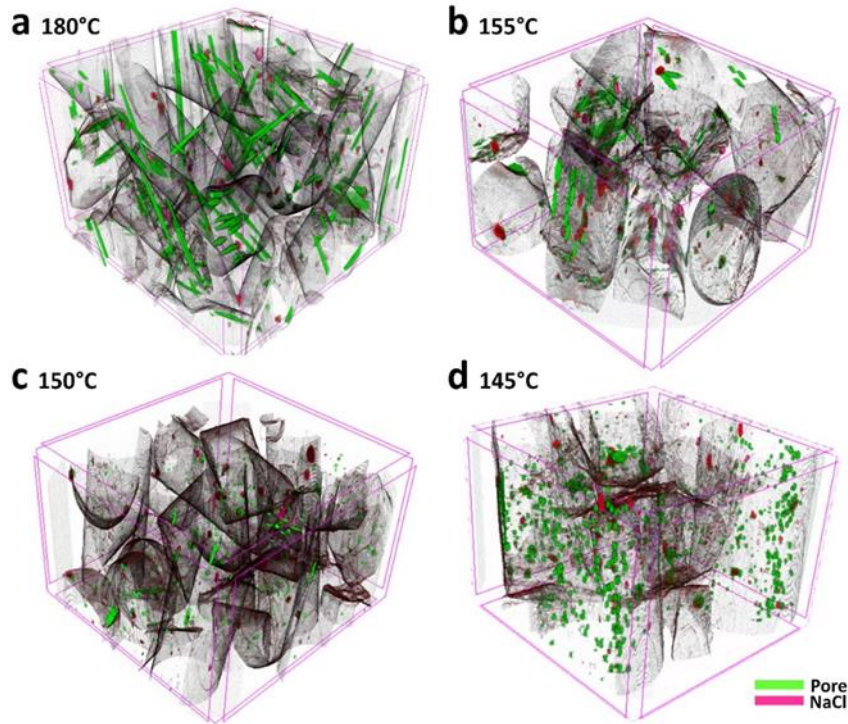


Figure 4.14. Segmented NaCl clusters and pores present within a 4000 x 4000 x 4000  $\mu\text{m}$  volume section present in the 50 wt% system extruded at different temperatures.

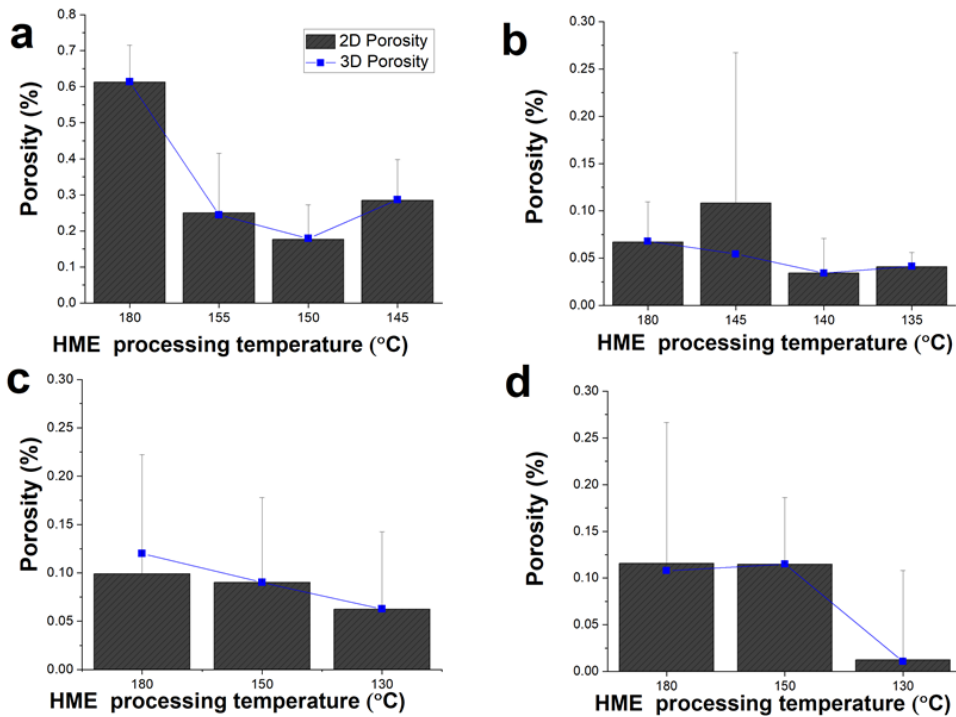


Figure 4.15. 2D and 3D pore quantification in a) 50 wt% system, b) 35 wt% system, c) 20 wt% system and d) 10 wt% system.

For the preparation of the aged samples with the 16 mm HME apparatus, the ventilation window was kept closed and the total porous content was found to vary from ~1% for the 10 wt% system to ~10% for the 50 wt% composition, as displayed in Figure 4.9.d. Porosity differences between the two extruding devices may also be driven by additional factors such as the channel fill level and feed rates differences. The higher porous percentage in the high drug loading systems for both devices is yet to be explained as the opposite trend was expected. Nevertheless, potential release of volatile components as a result of drug-related degradation is assumed.

#### **4.3.7.2 Pore size and shape**

The porous network structure was mainly characterised by closed porosity, where discrete occluded pores were dispersed within the ASD matrix without communicating with other pores or the lateral outer surface of the pellets (Figures 4.14). As an example, the pore shape derived from the elongation and flatness ratios of the ellipsoid fitting the pores is presented in Figure 4.17 for the 50 wt% system. The pore geometry was found to evolve from predominantly tubular/rod-like shapes at  $T_{extrusion} > T_S$  to spheroidal shapes at  $T_{extrusion} < T_S$ . This is in good agreement with the sphericity values calculated from volume/surface area ratios. As expected, spheroidal pores displayed sphericity values closer to 1, while tubular-like pores showed a sphericity value in the 0.10-0.40 range which corroborates the shape analysis extracted from the eigenvectors' ratio. Shape analysis results for the other compositions is shown in Appendix C 12 to C 14.

The pore length depicted in Figure 4.16 shows the presence of a multi-modal pore size distribution with longer pores present at higher drug loadings and higher processing temperatures. This supports formation of long tubular porous bodies within the melting regime and the gradual pore length decrease within the dissolution and suspension regimes until forming predominantly spheroidal pore shapes in the latter.

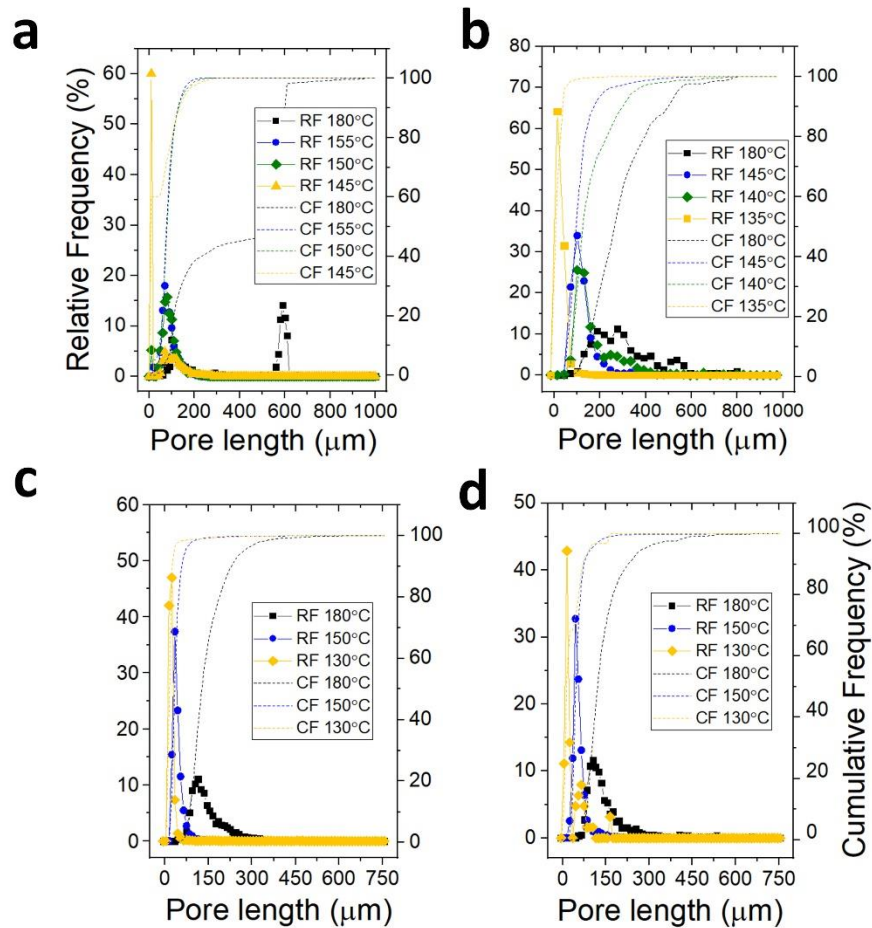


Figure 4.14. Pore size analysis of the a) 50 wt%, b) 35 wt%, c) 20 wt% and d) 10 wt% drug loading systems. Calculated as the length of the major eigenvector of the ellipsoid fitting the pores in 3D)

Pore connectivity changes reflected by the consistent trend in length and shape variations are thought to be related to shear and melt-viscosity variations during extrusion. As an indirect measure of viscosity, torque data was analysed and it was found to decrease with increasing drug loading levels and processing temperatures (data shown in Appendix C7). Thus, at  $T_{extrusion} > T_S$ , formation of long tubular porous structures is likely to form through coalescence of minor pores as a result of lower melt viscosity and higher porosity. This is likely to occur within the confines of the die section, where the material accumulates before forming a uniform filament upon exiting the extruder.

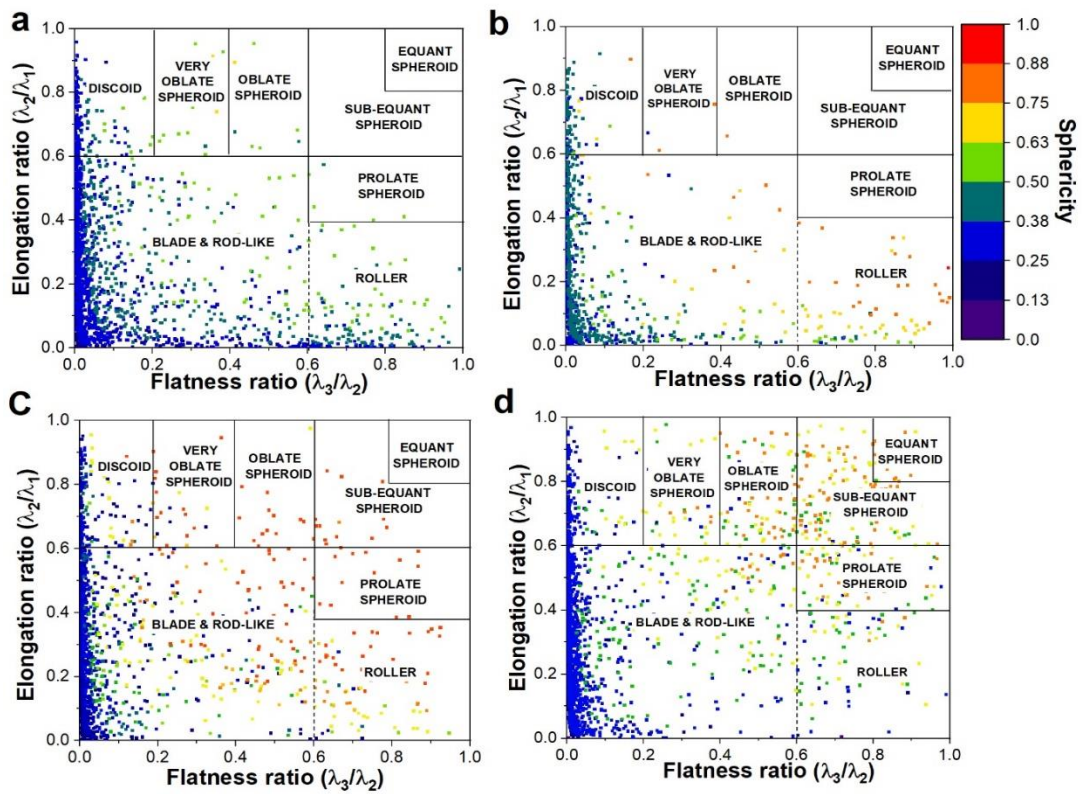


Figure 4.15. Shape analysis extracted from the flatness and elongation ratios for the 50wt% drug loading system extruded at a) 180°C, b) 155°C, c) 150°C and d) 145°C. Each point represents an individual pore. The same colour bar scale applies to all processing temperatures.

### 4.3.7.3 Pore orientation

To assess the orientation of the pores, the Euler angles of the eigenvectors describing the ellipsoid fitting the pores were extracted. Despite the random orientation of the pellets within the Kapton tubes Figure 4.18 shows a preferred orientation within  $\pm 20$  degrees (counterclockwise and clockwise, respectively) along the y and z-axis. In conjunction with the visual inspection of the orientation of the pores within the pellets, these results suggest the pore major axis is almost parallel to the direction of the material flow exiting the die.

It is well established in the literature that the inner structure, total porosity, size, shape, orientation and pore connectivity can impact the liquid imbibition pattern in pharmaceutical products and affect their dissolution profile, as well as their mechanical properties.<sup>249</sup> These results indicate that this effect could also be extended to ASD products. However, the impact of these microstructural differences on the dissolution properties of these systems remains an open question, as no dissolution tests were carried out. Nonetheless, higher porosity and the presence of open tubular porous structures are likely to have a positive impact upon dissolution by increasing the accessible surface area.

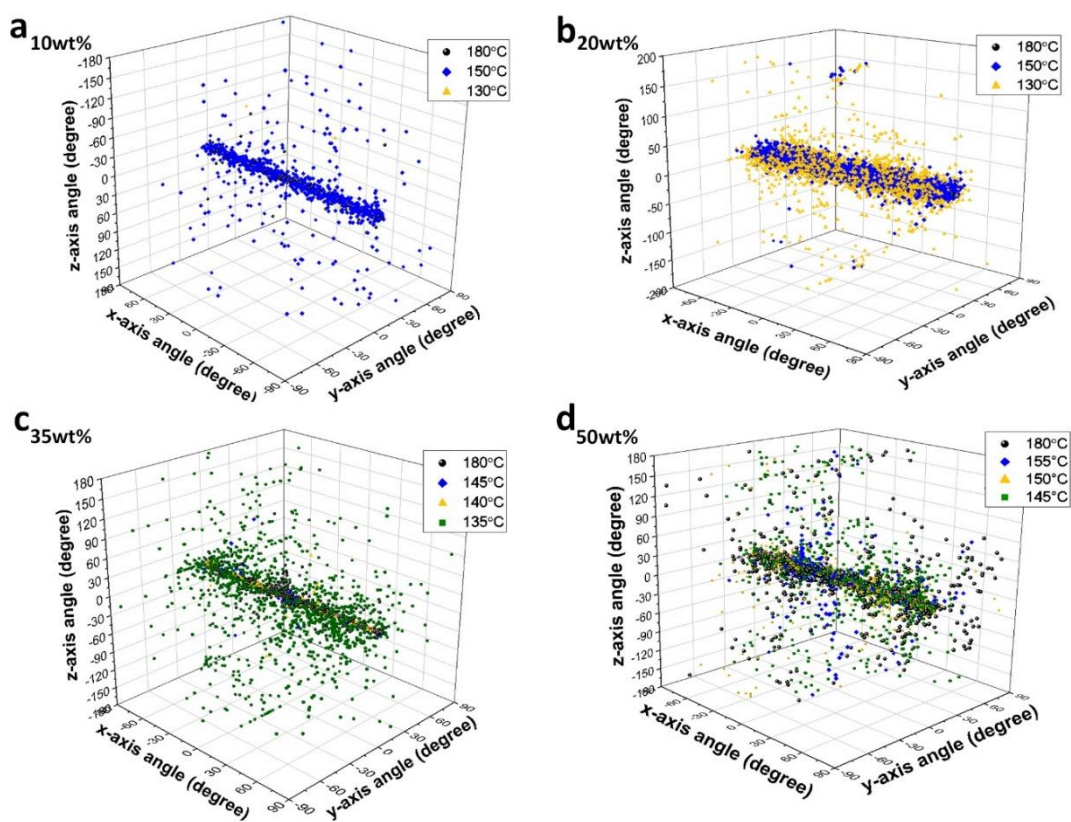


Figure 4.16. Pore orientation along the x, y and z axis.

### 4.3.8 Surface area measurements by N<sub>2</sub> physisorption

As an indirect validating measure of porosity, the ASD surface area was analysed via N<sub>2</sub> gas physisorption. For this analysis, a transversal approach across the temperature-composition space was taken. Thus, the 50wt % composition extruded at 180°C, 155°C, 150°C and 145°C was included in the analysis, as well as all drug loadings extruded within the melting regime (i.e., at 180°C). The plot of the resultant adsorption and desorption isotherms presented in Figures 4.19.a and 4.19.b displays open low-pressure hysteresis (at  $P/P_0 < 0.40$ ) and multiple steps present in both sorption branches.

This complex sorption behaviour suggests a combination of isotherms “Type IV” and “Type VI” according to the IUPAC classification,<sup>250</sup> however it cannot be fully explained by simple structural deformation/swelling or multilayer adsorption. Low-pressure hysteresis has been previously reported for microporous amorphous polymers and it is suggested to occur primarily due to N<sub>2</sub> diffusional limitations caused by pore blocking effects, as a result of closed/obstructing pore morphology and restricted connectivity.<sup>251</sup> These results are in good agreement with the closed macropores (>50nm) visualised in the tomograms and further suggest the presence of micropores (< 2nm) that cannot be visualised with Sync-PC- $\mu$ CT. Moreover, the presence of crystalline API material in the suspension regime is also expected to contribute to the open hysteresis by providing an additional obstructing surface. The step-wise sorption isotherms have been ascribed to sequential filling of pores of different sizes and indicate presence of micro and mesopores (2-50 nm).<sup>252</sup>

For surface area calculations, the Non-Local Density Functional Theory (NLDFT) was used because it incorporates both micropore filling and capillary condensation processes<sup>253</sup> and provided a better fit to the experimental data than conventional BET analysis. The surface area presented in Figures 4.19.c and 4.19.d shows a variation across the temperature-composition space that corroborates the porosity trend derived from the Sync-PC- $\mu$ CT image analysis. Nonetheless, due to the remarkably low surface area these materials could benefit from Krypton physisorption analysis for more accurate data.

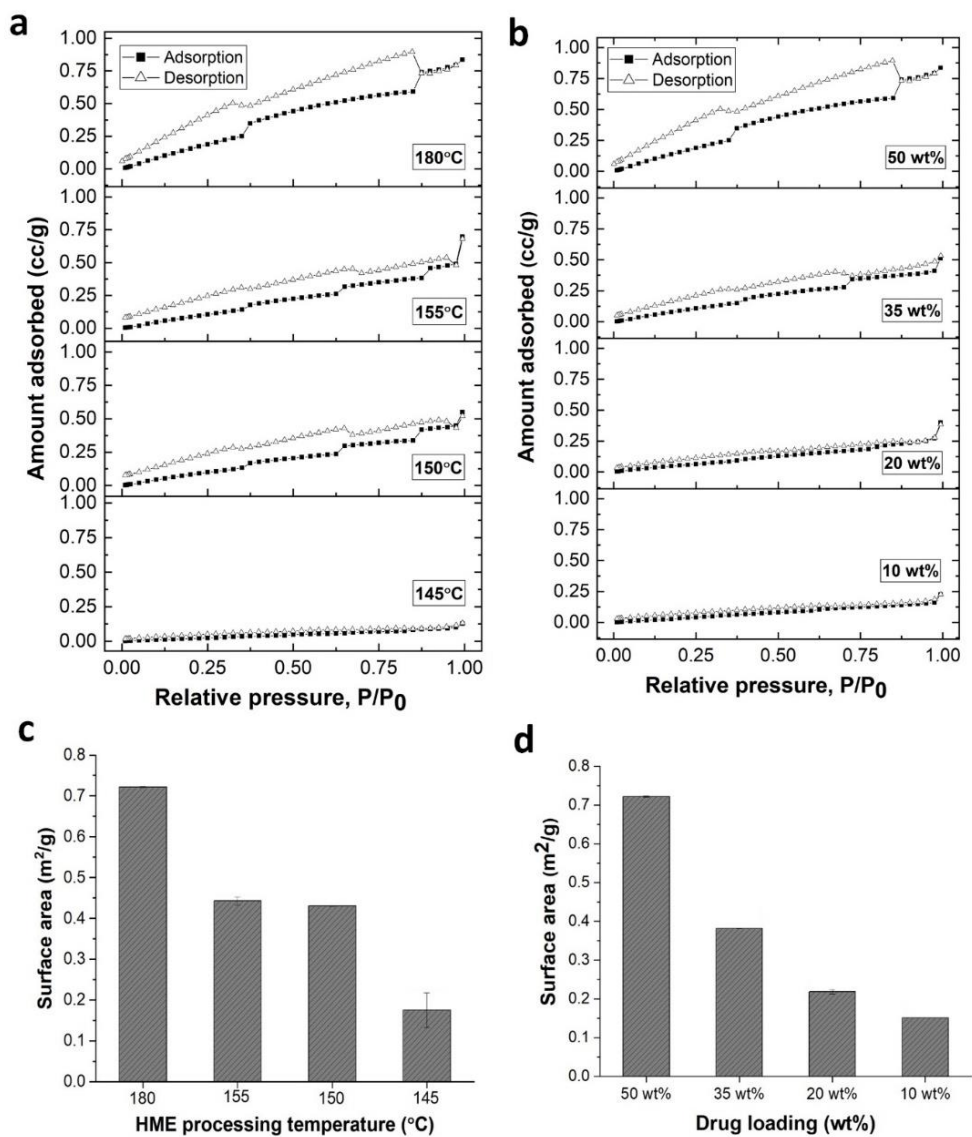


Figure 4.17. Impact of HME processing temperature and drug loading on the  $N_2$  physisorption behaviour and surface area. a) and c) 50wt% solid dispersions extruded at different processing temperatures and b) and d) solid dispersions with varying drug loadings extruded at 180°C (meting regime).

## 4.4 Conclusions

This work demonstrates the potential of Sync-PC- $\mu$ CT as a novel tool for the investigation of ASD internal structure. In combination with a tailored image analysis strategy, Sync-PC- $\mu$ CT provided sufficient contrast to reveal spatially resolved information on the phase distribution homogeneity and existing microstructure within ASDs produced under different saturation conditions, thus linking drug-polymer solubility to ASD microstructure. Despite minimal elemental difference between the drug and polymer used in the study (paracetamol and HPMC), Sync-PC- $\mu$ CT revealed multiple structural domains/defects, such as drug-rich crystalline clusters, impurities, polymer-related heterogeneities (PRH) and voids/pores. Supersaturated ASDs (> 20wt% drug loading) displayed higher structural complexity and exhibited a plethora of pores and API-rich crystalline domains upon ageing, which were absent in the undersaturated ASDs. The HME processing temperature/regime was found to affect not only residual API crystallinity, but also the pore network structure and the polymer softening behaviour. The presence of the PRH domains is indicative of partial amorphous phase separation and varying local compositions, which could have a negative impact on performance and stability. Further work is required to assess whether this effect could be mitigated by the addition of plasticisers or by improving barrel mixing through screw speed increase or by increasing processing temperature to the melting regime to promote complete softening/liquefaction of the polymeric carrier.

Furthermore, in the development of HME-based formulations the general assumption is of a homogeneous ASD microstructure assuming true thermodynamic equilibrium has been reached. The use of advanced analytical tools, such as Sync-PC- $\mu$ CT, adds a new complexity dimension and shows different degrees of structural heterogeneity (i.e., level of defects) across the temperature-composition space as a result of HME processing conditions even when the drug is solubilised. This suggests that the implications of the API-polymer solubility phase diagram go beyond the crystalline-amorphous dichotomy and that it can map out the ASD internal structure. Furthermore, the combined capabilities of low-frequency Raman and Sync-PC- $\mu$ CT provide an effective means of assessing HME performance and efficiency when manufacturing

ASDs. In the future, this could be used for the targeted manufacture of stable ASD systems with desired structural and functional features.

# Chapter 5

## ASD Surface Crystallisation as a Strategy for Early-Stage Physical Stability Assessment

**The work carried out in this Chapter was partially published in a peer-reviewed journal.**

Paladino, E., Doerr, F., **Bordos, E.**, Onyemelukwe, I., Lamprou, D., Florence, A., Gilmore, I. and Halbert, G. W. High spatial resolution ToF-SIMS imaging and image analysis strategies to monitor and quantify early phase separation in amorphous solid dispersions. *Int. J. Pharm.* 628, 122191 (2022).

## 5.1 Introduction

It is well known that the properties of materials at the surfaces and in the bulk can vary significantly. However, little effort has been dedicated to understanding physical stability at the surface of amorphous solid dispersions, with the vast majority of studies focusing almost exclusively on bulk physical stability indicators (i.e., bulk crystallinity). Different crystallisation rates in the bulk and on the surface of various single component amorphous drugs have been reported. For example, the rate of surface crystallisation of pure amorphous griseofulvin, indomethacin and nifedipine was shown to be several orders of magnitude faster than that of bulk crystallisation at temperatures below the glass transition.<sup>254–256</sup> This frequently occurs as a result of higher molecular mobility at the surface because of the reduced diffusional barrier for crystallisation.<sup>257</sup> Most amorphous pharmaceutical solids will be subjected to intensive downstream processing, such as pelletisation, milling and compression that can impart high mechanical stress and affect surface properties. Hence, surface crystallisation could be a key aspect in understanding and controlling ASD physical stability. Accordingly, there is scope for early stage detection of physical instability through a targeted study of the ASD surface. Time of flight-secondary ion mass spectrometry (ToF-SIMS) is a highly sensitive surface analytical technique with high spatial resolution (~200 nm) and low probing depth (1-5nm) that enables determination of surface chemistry and surface chemical mapping.<sup>258–261</sup> Therefore, the primary objectives of this Chapter are to (1) investigate the surface stability of ASDs through a long-term stability study focusing on the local distribution evolution of the API and polymer via ToF-SIMS chemical analysis, and to (2) further assess the effect of drug loading and HME processing temperature - as coordinates of the API-polymer solubility phase diagram – on the ASD surface stability.

## 5.2 Materials and methods

### 5.2.1 Materials

The same materials as described in Section 4.2.1 in Chapter 4 were used. All compounds were used as obtained, without further purification.

### 5.2.2 Methods

#### 5.2.2.1 Preparation of amorphous solid dispersions by hot melt extrusion (HME)

HME was performed with an 11 mm co-rotating twin-screw extruder in combination with a loss-in-weight gravimetric feeder as described in Chapter 4. Table 5.1 illustrates the specific drug loadings and processing temperatures. Collected extrudates were allowed to cool to ambient temperature by natural convection prior to pelletisation (Thermo Scientific™ VariCut Pelletizer, Thermo Fisher Scientific, UK) and storage at room temperature ( $23.0 \pm 0.3^\circ\text{C}$ ) in a desiccator until further analysis.

Table 5.1. HME processing conditions.

Drug loading (wt %)	Process set temperature ( $^\circ\text{C}$ )	Screw speed (rpm)	Feed rate (kg/hr)
10	170, 150, 130	100	0.100
20	170, 150, 130	100	0.100
35	170, 150, 145, 140, 135	100	0.100
50	170, 155, 145	100	0.100

#### 5.2.2.3 Differential Scanning Calorimetry (DSC)

DSC analysis was performed from  $0^\circ\text{C}$  to  $180^\circ\text{C}$  at a heating rate of  $20^\circ\text{C}/\text{min}$  according to the methodology described in Section 2.2.2.6 in Chapter 2. Measurements

were performed in triplicate. The percentage of crystalline drug in the ASDs was determined according to Equation 5.1:

$$\text{Crystallinity (\%)} = \frac{\Delta H}{\Delta H_c} \cdot 100 \quad (5.1)$$

where  $\Delta H$  is the melting enthalpy of the crystallised drug fraction, which is calculated as the ratio of melting enthalpy of the sample divided by the drug fraction and  $\Delta H_c$  represents the melting enthalpy of pure crystalline PCM ( $180.2 \pm 0.3$  J/g).

#### **5.2.2.4 X-ray diffraction (XRD)**

XRD data was collected as described in Section 2.2.2.7 in Chapter 2.

#### **5.2.2.5 Time-of-flight secondary ion mass spectroscopy (ToF-SIMS)**

ToF-SIMS data was acquired with an IONTOF TOF.SIMS 5 instrument (IONTOF GmbH, Münster, Germany), equipped with a bismuth liquid metal ion gun and a gridless reflectron time-of-flight mass analyser. All analyses were recorded with SurfaceLab software package (versions 6.7, 6.8 and 7, IONTOF GmbH, Münster, Germany). Reference mass spectra of PCM and HPMC were collected on pure powder samples secured with double sided tape on a flat aluminium substrate to produce an immobile surface suitable for ToF-SIMS. Analysis was performed employing a bunched 30 keV  $\text{Bi}^{+3}$  primary ion beam. Data was acquired in the positive and negative secondary ion polarities, from different  $50 \mu\text{m} \times 50 \mu\text{m}$  areas of the surface, delivering a total primary ion dose (PID) of approximately  $5 \times 10^{11}$  (primary ions/ $\text{cm}^2$ ) for each acquisition ( $n=3$ ). PCM was identified by its protonated molecular ion  $\text{C}_8\text{H}_{10}\text{NO}^{+2}$  at  $m/z$  152.07 and by the fragments  $\text{C}_6\text{H}_8\text{NO}^+$  ( $m/z$  110.06),  $\text{C}_6\text{H}_7\text{NO}^+$  ( $m/z$  109.05) and  $\text{C}_5\text{H}_6\text{N}^+$  ( $m/z$  80.05), whilst HPMC exhibits the characteristic secondary ions  $\text{C}_4\text{H}_9\text{O}^+$  ( $m/z$  73.07),  $\text{C}_3\text{H}_7\text{O}^+$  ( $m/z$  59.05) and  $\text{C}_2\text{H}_5\text{O}^+$  ( $m/z$  45.03), which were not present in the PCM reference spectra.

High spatial resolution ToF-SIMS data of the pelletised PCM-HPMC extrudates was acquired with an unbunched 30 keV  $\text{Bi}^{+3}$  primary ion beam over a  $500 \mu\text{m} \times 500 \mu\text{m}$

field of view (FoV) in randomly selected locations on the surface of the pellets over a period of 150 days. After the first analysis time-point, supplementary images were collected on the same location to visually assess growth of the API-rich clusters/crystals. The PID, spatial resolution and pixel width were respectively  $2 \times 10^{11}$  (primary ions/cm<sup>2</sup>), 0.55  $\mu\text{m}$  and 0.49  $\mu\text{m}$ . Within the 500  $\mu\text{m}$  x 500  $\mu\text{m}$  FoV, additional 100  $\mu\text{m}$  x 100  $\mu\text{m}$  images were acquired, using an unbunched 60 keV Bi<sup>+3</sup> primary ion beam for improved spatial resolution. For these, the spatial resolution and pixel width were 0.15  $\mu\text{m}$  and 0.099  $\mu\text{m}$ , respectively. The mass spectral data was collected in the positive secondary ion polarity with a 0.055  $\mu\text{s}$  delayed extraction. The mass range was recorded between 0 and 900 Da.

The ToF-SIMS chemical mapping images were used to extract quantitative data of the overall drug and polymer surface coverage and evaluate the kinetics of surface phase-separation/crystallisation. Image analysis was performed with MATLAB 2019 (The MathWorks, Inc. USA) according to the methodology described by E. Paladino *et al.*<sup>262</sup>

### 5.2.2.6 Kinetics of surface crystallisation

The crystallisation process of a drug–polymer system can be quantitatively described by several kinetics models. Among these models, the Avrami model/Equation is most frequently used to express and predict the solid-state crystallisation processes.<sup>263–266</sup> According to this model, the relative crystalline fraction ( $\alpha_s(t)$ ) is correlated with the storage time (t) according to Equation 5.2:

$$\alpha_s(t) = 1 - \exp[-k \cdot t^{n_A}] \quad (5.2)$$

where  $k$  is the crystallisation rate constant and  $n_A$  the Avrami exponent constant that reflects the nucleation rate and/or the dimensionality of crystal growth. The exponent  $n_A$  takes on values between 1 and 4 and can be interpreted as  $n_A = D + 1$ , where D represents the dimensionality of crystal growth and 1 is the contribution of crystal nucleation. In the present study, Equation 5.2 was used to quantify kinetics of crystallisation for cases where growth was predominant over nucleation, assuming diffusion controlled crystal growth kinetics of needle and plate-like structures ( $n_A = 1$ ). The classic Avrami model assumes a constant nucleation rate for the phase transition,

which is not applicable in cases where the available nucleation sites and the amorphous fraction ( $1 - \alpha_s(t)$ ) decrease significantly during the crystallisation process.<sup>263,267</sup> This leads to an overprediction of phase transformation rates at later stages of the crystallisation process. Yang *et al.*<sup>267</sup> derived a modified version of the Avrami model accounting for non-constant nucleation rates (Equation 5.3) and proposed that the nucleation rate is proportional to the total amorphous fraction of the surface ( $1 - \alpha_s(t)$ ). Thus, the crystalline fraction  $\alpha_s(t)$  increases as a function of storage time ( $t$ ), according to Equation 5.3:

$$\alpha_s(t) = 1 - \frac{1}{1 + k \cdot t^{n_A}} \quad (5.3)$$

where  $k$  is the crystallisation rate constant and the exponent  $n_A$  represents the dimensionality of crystal growth. For conditions of homogeneous nucleation  $n_A$  assumes values of 2 for rod, 3 for plate and 4 for spherical geometry. Equation 5.3 was applied to calculate the crystallisation rate constants ( $k$ ) considering plate-like crystal growth and homogeneous nucleation ( $n_A = 3$ ).

### 5.2.2.7 Scanning electron microscopy (SEM)

The pelletised extrudate material was added to aluminium stubs with adhesive carbon tabs with the side of the filaments and the cross-section surface exposed. Samples were sputter coated with 20 nm gold layer to minimise charging in the SEM. Samples were then placed under vacuum for 2 min prior to transfer to SEM for analysis using a TM4000Plus SEM (Hitachi, Tokyo, Japan). The SEM was operated at a beam voltage of 10,000 eV and data was collected in backscattered electron mode at magnifications of x50, x100, x1000.

### 5.2.2.8 Optical microscopy

Optical microscopy was performed using a Leica DM2700 transmission optical microscope (Leica Microsystems, Milton Keynes, UK) under a bright field or using a

cross-polarized light. The apparatus was equipped with a Leica DF320 digital camera (Leica Microsystems, Milton Keynes, UK).

## **5.3. Results and discussion**

### **5.3.1. ASD surface stability**

#### **5.3.1.1 Drug-rich clusters surface coverage**

The spatial distribution of the drug and polymer on the surface of the ASDs was studied over a period of 150 days with ToF-SIMS by selecting ion-peaks with distinctive mass-to-charge ratios for each component, as described in Section 5.2.2.5. For the various drug-loadings, ToF-SIMS data was acquired at different time-points depending on the level of drug saturation and expected physical stability profile: 10 wt% drug loading – undersaturated/stable, 20 wt% drug loading – saturated/metastable, 35 wt% and 50 wt% drug loadings – supersaturated/unstable.

Representative ToF-SIMS images are displayed in Figure 5.1. The 10 wt% drug loading system remained stable and did not present any physical changes indicative of phase separation or crystallisation within the 150 days of storage. All remaining compositions showed evidence of surface physical instability in the form of phase separated sub-micrometer sized drug-rich clusters (20 wt% and 35 wt% drug loadings) or larger drug-rich structures that resemble agglomerates of crystallites (50 wt% drug loading) from the first analysed time-point. Independently of the initial size, the drug-rich clusters were found to grow, indicating incremental surface drug enrichment upon ageing. The extent of phase separation and the morphologies of these drug-rich clusters suggest formation of crystalline material on sample surface (further discussed in the Sections below). Furthermore, the 10 wt% drug loading samples present additional  $\text{Na}^+$  ( $m/z$  22.99) clusters that are attributed to NaCl salt particulates, which is a known impurity present in the polymer. This provides additional chemical confirmation of the NaCl particulates visualised with phase-contrast tomography in Chapter 4, Section 4.3.5. The  $\text{Na}^+$  clusters were not visible in the remaining compositions due to lower polymer fraction.

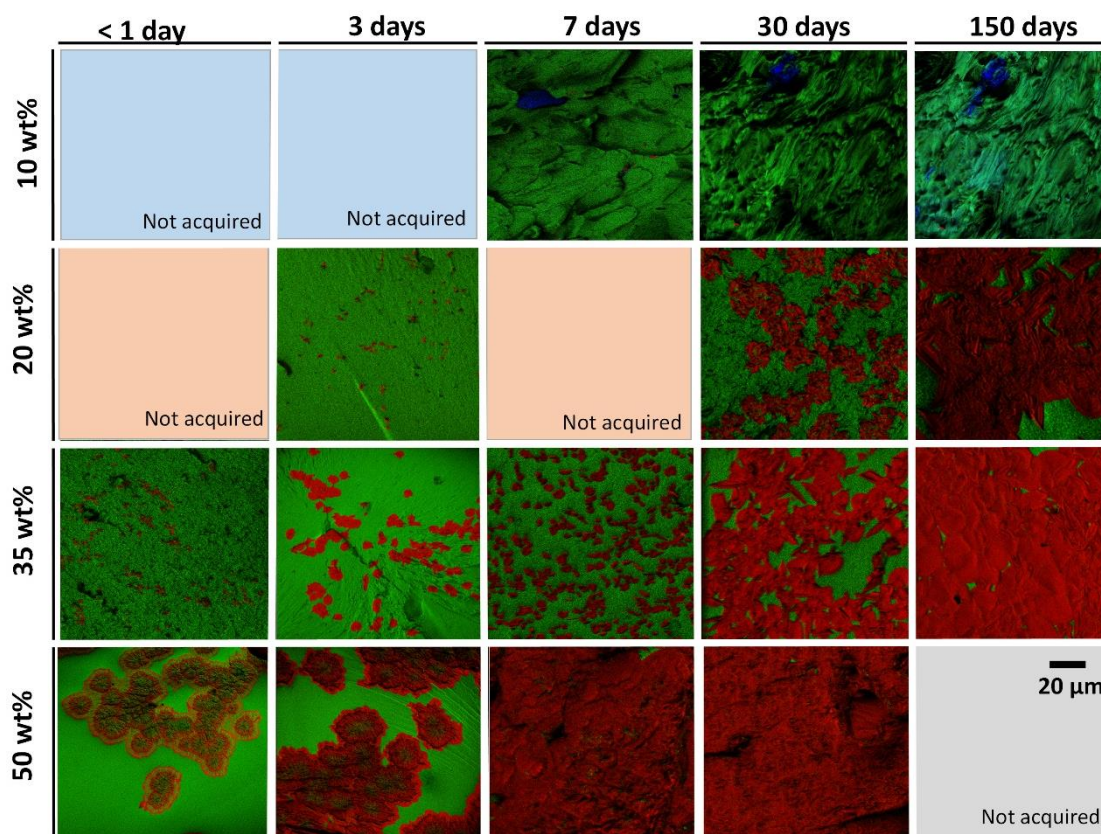


Figure 5.1. Representative ToF-SIMS images of all drug loadings processed at the respective lowest temperature: 130°C for the 10 wt% and 20 wt% systems, 140°C for the 35 wt% system and 145°C for the 50 wt% drug loading system. The molecular ions/fragments corresponding to the drug are displayed in red, the polymer in green and Na in blue

The drug coverage of the ASD surface and the surface enrichment rate results are shown in Figures 5.2.a and 5.2.b, respectively. At any given time-point, there is a marked surface coverage increase with increasing drug-loading and a less pronounced effect with decreasing processing temperature. The two supersaturated systems (i.e., 50 wt% and 35 wt% drug loadings), exhibit intense drug phase-separation/crystallisation, with a surface coverage of ~90% at all processing temperatures after approximately 30 days of storage. For the same time period the 20 wt% system displays a modest drug surface coverage of ~30% at 130°C and 150°C, and ~20% at 170°C. Included with the experimental data in Figure 5.2.a are the crystallisation predictions based on the classical Avrami model (Equation 5.2) or its modified version accounting for non-constant nucleation rate as derived by Yang *et al.*<sup>267</sup> (Equation 5.3). The 10 wt% drug loading system was excluded from the Avrami

fitting approaches because no drug-rich clusters or crystals were detected. The 20 wt% and 35 wt% systems are best described by a sigmoidal shaped curve (Equation 5.3 with  $n_A = 3$ ). The characteristic “S” shaped crystallisation curve is formed by 3 phases: an initial onset phase, where nuclei are formed, followed by a rapid crystallisation phase, and final stage where a decline in crystallisation rate occurs due to the consumption of available nucleation sites, until reaching a plateau. Thus, the inflection point describes the end of a nucleation-dominated stage and the beginning of a growth-dominated stage. Figure D 1 demonstrates that crystallisation takes place from the initial sub-micrometer drug-rich clusters formed during the onset stage. Although it is not clear whether the initial clusters are amorphous or nano-crystalline, they are precursors for the crystalline phase and constitute active nucleation sites.

For the 50 wt% system the initial onset phase is not observed and a logarithmic-shaped curve (Equation 5.2 with  $n_A = 1$ ) describes the data at all processing temperatures. At this drug-loading, there are minor disagreements between experimental data and the predictions from the classic Avrami model. This is particularly evident for the time-points  $> 7$  days for the system processed at 145°C where residual crystallinity is present. The Avrami overprediction results from the implicit assumption of constant nucleation rate, which is not applicable here due to the reduction of the amorphous surface area throughout the crystallisation process. The absence of the onset phase indicates formation of nuclei within hours after extrusion. For this highly supersaturated system, growth becomes dominant and further nucleation contributes less to the overall increment of the drug coverage. This behaviour is illustrated in Figure 5.3 that displays ToF-SIMS images acquired on the same location on the surface of a 50 wt% pellet processed at 170°C at 4 time-points between 0 and 28 days of storage. Large drug-rich clusters are present on the ASD surface already from the day of extrusion and their subsequent growth upon ageing is evident. The crystal growth rate is higher during the first 7 days. Thereafter, a slower growth of the pre-existent crystals is observed, despite the appearance of secondary (late-stage) crystallisation points as seen in Figure 5.3.a at 14 days of storage (denoted by the yellow arrows). Similar results were reported for single component indomethacin glasses, wherein a rapid initial increase of surface crystallinity was followed by an abrupt slowdown of crystallisation.<sup>268</sup>

The ASD surface enrichment rates displayed in Figure 5.2.b highlight the impact of drug-loading and processing temperature on the surface crystallisation kinetics. For the 20 wt% and 35 wt% drug-loadings, the fast surface coverage/crystallisation phase lasts for 30 days when the drug surface coverage reaches ~30 % and 90 %, respectively. Thereafter the surface coverage rate decreases as the nucleation rate decreases due to the decline of available nucleation sites. This effect is even more pronounced for the 50 wt% system, where a steep surface coverage increase is observed during the first 7 days, when the drug crystalline clusters cover ~90 % of the surface and thereafter an abrupt surface coverage slowdown occurs.

For all drug-loadings, the HME processing temperature appears to have a strong impact on the ASD surface coverage rate. At processing temperature below the saturated solubility temperature ( $T_S$ ), the presence of residual crystallinity seeds further crystallisation and promotes faster surface coverage/crystallisation rates. However, at HME processing temperatures corresponding to the drug's melting point ( $T_M = 170^\circ\text{C}$ ), the surface coverage rate/crystallisation is higher than at temperatures between  $T_M$  and  $T_S$ . This could suggest different molecular arrangements in the amorphous state (i.e., different degrees of disorder / polyamorphism) as a result of the processing regime. At the drug's melting point, higher molecular mobility is expected due to lower polymer viscosity and drug liquefaction, which could facilitate molecular rearrangement and formation of pre-nucleation clusters that could promote faster surface coverage rates upon storage. Conversely, at lower processing temperatures this would occur to a lesser extent because of hindered molecular mobility. This would explain the slower surface coverage/crystallisation rates and the longer induction times. However, temperature-induced differences in the drug-polymer molecular interaction pattern as a result of different chain orientation of the polymeric molecules could also contribute. Similar results were observed by M. Mosharraf that reported different solid-state structures in the amorphous state as a result of different processing environment.<sup>269</sup>

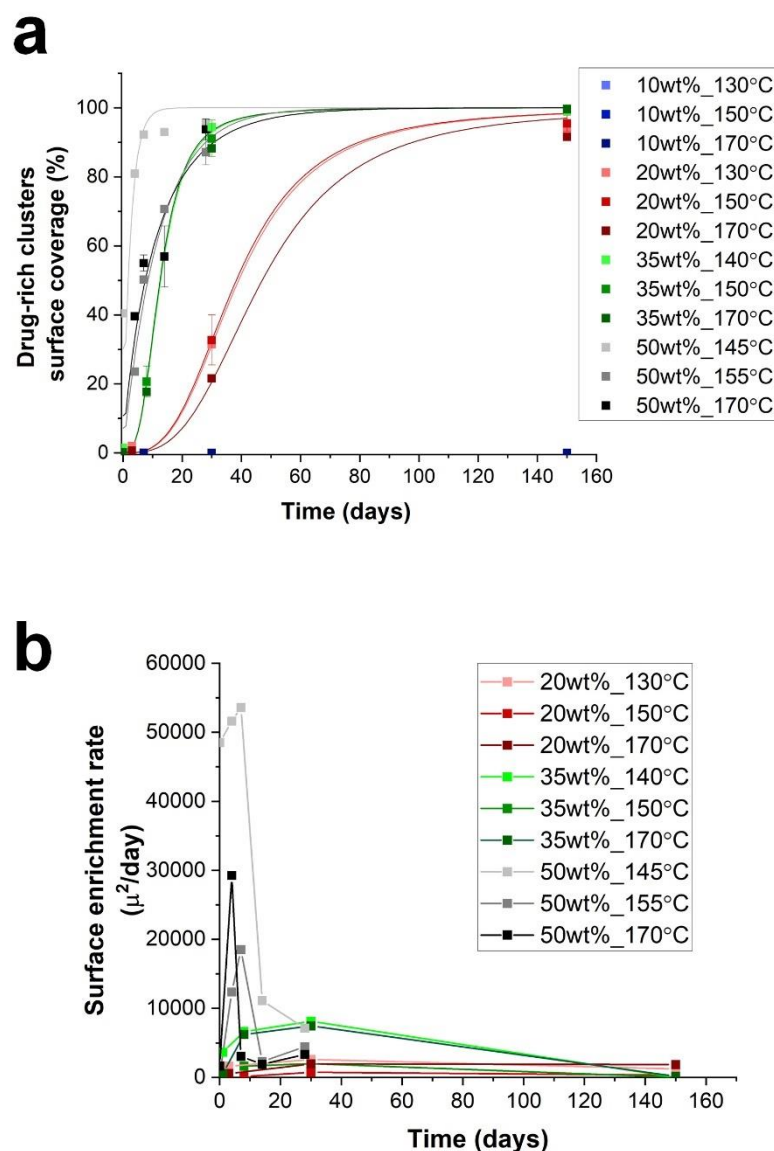


Figure 5.2. a) Drug surface coverage quantification over 150 days. The error bar denotes the standard deviation of various ToF-SIMS images acquired on individual pellets ( $n > 3$ ). Individual data points denote experimental values, which were fitted to the Avrami model. b) Drug enrichment rate on the surface of the solid dispersions

The crystallisation rate constant ( $k$ ), the Avrami exponential constant ( $n_A$ ) and the mean squared error (MSE) obtained from the Avrami fittings are shown in Table 5.2. The crystallisation rate constant increases by several orders of magnitude from 20wt% to 50 wt% drug loading indicating decreasing crystallisation activation energy ( $E_A$ ) values.  $E_A$  is usually determined by the slope of the linear regression of the semi-log plot of the crystallisation rate constant ( $k$ ) versus  $1/T$  according to the Arrhenius

Equation.<sup>270</sup> The system with the greater slope indicates lower activation energy and faster crystallisation rate. Thus, as an approximate of the activation energy, the logarithm of the crystallisation rate constant was plotted as a function of the polymer content for all systems. The observed linear relationship suggests that  $E_A$  increases linearly with respect to the polymer fraction. Furthermore, the slope of the semi-log plots indicates the following  $E_A$  ranking for the different HME processing temperatures: low < high < middle. This suggests that the systems processed at the drug's melting point have lower energetic barrier to crystallisation when compared to processing temperatures at drug's solubilisation end point. This provides further support to the hypothesis of different molecular arrangements in the amorphous state as a result of the processing environment.

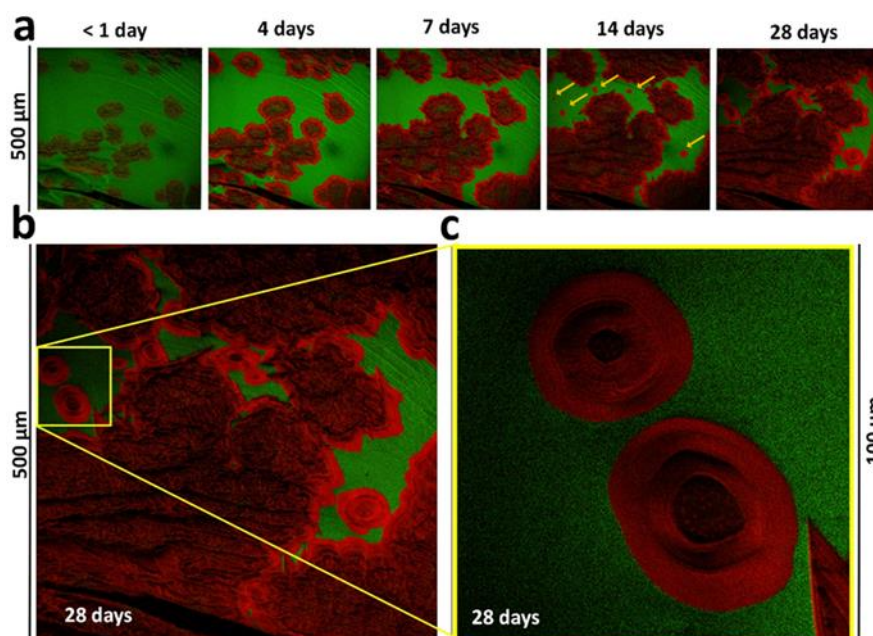


Figure 5.3. a) ToF SIMS images acquired on the surface of 50 wt% pellets from day 1 to day 28 of storage. The yellow arrows at 14 days of storage denote the appearance of secondary/late-stage nucleation of PCM-rich domains. b) Enlarged ToF SIMS image at 28 days of storage with b) high resolution inset (yellow frame) displaying drug terraced circular crystallites.

Drug loading (wt %)	Processing temperature (°C) <sup>a</sup>	k	n <sub>A</sub>	MSE
20	170	9.61E-06	3	7.66E-04
20	150	1.78E-06	3	2.93E-04
20	130	1.68E-05	3	6.68E-04
35	170	5.2E-04	3	8.9E-04
35	150	4.9E-04	3	9.5E-05
35	140	5.2E-04	3	1E-04
50	170	1.28E-01	1	7.48E-03
50	155	8.2E-02	1	2.88E-03
50	145	3.97E-01	1	3.4E-02

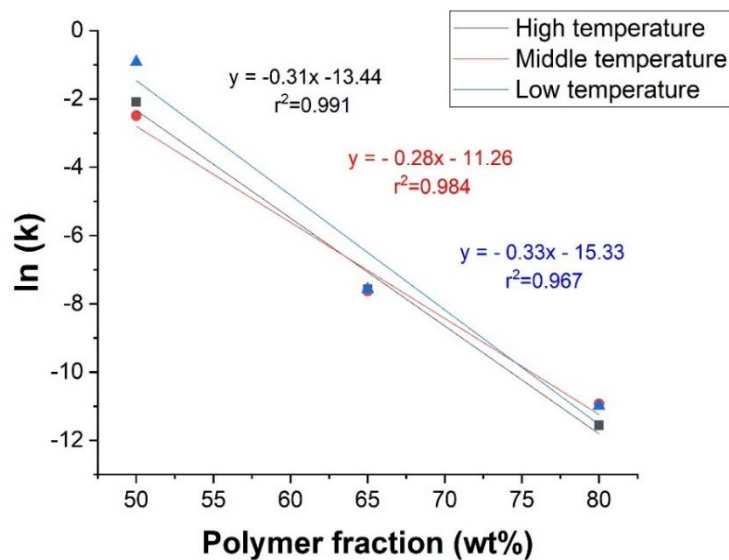


Figure 5.4. Logarithm plot of the crystallisation rate constant (k) as a function of polymer content. High temperature corresponds to 170°C for all drug loadings, middle temperature corresponds to 150°C for the 20 wt% and 30 wt% drug loading systems and 155°C for the 50 wt% system. Low temperature corresponds to 130°C for the 20 wt% system, 140°C for 35 wt% system and 145°C for the 50 wt% system.

Although ToF-SIMS is not a standard technique to differentiate between the amorphous and crystalline states, based on the extent of phase-separation and morphology of the different domains, it is possible to distinguish between the amorphous matrix that is relatively homogeneous and mostly polymer-dominated and the drug-rich crystalline regions on the ASD surface. Similarly, residual crystallinity resultant from processing below  $T_s$  is easily distinguished from the crystalline drug-rich clusters formed upon ageing. Figures 5.5.a and 5.5.b exhibit the ToF-SIMS images for the 35wt% drug loading system which was purposely extruded across a wider range of processing temperatures from 135°C to 170°C to illustrate this distinction. At both temperatures below  $T_s$  (i.e., at 135°C and 140°C) large, rounded drug particulates are observed and these remain unchanged upon ageing. Such particles were not observed above  $T_s$ . On the contrary, the newly phase-separated drug-rich domains are present across all temperatures, display a thin appearance and grow substantially overtime.

Optical microscopy (OM) provides further confidence in the ToF-SIMS distinction between the amorphous matrix, residual crystallinity and the drug-rich clusters formed upon ageing. Figure 5.5.d and 5.5.e illustrate the morphological differences between residual drug crystals which appear darker in the bright field due to their three-dimensional depth, blocking out more light, and the circular, thin and highly reflective crystallites formed upon ageing. Further OM images for the remaining compositions are shown in Appendix D.

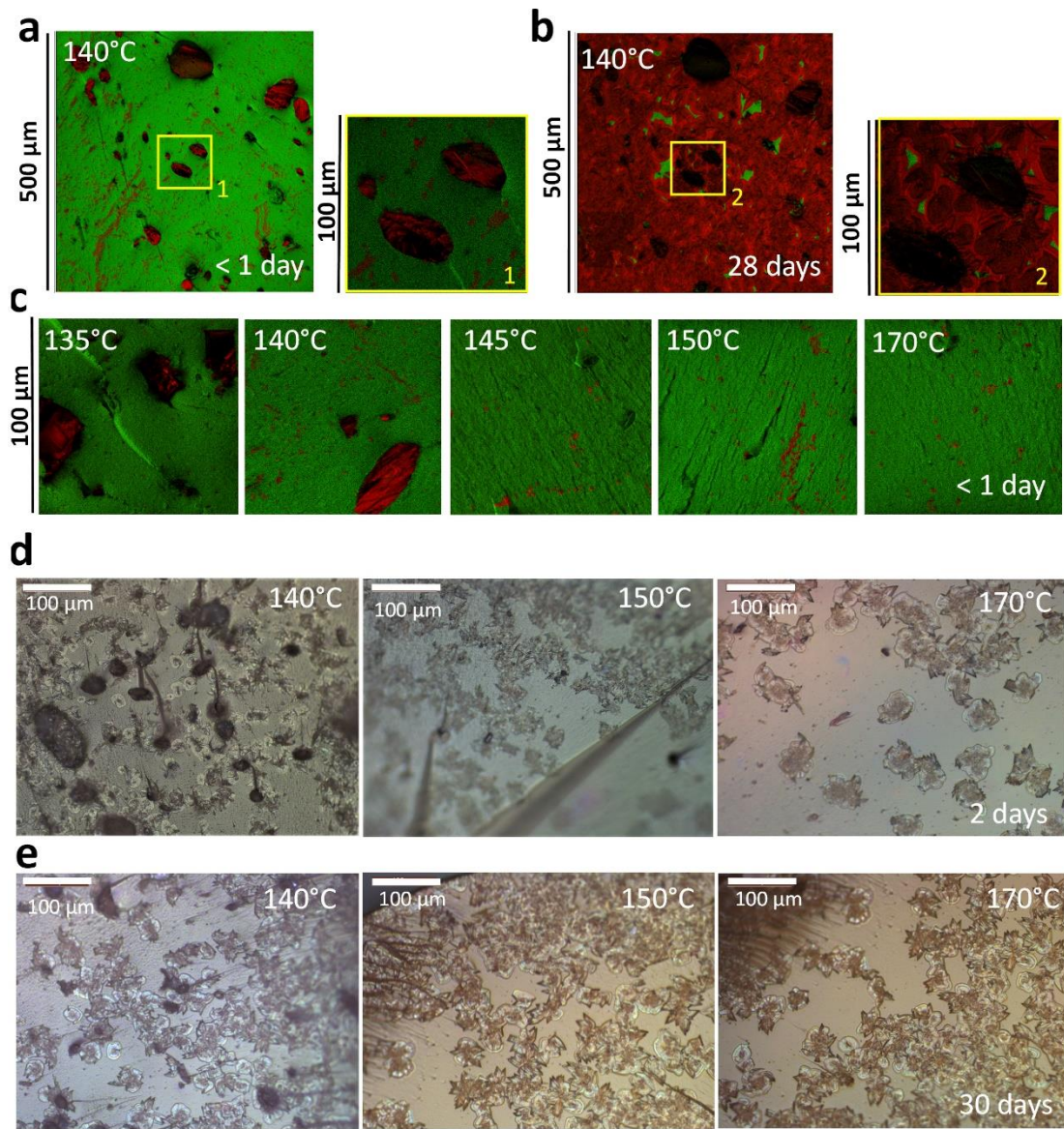


Figure 5.5. Impact of processing temperature on the ASD surface of the 35 wt% drug loading system. a), b) and c) ToF SIMS images showing residual crystallinity at 135°C and 140°C and newly formed surface crystals at <1 and 28 days of ageing. d) and e) Optical microscopy images taken on the cross-Sectional surface displaying the presence of residual crystallinity at 140°C and circular crystallites across all processing temperatures at 2 and 30 days of ageing, respectively.

### 5.3.1.2 Crystal morphology

Crystallised PCM on the surface of the ASDs shows a variety of crystal morphologies, ranging from coarse circular agglomerates, plates and circular terraced growth forms as displayed in Figure 5.6. The larger structures that resemble agglomerates of crystallites are formed in regions of topographic irregularity/roughness and display an outward-lateral growth with smooth growth fronts (Figures 5.6.a & b). This morphology is mostly observed at 50wt% drug loading. Optical microscopy analysis supports these findings (Figure B.3, appendix B). The plate-like forms (Figures 5.6.c & d) display an outward-lateral growth and are present at all drug loadings. Interestingly, the terraced growth forms (Figures 5.6.d, e and f) present multiple growth “rings” radiating from a central growth point that resemble a crater-like structure and displays an apparent inward-lateral growth direction.

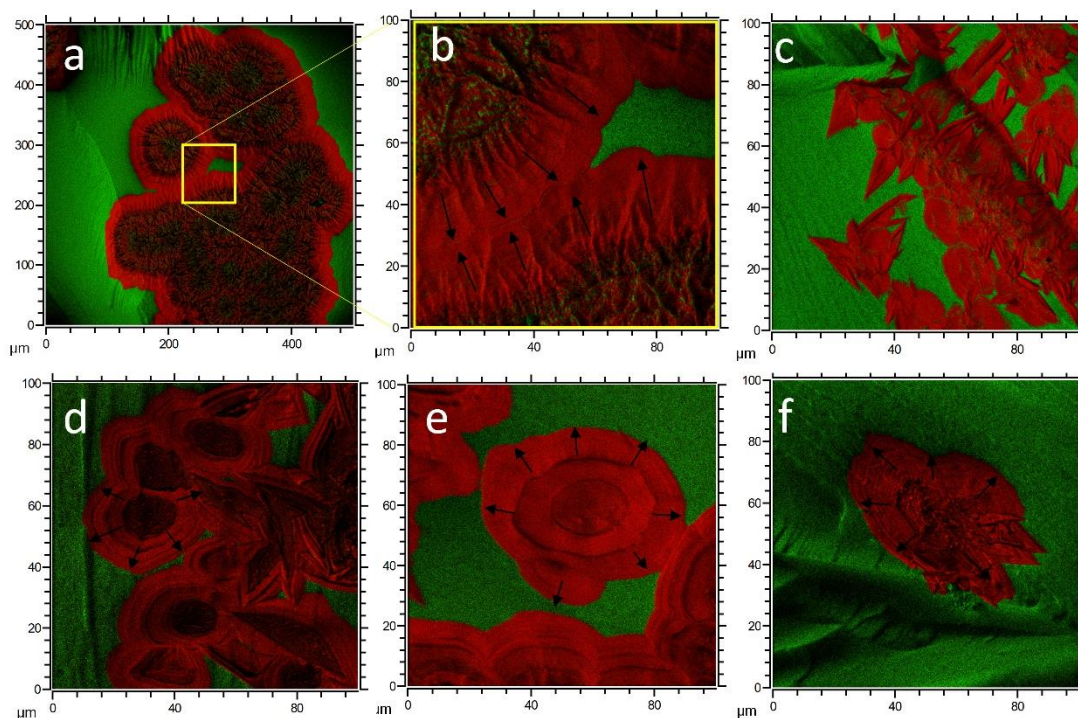


Figure 5.6. Crystal morphology captured by ToF-SIMS. a) and b) Agglomerates of crystallites, c) plate-like crystallites, d) and e) spiral-growth forms growing laterally and towards the bulk, f) spiral-growth forms growing laterally and upwards. The black arrows denote the lateral growth direction.

Formation of craters with terraced forms was previously described for paracetamol crystals emerging on the surface of single component glasses by L. Shi and C. Sun.<sup>271</sup> The authors reported that the crater-like structures are formed as a result of subsurface crystallisation. In particular, the growth of a subsurface crystal, would create an inward tensile stress at the crystal growth front as molecules are rearranged into a denser crystalline phase. The build-up of such stress will either form cracks or draw more mobile surface layers inward. The latter would lead to craters as observed here. This mechanism is illustrated in Figure 5.7. below.

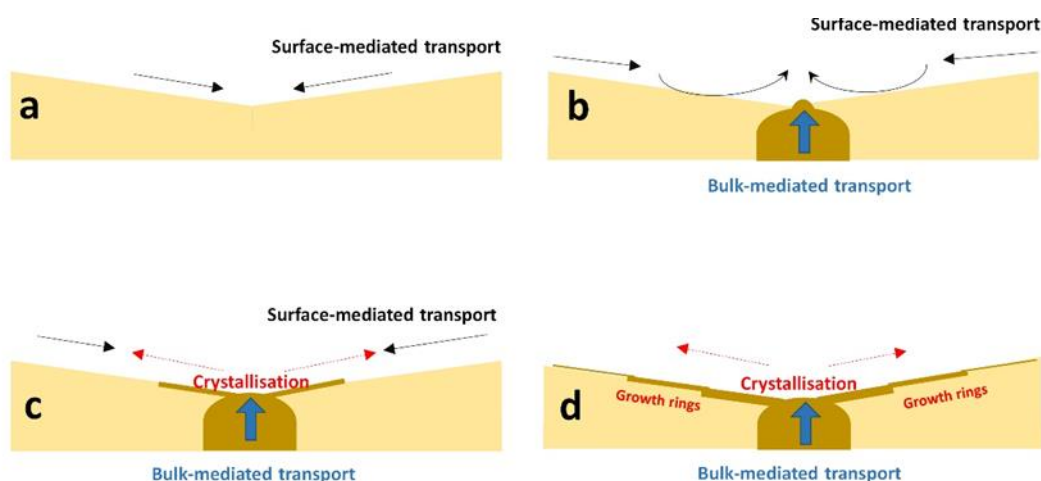


Figure 5.7. Growth schematics of the terraced forms.

The SEM images of the 50 wt% drug loading system acquired at 30 days of storage show significant topographical evidence to support formation of circular terraced growth forms with depressed growth centres (Figure 5.8), as well as plate-like crystallites as evidenced by ToF-SIMS. SEM images for the remaining compositions are shown in Appendix C.

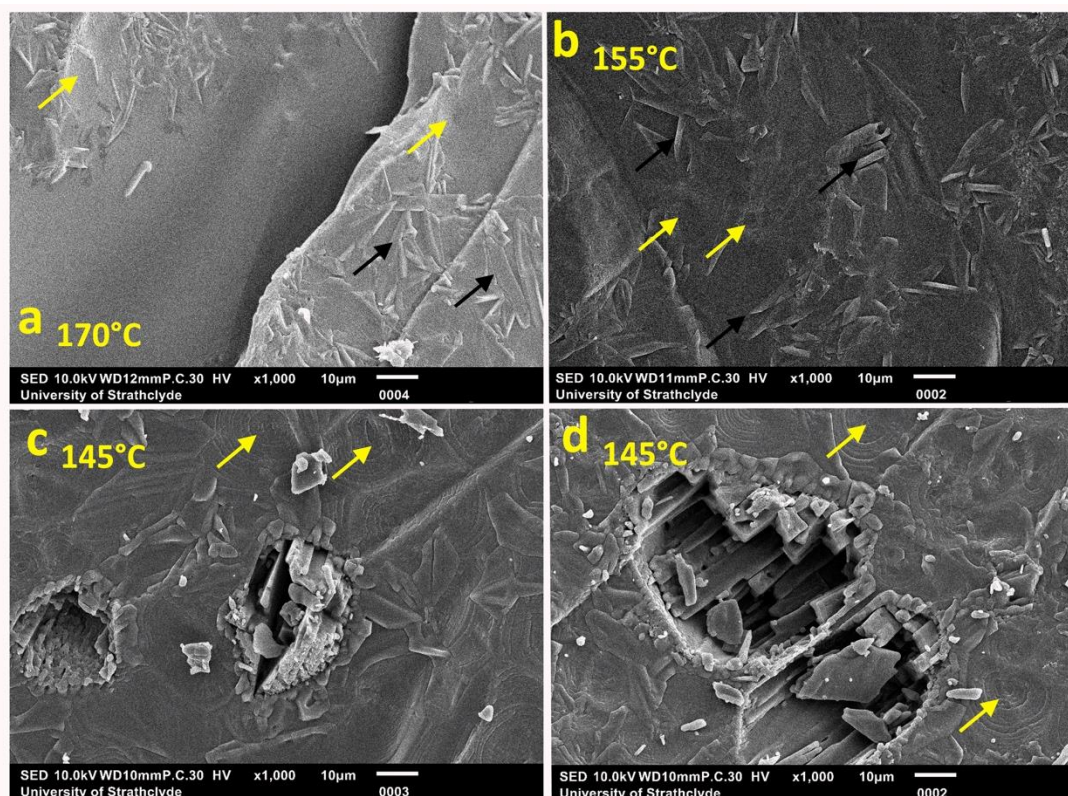


Figure 5.8. SEM images of the 50 wt% system processed at 145°C after 30 days of storage. The yellow arrows point to the circular terraced growth forms and black one to the plate-like crystallites.

It is interesting to note that drug molecular mobility is sufficiently high to enable its diffusion through the polymer matrix and its molecular rearrangement to form these variate crystal habits on the ASDs' surface. This is particularly remarkable as Affinisol is a highly viscous HPMC polymer specially designed to hinder drug crystallisation.<sup>272</sup> Different mechanisms of material transport are possible depending on whether molecules reach the crystals through the bulk/sub-surface or across the surface and whether they join the bottom of the crystal, the side or top of the crystal. If bulk transport sustains the growth of surface crystals on PCM-HPMC ASDs, the growth should not stop after the surface is covered by the propagating surface crystal layer as there is still amorphous material underneath. From a qualitative comparison it is evident that the morphology of any given fully drug-covered Section continues to change overtime, but bulk crystallisation is detected at later time-points (see the bulk crystallinity Section). This is most likely the main material transport mechanism for

the terraced growth forms displaying and inward-lateral growth. For the remaining crystallite forms, the most plausible scenario for the upward-lateral growth of surface crystals appears to be that crystallising molecules originate from the ASD surface, are drawn to the crystal by its lower chemical potential, and deposit at growth sites either at or above the glass surface. This would create a crystalline shell around the ASDs that would propagate towards the bulk at later stages. Further studies via ToF-SIMS depth profiling could elucidate the exact mechanism since if bulk-transport sustains the growth of surface crystals, there would be drug-depleted regions in the sub-surface layers creating a concentration gradient towards the bulk/sample core. Additionally, atomic force microscopy (AFM) could also provide further information regarding the height/depth of the surface crystals and aid the amorphous-crystalline differentiation of initial drug-rich clusters based on the peak energy dissipation approach as described by.

### **5.3.2 Bulk crystallinity**

#### **5.3.2.1 DSC crystallinity quantification**

The ASD bulk crystallisation (i.e., overall crystallisation) results are shown in Figure 5.9. The 50 wt% drug loading system was excluded from the DSC crystallinity quantification experiments because it displayed temperature-induced recrystallisation exotherms during the DSC scan at  $\sim 120^{\circ}\text{C}$  to PCM form II with subsequent melting at  $160^{\circ}\text{C}$ . This prevented accurate quantification of the melting enthalpy resultant from crystallisation due to physical instability upon ageing. With exception of 10 wt% drug loading system, that remained stable, melting endothermic peaks suggesting presence of crystalline API were observed for all remaining compositions from the first analysed time-point. At 20wt% drug loading, the total sample crystallinity remained below 1.2% for all processing temperatures even after 150 days of ageing, whilst at 35 wt% drug loading crystallinity values of  $5.5 \pm 2.38 \%$  were observed at  $150^{\circ}\text{C}$  and  $5.1 \pm 1.4 \%$  at  $170^{\circ}\text{C}$  for the same time period. For the system processed below  $T_s$ , residual crystallinity values were of  $11.1 \pm 1.9 \%$  were seen immediately after extrusion with further increase to  $16.2 \pm 1.66 \%$  at 150 days of storage.

Nonetheless, care should be taken when interpreting weak endothermic peaks as the ones seen for the 20 wt% drug-loading system (0.25 to 0.44 J/g), as it is difficult to attribute significance threshold values. On the other hand, the relatively slow heating rate (20°C/min) employed could have allowed for temperature-induced mixing and solubilisation of small drug-rich crystallites, such as those detected on the surface of the ASDs. It should be noted that both the classic Avrami model and its modified version provided a terrible fit to the DSC crystallisation data. Therefore, crystallisation kinetic information could not be extracted from the DSC experiments.

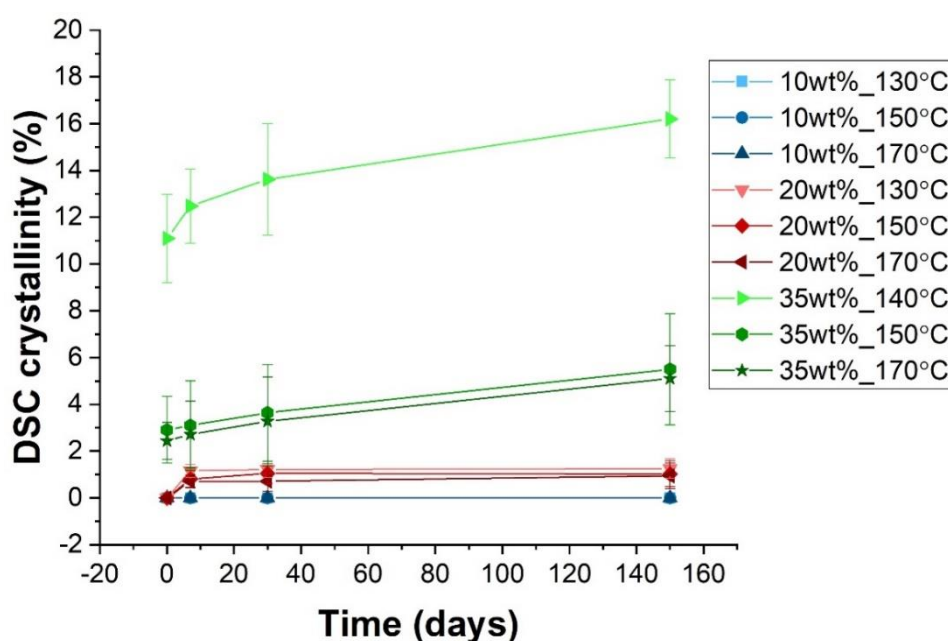


Figure 5.9. DSC crystallinity quantification at 0, 7, 30 and 150 days of storage. The error bar denotes the standard deviation for different pellets (n=3).

### 5.3.2.2 XRD crystallinity

XRD, which is considered the gold-standard technique for crystallinity detection, enabled detection of crystallinity at later time-points when compared to DSC and ToF-SIMS. Diffraction peaks were found from the first analysis time-point for processing temperatures below  $T_s$  at 35 wt% and 50 wt% drug-loading, confirming residual crystallinity (Figure 5.10). However, at processing temperature above  $T_s$ , XRD

denoted the presence of crystallinity only after 150 days of storage for the 35 wt% drug loading system and after 7 days for the 50 wt% system. For the 10 wt% and 20 wt% drug loading systems, a characteristic amorphous halo was seen until the end of the study for all processing temperatures. These results are in good agreement with the DSC crystallinity results, as well as with literature XRD crystallinity detection limits of ~1-5%.<sup>126</sup>

Comparing ToF-SIMS, DSC and XRD crystallinity these results indicate that crystallisation is much faster at the surface than in the bulk of PCM-HPMC ASDs. Overall, based on the surface drug crystallisation behaviour these results suggest the following stability ranking: 10 wt% >> 20 wt% > 35 wt% > 50 wt%. The 10 wt% system remained stable and did not present any signs of phase separation or crystallisation upon ageing. This system presented a homogenous drug and polymer distribution until the end of the study. Although the 20 wt% system presented significant surface drug phase-separation/crystallisation upon ageing, it has longer induction times and slower crystallisation rates when compared to the two supersaturated systems. Thus, the likely solubility limit for this system is between 10 and 20 wt% drug loading as discussed in Chapter 3. The stability grouping of the various drug loadings is in good agreement with the drug-polymer solubility data obtained from the low-frequency Raman approach and shows that the thermodynamic driving force for crystallisation is a key factor dictating ASD physical stability even at the ASD surfaces where molecular mobility is higher.

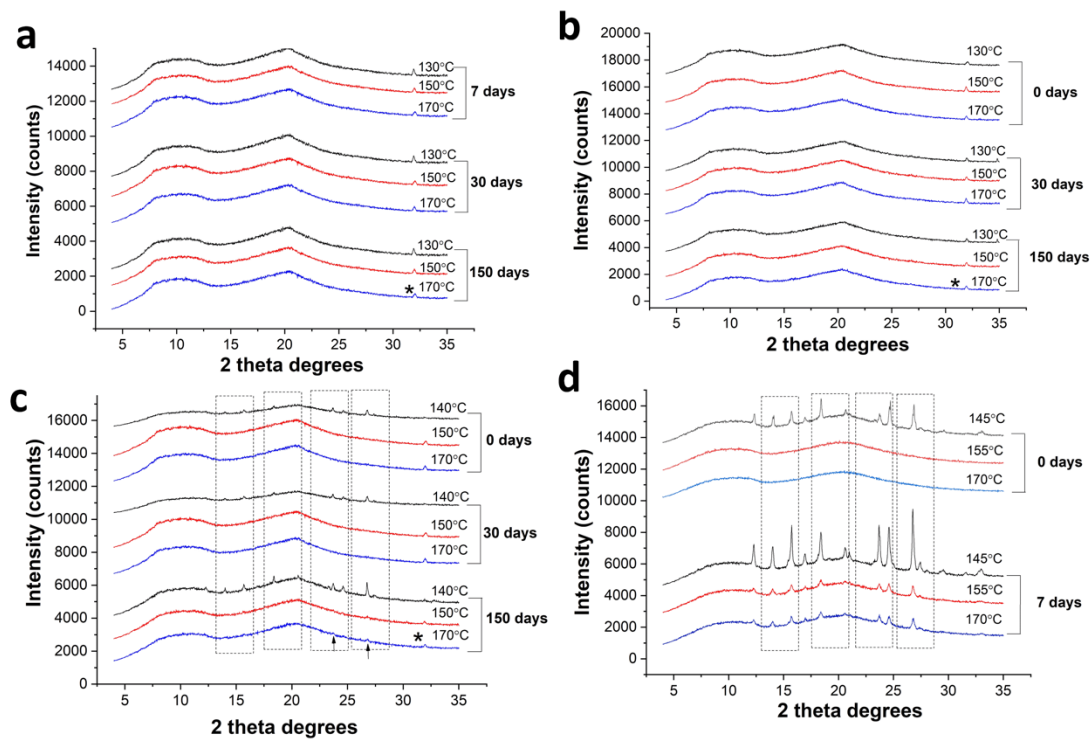


Figure 5.10. XRPD analysis results at different time points for a) 10wt%, b) 20wt%, c) 35wt% and d) 50wt% drug loading system.

## 5.4. Conclusions

This Chapter aimed to study the surface stability of ASDs produced under different saturation conditions in order to further assess the limits and overall stability implications of the drug-polymer solubility phase-diagram constructed in the previous Chapters. This was achieved by means of ToF-SIMS chemical mapping and subsequent image analysis over a stability study of 150 days. ToF-SIMS analysis enabled extraction of surface-specific chemical information that permitted to monitor and quantify the local distribution evolution of the drug and polymer at the ASD surfaces with micron-level resolution. The 10wt% system remained stable and did not present any drug-polymer distribution heterogeneities congruent with phase separation or crystallisation. All remaining compositions showed significant surface drug enrichment demonstrating intense phase-separation and crystallisation upon ageing. The 20 wt% system displayed higher induction times and lower surface coverage/crystallisation rates when compared to the supersaturated systems at 35 wt% and 50 wt% drug loadings. Despite significant surface crystallisation at the critical concentration (20 wt% drug loading), these results are in good agreement with the drug-polymer solubility data obtained from the low-frequency Raman approach, as well as the remaining thermodynamic approaches used in Chapter 3. These findings reiterate the importance of the solubility of the drug in the polymer matrix as one of the main thermodynamic driving forces for crystallisation and show that this is still valid at the ASD surface where molecular mobility is deemed higher. Nonetheless, according to the surface ASD stability the exact stability/metastability threshold limit is likely to be slightly below 20 wt% drug loading. Furthermore, standard techniques for as DSC and XRD analysis, it is evident that crystallisation is faster at the surface than in the bulk of PCM-HPMC ASDs.

Overall, this Chapter demonstrated the importance of surface-mediated phase separation and crystallisation, as well as the use of the surface drug-coverage quantification via image analysis of the ToF-SIMS chemical maps as an important strategy for early-stage stability assessment of drug-polymer ASD systems.

# **Chapter 6**

## **Application of the Low-frequency Raman Solubility Method to a Commercially Relevant Model Compound**

### **6.1 Introduction**

In Chapter 2, a new method was developed for determining the API saturated solubility in a polymer matrix. This method combines low-frequency Raman spectroscopy as PAT tool and HME processing, as a heating and mixing platform. In this Chapter, this approach will be applied to a model system of commercial and therapeutic relevance to further validate and test the aforementioned use. Additionally, selected ion flow tube mass spectroscopy (SIFT-MS) will be used as a new technique to assess the volatile organic components (VOCs) emitted during extrusion to inform potential degradation

pathways as a result of processing conditions and thus, aid the optimisation of the HME processing window.

SIFT-MS applies highly controlled soft chemical ionisation coupled with mass spectrometric detection to rapidly detect and quantify VOCs to part-per-trillion concentrations by volume (pptV).<sup>273</sup> It does not require any pre-concentration, separation or drying steps prior to analysis, thus it provides an alternative to costly and time consuming gold-standard gas chromatography - mass spectrometry (GC-MS) analysis with up to fourfold higher sample throughput.<sup>273</sup> SIFT-MS has been used across a wide range of disciplines and areas where direct VOC analysis is required, including the food industry, environmental VOC analysis and exhaled breath analysis for the diagnosis of hepatic encephalopathy, end-stage renal failure and dialysis efficiency assessment, amongst others.<sup>274–277</sup> In brief, SIFT-MS allows chemical reactions between sample trace gas molecules and precursor reagent ions ( $\text{H}_3\text{O}^+$ ,  $\text{NO}^+$  and  $\text{O}_2^+$  in this study) to occur in a helium or nitrogen carrier stream flow reactor and originate product ions. These are subsequently filtered and injected into a flow tube for downstream detection. Due to the potential of direct real-time VOC analysis, SIFT-MS was thus investigated as a new PAT tool to assess potential volatile organic compounds released during extrusion.

## **6.2. Materials and methods**

### **6.2.1 Materials**

The model compound (i.e., compound Z) micronised grade was provided by AstraZeneca, (Macclesfield, UK). Soluplus was kindly donated by BASF, (Ludwigshafen, Germany). All materials were used as obtained, without further purification.

## **6.2.2 Methods**

### **6.2.2.1 Blending**

Binary mixtures of crystalline drug and polymer were prepared at 2.5 wt % mass ratio intervals from 7.5 wt% to 30 wt% drug load using a bin blender (AgiBlend MB015AB Blender, Pharmatech, Warwickshire, UK) with a 1L vessel at 68% bin volume fill. Additional ratios of 40 and 50 wt% drug loadings were prepared in the same manner. Each formulation was blended for 10 minutes at a set blend speed and agitation of 25 rpm and 100 rpm, respectively. Prior to blending, materials were sieved through a 710 µm mesh to remove powder agglomerates.

### **6.2.2.2 Hot melt extrusion (HME)**

HME was performed with an 11 mm co-rotating twin-screw extruder (Process 11, 40: 3/4 L/D Thermo Fisher Scientific, Karlsruhe, Germany) in combination with a loss-in-weight gravimetric feeder (Brabender Gravimetric feeder DDW-MD-MT, Brabender Technologie, Duisburg, Germany). Materials were fed at a constant feed rate of 0.1 kg/h. Barrel section 1 is not heated, whilst sections 2 and 3 were run at set-point values of 50°C and 100°C, respectively, to prevent blockage of the feeding zone. Barrel sections 4 to 8 and the die zone were operated at the same set-point temperature values, which varied according to the drug-polymer composition as reported in Table 6.1. Variable screw speeds were employed as per Table 6.1. A round 1.8mm diameter die was used. Collected extrudates were allowed to cool to ambient temperature by natural convection prior to further analysis.

<b>Drug loading (wt %)</b>	<b>Process set temperature (°C)<sup>a</sup></b>	<b>Screw speed (rpm)</b>	<b>Feed rate (kg/hr)</b>
0 <sup>b</sup>	200, 190, 180, 170, 160, 150	100, 300, 500	0.100
7.5	160, 150, 140, 130	100	0.100
10	180, 170, 160, 150, 140	100, 300 500	0.100
12.5	180, 170, 160, 150, 140, 130	100	0.100
15	180, 170, 160, 150, 140, 130	100, 300, 500	0.100
17.5	180, 170, 160, 150, 140	100	0.100
20	180, 170, 160, 150, 140	100	0.100
22.5	190, 180, 180, 160	100	0.100
25	190, 180, 180, 160	100	0.100
27.5	190, 180, 180, 160	100	0.100
30	190, 180, 180, 160	100	0.100
40	210, 190, 180, 170	100	0.100
50	210, 190, 180, 170, 160	100	0.100

<sup>a</sup> Refers to set-point temperature values of barrel sections 4 to 8 and the die zone.

<sup>b</sup> Pure polymer extrusion trials

Table 6.1. Hot melt extrusion operating conditions.

### **6.2.2.3 API-polymer solubility determination**

The solubility of the API in the polymer matrix was determined with the low-frequency Raman methodology outlined in Chapter 2, Section 2.2.2.3 based on the amorphous-crystalline switch of the API. A principal component analysis (PCA) method based on the covariance matrix was applied to the low frequency region (-8 to 200cm<sup>-1</sup>) to interpret spectral variations using Origin Pro software (Origin Pro 2018b, OriginLab Corporation, USA). Given its strong response to varying processing conditions, the spectral region corresponding to the Rayleigh scattering phenomena (with peak maxima at 0cm<sup>-1</sup>) was included in the multivariate analysis to improve the amorphous-crystalline differentiation.

### **6.2.2.4 Differential Scanning Calorimetry (DSC)**

DSC analysis was performed from 0°C to 250°C at a heating rate of 20°C/min according to the procedure described in Section 2.2.2.6.

### **6.2.2.5 X-ray diffraction (XRD)**

XRD data was collected as described in Section 2.2.2.7.

### **6.2.2.6 Selected Ion Flow Tube - Mass Spectrometry (SIFT-MS)**

Automated real-time VOC analysis was carried out with a Voice200ultra (Syft Technologies, Christchurch, New Zealand) provided by Anatune. The reagent ions used for analysis were H<sub>3</sub>O<sup>+</sup>, NO<sup>+</sup> and O<sub>2</sub><sup>+</sup>, and the carrier gas was nitrogen. Analysis was run in full mass spec mode (15-300 m/z) over 10min at steady-state HME conditions (judged based on the residence time for empty barrel conditions, torque and pressure data). Sampling was done directly from the HME vent port with an added nitrogen dilution line to avoid overconsumption of the reagents (see Figure 6.1). The sample inlet temperature on the Voice200ultra was set to 150°C to maintain a vapour phase of the sampled aliquot. Data was plotted as an overlay of all product ions after removing the peaks corresponding to the reagent ions at 19m/z (H<sub>3</sub>O<sup>+</sup>), 37m/z

( $\text{H}_3\text{O}^+(\text{H}_2\text{O})$ ), 55m/z ( $\text{H}_3\text{O}^+(\text{H}_2\text{O})_2$ ), 30m/z ( $\text{NO}^+$ ) and 32m/z ( $\text{O}_2^+$ ). Before each experiment, the equipment is calibrated by using standard analytes (tetrafluoro benzene, benzene, ethylene, isobutene, octafluorotoluene, xylene, perfluorobenzene and toluene) of known concentrations (2ppm).

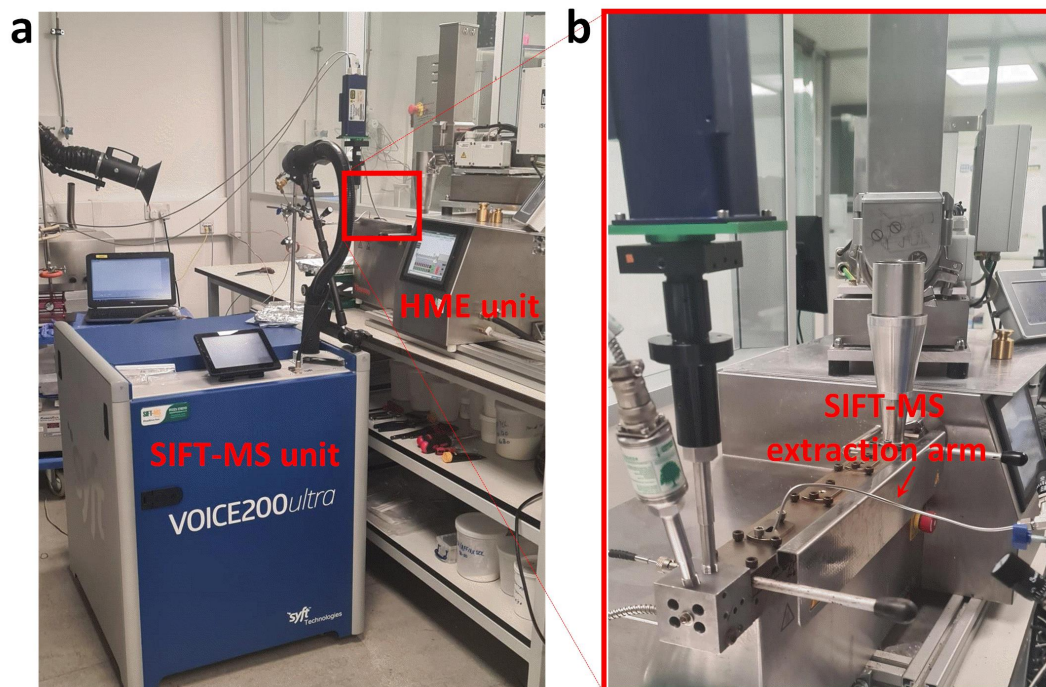


Figure 6.1. a) SIFT-MS set-up for online VOC analysis. b) sampling position.

### 6.2.2.7 Time-resolved X-ray Diffraction

Time-resolved X-ray diffraction experiments were carried out on a small angle X-ray scattering device (Xenocs Xeuss 2.0) equipped with a Cu source ( $\lambda=1.5406 \text{ \AA}$ ) operating at 50kV and 40mA and an area detector. To allow these measurements, the device was modified by shortening the sample to detector distance to 170mm, which provided an accessible two theta range of about 5-40°. 2D X-ray patterns were collected with a Pilatus 100 K area detector (Dectris, Baden-Daetwill, Switzerland). A small section of the extrudate filament was placed inside a sample holder cell in front of the area detector (see Figure 6.2) and 0.2 ml of water was added at  $t = 0 \text{ h}$ ,  $t = 1 \text{ h}$ ,  $t = 2 \text{ h}$ ,  $t = 3 \text{ h}$  or  $t = 4 \text{ h}$  with a 1 ml syringe. Data was continuously acquired for 60 min over a maximum of 8 hours using an exposure time of 60 s. The final X-ray

diffractograms display the 1h average after subtracting the sample holder + water background (acquired for 1h)

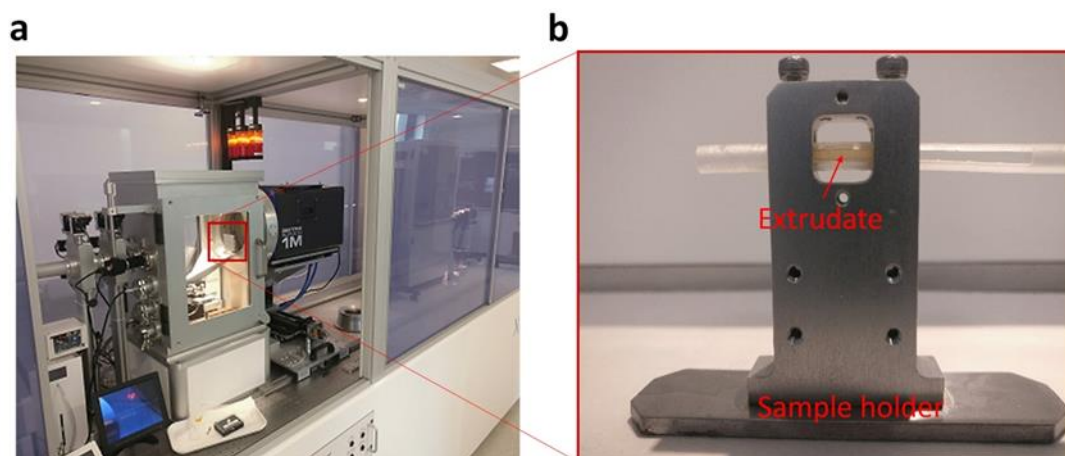


Figure 6.2. Time-resolved X-ray diffraction set-up. a) Device overview displaying the sampling arm and the short sample-to-detector distance. b) Sample holder unit.

## 6.3 Results and discussion

### 6.3.1 Low-frequency Raman solubility determination

The first extrusion investigation aimed to test the applicability of the solubility methodology developed in Chapter 2 to the new model drug system. For this purpose the initial extrusion experiments were performed at 20 wt% drug loading from 180°C to 140°C. This concentration corresponds to an excess of ~5 wt% above the company's targeted ASD drug loading and could provide an excess of crystalline material to enable detection of residual crystallinity and guide the following extrusion experiments. Figure 6.3 displays the low-frequency Raman spectra as a function of the extrusion temperature. The solid dispersions processed at 180°C displayed a broad amorphous shoulder with peak maxima in the Stokes region at 11 cm<sup>-1</sup> and a sharp peak in the Rayleigh region at 0 cm<sup>-1</sup>. Upon temperature decrease to lower temperatures, the onset of crystallinity was associated with a peak intensity decrease at 11 cm<sup>-1</sup> and an intensity increase at 0 cm<sup>-1</sup>. The plot of the peak intensity variation at 0 cm<sup>-1</sup> and 11 cm<sup>-1</sup> shown in Figure 6.3.c. displays an inflection point at temperatures corresponding to the amorphous-crystalline transition. This behaviour was further corroborated by the principal component analysis displayed in Figure 6.3.d. It is possible to observe that this transition was described by a change in the principal component 1 (PC1) scores upon API solubilisation. For this composition, this change occurred from 180°C to 170°C with an estimated saturated solubility temperature (T<sub>s</sub>) of 175°C.

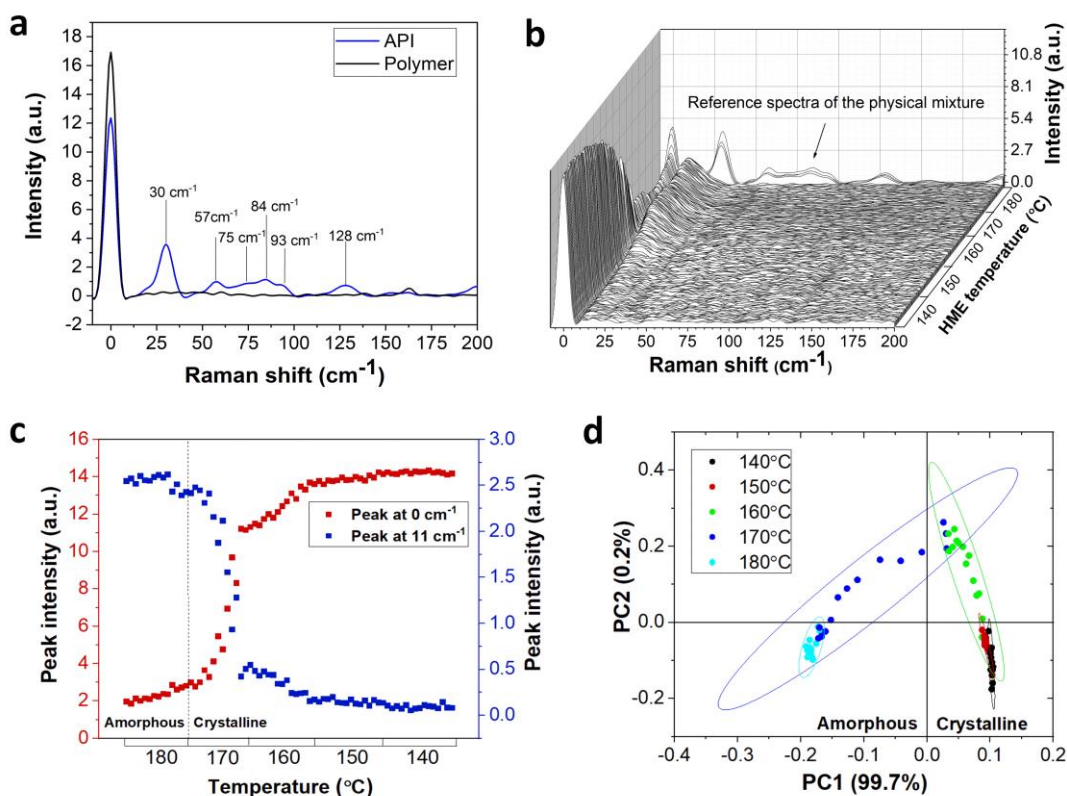


Figure 6.3. Low-frequency Raman results at 20 wt% drug loading. a) Individual component reference spectra. b) Spectra obtained upon extrusion from 180°C to 140°C. c) Rayleigh and Stokes peak intensity plot. d) Principal component analysis score plot.

Using the same approach, the amorphous and crystalline coordinates, as well as the saturated solubility temperature were determined for all API-polymer compositions (Appendix E 1 to E 5). However, at 7.5 wt% and 10 wt% drug loadings, there were no spectral changes indicative of undissolved API at any of the extrusion temperatures (Figure 6.4). Following the rationale developed in Chapter 2, this suggests a potential solid solution capacity of 10 wt%, which was further explored in Section 6.3.3. Furthermore, at 40 wt% and 50 wt% drug loadings (Figure 6.5), the crystalline suspensions (i.e., residual crystallinity) also displayed a peak at  $28\text{ cm}^{-1}$  that corresponds to the major crystalline lattice vibration mode of the as received crystalline API (Figure 6.3.a). In the presence of the polymer, this peak is shifted to lower frequencies (from  $30\text{ cm}^{-1}$  to  $28\text{ cm}^{-1}$ ). It should be noted that for this API, solubilisation within the polymer matrix originates a stronger response in the amorphous signal than in the crystalline one, at least at low residual crystallinity.

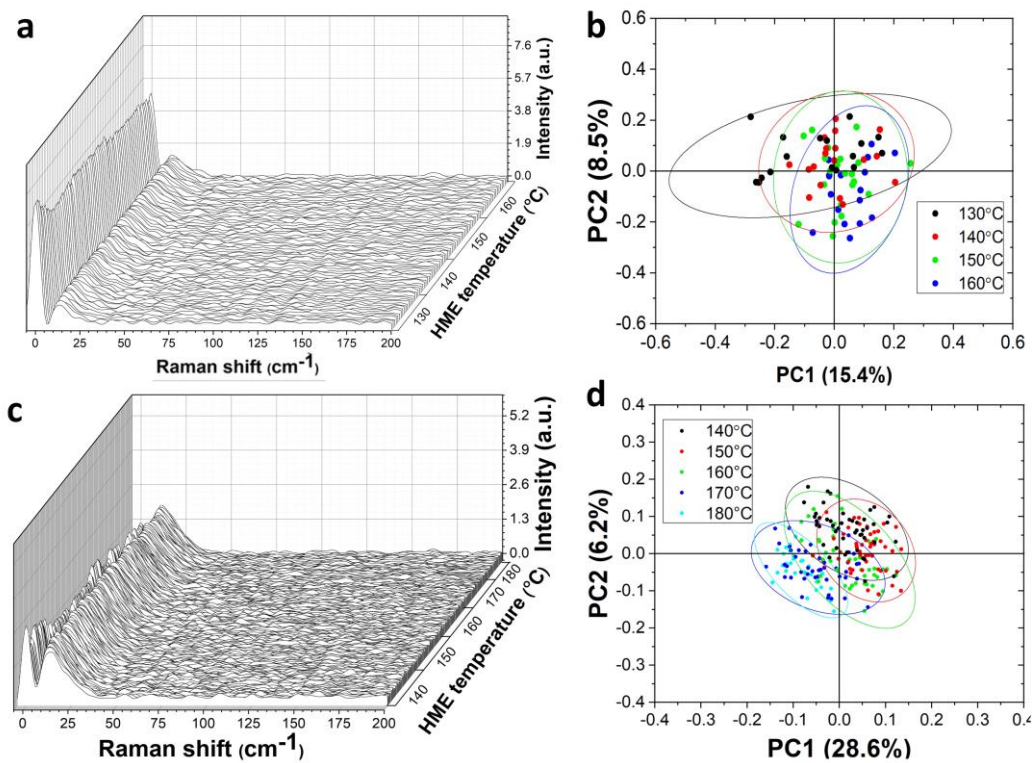


Figure 6.4. Low-frequency Raman results at a) 10 wt% drug loading and c) 7.5 wt% drug loadings with the respective principal component analysis score plot.

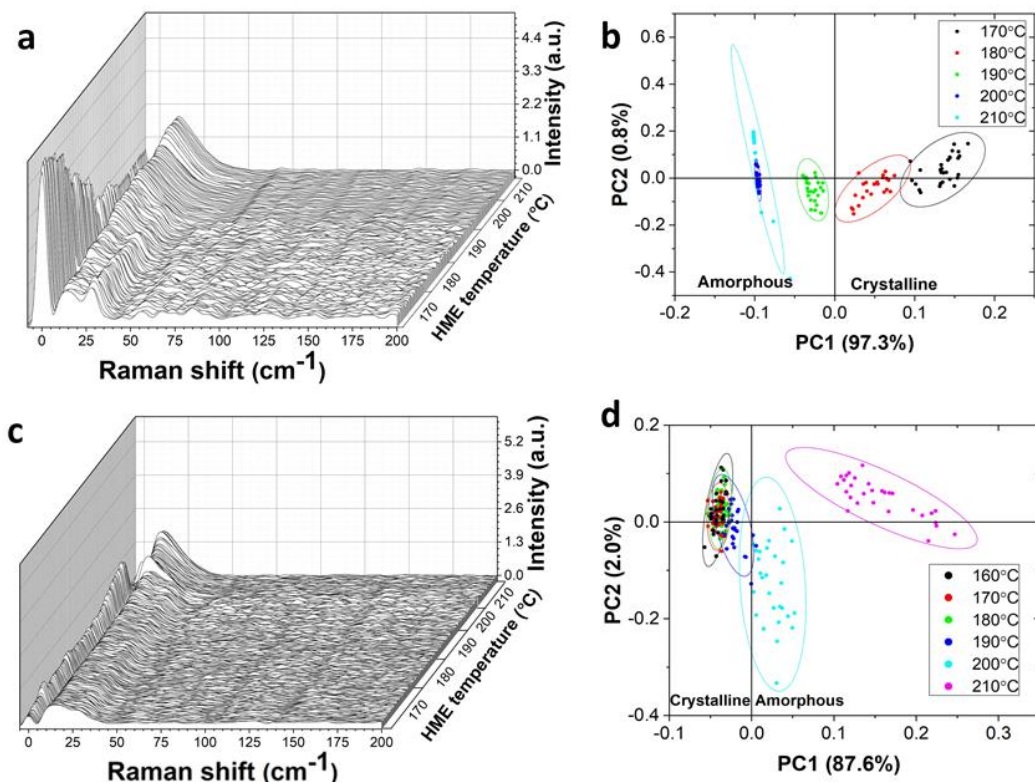


Figure 6.5. Low-frequency Raman results at a) 10 wt% drug loading and c) 7.5 wt% drug loadings with the respective principal component analysis score plot.

The Rayleigh peak at  $0\text{ cm}^{-1}$  describes the elastic process, where the energy absorbed by the electrons when excited by the incident beam is of the same wavelength as the emitted one, i.e., the electrons fall down to the ground state and there is no energy difference between the incident and the emitted lights. This peak is attributed to reflection from the sample surface or internal interfaces where refractive index mismatches occur. Under normal conditions, Rayleigh scattering should be effectively removed by the notch filter, which in this system has a sharp cut-off at approximately  $\pm 5\text{ cm}^{-1}$ . The appearance of residual intensity at  $0\text{ cm}^{-1}$  despite this filter suggests that enhanced backscattering or reflection from the sample is sufficiently strong to partially bypass the filter suppression, particularly in the presence of certain structural features. Importantly, any possibility of instrument-related artifacts can be excluded, as daily performance checks are carried out using standard reference materials such as sulfur and cyclohexene to verify both peak position and spectral accuracy prior to each analysis. These calibrations confirm the correct alignment of the laser line ( $0\text{ cm}^{-1}$ ) and the reliable performance of the low-frequency detection system. The presence of a prominent Rayleigh peak in this context is therefore attributed to increased backscattering caused by microstructural features within the sample. In particular, the appearance or intensification of this peak when residual crystallinity is present suggests that the ordered domains associated with crystalline API enhance scattering efficiency.

Thus, in order to validate the Rayleigh/Stokes peak intensity inflection approach and assure this is not an equipment artifact, the 15 wt% drug loading system extruded at  $140^{\circ}\text{C}$  was subjected to varying screw speeds (100 rpm, 200 rpm and 300 rpm) to promote the solubilisation of the residual crystalline material. This would be detected by an intensity decrease of peak at  $0\text{ cm}^{-1}$ . Figure 6.6 shows the impact of the screw speed on the API solubilisation dynamics. It indicates that increasing screw speed promotes the solubilisation of the API even at temperatures below  $T_s$  as a result of shear / mechanical energy increase, as observed by the intensity decrease of the peak at  $0\text{ cm}^{-1}$ . In addition, it also shows the Rayleigh/Stokes inflection approach is valid and describes both, the cryst-to-amorph and amorph-to-cryst dynamics. These results suggest the need to further investigate the influence of mechanical energy / shear in

the context of API-polymer solubility. This represents a potential gap in the LFR & HME solubility approach, as this was not further investigated.

278

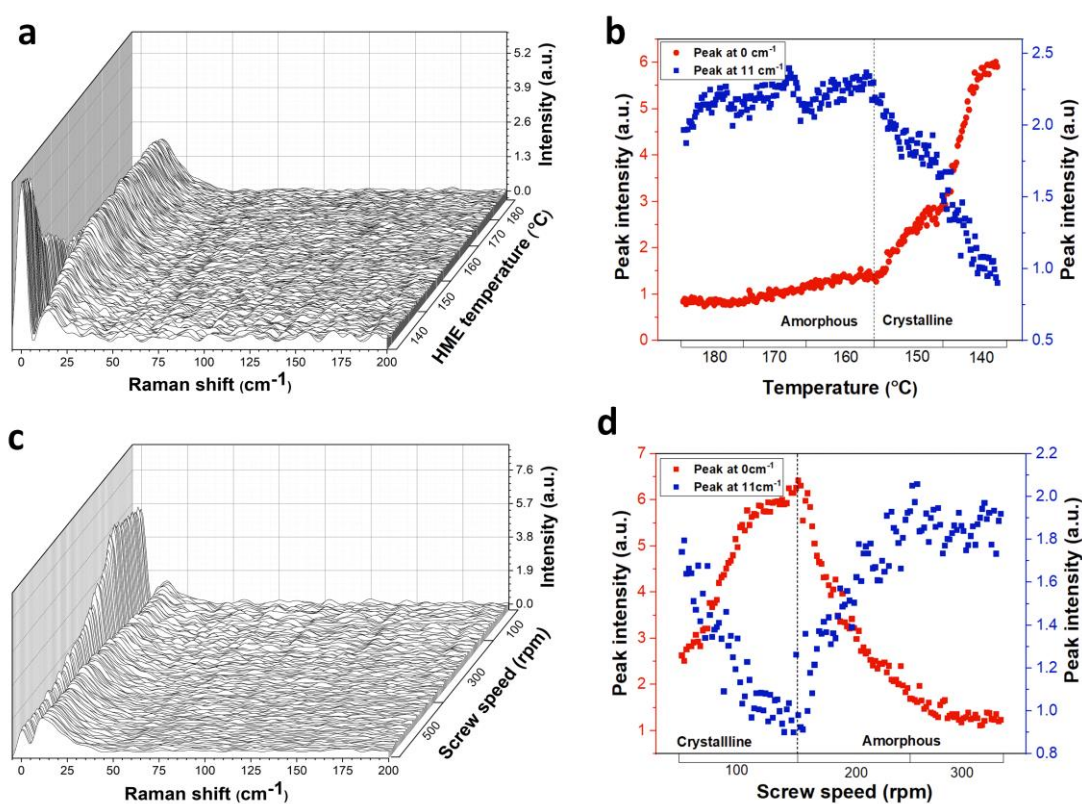


Figure 6.4. Low-frequency Raman spectra at 15 wt% drug loading. a) Spectra obtained upon extrusion from 180°C to 140°C with b) the respective Rayleigh and Stokes peak intensity plot. c) Spectra obtained upon extrusion at 100 rpm, 300 rpm and 500 rpm at 140°C with d) the respective Rayleigh /Stokes intensity plot.

Figure 6.7 displays the temperature-composition phase diagram depicting the API-polymer solubility phase equilibria with an error of at least  $\pm 5^\circ\text{C}$ , which results from the temperature steps taken between processing conditions ( $10^\circ\text{C}$  per step). It should be noted that the product melt temperature was monitored in the die section and the typical  $\pm$  variation was below  $2^\circ\text{C}$  compared to set-point values (Figure 6.7.a). Thus, no temperature correction was necessary. As a reference, the critical concentration ( $C_c$ ) corresponding to the maximum drug loading up to which no crystallinity was detected at any of the processing temperatures (i.e., the potential solid solution capacity) is identified by the black arrow. Additionally, the compositions that resulted

in yellow / brownish discoloration after HME processing at temperatures required for full API solubilisation are also identified (i.e., compositions  $> 25$  wt% drug loading). Although extrusion was possible up to 50 wt% drug loading, these findings restrict the operational HME processing window to compositions  $\leq 25$  wt% drug loading to avoid obvious signs of degradation as seen by color change and further down to  $\leq 10$  wt% drug loading to avoid physical instability issues.

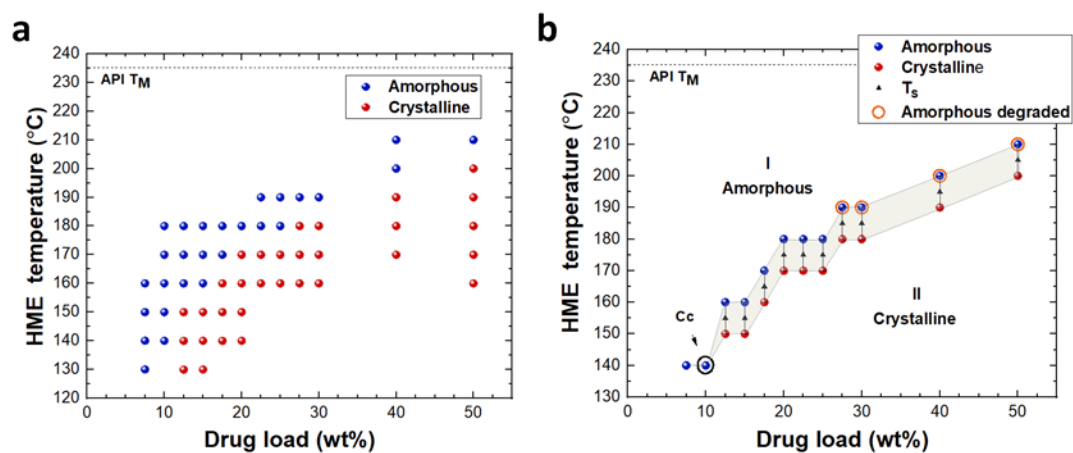


Figure 6.7. a) Experimental points and b) API-polymer solubility phase diagram. The black arrow denotes the critical concentration (C<sub>c</sub>) corresponding to the solid solution capacity

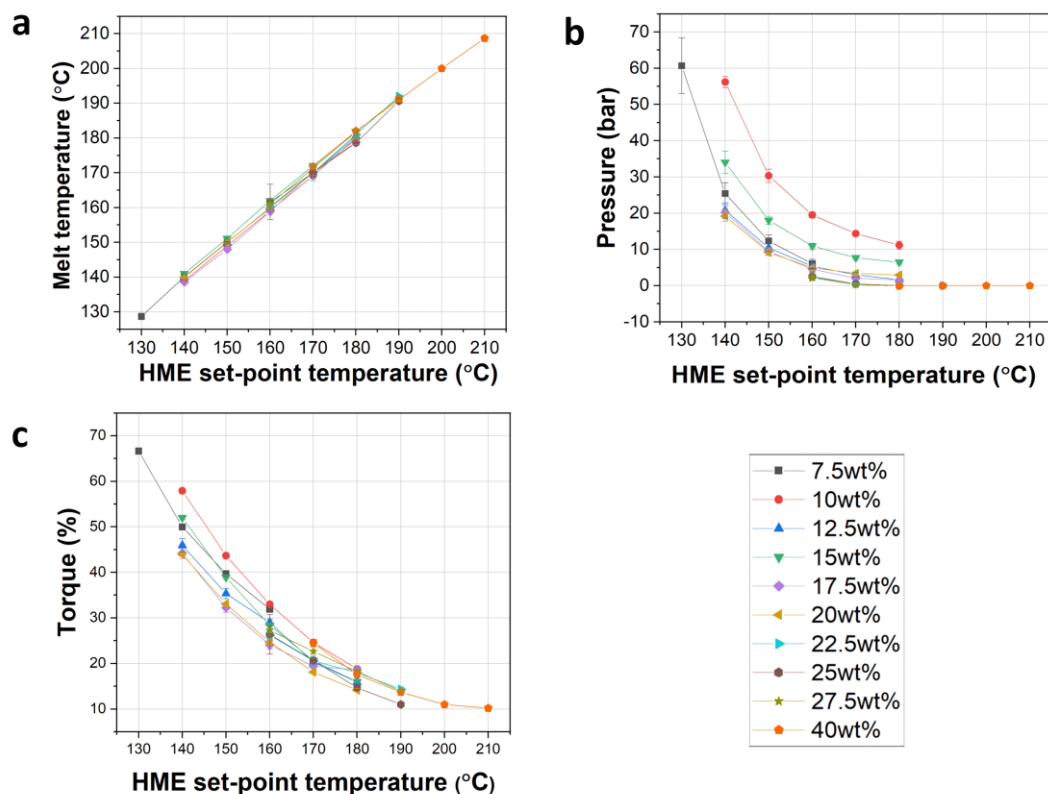


Figure 6.8. HME monitored parameters: a) product melt temperature, b) pressure and c) torque.

### 6.3.2 DSC and XRD analysis

DSC and XRPD analysis were performed to validate the low-frequency solubility data based on the API crystallinity detected immediately after HME processing. Results are shown in Appendix C. Overall, both DSC and XRD were in good agreement with the low-frequency Raman data, (i.e., melting endotherms and diffraction peaks were present at temperatures below  $T_s$ ). However, crystallinity as per XRD detection was only possible at concentrations  $\geq 15$  wt% drug loading due to detection limitations (see Appendix E 6 to E 8).

### 6.3.3 Accelerated stability study – rapid screening tool

To investigate the use of the critical concentration as an indicator of the maximum stable drug loading (i.e., solid solution capacity) the 10wt% and 20 wt% drug loadings were subjected to an accelerated stability study by exposing a section of the filament coil to water and assessing the recrystallisation behaviour via time-resolved X-ray diffraction. The results are shown in Figure 6.9. At 10 wt% drug loading the extrudates were fully dissolved in 5 ml of water (Figure 6.9.a). Conversely, at 20 wt% drug loading, the filaments became opaque with a whitish appearance suggesting potential recrystallisation. This was confirmed by XRD where four diffraction peaks were observed at  $2\theta$  values of  $24^\circ$ ,  $27^\circ$ ,  $32^\circ$  and  $34^\circ$  (Figure 6.9.b).

The time-resolved XRD experiment aimed to monitor the recrystallisation kinetics for the 20 wt% drug loading system. Nonetheless, this system remained amorphous even after 4 doses of 0.2 ml of water added at  $t=1$ ,  $t=2$ ,  $t=3$  and  $t=4$  up to 8h of analysis. Evidence of crystallisation was found for the 25 wt% drug loading system at  $t=6$ h after a single dose of water added at  $t=0$ . This was indicated by the emergence of two diffraction peaks at  $2\theta$  values of  $24^\circ$  and  $27^\circ$  (Figure 6.9.d). For both of these compositions, an additional broad shoulder associated to the amorphous phase is observed at  $2\theta$  values of  $19^\circ$  and its intensity was found to increase overtime. This is most likely due to water evaporation allowing more flux to directly hit the sample, however polymer-related artifacts resultant from increased chain mobility and mesophase formation are also possible.

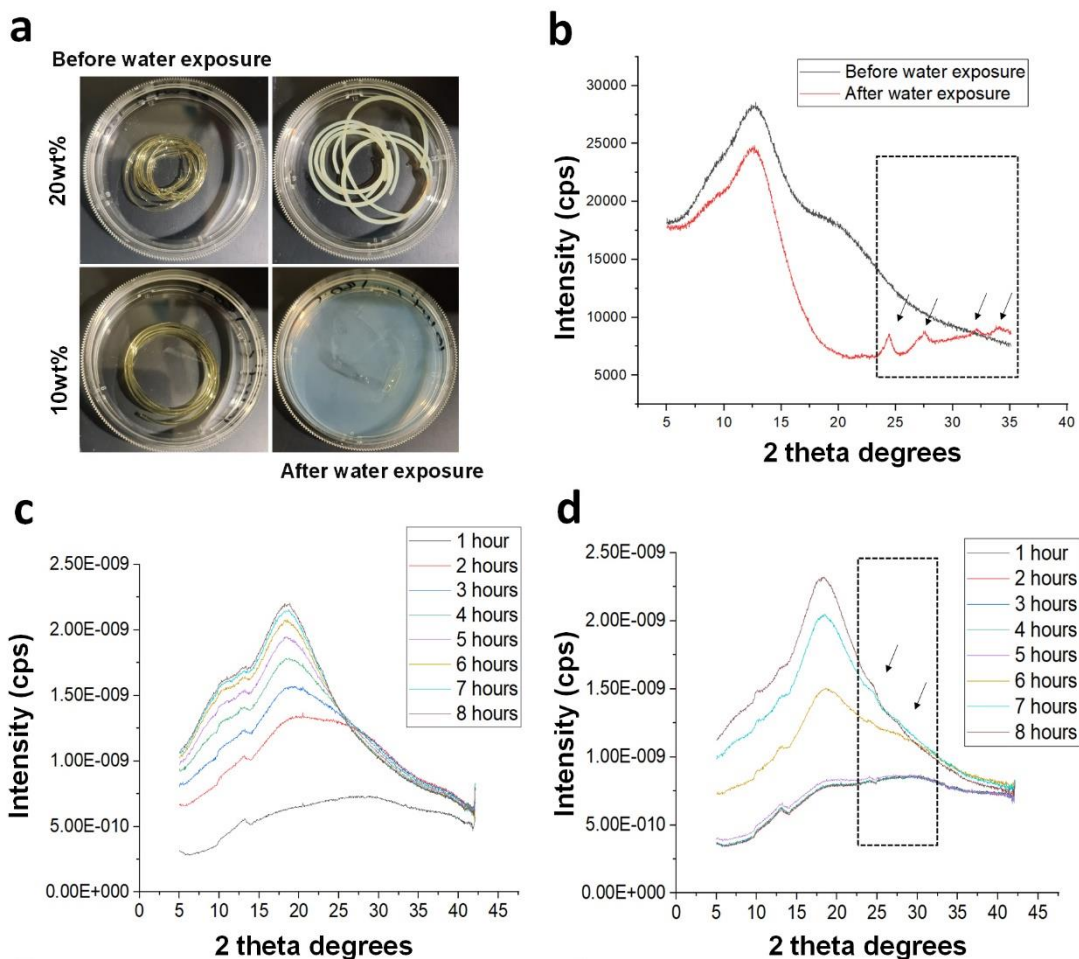


Figure 6.5. Accelerated stability study. a) Extrudates before and after 30 minutes of water exposure, b) XRD result for the 20 wt% system, c) and d) time-resolved XRD results for the 20 wt% and 25 wt% drug loadings, respectively.

The crystallisation differences between the static XRD and the time-resolved XRD experiments with the area detectors are because of the difference in the volume of water added to the extrudates and the water blocking effect present in the time-resolved experiments that hindered detection of crystallisation at 20 wt% drug loading. Overall, these results show that (1) the 10 wt% critical concentration could be used a stability predictor based on the recrystallisation behaviour upon water exposure and (2) this approach could be used as a fast screening tool for early-stage ASD stability assessment.

### 6.3.4 Volatiles emitted during extrusion

The potential of using SIFT-MS for real-time VOC analysis during extrusion was investigated by assessing the impact of temperature, screw speed and drug loading on the volatile components emitted during extrusion. The initial exploratory experiments were performed with pure polymer to obtain the polymer reference mass spectra. In Figure 6.10, the SIFT mass spectra profiles obtained during extrusion of Soluplus from 200°C to 150°C at 100 rpm are compared. The main ion peaks were found at mass-to-charge ratios ( $m/z$ ) of 56, 99, 103, 112, 132 and 169. A marked intensity increase was observed upon decreasing processing temperature from 200°C to 160°C, with the 200°C and 150°C processing temperatures displaying the lowest intensity values. Principal component analysis corroborated this observation, as similar scores were obtained for the two extreme temperatures. This unexpected and inversely correlated trend suggests that at conditions prone to degradation (i.e., high temperature and high shear stress) the volatile fraction is reduced and the main degradation products may be embedded in the polymer matrix. However, it should be noted that, these plots combine all ionic products and that their subsequent identification taking into account specific reagents ions could change this interpretation. Likewise, additional off-line experiments at lower temperatures are required.

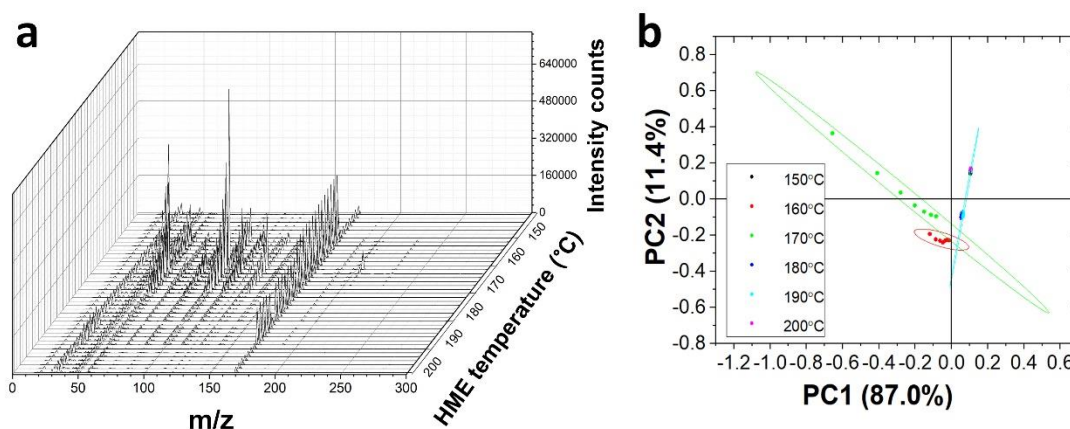


Figure 6.6. Impact of processing temperature on pure polymer. a) SIFT mass spectra upon extrusion from 200°C to 150°C at 100 rpm and b) the respective PCA score plot

This effect became more apparent upon increasing screw speed from 100 rpm to 500 rpm at 200°C (Figure 6.11). As screw speed increases, the peak at 169 m/z remains unchanged while the lower mass fraction peaks gradually decrease. Concomitantly, the extrudates became darker with visible signs of degradation.

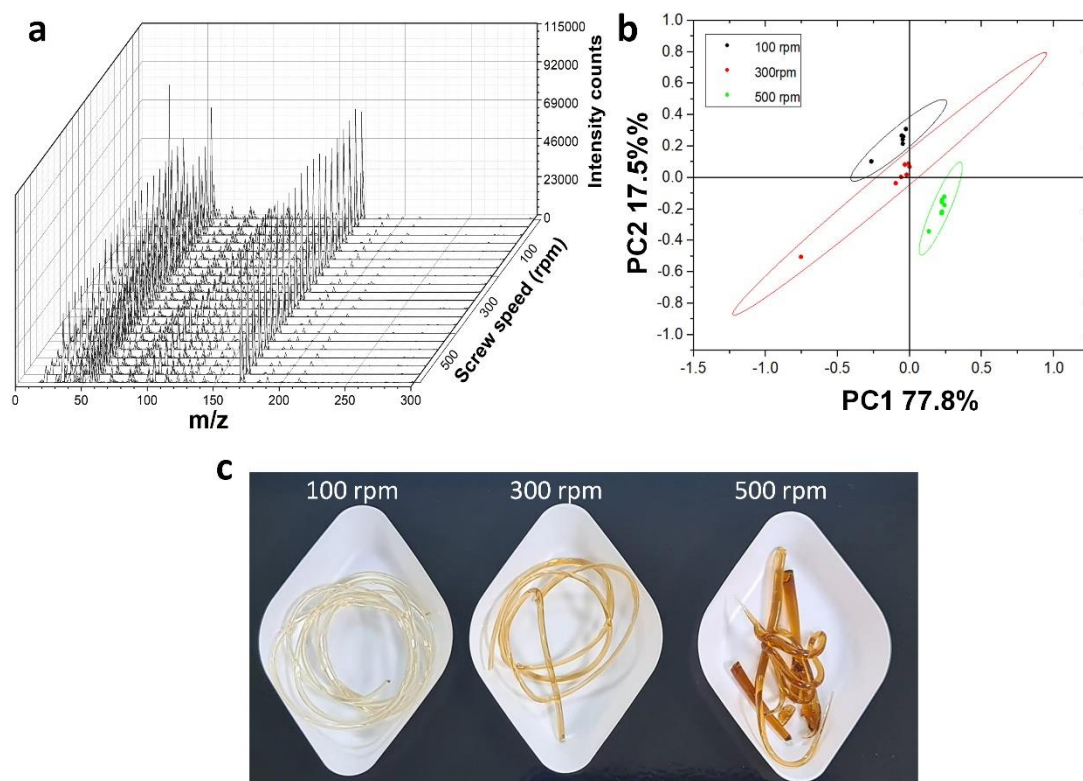


Figure 6.7. Impact of screw speed on the volatile components emitted during extrusion of pure Soluplus. a) SIFT-MS spectra of Soluplus extruded at 200°C and variable screw speed. b) Principal component analysis of SIFT-MS spectra. c) Extrudate appearance showing increasing browning above 300 rpm.

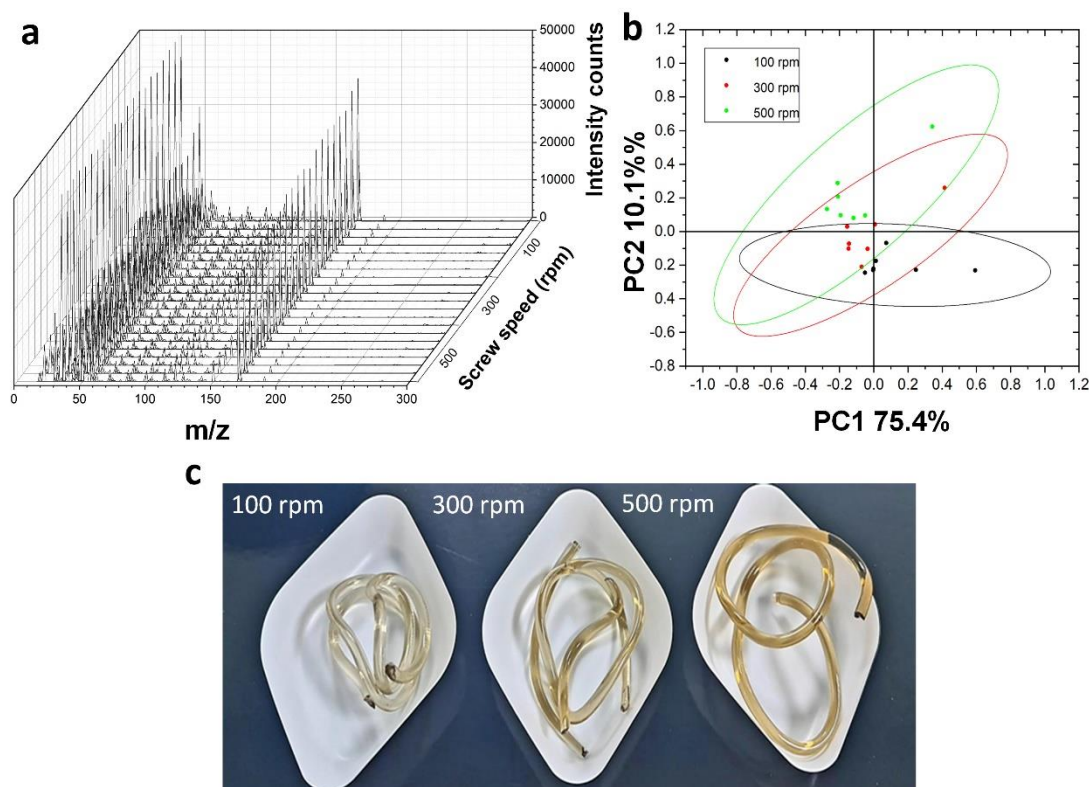


Figure 6.8. Impact of screw speed on the volatile components emitted during extrusion of pure Soluplus. a) SIFT-MS spectra of Soluplus extruded at 200°C and variable screw speed. b) Principal component analysis of SIFT-MS spectra. c) Extrudate appearance showing increasing browning above 300 rpm.

Interestingly, the impact of screw speed at 150°C (Figure 6.12) shows a marked change in the ion fragments pattern. The peak at 34 m/z becomes dominant over the one at 169 m/z and the extrudates display a green hue discoloration. This could suggest different degradation pathways for temperature and shear.

The mass spectra of the 50 wt% drug loading system upon extrusion in the 210°C-160°C range display new ion peaks above 169 m/z, in particular at 183 m/z, 213 m/z, 257 m/z and 287 m/z, which are absent in the pure polymer melt (Figure 6.13). However, these ion products could be related solely to the drug or to a drug-polymer adduct. The same temperature effect was observed, with the highest and lowest HME set-point temperature extremes displaying lower peak intensity.

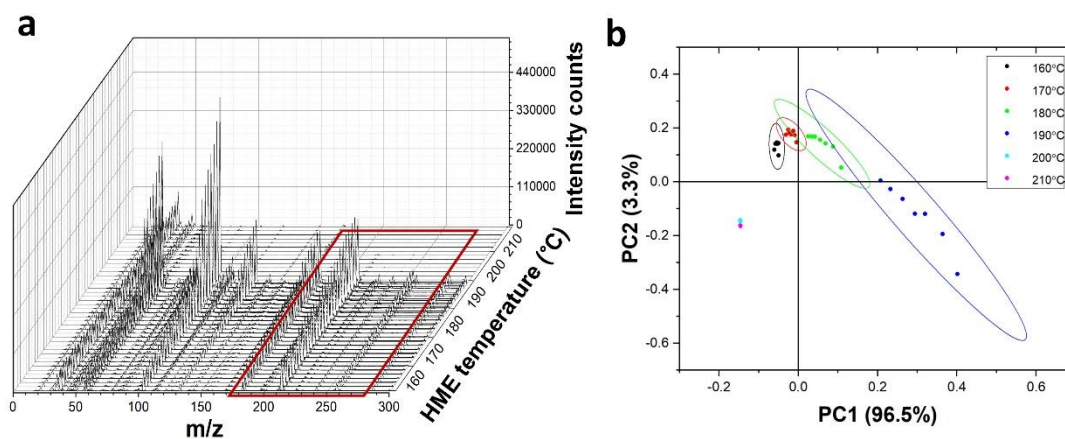


Figure 6.9. a) SIFT mass spectra at 50 wt% drug loading with b) the respective PCA score plot.

At 10 wt% drug loading (Figure 6.14), processing temperature was found to have minimum impact on the detected VOCs. Nonetheless, the screw speed increase at both temperature extremes showed the same peak intensity decrease trend.

Although further work is necessary to identify the ion fragments, exclude secondary reactions and validate the SIFT-MS method, these preliminary results show promising potential for real-time HME applications. Automated sampling directly from the HME vent port situated in the downstream sections of the extruder, permits to monitor volatile components released when material is exposed at the high temperatures in real time. This allows for the identification of optimum HME processing temperature and screw speeds to minimise or eliminate potential degradation reactions and thus further understand the stability of the of amorphous solid dispersions during HME processing. Due to time constrains and equipment failure further SIFT-MS experiments were not possible in this study.

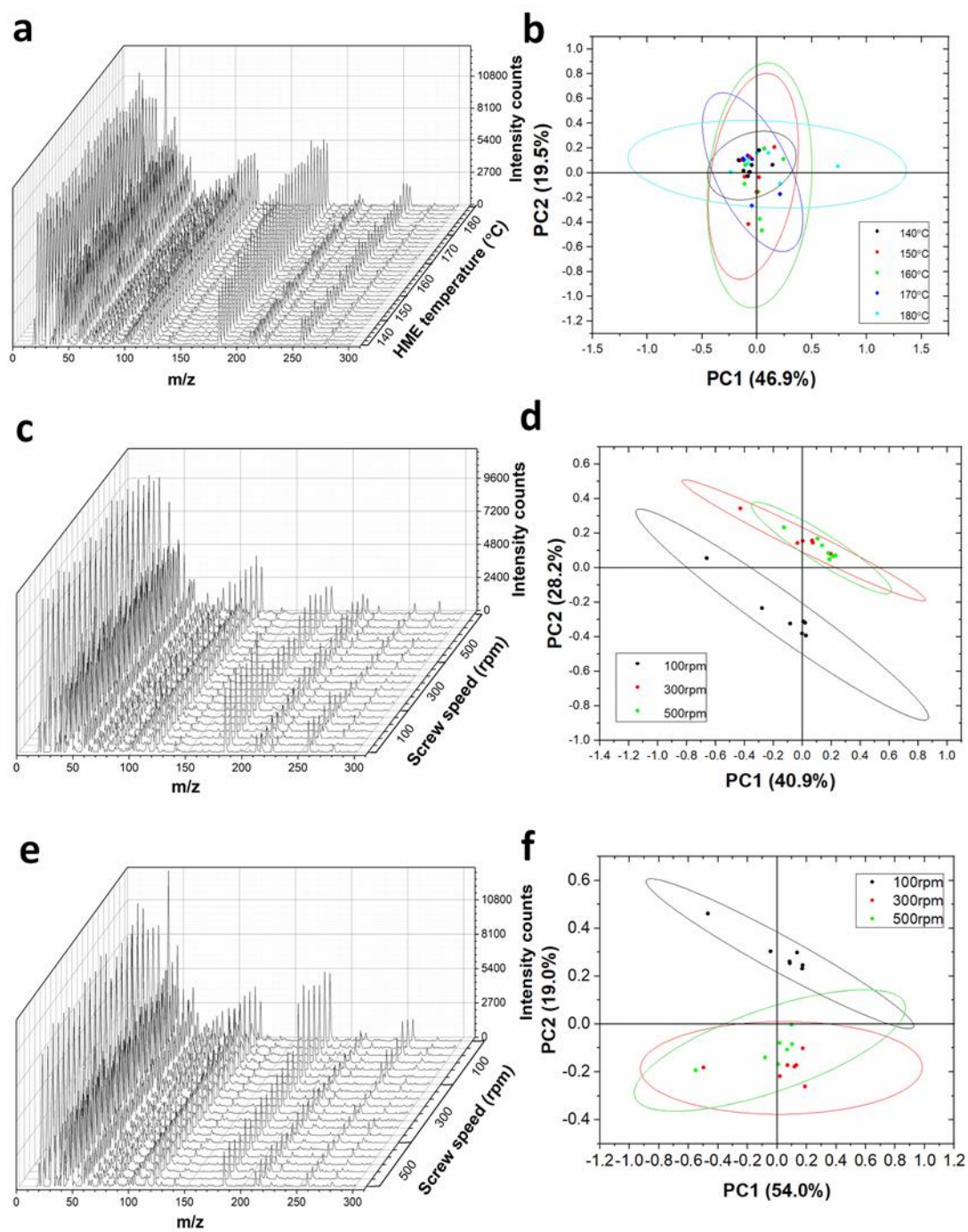


Figure 6.10. a) SIFT mass spectra at 10 wt% drug loading upon variable temperature extrusion with b) the respective PCA score plot. c) SIFT mass spectra at 180°C and variable screw speed with d) the respective PCA

## 6.4 Conclusions

The core objectives of this chapter were to test the applicability of the API-polymer solubility method developed in Chapter 2 to a new drug-polymer system of commercial and industrial interest and to investigate the feasibility of SIFT-MS application to HME for on-line detection and potential analysis of volatile components. The former was successfully accomplished and a temperature-composition phase diagram was built based on the low-frequency Raman peaks. The evolution of these peaks described the amorphous-crystalline switch of the API and provided access to the saturated solubility temperature for each composition. From the solubility phase diagram a critical concentration of 10 wt% drug loading was identified as the potential solid solution capacity. Accelerated stability studies upon water exposure supported the stability predicting potential of this concentration and provided a fast screening tool for early-stage ASD stability assessment.

For the first time SIFT-MS was coupled to HME for real-time analysis of volatile organic components during ASD manufacture. SIFT-MS demonstrated promising potential to detect and monitor potential HME-induced degradation products as a result of temperature and shear, as well to distinguish between drug and polymer-related VOCs. Furthermore, it showed evidence of different temperature- and shear-induced degradation pathways. This feasibility study opens the possibility for routine in-situ real-time VOCs analysis during extrusion. This provides a significant step forward in understanding and minimising the potential risk of thermomechanical degradation during HME processing.

# **Chapter 7**

## **General Conclusions and Future Work**

### **7.1 General conclusions**

The presented research has attempted to advance the amorphous solid dispersion field by focusing on the saturated solubility of crystalline API in the polymer matrix as a tool for the predictive design and manufacture of stable polymer-based ASD systems. Throughout this thesis, new tools and characterisation methods were applied allowing for increased scrutiny of ASD properties to investigate the structure-process link for a rational formulation strategy. In Chapter 2, advances in the understanding and study of API-polymer solubility included a paradigm shift from DSC-based methods towards a novel empirical approach combining hot-melt extrusion (HME) processing, as a robust heating and mixing platform, and low-frequency Raman (LFR) spectroscopy, as an in-line PAT tool, for real-time API solubility determination. LFR was employed for the first time to monitor the crystalline-amorphous phase transitions of the API to determine the saturated solubility temperature ( $T_S$ ) and build solubility

phase diagrams for binary ASD systems. From the phase-diagrams generated in this manner two major outputs were obtained: the identification of a critical concentration that defines the maximum drug loading in order to obtain stable ASDs after HME processing and the identification of safe processing windows to avoid residual API crystallinity at temperatures well below the API  $T_M$ . Complimentary characterisation via DSC and XRPD analysis, confirmed the use of the critical concentration as a physical stability predictor to inform maximum drug loadings and aid polymer selection for maximum API-polymer solubility and ASD stability.

In Chapter 3, a direct comparison between the solubility curve obtained from the LFR method discussed above and well established DSC-based approaches, such as Flory-Huggins and the Kyeremateng modelling approaches, was carried out. Equilibrium assumptions and potential shortfalls leading to under or overestimations were discussed. Substantial solubilisation temperature differences were found between the DSC-based approaches and the LFR method, especially at low drug loadings. This suggested the  $T_S$  values obtained from the LFR approach provide a more accurate reflection of the likely solubility equilibrium throughout the entire composition range. Thus, the newly developed LFR method provides a reliable alternative solubility measurement for determining stable amorphous solid dispersions.

An investigation into the effects of drug loading and processing temperature (as coordinates of the solubility phase diagram) on the ASD internal structure was carried out in Chapter 4 by means of synchrotron phase-contrast micro-computed tomography (Sync-PC- $\mu$ CT). For this purpose the phase diagram developed in Chapter 2 was extended to a broader compositional range and the crystalline-amorphous transitions were further corroborated by principal component analysis. The Sync-PC- $\mu$ CT investigation was coupled with a bespoke image analysis strategy to extract qualitative and quantitative morphological descriptors for the various structural domains/defects identified, such as drug-rich crystalline clusters, impurities, polymer-related heterogeneities and pores. Supersaturated ASDs (above the critical concentration) displayed higher structural complexity and exhibited a plethora of pores and API-rich crystalline domains upon ageing, which were absent in the undersaturated ASDs. The HME processing temperature was found to affect not only residual API crystallinity, but also the pore network structure and the polymer softening behaviour which could

affect ASD performance. The increased scrutiny of the ASD internal structure adds a new complexity dimension and shows the implications of the API-polymer phase diagram extend beyond solubility to ASD microstructure.

In Chapter 5, the local distribution evolution of the API and polymer on the ASD surface was investigated through time of flight-secondary ion mass spectrometry (ToF-SIMS) chemical mapping. Surface phase-separation and crystallisation kinetics were determined and compared to bulk crystallisation phenomena. Surface crystallisation was detected and quantified as early as within hours after extrusion, thus showing potential as a strategy for early-stage ASD physical stability assessment. The crystallisation induction time and the crystallisation rate were found intrinsically correlated to the drug loading and processing temperature, indicating a close link between the phase diagram coordinates and the API crystallisation kinetics after manufacture.

Finally, to further validate and test the applicability of the low-frequency Raman solubility method beyond proof-of-concept systems, this method was applied to an API-polymer system of commercial and therapeutic interest in Chapter 6. In addition to the crystalline lattice vibration modes, the Rayleigh signal and the broad amorphous shoulder in the Stokes region were used to aid the crystalline-amorphous differentiation. The evolution of these peaks described the amorphous-crystalline switch of the API and provided access to the saturated solubility temperature for each composition. From the solubility phase diagram a critical concentration was identified as the potential solid solution capacity. Accelerated stability studies upon water exposure supported the stability predicting potential of this concentration and provided a fast screening tool for ASD stability assessment. In addition to LFR, selected ion flow tube mass spectrometry (SIFT-MS) was also investigated as a novel PAT tool for HME processing. It showed potential to detect and monitor HME-induced degradation products, as well as to distinguish between drug- and polymer-related volatiles. Furthermore, it suggested different temperature- and shear-induced degradation pathways. Although further work is necessary to validate the method and identify the ionic fragments, this feasibility study opens the possibility for routine in-situ real-time VOCs analysis during extrusion. This provides a significant step forward in

understanding and minimising the risk of thermomechanical degradation during HME processing.

To summarise, the work presented in this research focused on the API saturated solubility as one of the main thermodynamic aspects determining ASD physical stability. Although this topic has been extensively studied in the last decades, the hurdles associated with its determination are still valid today and need to be addressed. This was made by four main contributions: the development of a novel empirical method for the API-polymer solubility determination, its comparison to well established thermodynamic methods, the study of the impact of the solubility phase diagram coordinates on the ASD internal microstructure, as well as on the ASD surface phase separation/crystallisation kinetics. Together, these contributions enable further understanding of the link between API-polymer solubility and ASD physical stability and provide a significant step forward in the challenge of predicting and developing stable polymer-based ASDs.

## **7.2 Future work**

The work developed in this project provides a starting point for a range of future work involving API-polymer solubility and ASD stability prediction. Following the conclusions discussed above, some recommendations for future work are given in the sections below.

### **7.2.1 Equilibrium assumption validation**

In Chapter 2, a new method was proposed to determine the saturated solubility of the API in polymer matrices directly during HME processing. Whilst this method is well supported by the data herein presented, further work in this area could be relevant to validate equilibrium solubility assumptions. This could be achieved by (1) varying the API-polymer mixing length through the use of recirculation channels/ reprocessing and (2) by varying screw speed to add a new shear/kinetic dimension and investigate the contribution of mechanical energy to  $T_S$ .

Additionally, the API-polymer composition and the temperature steps taken during the API solubility determination could be further expanded to refine the critical API concentration and the saturated solubility temperature, respectively.

The domain size of solubilised API is an additional aspect that could be investigated. The assumption is formation of molecular API dispersions above the saturated solubility temperature, however solid-state NMR could help elucidate the domain size and inform potential structure beyond short-range order.

### **7.2.2 Refine and validate stability prediction**

Formulation of amorphous solid dispersions into final dosage forms and the study of their physical stability is a logical progression of this work. Further validation of the critical concentration as a physical stability predictor would be advantageous. It would be particularly relevant to investigate whether it remains valid upon further downstream processing such 3D printing and tablet compression.

### **7.2.3 Explore the mechanisms of phase separation on the ASD**

#### **surface**

The determination of the exact mechanism leading to phase separation and crystallisation phenomena on the ASD surface via ToF-SIMS depth profiling could inform additional strategies to assure ASD physical stability.

### **7.2.4 Investigate spectral features in the low-frequency Raman**

#### **region**

Additional work is necessary to deconvolute and better understand the information present in the low-frequency Raman region. This spectral region can provide substantial characterisation of pharmaceutical solid-state forms and offer information on a wide range of physico-chemical properties beyond the crude crystalline-amorphous differentiation explored in this study.

## Bibliography

1. Aulton, M. Dosage form design and manufacture. in *Pharmaceutics: The science of dosage form design* 307–553 (Churchill Livingstone, 2001).
2. Law, D. *et al.* Physicochemical considerations in the preparation of amorphous ritonavir-poly(ethylene glycol) 8000 solid dispersions. *J Pharm Sci* **90**, 1015–1025 (2001).
3. Lipinski, C. A., Lombardo, F., Dominy, B. W. & Feeney, P. J. Experimental and computational approaches to estimate solubility and permeability in drug discovery and development settings. *Adv Drug Deliv Rev* **23**, 3–25 (1997).
4. Ting, J. M., Porter, W. W., Mecca, J. M., Bates, F. S. & Reineke, T. M. Advances in polymer design for enhancing oral drug solubility and delivery. *Bioconjug Chem* **29**, 939–952 (2018).
5. Shultz, M. D. Two decades under the influence of the rule of five and the changing properties of approved oral drugs. *J Med Chem* **62**, 1701–1714 (2019).
6. Benet, L. Z., Hosey, C. M., Ursu, O. & Oprea, T. I. BDDCS, the rule of 5 and drugability. *Adv Drug Deliv Rev* **101**, 89 (2016).
7. Amidon, G. L., Lennernäs, H., Shah, V. P. & Crison, J. R. A Theoretical Basis for a Biopharmaceutic Drug Classification: The Correlation of in Vitro Drug Product Dissolution and in Vivo Bioavailability. *Pharm Res* **12**, 413–420 (1995).
8. Step. *Committee for Medicinal Products for Human Use ICH M9 Guideline on Biopharmaceutics Classification System-Based Biowaivers ICH M9 on Biopharmaceutics Classification System-Based Biowaivers*. [www.ema.europa.eu/contact](http://www.ema.europa.eu/contact) (2020).
9. Savjani, K. T., Gajjar, A. K. & Savjani, J. K. Drug solubility: importance and enhancement techniques. *ISRN Pharm* **2012**, 195727 (2012).
10. Miller, J. M., Beig, A., Carr, R. A., Webster, G. K. & Dahan, A. The solubility-permeability interplay when using cosolvents for solubilization: Revising the way we use solubility-enabling formulations. *Mol Pharm* **9**, 581–590 (2012).
11. Dahan, A. & Miller, J. M. The solubility-permeability interplay and its implications in formulation design and development for poorly soluble drugs. *AAPS Journal* **14**, 244–251 (2012).
12. Butler, J. M. & Dressman, J. B. The developability classification system: Application of biopharmaceutics concepts to formulation development. *J Pharm Sci* **99**, 4940–4954 (2010).
13. Bergström, C. A. S., Charman, W. N. & Porter, C. J. H. Computational prediction of formulation strategies for beyond-rule-of-5 compounds. *Adv Drug Deliv Rev* **101**, 6–21 (2016).

14. Pandi, P., Bulusu, R., Kommineni, N., Khan, W. & Singh, M. Amorphous solid dispersions: An update for preparation, characterization, mechanism on bioavailability, stability, regulatory considerations and marketed products. *Int J Pharm* **586**, 119560 (2020).
15. Williams, H. D. *et al.* Strategies to address low drug solubility in discovery and development. *Pharmacol Rev* **65**, 315–499 (2013).
16. Huang, L. F. & Tong, W. Q. Impact of solid state properties on developability assessment of drug candidates. *Adv Drug Deliv Rev* **56**, 321–334 (2004).
17. Laitinen, R., Priemel, P., Surwase, S. & Graeser, K. Theoretical Considerations in Developing Amorphous Solid Dispersions. in *Amorphous Solid Dispersions, Theory and Practice* (eds. Shah, N., Sandhu, H., Choi, D. S. & Mallick, A. W.) 637–663 (Springer, 2014). doi:10.1007/978-1-4939-1598-9.
18. Taylor, L. S. & Zografi, G. Spectroscopic characterization of interactions between PVP and indomethacin in amorphous molecular dispersions. *Pharm Res* **14**, 1691–1698 (1997).
19. Pokharkar, V. B. *et al.* Development, characterization and stabilization of amorphous form of a low Tg drug. *Powder Technol* **167**, 20–25 (2006).
20. Van Eerdenbrugh, B. & Taylor, L. S. An ab initio polymer selection methodology to prevent crystallization in amorphous solid dispersions by application of crystal engineering principles. *CrystEngComm* **13**, 6171–6178 (2011).
21. Kestur, U. S. & Taylor, L. S. Role of polymer chemistry in influencing crystal growth rates from amorphous felodipine. *CrystEngComm* **12**, 2390–2397 (2010).
22. Trasi, N. S. & Taylor, L. S. Effect of polymers on nucleation and crystal growth of amorphous acetaminophen. *CrystEngComm* **14**, 5188–5197 (2012).
23. Vasconcelos, T., Sarmiento, B. & Costa, P. Solid dispersions as strategy to improve oral bioavailability of poor water soluble drugs. *Drug Discov Today* **12**, 1068–1075 (2007).
24. Huang, Y. & Dai, W.-G. Fundamental aspects of solid dispersion technology for poorly soluble drugs. *Acta Pharm Sin B* **4**, 18–25 (2014).
25. Zhang, Z. *et al.* Prediction of the physical stability of amorphous solid dispersions: relationship of aging and phase separation with the thermodynamic and kinetic models along with characterization techniques. *Expert Opin Drug Deliv* **18**, 249–264 (2021).
26. LaFontaine, J. S., McGinity, J. W. & Williams, R. O. Challenges and Strategies in Thermal Processing of Amorphous Solid Dispersions: A Review. *AAPS PharmSciTech* **17**, 43–55 (2016).
27. He, Y. & Ho, C. Amorphous Solid Dispersions: Utilization and Challenges in Drug Discovery and Development. *J Pharm Sci* **104**, 3237–3258 (2015).

28. Wouters, O. J., McKee, M. & Luyten, J. Estimated research and development investment needed to bring a new medicine to market, 2009-2018. *JAMA - Journal of the American Medical Association* **323**, 844–853 (2020).
29. Statista. • R&D cost for new pharmaceutical compounds 2010-2019 | Statista. <https://www.statista.com/statistics/825727/randd-cost-for-new-pharma-compounds-by-cohort/> (2020).
30. Chiou, W. L. & Riegelman, S. Pharmaceutical applications of solid dispersion systems. *J Pharm Sci* **60**, 1281–1302 (1971).
31. Vasconcelos, T., Sarmiento, B. & Costa, P. Solid dispersions as strategy to improve oral bioavailability of poor water soluble drugs. *Drug Discov Today* **12**, 1068–1075 (2007).
32. Jachowicz, R. Dissolution rates of partially water-soluble drugs from solid dispersion systems. I. Prednisolone. *Int J Pharm* **35**, 1–5 (1987).
33. Sekiguchi, K. & Obi, N. Studies on absorption of eutectic mixture. I. A comparison of the behavior of eutectic mixture of sulfathiazole and that of ordinary sulfathiazole in man. *Chem Pharm Bull (Tokyo)* **9**, 866–872 (1961).
34. Vo, C. L. N., Park, C. & Lee, B. J. Current trends and future perspectives of solid dispersions containing poorly water-soluble drugs. *European Journal of Pharmaceutics and Biopharmaceutics* **85**, 799–813 (2013).
35. Nair, A. R. *et al.* Overview of extensively employed polymeric carriers in solid dispersion technology. *AAPS PharmSciTech* **21**, (2020).
36. Van Duong, T. & Van den Mooter, G. The role of the carrier in the formulation of pharmaceutical solid dispersions. Part II: amorphous carriers. *Expert Opin Drug Deliv* **13**, 1681–1694 (2016).
37. Lin, Y., Cogdill, R. P. & Wildfong, P. L. D. Informatic calibration of a materials properties database for predictive assessment of mechanically activated disordering potential for small molecule organic solids. *J Pharm Sci* **98**, 2696–2708 (2009).
38. Adrjanowicz, K. *et al.* Effect of Cryogrinding on Chemical Stability of the Sparingly Water-Soluble Drug Furosemide. *Pharmaceutical Research* **28**, 3220–3236 (2011).
39. Wyttenbach, N. & Kuentz, M. Glass-forming ability of compounds in marketed amorphous drug products. *European Journal of Pharmaceutics and Biopharmaceutics* **112**, 204–208 (2017).
40. Agrawal, A. M., Dudhedia, M. S., Patel, A. D. & Raikes, M. S. Characterization and performance assessment of solid dispersions prepared by hot melt extrusion and spray drying process. *Int J Pharm* **457**, 71–81 (2013).
41. Haser, A. *et al.* Melt extrusion vs. spray drying: The effect of processing methods on crystalline content of naproxen-povidone formulations. *European Journal of Pharmaceutical Sciences* **102**, 115–125 (2017).

42. Crowley, M. M. *et al.* Pharmaceutical Applications of Hot-Melt Extrusion: Part I. *Drug Dev Ind Pharm* **33**, 909–926 (2007).
43. Evans, R. C., Bochmann, E. S., Kyeremateng, S. O., Gryczke, A. & Wagner, K. G. Holistic QbD approach for hot-melt extrusion process design space evaluation: Linking materials science, experimentation and process modeling. *European Journal of Pharmaceutics and Biopharmaceutics* **141**, 149–160 (2019).
44. Mugheirbi, N. A. A., Mosquera-Giraldo, L. I., Borca, C. H., Slipchenko, L. V. & Taylor, L. S. Phase Behavior of Drug-Hydroxypropyl Methylcellulose Amorphous Solid Dispersions Produced from Various Solvent Systems: Mechanistic Understanding of the Role of Polymer using Experimental and Theoretical Methods. *Mol Pharm* **15**, 3236–3251 (2018).
45. Paudel, A. & Mooter, G. Van den. Influence of Solvent Composition on the Miscibility and Physical Stability of Naproxen/PVP K 25 Solid Dispersions Prepared by Cosolvent Spray-Drying. *Pharmaceutical Research* **29**:1 **29**, 251–270 (2011).
46. Lin, X. *et al.* Physical Stability of Amorphous Solid Dispersions: a Physicochemical Perspective with Thermodynamic, Kinetic and Environmental Aspects. *Pharm Res* **35**, (2018).
47. Theil, F., Milsmann, J., Anantharaman, S. & Van Lishaut, H. Manufacturing Amorphous Solid Dispersions with a Tailored Amount of Crystallized API for Biopharmaceutical Testing. *Mol Pharm* **15**, 1870–1877 (2018).
48. Knopp, M. M., Wendelboe, J., Holm, R. & Rades, T. Effect of amorphous phase separation and crystallization on the in vitro and in vivo performance of an amorphous solid dispersion. *European Journal of Pharmaceutics and Biopharmaceutics* **130**, 290–295 (2018).
49. Li, N. & Taylor, L. S. Microstructure Formation for Improved Dissolution Performance of Lopinavir Amorphous Solid Dispersions. *Mol Pharm* **16**, 1751–1765 (2019).
50. Stewart, A. M. *et al.* Development of a Biorelevant, Material-Sparing Membrane Flux Test for Rapid Screening of Bioavailability-Enhancing Drug Product Formulations. *Mol Pharm* **14**, 2032–2046 (2017).
51. Indulkar, A. S., Gao, Y., Raina, S. A., Zhang, G. G. Z. & Taylor, L. S. Exploiting the Phenomenon of Liquid-Liquid Phase Separation for Enhanced and Sustained Membrane Transport of a Poorly Water-Soluble Drug. *Mol Pharm* **13**, 2059–2069 (2016).
52. Tao, J., Sun, Y., Zhang, G. G. Z. & Yu, L. Solubility of small-molecule crystals in polymers: D-Mannitol in PVP, indomethacin in PVP/VA, and nifedipine in PVP/VA. *Pharm Res* **26**, 855–864 (2009).
53. Sun, Y. E., Tao, J., Zhang, G. G. Z. & Yu, L. Solubilities of crystalline drugs in polymers: An improved analytical method and comparison of solubilities of indomethacin and nifedipine in PVP, PVP/VA, and PVAc. *J Pharm Sci* **99**, 4023–4031 (2010).

54. Amharar, Y., Curtin, V., Gallagher, K. H. & Healy, A. M. Solubility of crystalline organic compounds in high and low molecular weight amorphous matrices above and below the glass transition by zero enthalpy extrapolation. *Int J Pharm* **472**, 241–247 (2014).
55. Mahieu, A., Willart, J. F., Dudognon, E., Daneide, F. & Descamps, M. A new protocol to determine the solubility of drugs into polymer matrixes. *Mol Pharm* **10**, 560–566 (2013).
56. Marsac, P. J., Shamblin, S. L. & Taylor, L. S. Theoretical and practical approaches for prediction of drug-polymer miscibility and solubility. *Pharm Res* **23**, 2417–2426 (2006).
57. Nishi, T. & Wang, T. T. Melting point depression and kinetic effects of cooling on crystallization in poly(vinylidene fluoride)-poly(methyl methacrylate) mixtures. *Macromolecules* **8**, 909–915 (1975).
58. Zhang, S., Lee, T. W. Y. & Chow, A. H. L. Thermodynamic and kinetic evaluation of the impact of polymer excipients on storage stability of amorphous itraconazole. *Int J Pharm* **555**, 394–403 (2019).
59. Tian, Y. *et al.* The design and development of high drug loading amorphous solid dispersion for hot-melt extrusion platform. *Int J Pharm* **586**, 119545 (2020).
60. Moseson, D. E. & Taylor, L. S. The application of temperature-composition phase diagrams for hot melt extrusion processing of amorphous solid dispersions to prevent residual crystallinity. *Int J Pharm* **553**, 454–466 (2018).
61. Wlodarski, K., Sawicki, W., Kozyra, A. & Tajber, L. Physical stability of solid dispersions with respect to thermodynamic solubility of tadalafil in PVP-VA. *European Journal of Pharmaceutics and Biopharmaceutics* **96**, 237–246 (2015).
62. Kyeremateng, S. O., Pudlas, M. & Woehle, G. H. A fast and reliable empirical approach for estimating solubility of crystalline drugs in polymers for hot melt extrusion formulations. *J Pharm Sci* **103**, 2847–2858 (2014).
63. Prudic, A., Ji, Y., Luebbert, C. & Sadowski, G. Influence of humidity on the phase behavior of API/polymer formulations. *European Journal of Pharmaceutics and Biopharmaceutics* **94**, 352–362 (2015).
64. Lehmkemper, K., Kyeremateng, S. O., Heinzerling, O., Degenhardt, M. & Sadowski, G. Long-term physical stability of PVP- and PVPVA-amorphous solid dispersions. *Mol Pharm* **14**, 157–171 (2016).
65. Paus, R., Ji, Y., Vahle, L. & Sadowski, G. Predicting the solubility advantage of amorphous pharmaceuticals: a novel thermodynamic approach. *Mol Pharm* **12**, 2823–2833 (2015).
66. Gordon, M. & Taylor, J. S. Ideal copolymers and the second-order transitions of synthetic rubbers. i. non-crystalline copolymers. *Journal of Applied Chemistry* **2**, 493–500 (1952).

67. Simha, R. & Boyer, R. F. On a general relation involving the glass temperature and coefficients of expansion of polymers. *J Chem Phys* **37**, 1003–1007 (1962).
68. Salem, A., Nagy, S., Pál, S. & Széchenyi, A. Reliability of the Hansen solubility parameters as co-crystal formation prediction tool. *Int J Pharm* **558**, 319–327 (2019).
69. Greenhalgh, D. J., Williams, A. C., Timmins, P. & York, P. Solubility parameters as predictors of miscibility in solid dispersions. *J Pharm Sci* **88**, 1182–1190 (1999).
70. DeBoyace, K., Wildfong, P. L. D. D. & Wildfong, P. L. D. D. The Application of Modeling and Prediction to the Formation and Stability of Amorphous Solid Dispersions. *J Pharm Sci* **107**, 57–74 (2018).
71. Turpin, E. R. *et al.* In Silico Screening for Solid Dispersions: The Trouble with Solubility Parameters and FH. *Mol Pharm* **15**, 4654–4667 (2018).
72. Seo, Y., Zuo, B., Cangialosi, D. & Priestley, R. D. Physical aging of hydroxypropyl methylcellulose acetate succinate via enthalpy recovery. *Soft Matter* **12**, 8331–8341 (2022).
73. Cowie, J. M. G. & Arrighi, V. Physical aging of polymer blends. in *Polymer Blends Handbook* 1357–1394 (Springer Netherlands, 2014).
74. Baghel, S. *et al.* Polymeric Amorphous Solid Dispersions: A Review of Amorphization, Crystallization, Stabilization, Solid-State Characterization, and Aqueous Solubilization of Biopharmaceutical Classification System Class II Drugs. *J Pharm Sci* **105**, 2527–2544 (2016).
75. Graeser, K. A., Patterson, J. E., Zeitler, J. A. & Rades, T. The role of configurational entropy in amorphous systems. *Pharmaceutics* **2**, 224–244 (2010).
76. Hancock, B. C., Dupuis, Y. & Thibert, R. Determination of the viscosity of an amorphous drug using thermomechanical analysis (TMA). *Pharm Res* **16**, 672–675 (1999).
77. Johari, C. P. & Goidstein, M. Viscous liquids and the glass transition. II. Secondary relaxations in glasses of rigid molecules. *J Chem Phys* **53**, 2372–2388 (1970).
78. Hancock, B. C., Shamblin, S. L. & Zografi, G. Molecular Mobility of Amorphous Pharmaceutical Solids Below Their Glass Transition Temperatures. *Pharmaceutical Research: An Official Journal of the American Association of Pharmaceutical Scientists* **12**, 799–806 (1995).
79. Su, Y., Yu, L. & Cai, T. Enhanced Crystal Nucleation in Glass-Forming Liquids by Tensile Fracture in the Glassy State. *Cryst Growth Des* **19**, 40–44 (2018).
80. Willart, J. F. *et al.* The role of cracks in the crystal nucleation process of amorphous griseofulvin. *Eur. Phys. J. Special Topics* **226**, 837–847 (2017).
81. Vyazovkin, S. & Dranca, I. Effect of physical aging on nucleation of amorphous indomethacin. *Journal of Physical Chemistry B* **111**, 7283–7287 (2007).

82. Bhugra, C., Shmeis, R., Krill, S. L. & Pikal, M. J. Prediction of onset of crystallization from experimental relaxation times. II. Comparison between predicted and experimental onset times. *J Pharm Sci* **97**, 455–472 (2008).
83. Kissi, E. O. *et al.* Glass-Transition Temperature of the  $\beta$ -Relaxation as the Major Predictive Parameter for Recrystallization of Neat Amorphous Drugs. *Journal of Physical Chemistry B* **122**, 2803–2808 (2018).
84. Li, Y. *et al.* *Interactions between Drugs and Polymers Influencing Hot Melt Extrusion. Journal of Pharmacy and Pharmacology* vol. 66 148–166 (John Wiley & Sons, Ltd, 2014).
85. Kindermann, C., Matthée, K., Strohmeyer, J., Sievert, F. & Breitzkreutz, J. Tailor-made release triggering from hot-melt extruded complexes of basic polyelectrolyte and poorly water-soluble drugs. *European Journal of Pharmaceutics and Biopharmaceutics* **79**, 372–381 (2011).
86. Andrews, G. P., Abudiak, O. A. & Jones, D. S. Physicochemical characterization of hot melt extruded bicalutamide- polyvinylpyrrolidone solid dispersions. *J Pharm Sci* **99**, 1322–1335 (2010).
87. Marsac, P. J., Li, T. & Taylor, L. S. Estimation of drug-polymer miscibility and solubility in amorphous solid dispersions using experimentally determined interaction parameters. *Pharm Res* **26**, 139–151 (2009).
88. Piccinni, P. *et al.* Solubility parameter-based screening methods for early-stage formulation development of itraconazole amorphous solid dispersions. *Journal of Pharmacy and Pharmacology* **68**, 705–720 (2016).
89. Broman, E., Khoo, C. & Taylor, L. S. A comparison of alternative polymer excipients and processing methods for making solid dispersions of a poorly water soluble drug. *Int J Pharm* **222**, 139–151 (2001).
90. Kothari, K., Ragoonanan, V. & Suryanarayanan, R. The role of drug-polymer hydrogen bonding interactions on the molecular mobility and physical stability of nifedipine solid dispersions. *Mol Pharm* **12**, 162–170 (2015).
91. Miller, D. A., DiNunzio, J. C., Yang, W., McGinity, J. W. & Williams, R. O. Enhanced in vivo absorption of itraconazole via stabilization of supersaturation following acidic-to-neutral pH transition. *Drug Dev Ind Pharm* **34**, 890–902 (2008).
92. Raghavan, S. L., Trividic, A., Davis, A. F. & Hadgraft, J. Crystallization of hydrocortisone acetate: Influence of polymers. *Int J Pharm* **212**, 213–221 (2001).
93. Doreth, M. *et al.* Glass solution formation in water - In situ amorphization of naproxen and ibuprofen with Eudragit® E PO. *J Drug Deliv Sci Technol* **34**, 32–40 (2016).
94. Marsac, P. J., Shamblin, S. L. & Taylor, L. S. Theoretical and Practical Approaches for Prediction of Drug-Polymer Miscibility and Solubility. *Pharm Res* **23**, 2417–2426 (2006).

95. Raviña-Eirín, E., Gómez-Amoza, J. L. & Martínez-Pacheco, R. Utility of the hyperbranched polymer Hybrane S1200 for production of instant-release particles by hot melt extrusion. *Drug Dev Ind Pharm* **39**, 1107–1112 (2013).
96. Djuris, J., Nikolakakis, I., Ibric, S., Djuric, Z. & Kachrimanis, K. Preparation of carbamazepine-Soluplus solid dispersions by hot-melt extrusion, and prediction of drug-polymer miscibility by thermodynamic model fitting. *Eur J Pharm Biopharm* **84**, 228–37 (2013).
97. Qi, S., Gryczke, A., Belton, P. & Craig, D. Q. M. Characterisation of solid dispersions of paracetamol and EUDRAGIT® E prepared by hot-melt extrusion using thermal, microthermal and spectroscopic analysis. *Int J Pharm* **354**, 158–167 (2008).
98. Liu, X. *et al.* Improving the chemical stability of amorphous solid dispersion with cocrystal technique by hot melt extrusion. *Pharm Res* **29**, 806–817 (2012).
99. Guo, Z. *et al.* The utilization of drug-polymer interactions for improving the chemical stability of hot-melt extruded solid dispersions. *Journal of Pharmacy and Pharmacology* **66**, 285–296 (2014).
100. Baird, J. A., Van Eerdenbrugh, B. & Taylor, L. S. A classification system to assess the crystallization tendency of organic molecules from undercooled melts. *J Pharm Sci* **99**, 3787–3806 (2010).
101. Blaabjerg, L. I., Lindenberg, E., Löbmann, K., Grohgan, H. & Rades, T. Glass forming ability of amorphous drugs investigated by continuous cooling and isothermal transformation. *Mol Pharm* **13**, 3318–3325 (2016).
102. Wyttenbach, N. & Kuentz, M. Glass-forming ability of compounds in marketed amorphous drug products. *European Journal of Pharmaceutics and Biopharmaceutics* **112**, 204–208 (2017).
103. Blaabjerg, L. I. *et al.* Influence of Glass Forming Ability on the Physical Stability of Supersaturated Amorphous Solid Dispersions. *J Pharm Sci* **108**, 2561–2569 (2019).
104. Panini, P., Rampazzo, M., Singh, A., Vanhoutte, F. & Van den Mooter, G. Myth or Truth: The Glass Forming Ability Class III Drugs Will Always Form Single-Phase Homogenous Amorphous Solid Dispersion Formulations. *Pharmaceutics* **11**, 529 (2019).
105. Vasanthavada, M., Tong, W. Q., Joshi, Y. & Kislalioglu, M. S. Phase behavior of amorphous molecular dispersions I: Determination of the degree and mechanism of solid solubility. *Pharm Res* **21**, 1598–1606 (2004).
106. Tang, X. C., Pikal, M. J. & Taylor, L. S. The effect of temperature on hydrogen bonding in crystalline and amorphous phases in dihydropyridine calcium channel blockers. *Pharm Res* **19**, 484–490 (2002).
107. Luebbert, C. & Sadowski, G. Moisture-induced phase separation and recrystallization in amorphous solid dispersions. *Int J Pharm* **532**, 635–646 (2017).

108. Xie, T. & Taylor, L. S. Effect of Temperature and Moisture on the Physical Stability of Binary and Ternary Amorphous Solid Dispersions of Celecoxib. *J Pharm Sci* **106**, 100–110 (2017).
109. Elkhazab, A., Sarkar, S., Simpson, G. J. & Taylor, L. S. Characterization of Phase Transformations for Amorphous Solid Dispersions of a Weakly Basic Drug upon Dissolution in Biorelevant Media. *Pharm Res* **36**, 1–17 (2019).
110. Moseson, D. E. *et al.* Amorphous Solid Dispersions Containing Residual Crystallinity: Competition Between Dissolution and Matrix Crystallization. **23**, 1–18 (2021).
111. Ayenew, Z., Paudel, A. & Van Den Mooter, G. Can compression induce demixing in amorphous solid dispersions? A case study of naproxen-PVP K25. *European Journal of Pharmaceutics and Biopharmaceutics* **81**, 207–213 (2012).
112. Yang, Z., Nollenberger, K., Albers, J. & Qi, S. Molecular implications of drug-polymer solubility in understanding the destabilization of solid dispersions by milling. *Mol Pharm* **11**, 2453–2465 (2014).
113. Németh, Z., Sztatisz, J. & Demeter, Á. Polymorph transitions of bicalutamide: A remarkable example of mechanical activation. *J Pharm Sci* **97**, 3222–3232 (2008).
114. Theil, F. *et al.* Frozen in Time : Kinetically Stabilized Amorphous Solid Dispersions of Nifedipine Stable after a Quarter Century of Storage. *Mol Pharm* **14**, 183–192 (2016).
115. Krause, S. & Iskandar, M. Phase Separation in Styrene- $\alpha$ -Methyl Styrene Block Copolymers. in *Polymer Alloys* 231–243 (Springer US, Boston, MA, 1977). doi:10.1007/978-1-4684-0874-4\_15.
116. Newman, A. *et al.* Characterization of Amorphous API:Polymer Mixtures Using X-Ray Powder Diffraction. *J Pharm Sci* **97**, 4840–4856 (2008).
117. Bellantone, R. A. Fundamentals of Amorphous Systems: Thermodynamic Aspects. in *Amorphous Solid Dispersion Technologies Theory and Practice* (eds. Shah, N., Sandhu, H., Choi, D. S. & Chokshi, H.) 3–34 (Springer New York Heidelberg Dordrecht London, 2014). doi:10.1007/978-1-4939-1598-9\_3.
118. Royall, P. G. *et al.* The development of DMA for the detection of amorphous content in pharmaceutical powdered materials. *Int J Pharm* **301**, 181–191 (2005).
119. Li, B., Calvet, A., Casamayou-Boucau, Y., Morris, C. & Ryder, A. G. Low-Content Quantification in Powders Using Raman Spectroscopy: A Facile Chemometric Approach to Sub 0.1% Limits of Detection. *Anal Chem* **87**, 3419–3428 (2015).
120. Shah, B., Kakumanu, V. K. & Bansal, A. K. Analytical techniques for quantification of amorphous/crystalline phases in pharmaceutical solids. *Journal of Pharmaceutical Sciences* vol. 95 1641–1665 Preprint at <https://doi.org/10.1002/jps.20644> (2006).
121. Almeida, J. *et al.* Development and validation of an in-line API quantification method using AQbD principles based on UV-vis spectroscopy to monitor and optimise continuous hot melt extrusion process. *Pharmaceutics* **12**, 150 (2020).

122. Schlindwein, W. *et al.* In-Line UV-Vis Spectroscopy as a Fast-Working Process Analytical Technology (PAT) during Early Phase Product Development Using Hot Melt Extrusion (HME). *Pharmaceutics* **10**, 166 (2018).
123. Strachan, C. J. *et al.* Using terahertz pulsed spectroscopy to quantify pharmaceutical polymorphism and crystallinity. *J Pharm Sci* **94**, 837–846 (2005).
124. Munson, E. Solid-state NMR spectroscopy of drug substances and drug products: an overview. *European Pharmaceutical Review* **25**, 10–13 (2020).
125. Moseson, D. E., Mugheirbi, N. A., Stewart, A. A. & Taylor, L. S. Nanometer-Scale Residual Crystals in a Hot Melt Extruded Amorphous Solid Dispersion: Characterization by Transmission Electron Microscopy. *Cryst Growth Des* **18**, 7633–7640 (2018).
126. Newman, J. A. *et al.* Parts per Million Powder X-ray Diffraction. *Anal Chem* **87**, 10950–10955 (2015).
127. EAG Laboratories. Energy Dispersive X-ray Spectroscopy | EDS Services | EAG Laboratories. <https://www.eag.com/techniques/spectroscopy/energy-dispersive-x-ray-spectroscopy-eds/> (2017).
128. Kollmer, F., Paul, W., Krehl, M. & Niehuis, E. Ultra high spatial resolution SIMS with cluster ions. in *Surface and Interface Analysis* vol. 45 312–314 (John Wiley & Sons, Ltd, 2013).
129. Richardson, M. J. & Savill, N. G. Derivation of accurate glass transition temperatures by differential scanning calorimetry. *Polymer (Guildf)* **16**, 753–757 (1975).
130. Feng Qiana\*, Jun Huanga, Qing Zhub, Raja Haddadina, John Gawel, R. G. *et al.* Is a distinctive single Tg a reliable indicator for the homogeneity of amorphous solid dispersion? *Int J Pharm* **395**, 232–235 (2010).
131. Toye Ojo, A. & Lee, P. I. Applications of Dynamic Mechanical Analysis in the Engineering of Amorphous Solid Dispersions. *Pharmaceut Fronts* **2**, 55–63 (2020).
132. Gupta, P. & Bansal, A. K. Devitrification of amorphous celecoxib. *AAPS PharmSciTech* **6**, (2005).
133. Jones, D. S., Tian, Y., Abu-Diak, O. & Andrews, G. P. Pharmaceutical applications of dynamic mechanical thermal analysis. *Adv Drug Deliv Rev* **64**, 440–448 (2012).
134. Derkaoui, S. M., Avramoglou, T., Barbaud, C. & Letourneur, D. Synthesis and characterization of a new polysaccharide-graft-polymethacrylate copolymer for three-dimensional hybrid hydrogels. *Biomacromolecules* **9**, 3033–3038 (2008).
135. Sarasam, A. R., Krishnaswamy, R. K. & Madihally, S. V. Blending chitosan with polycaprolactone: Effects on physicochemical and antibacterial properties. *Biomacromolecules* **7**, 1131–1138 (2006).

136. Lafferty, S. V., Newton, J. M. & Podczec, F. Characterisation of the mechanical properties of polymer films formed from aqueous polymer dispersions by creep testing. *Int J Pharm* **239**, 143–148 (2002).
137. Yang, M., Wang, P., Suwardie, H. & Gogos, C. Determination of acetaminophen's solubility in poly(ethylene oxide) by rheological, thermal and microscopic methods. *Int J Pharm* **403**, 83–89 (2011).
138. Bhardwaj, S. P. & Suryanarayanan, R. Use of dielectric spectroscopy to monitor molecular mobility in glassy and supercooled trehalose. *Journal of Physical Chemistry B* **116**, 11728–11736 (2012).
139. Valenti, S. *et al.* Amorphous binary dispersions of chloramphenicol in enantiomeric pure and racemic poly-lactic acid: Morphology, molecular relaxations, and controlled drug release. *Int J Pharm* **568**, (2019).
140. Fung, M. H. & Suryanarayanan, R. Use of a Plasticizer for Physical Stability Prediction of Amorphous Solid Dispersions. *Cryst Growth Des* **17**, 4315–4325 (2017).
141. Caron, V., Bhugra, C. & Pikal, M. J. Prediction of onset of crystallization in amorphous pharmaceutical systems: Phenobarbital, nifedipine/PVP, and phenobarbital/PVP. *J Pharm Sci* **99**, 3887–3900 (2010).
142. Shmeis, R. A., Wang, Z. & Krill, S. L. A mechanistic investigation of an amorphous pharmaceutical and its solid dispersions, part I: A comparative analysis by thermally stimulated depolarization current and differential scanning calorimetry. *Pharm Res* **21**, 2025–2030 (2004).
143. Kapourani, A., Valkanioti, V., Kontogiannopoulos, K. N. & Barmpalexis, P. Determination of the physical state of a drug in amorphous solid dispersions using artificial neural networks and ATR-FTIR spectroscopy. *Int J Pharm X* **2**, 100064 (2020).
144. Wlodarski, K. *et al.* Physicochemical properties of tadalafil solid dispersions - Impact of polymer on the apparent solubility and dissolution rate of tadalafil. *European Journal of Pharmaceutics and Biopharmaceutics* **94**, 106–115 (2015).
145. Palermo, R. N., Short, S. M., Anderson, C. A., Tian, H. & Drennen, J. K. Determination of figures of merit for near-infrared, Raman and powder X-ray diffraction by net analyte signal analysis for a compacted amorphous dispersion with spiked crystallinity. *J Pharm Innov* **7**, 56–68 (2012).
146. Padilla, A. M. & Pikal, M. J. The study of phase separation in amorphous freeze-dried systems, part 2: Investigation of raman mapping as a tool for studying amorphous phase separation in freeze-dried protein formulations. *J Pharm Sci* **100**, 1467–1474 (2011).
147. Rumondor, A. C. F. & Taylor, L. S. Application of Partial Least-Squares (PLS) modeling in quantifying drug crystallinity in amorphous solid dispersions. *Int J Pharm* **398**, 155–160 (2010).

148. Rahman, Z., Siddiqui, A., Bykadi, S. & Khan, M. A. Near-infrared and fourier transform infrared chemometric methods for the quantification of crystalline tacrolimus from sustained-release amorphous solid Dispersion. *J Pharm Sci* **103**, 2376–2385 (2014).
149. Bugay, D. E. Characterization of the solid-state: spectroscopic techniques. *Adv Drug Deliv Rev* **48**, 43–65 (2001).
150. Erxleben, A. Application of Vibrational Spectroscopy to Study Solid-state Transformations of Pharmaceuticals. *Curr Pharm Des* **22**, 4883–4911 (2016).
151. Larkin, P. J., Wasylyk, J. & Raglione, M. Application of Low- and Mid-Frequency Raman Spectroscopy to Characterize the Amorphous-Crystalline Transformation of Indomethacin. *Appl Spectrosc* **69**, 1217–1228 (2015).
152. Ibrahim, M., Zhang, J., Repka, M. & Chen, R. Characterization of the Solid Physical State of API and Its Distribution in Pharmaceutical Hot Melt Extrudates Using Terahertz Raman Imaging. *AAPS PharmSciTech* **20**, 1–8 (2019).
153. Tres, F. *et al.* Monitoring the Dissolution Mechanisms of Amorphous Bicalutamide Solid Dispersions via Real-Time Raman Mapping. *Mol Pharm* **12**, 1512–1522 (2015).
154. Zeitler, J. A. *et al.* Terahertz pulsed spectroscopy and imaging in the pharmaceutical setting - a review. *Journal of Pharmacy and Pharmacology* **59**, 209–223 (2010).
155. Smith, G., Hussain, A., Bukhari, N. I. & Ermolina, I. Quantification of residual crystallinity of ball-milled, commercially available, anhydrous  $\beta$ -lactose by differential scanning calorimetry and terahertz spectroscopy. *J Therm Anal Calorim* **121**, 327–333 (2015).
156. Sibik, J., Sargent, M. J., Franklin, M. & Zeitler, J. A. Crystallization and Phase Changes in Paracetamol from the Amorphous Solid to the Liquid Phase. *Mol Pharm* **11**, 1326–1334 (2014).
157. Zeitler, J. A. *et al.* Characterization of temperature-induced phase transitions in five polymorphic forms of sulfathiazole by terahertz pulsed spectroscopy and differential scanning calorimetry. *J Pharm Sci* **95**, 2486–2498 (2006).
158. Purohit, H. S. *et al.* Insights into Nano- and Micron-Scale Phase Separation in Amorphous Solid Dispersions Using Fluorescence-Based Techniques in Combination with Solid State Nuclear Magnetic Resonance Spectroscopy. *Pharm Res* **34**, 1364–1377 (2017).
159. Byrn, S. R., Zografi, G. & Chen, X. S. Solid-State Properties and Pharmaceutical Development. in *Solid State Properties of Pharmaceutical Materials* 1–21 (John Wiley & Sons, Ltd, 2017).
160. Zhu, Q., Harris, M. T. & Taylor, L. S. Time-resolved SAXS/WAXS study of the phase behavior and microstructural evolution of drug/PEG solid dispersions. *Mol Pharm* **8**, 932–939 (2011).

161. Billinge, S. J. L. *et al.* Characterisation of amorphous and nanocrystalline molecular materials by total scattering. *CrystEngComm* **12**, 1366–1368 (2009).
162. Terban, M. W. *et al.* Local Structural Effects Due to Micronization and Amorphization on an HIV Treatment Active Pharmaceutical Ingredient. *Mol Pharm* **17**, 2370–2389 (2020).
163. Iuraş, A. *et al.* Imaging of Crystalline and Amorphous Surface Regions Using Time-of-Flight Secondary-Ion Mass Spectrometry (ToF-SIMS): Application to Pharmaceutical Materials. *Anal Chem* **88**, 3481–3487 (2016).
164. Que, C. *et al.* Insights into the Dissolution Behavior of Ledipasvir-Copovidone Amorphous Solid Dispersions: Role of Drug Loading and Intermolecular Interactions. *Mol Pharm* **16**, 5054–5067 (2019).
165. Lamm, M. S. *et al.* Probing the effect of drug loading and humidity on the mechanical properties of solid dispersions with nanoindentation: Antiplasticization of a polymer by a drug molecule. *Mol Pharm* **9**, 3396–3402 (2012).
166. Ricarte, R. G., Lodge, T. P. & Hillmyer, M. A. Detection of pharmaceutical drug crystallites in solid dispersions by transmission electron microscopy. *Mol Pharm* **12**, 983–990 (2015).
167. Mathers, A., Hassouna, F., Klajmon, M. & Fulem, M. Comparative Study of DSC-Based Protocols for API-Polymer Solubility Determination. *Mol Pharm* **18**, 1742–1757 (2021).
168. Zhou, D., Zhang, G. G. Z., Law, D., Grant, D. J. W. & Schmitt, E. A. Physical stability of amorphous pharmaceuticals: Importance of configurational thermodynamic quantities and molecular mobility. *J Pharm Sci* **91**, 1863–1872 (2002).
169. Graeser, K. A., Patterson, J. E., Zeitler, J. A., Gordon, K. C. & Rades, T. Correlating thermodynamic and kinetic parameters with amorphous stability. *European Journal of Pharmaceutical Sciences* **37**, 492–498 (2009).
170. Bhujbal, S. V. *et al.* Pharmaceutical amorphous solid dispersion: A review of manufacturing strategies. *Acta Pharm Sin B* **11**, 2505–2536 (2021).
171. Bennett-Lenane, H., O’Shea, J. P., O’Driscoll, C. M. & Griffin, B. T. A retrospective biopharmaceutical analysis of >800 approved oral drug products: are drug properties of solid dispersions and lipid-based formulations distinctive? *J Pharm Sci* **109**, 3248–3261 (2020).
172. Lehmkemper, K., Kyeremateng, S. O., Bartels, M., Degenhardt, M. & Sadowski, G. Physical stability of API/polymer-blend amorphous solid dispersions. *European Journal of Pharmaceutics and Biopharmaceutics* **124**, 147–157 (2018).
173. Luebbert, C., Klanke, C. & Sadowski, G. Investigating phase separation in amorphous solid dispersions via Raman mapping. *Int J Pharm* **535**, 245–252 (2018).

174. Mahieu, A., Willart, J.-F. O., Dudognon, E., Danè De, F. & Descamps, M. A New Protocol To Determine the Solubility of Drugs into Polymer Matrixes. (2012) doi:10.1021/mp3002254.
175. Rask, M. B., Knopp, M. M., Olesen, N. E., Holm, R. & Rades, T. Comparison of two DSC-based methods to predict drug-polymer solubility. *Int J Pharm* **540**, 98–105 (2018).
176. Janssens, S. *et al.* Influence of Preparation Methods on Solid State Supersaturation of Amorphous Solid Dispersions: A Case Study with Itraconazole and Eudragit E100. *Pharm Res* **27**, 775–785 (2010).
177. Caron, V., Tajber, L., Corrigan, O. I. & Healy, A. M. A Comparison of Spray Drying and Milling in the Production of Amorphous Dispersions of Sulfathiazole/Polyvinylpyrrolidone and Sulfadimidine/Polyvinylpyrrolidone. *Mol. Pharmaceutics* **8**, 532–542 (2011).
178. Yang, Z. *et al.* The effect of processing on the surface physical stability of amorphous solid dispersions. *European Journal of Pharmaceutics and Biopharmaceutics* **88**, 897–908 (2014).
179. Nanubolu, J. B. & Burley, J. C. Investigating the recrystallization behavior of amorphous paracetamol by variable temperature Raman studies and surface raman mapping. *Mol Pharm* **9**, 1544–1558 (2012).
180. Al-Dulaimi, S., Aina, A. & Burley, J. Rapid polymorph screening on milligram quantities of pharmaceutical material using phonon-mode Raman spectroscopy †. *CrystEngComm* **12**, 1038–1040 (2010).
181. Terao, W. *et al.* Boson peak dynamics of natural polymer starch investigated by terahertz time-domain spectroscopy and low-frequency Raman scattering. *Spectrochim Acta A Mol Biomol Spectrosc* **192**, 446–450 (2018).
182. Singh, R., George, D. K., Benedict, J. B., Korter, T. M. & Markelz, A. G. Improved Mode Assignment for Molecular Crystals Through Anisotropic Terahertz Spectroscopy. *J Phys Chem A* **116**, 10359–10364 (2012).
183. Ma, X. *et al.* Influence of mechanical and thermal energy on nifedipine amorphous solid dispersions prepared by hot melt extrusion: Preparation and physical stability. *Int J Pharm* **561**, 324–334 (2019).
184. Knopp, M. M. *et al.* Comparative Study of Different Methods for the Prediction of Drug-Polymer Solubility. *Mol Pharm* **12**, 3408–3419 (2015).
185. Prasad, E. *et al.* Development of a hot-melt extrusion (HME) process to produce drug loaded Affinisol™ 15LV filaments for fused filament fabrication (FFF) 3D printing. *Addit Manuf* **29**, 100776 (2019).
186. Du, Q., Harding, D. R. & Yang, H. Helical peanut-shaped poly(vinyl pyrrolidone) ribbons generated by electrospinning. *Polymer (Guildf)* **54**, 6752–6759 (2013).

187. Perrin, M.-A., Neumann, M. A., Elmaleh, H. & Zaske, L. Crystal structure determination of the elusive paracetamol Form III. *Chemical Communications* **0**, 3181 (2009).
188. Shekunov, B. Y., Aulton, M. E., Adama-Acquah, R. W. & Grant', D. J. W. *Effect of Temperature on Crystal Growth and Crystal Properties of Paracetamol*. *J. Chem. SOC., Faraday Trans* vol. 92 <https://pubs.rsc.org/en/content/articlepdf/1996/ft/ft9969200439> (1996).
189. Qi, S., Avalle, P., Saklatvala, R. & Craig, D. Q. M. An investigation into the effects of thermal history on the crystallisation behaviour of amorphous paracetamol. *European Journal of Pharmaceutics and Biopharmaceutics* **69**, 364–371 (2008).
190. Qian, F., Huang, J. & Hussain, M. A. Drug-polymer solubility and miscibility: Stability consideration and practical challenges in amorphous solid dispersion development. *J Pharm Sci* **99**, 2941–2947 (2010).
191. Blaabjerg, L. I., Lindenberg, E., Löbmann, K., Grohgan, H. & Rades, T. Is there a correlation between the glass forming ability of a drug and its supersaturation propensity? *Int J Pharm* **538**, 243–249 (2018).
192. Butreddy, A., Bandari, S. & Repka, M. A. Quality-by-design in hot melt extrusion based amorphous solid dispersions: An industrial perspective on product development. *European Journal of Pharmaceutical Sciences* vol. 158 105655 Preprint at <https://doi.org/10.1016/j.ejps.2020.105655> (2021).
193. Tian, Y. *et al.* The investigation of flory-huggins interaction parameters for amorphous solid dispersion across the entire temperature and composition range. *Pharmaceutics* **11**, (2019).
194. Li, S., Tian, Y., Jones, D. S. & Andrews, G. P. Optimising Drug Solubilisation in Amorphous Polymer Dispersions: Rational Selection of Hot-melt Extrusion Processing Parameters. *AAPS PharmSciTech* **17**, 200–213 (2016).
195. Knopp, M. M. *et al.* Comparative Study of Different Methods for the Prediction of Drug–Polymer Solubility. *Mol Pharm* **12**, 3408–3419 (2015).
196. Ousset, A. *et al.* Prediction of phase behavior of spray-dried amorphous solid dispersions: Assessment of thermodynamic models, standard screening methods and a novel atomization screening device with regard to prediction accuracy. *Pharmaceutics* **10**, 29 (2018).
197. Mahieu, A. A. *et al.* A new protocol to determine the solubility of drugs into polymer matrixes. *Mol Pharm* **10**, 560–566 (2013).
198. Donnelly, C., Tian, Y., Potter, C., Jones, D. S. & Andrews, G. P. Probing the Effects of Experimental Conditions on the Character of Drug-Polymer Phase Diagrams Constructed Using Flory-Huggins Theory. *Pharm Res* **32**, 167–179 (2015).
199. Wunderlich, B. *Differential Scanning Calorimetry, Second Edition* By G. W. Höhne (Retired from the Universität Ulm), W. F. Hemminger (Physikalisch-Technische

- Bundesanstalt), and H.-J. Flammersheim (Universität Jena). Springer Verlag: Berlin, Heidelberg, New York. 2003. xii + 298 pp. \$149.00. ISBN 3-540-00467-X. *J Am Chem Soc* **126**, 7411–7412 (2004).
200. Jha, D. K., Shah, D. S. & Amin, P. D. Thermodynamic aspects of the preparation of amorphous solid dispersions of Naringenin with enhanced dissolution rate. *Int J Pharm* **583**, 119363 (2020).
  201. Tian, Y. *et al.* Construction of drug-polymer thermodynamic phase diagrams using flory-huggins interaction theory: Identifying the relevance of temperature and drug weight fraction to phase separation within solid dispersions. *Mol Pharm* **10**, 236–248 (2013).
  202. Zhao, Y., Inbar, P., Chokshi, H. P., Malick, A. W. & Choi, D. S. Prediction of the thermal phase diagram of amorphous solid dispersions by flory-huggins theory. *J Pharm Sci* **100**, 3196–3207 (2011).
  203. Knopp, M. M. *et al.* Comparative Study of Different Methods for the Prediction of Drug-Polymer Solubility. *Mol Pharm* **12**, 3408–3419 (2015).
  204. Mathers, A., Hassouna, F., Klajmon, M. & Fulem, M. Comparative Study of DSC-Based Protocols for API-Polymer Solubility Determination. *Mol Pharm* **18**, 1742–1757 (2021).
  205. Brostow, W., Chiu, R., Kalogeras, I. M. & Vassilikou-Dova, A. Prediction of glass transition temperatures: Binary blends and copolymers. *Mater Lett* **62**, 3152–3155 (2008).
  206. Kwei, T. K., Pearce, E. M. & Min, B. Y. Effect of Hydrogen Bonding on the Lower Critical Solution Temperature of a Polymer Mixture. *Macromolecules* **18**, 2326–2327 (1985).
  207. Iemtsev, A. *et al.* Physical stability of hydroxypropyl methylcellulose-based amorphous solid dispersions: Experimental and computational study. *Int J Pharm* **589**, 119845 (2020).
  208. Meaurio, E. *et al.* Predicting miscibility in polymer blends using the Bagley plot: Blends with poly(ethylene oxide). *Polymer (Guildf)* **113**, 295–309 (2017).
  209. Marsac, P. J. *et al.* Effect of temperature and moisture on the miscibility of amorphous dispersions of felodipine and poly(vinyl pyrrolidone). *J Pharm Sci* **99**, 169–185 (2010).
  210. Pinal, R. Entropy of Mixing and the Glass Transition of Amorphous Mixtures. *Entropy* **10**, 207–223 (2008).
  211. Lu, J. *et al.* Investigation of phase diagrams and physical stability of drug-polymer solid dispersions. *Pharm Dev Technol* **20**, 105–117 (2015).
  212. Forster, A., Hempenstall, J., Tucker, I. & Rades, T. Selection of excipients for melt extrusion with two poorly water-soluble drugs by solubility parameter calculation and thermal analysis. *Int J Pharm* **226**, 147–161 (2001).

213. Leyk, E. & Wesolowski, M. Interactions Between Paracetamol and Hypromellose in the Solid State. *Front Pharmacol* **10**, 1–11 (2019).
214. Mori, T. *et al.* Design of temperature-responsive polymers with enhanced hysteresis:  $\alpha,\alpha$ -disubstituted vinyl polymers. *Langmuir* **26**, 9224–9232 (2010).
215. Repka, M. A. *et al.* Melt extrusion with poorly soluble drugs – An integrated review. *Int J Pharm* **535**, 68–85 (2018).
216. Vaka, S. R. K. *et al.* Excipients for Amorphous Solid Dispersions. in *morphous Solid Dispersions, Advances in Delivery Science and Technology* 123–161 (2014).
217. Brown, C. *et al.* HME for solid dispersions: scale-Up and late-stage development. in *Amorphous Solid Dispersions, Advances in Delivery Science and Technology* 231–260 (2014).
218. Brown, C. *et al.* Hot-Melt Extrusion for Solid Dispersions: Composition and Design Considerations. in *Amorphous Solid Dispersions, Advances in Delivery Science and Technology* 197–230 (2014).
219. Van Renterghem, J. *et al.* Elucidation and visualization of solid-state transformation and mixing in a pharmaceutical mini hot melt extrusion process using in-line Raman spectroscopy. *Int J Pharm* **517**, 119–127 (2017).
220. Li, M., Gogos, C. G. & Ioannidis, N. Improving the API dissolution rate during pharmaceutical hot-melt extrusion I: Effect of the API particle size, and the co-rotating, twin-screw extruder screw configuration on the API dissolution rate. *Int J Pharm* **478**, 103–112 (2015).
221. Yang, Z., Nollenberger, K., Albers, J., Craig, D. & Qi, S. Microstructure of an Immiscible Polymer Blend and Its Stabilization Effect on Amorphous Solid Dispersions. *Mol Pharm* **10**, 2767–2780 (2013).
222. Li, P., Batey, D. & Rodenburg, J. An X-ray ptycho-tomography model of ‘Seeing order in “amorphous” materials’’. *Ultramicroscopy* **203**, 88–94 (2019).
223. Nommeots-Nomm, A. *et al.* Four-dimensional imaging and quantification of viscous flow sintering within a 3D printed bioactive glass scaffold using synchrotron X-ray tomography. *Materials Today Advances* vol. 2 (2019).
224. Jafarnejad, M. *et al.* Quantification of the Whole Lymph Node Vasculature Based on Tomography of the Vessel Corrosion Casts. *Sci Rep* **9**, 13380 (2019).
225. Croton, L. C. P. *et al.* In situ phase contrast X-ray brain CT. *Sci Rep* **8**, (2018).
226. Disney, C. M. *et al.* Synchrotron tomography of intervertebral disc deformation quantified by digital volume correlation reveals microstructural influence on strain patterns. *Acta Biomater* **92**, 290–304 (2019).
227. Mayo, S. C., Stevenson, A. W. & Wilkins, S. W. In-Line Phase-Contrast X-ray Imaging and Tomography for Materials Science. *Materials* **5**, 937–965 (2012).

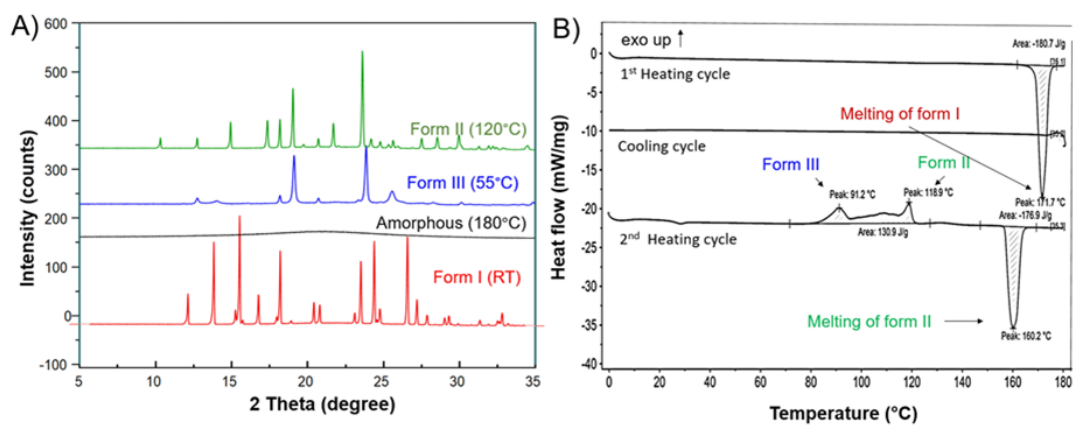
228. Marathe, S. *et al.* Development of synchrotron pink beam x-ray grating interferometer at the Diamond Light source I13-2 beamline. in *Developments in X-Ray Tomography XII* (eds. Müller, B. & Wang, G.) vol. 11113 42 (SPIE, 2019).
229. Rau, C. Imaging with Coherent Synchrotron Radiation: X-ray Imaging and Coherence Beamline (I13) at Diamond Light Source, Synchrotron Radiation News. *Technical RepoRTs Synchrotron radiation news* **30**, 19–25 (2017).
230. Rau, C. *et al.* Fast Multi-scale imaging using the Beamline I13L at the Diamond Light Source. in *Developments in X-Ray Tomography XII* (eds. Müller, B. & Wang, G.) vol. 11113 68 (SPIE, 2019).
231. Otsu, N. A Threshold Selection Method from Gray-Level Histograms. *IEEE Trans Syst Man Cybern C*, 62–66 (1979).
232. Zhang, H., Fritts, J. E. & Goldman, S. A. Image segmentation evaluation: A survey of unsupervised methods. *Computer Vision and Image Understanding* **110**, 260–280 (2008).
233. Measure properties of 3-D volumetric image regions - MATLAB regionprops3 - MathWorks United Kingdom.  
<https://uk.mathworks.com/help/images/ref/regionprops3.html>.
234. Axelsson, M. & Svensson, S. 3D pore structure characterisation of paper. *Pattern Analysis and Applications* **13**, 159–172 (2010).
235. Markl, D. *et al.* Characterization of the Pore Structure of Functionalized Calcium Carbonate Tablets by Terahertz Time-Domain Spectroscopy and X-Ray Computed Microtomography. *J Pharm Sci* **106**, 1586–1595 (2017).
236. Blott, S. J. & Pye, K. Particle shape: A review and new methods of characterization and classification. *Sedimentology* **55**, 31–63 (2008).
237. Bordos, E., Islam, M. T., Florence, A. J., Halbert, G. W. & Robertson, J. Use of Terahertz-Raman Spectroscopy to Determine Solubility of the Crystalline Active Pharmaceutical Ingredient in Polymeric Matrices during Hot Melt Extrusion. *Mol Pharm* **16**, 4361–4371 (2019).
238. Moseson, D. E. *et al.* Dissolution of Indomethacin Crystals into a Polymer Melt: Role of Diffusion and Fragmentation. *Cryst Growth Des* **19**, 3315–3328 (2019).
239. Qi, S. *et al.* Characterisation and prediction of phase separation in hot-melt extruded solid dispersions: A thermal, microscopic and NMR relaxometry study. *Pharm Res* **27**, 1869–1883 (2010).
240. Luebbert, C., Huxoll, F., Sadowski, G., Van Den Mooter, G. & Grohgan, H. Amorphous-amorphous phase separation in API/polymer formulations. *Molecules* **22**, 1–17 (2017).
241. Kawakami, K., Bi, Y., Yoshihashi, Y., Sugano, K. & Terada, K. Time-dependent phase separation of amorphous solid dispersions: Implications for accelerated stability studies. *J Drug Deliv Sci Technol* **46**, 197–206 (2018).

242. Lamm, M. S., DiNunzio, J., Khawaja, N. N., Crocker, L. S. & Pecora, A. Assessing Mixing Quality of a Copovidone-TPGS Hot Melt Extrusion Process with Atomic Force Microscopy and Differential Scanning Calorimetry. *AAPS PharmSciTech* **17**, 89–98 (2016).
243. Uetani, K. & Hatori, K. Thermal conductivity analysis and applications of nanocellulose materials. *Sci Technol Adv Mater* **18**, 877–892 (2017).
244. Gupta, S. S., Solanki, N. & Serajuddin, A. T. M. Investigation of Thermal and Viscoelastic Properties of Polymers Relevant to Hot Melt Extrusion, IV: Affinisol™ HPMC HME Polymers. *AAPS PharmSciTech* **17**, 148–157 (2016).
245. Khatri, P., Katikaneni, P., Desai, D. & Minko, T. Evaluation of Affinisol® HPMC polymers for direct compression process applications. *J Drug Deliv Sci Technol* **47**, 461–467 (2018).
246. Jain, A. K. *et al.* The influence of hydroxypropyl methylcellulose (HPMC) molecular weight, concentration and effect of food on in vivo erosion behavior of HPMC matrix tablets. *Journal of Controlled Release* **187**, 50–58 (2014).
247. Meere, M., Pontrelli, G. & McGinty, S. Modelling phase separation in amorphous solid dispersions. *Acta Biomater* **94**, 410–424 (2019).
248. Markl, D. *et al.* Characterisation of pore structures of pharmaceutical tablets: A review. *Int J Pharm* **538**, 188–214 (2018).
249. Naftaly, M., Tikhomirov, I., Hou, P. & Markl, D. Measuring open porosity of porous materials using thz-tds and an index-matching medium. *Sensors (Switzerland)* **20**, (2020).
250. Rouquerol, J. *et al.* Recommendations for the characterization of porous solids. *Pure and Applied Chemistry* **66**, 1739–1758 (1994).
251. Jeromenok, J. & Weber, J. Restricted access: On the nature of adsorption/desorption hysteresis in amorphous, microporous polymeric materials. *Langmuir* **29**, 12982–12989 (2013).
252. Yuan, D., Getman, R. B., Wei, Z., Snurr, R. Q. & Zhou, H. C. Stepwise adsorption in a mesoporous metal-organic framework: Experimental and computational analysis. *Chemical Communications* **48**, 3297–3299 (2012).
253. Landers, J., Gor, G. Y. & Neimark, A. V. Density functional theory methods for characterization of porous materials. *Colloids Surf A Physicochem Eng Asp* **437**, 3–32 (2013).
254. Zhu, L., Jona, J., Nagapudi, K. & Wu, T. Fast surface crystallization of amorphous griseofulvin below T<sub>g</sub>. *Pharm Res* **27**, 1558–1567 (2010).
255. Wu, T., Sun, Y., Li, N., De Villiers, M. M. & Yu, L. Inhibiting surface crystallization of amorphous indomethacin by nanocoating. *Langmuir* **23**, 5148–5153 (2007).

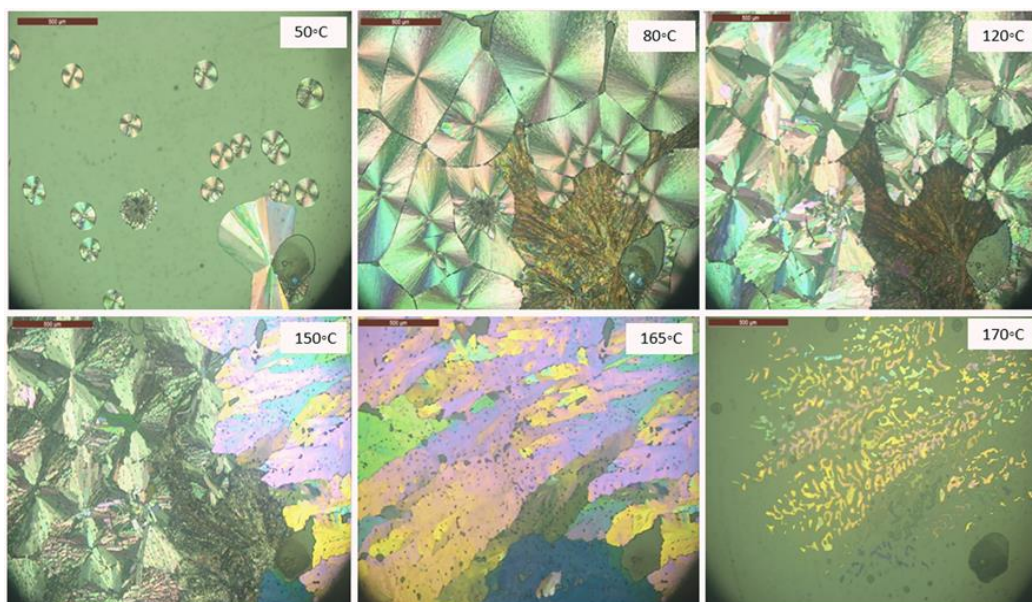
256. Wu, T. & Yu, L. Surface crystallization of indomethacin below  $T_g$ . *Pharm Res* **23**, 2350–2355 (2006).
257. Zhu, L., Wong, L. & Yu, L. Surface-enhanced crystallization of amorphous nifedipine. *Mol Pharm* **5**, 921–926 (2008).
258. Bhujbal, S. V. *et al.* Qualitative and quantitative characterization of composition heterogeneity on the surface of spray dried amorphous solid dispersion particles by an advanced surface analysis platform with high surface sensitivity and superior spatial resolution. *Mol Pharm* **15**, 2045–2053 (2018).
259. Barnes, T. J., Kempson, I. M. & Prestidge, C. A. Surface analysis for compositional, chemical and structural imaging in pharmaceuticals with mass spectrometry: A ToF-SIMS perspective. *Int J Pharm* **417**, 61–69 (2011).
260. Scoutaris, N. *et al.* ToF-SIMS analysis of chemical heterogeneities in inkjet micro-array printed drug/polymer formulations. *J Mater Sci Mater Med* **23**, 385–391 (2012).
261. Ottoboni, S. *et al.* Impact of Paracetamol Impurities on Face Properties: Investigating the Surface of Single Crystals Using TOF-SIMS. *Cryst Growth Des* **18**, 2750–2758 (2018).
262. Paladino, E. *et al.* High spatial resolution ToF-SIMS imaging and image analysis strategies to monitor and quantify early phase separation in amorphous solid dispersions. *Int J Pharm* **628**, 122191 (2022).
263. Feng, X. *et al.* Evaluation of the recrystallization kinetics of hot-melt extruded polymeric solid dispersions using an improved Avrami equation. *Drug Dev Ind Pharm* **41**, 1479–1487 (2015).
264. Yang, J., Grey, K. & Doney, J. An improved kinetics approach to describe the physical stability of amorphous solid dispersions. *Int J Pharm* **384**, 24–31 (2010).
265. Avrami, M. Kinetics of phase change. II Transformation-time relations for random distribution of nuclei. *J Chem Phys* **8**, 212–224 (1940).
266. Avrami, M. Kinetics of phase change. I: General theory. *J Chem Phys* **7**, 1103–1112 (1939).
267. Yang, J., Grey, K. & Doney, J. An improved kinetics approach to describe the physical stability of amorphous solid dispersions. *Int J Pharm* **384**, 24–31 (2010).
268. Wu, T. & Yu, L. Surface crystallization of indomethacin below  $T_g$ . *Pharm Res* **23**, 2350–2355 (2006).
269. Mosharraf, M. Assessment of degree of disorder (amorphicity) of lyophilized formulations of growth hormone using isothermal microcalorimetry. *Drug Dev Ind Pharm* **30**, 461–472 (2004).
270. Yoshioka, M., Hancock, B. C. & Zografi, G. Crystallization of Indomethacin from the Amorphous State below and above Its Glass Transition Temperature. *J Pharm Sci* **83**, 1700–1705 (1994).

271. Shi, L. & Sun, C. C. Subsurface nucleation of supercooled acetaminophen. *CrystEngComm* **20**, 6867–6870 (2018).
272. Huang, S. *et al.* A New Extrudable Form of Hypromellose: AFFINISOL™ HPMC HME. *AAPS PharmSciTech* **17**, 106–119 (2016).
273. Perkins, M. J. & Langford, V. S. Application of Routine Analysis Procedures to a Direct Mass Spectrometry Technique: Selected Ion Flow Tube Mass Spectrometry (SIFT-MS) Reviews in Separation Sciences. *Rev. Sep. Sci* **3**, 21003 (2021).
274. Hastie, C. *et al.* Selected ion flow tube-mass spectrometry (sift-ms) as an alternative to gas chromatography/mass spectrometry (gc/ms) for the analysis of cyclohexanone and cyclohexanol in plasma. *ACS Omega* **6**, 32818–32822 (2021).
275. Wang, M. H. *et al.* Use of a least absolute shrinkage and selection operator (LASSO) model to selected ion flow tube mass spectrometry (SIFT-MS) analysis of exhaled breath to predict the efficacy of dialysis: a pilot study. *J Breath Res* **10**, 046004 (2016).
276. Storer, M., Salmond, J., Dirks, K. N., Kingham, S. & Epton, M. Mobile selected ion flow tube mass spectrometry (SIFT-MS) devices and their use for pollution exposure monitoring in breath and ambient air–pilot study. *J Breath Res* **8**, 037106 (2014).
277. Olivares, A., Dryahina, K., Španěl, P. & Flores, M. Rapid detection of lipid oxidation in beef muscle packed under modified atmosphere by measuring volatile organic compounds using SIFT-MS. *Food Chem* **135**, 1801–1808 (2012).

## APPENDIX A – Additional data for Chapter 2

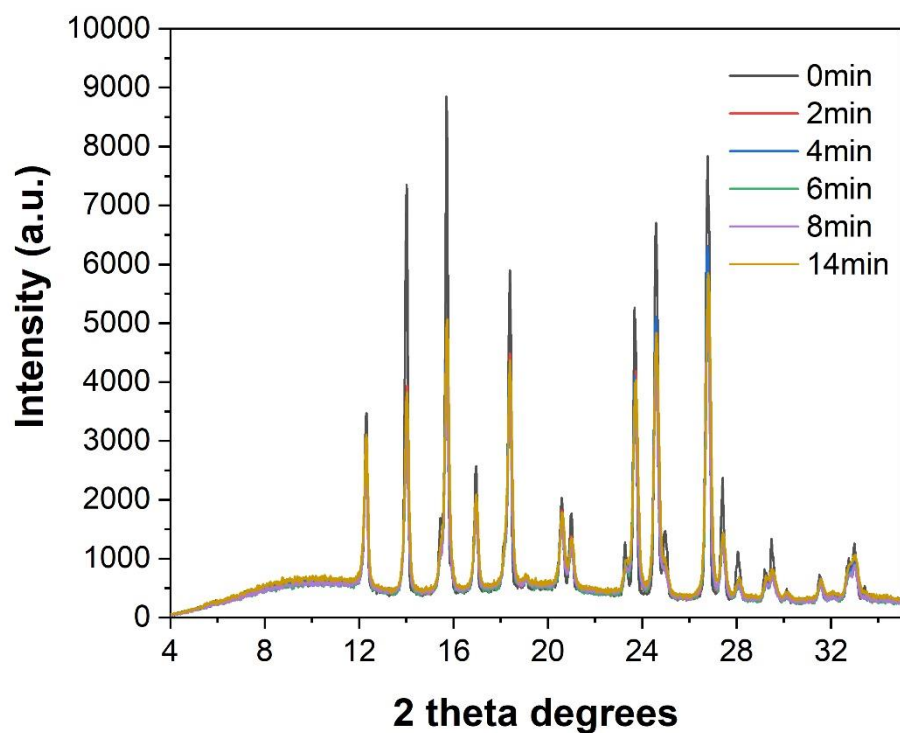


A 1. A) XRPD patterns and B) DSC thermograms of amorphous PCM and crystalline forms III, II and I with respective recrystallisation temperatures from the amorphous glass



A 2. Hot stage microscopy images showing thermally induced recrystallisation from the amorphous glass. PCM form III (identified by the characteristic spherulitic morphology) recrystallised at 50°C and experienced a solid-state transition to form II at 120°C, which was followed by polymorphic transition to form at 150°C, prior to melting at 170°C.

## APPENDIX B – Additional data for Chapter 3



B 1. XRPD of ball milled physical mixtures.

B 2. Physico-chemical properties used in the F-H and E-M calculations.

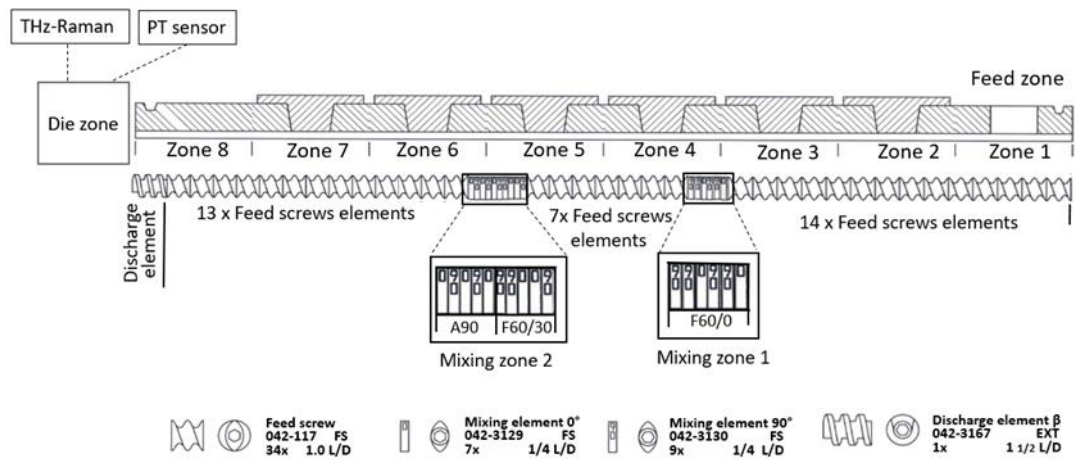
Component	Molecular weight <sup>a</sup> (g/mol)	Melting point <sup>b</sup> , T <sub>M</sub> (°C)	Glass transition, T <sub>g</sub> (°C)	Melting enthalpy <sup>b</sup> ΔH <sub>M</sub> (kJ/mol)	True density <sup>b</sup> (g/mol)	Molecular volume (cm <sup>3</sup> /mol) <sup>c</sup>
PCM	151,163	170.1 ± 0.18	24.7 ± 0.4	27.45	1.288	116.45
EPO	47,000		54.9 ± 2.95		1.186	39,830
PVA	32,000		67.55 ± 0.21		1.292	24,806
AFF	85,000		104.45 ± 6.43		1.24	68,548
PLSD	47,000		110.4 ± 0.84		0.975	48,205
SOL	118,000		73.6 ± 3.25		1.153	102,611

<sup>a</sup> Information provided by the supplier; <sup>b</sup> measured in this study; <sup>c</sup> calculated by dividing molecular weight by true density.

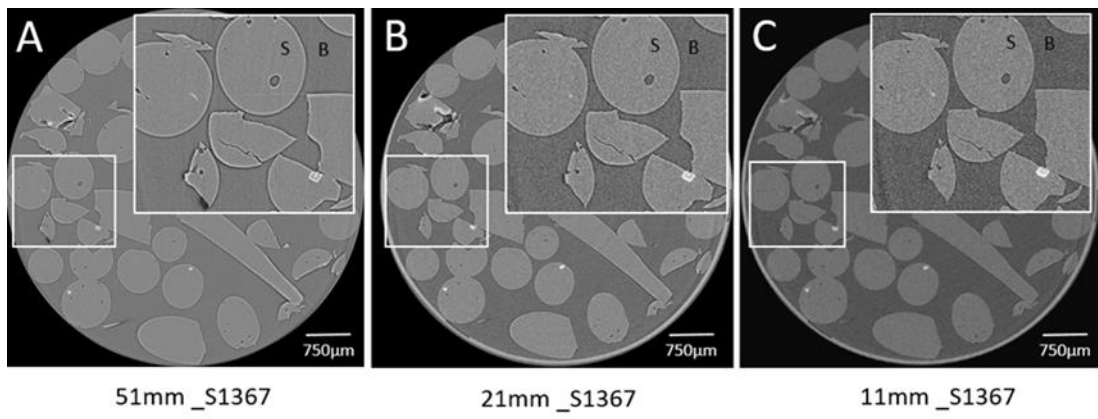
B 3. Hansen solubility parameters.

<b>Component</b>	<b><math>\delta_D</math></b>	<b><math>\delta_P</math></b>	<b><math>\delta_H</math></b>	<b><math>\delta_V</math></b>	<b><math>\delta_{Total}</math></b>	<b><math>\Delta\delta_{Total}</math></b>
PCM	20.2	13.3	14.4	24.18	28.1	-
PLSD	18.44	8.58	8.22	20.33	21.93	6.16
SOL	18.244	7.84	8.424	19.85	21.57	6.52
AFF	16.335	8.25	8.448	18.30	20.15	7.94
PVA	20	12.6	22.4	23.63	32.6	4.5
EPO	16.55	3.975	5.95	17.02	18.03	10.06

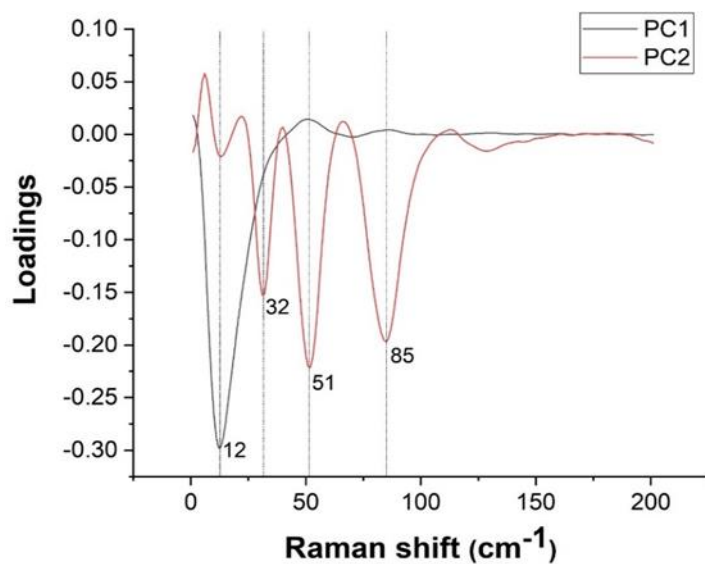
## APPENDIX C – Additional data for Chapter 4



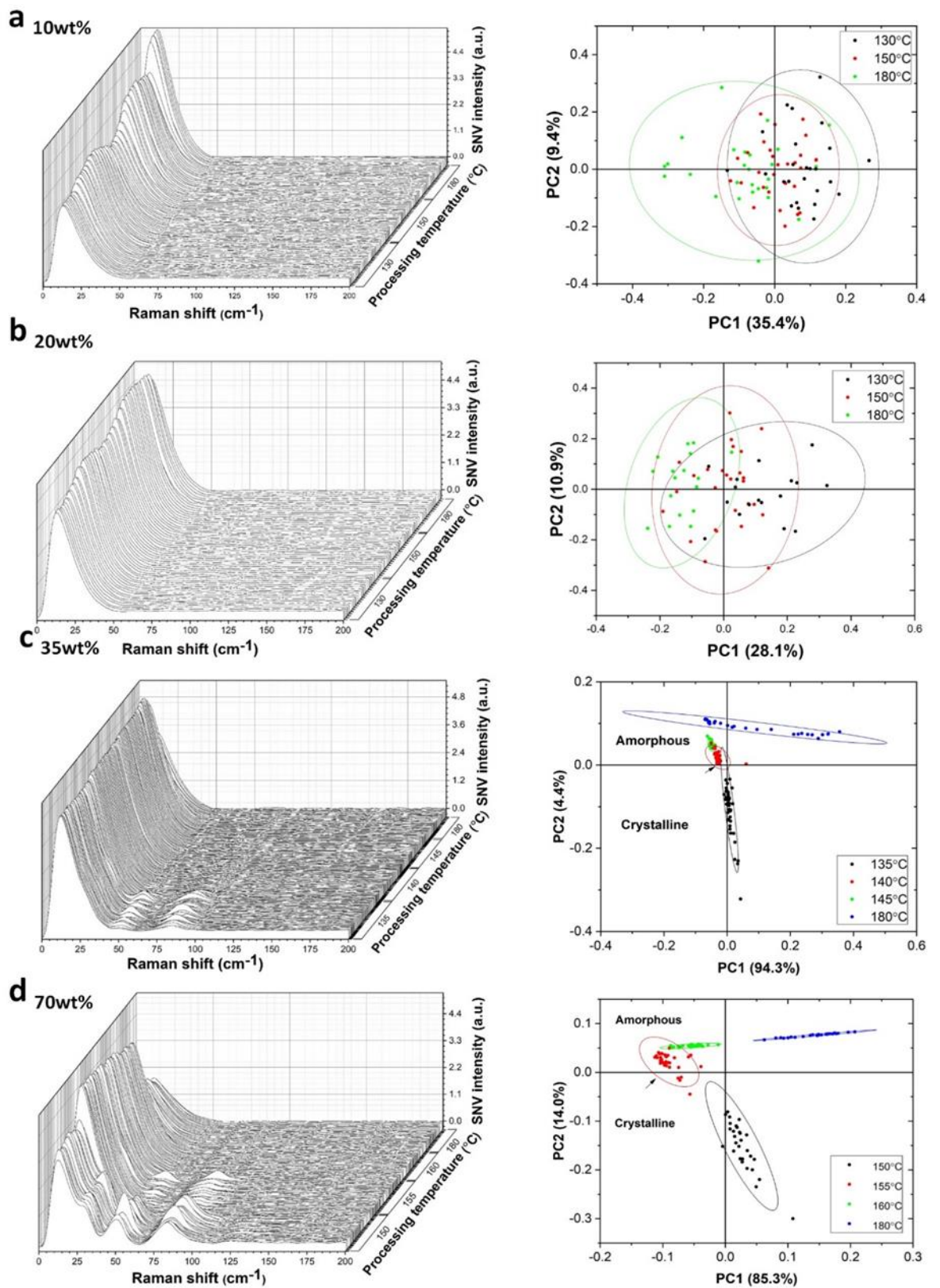
C 1. Schematic representation of the HME set-up and screw configuration.



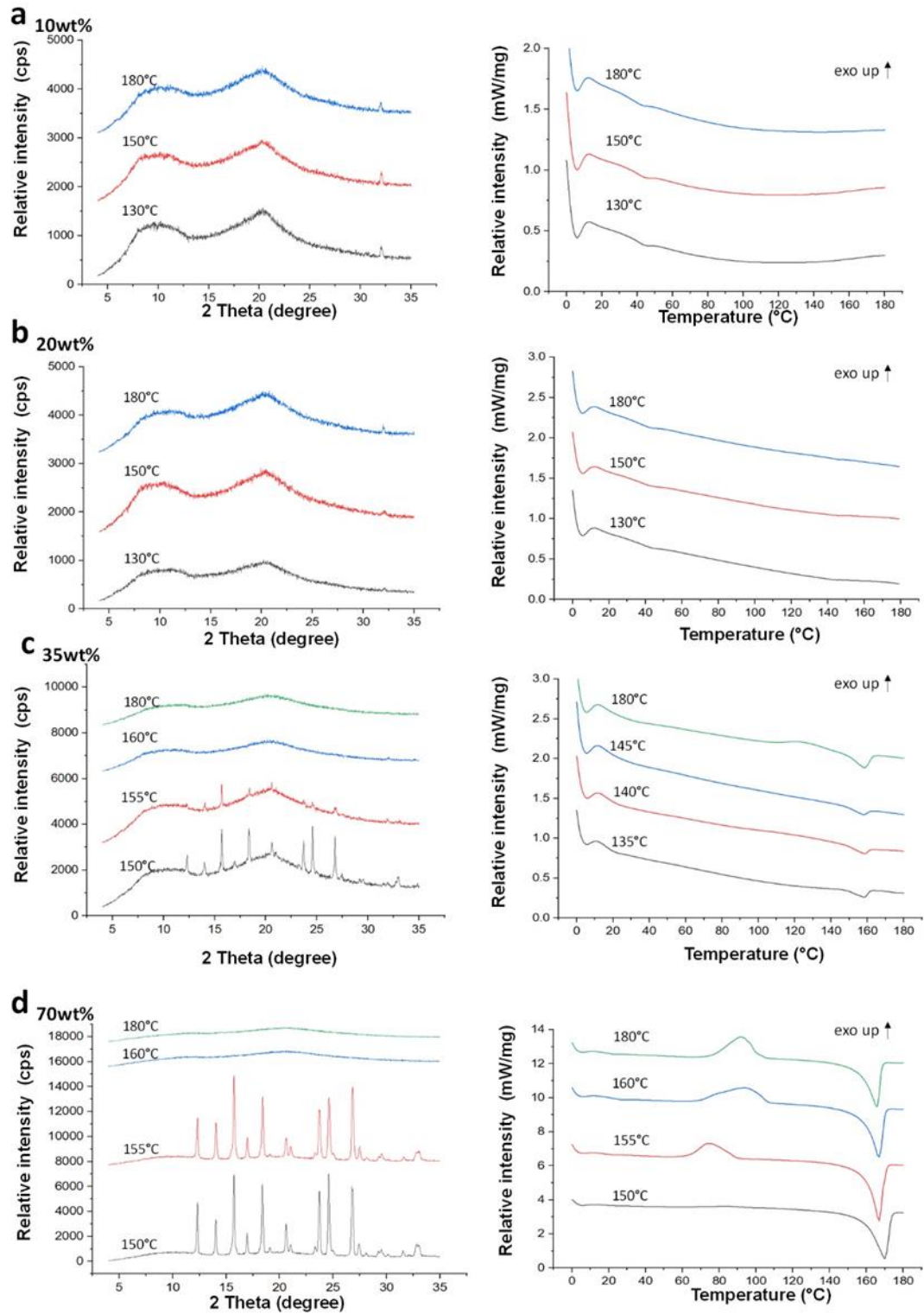
C 2. Example of the sample-to-detector distance optimisation: A) tomograms acquired at a distance of 51 mm from the sample, B) at 21 mm and C) at 11 mm for the 50wt% drug-loading system extruded at 180°C



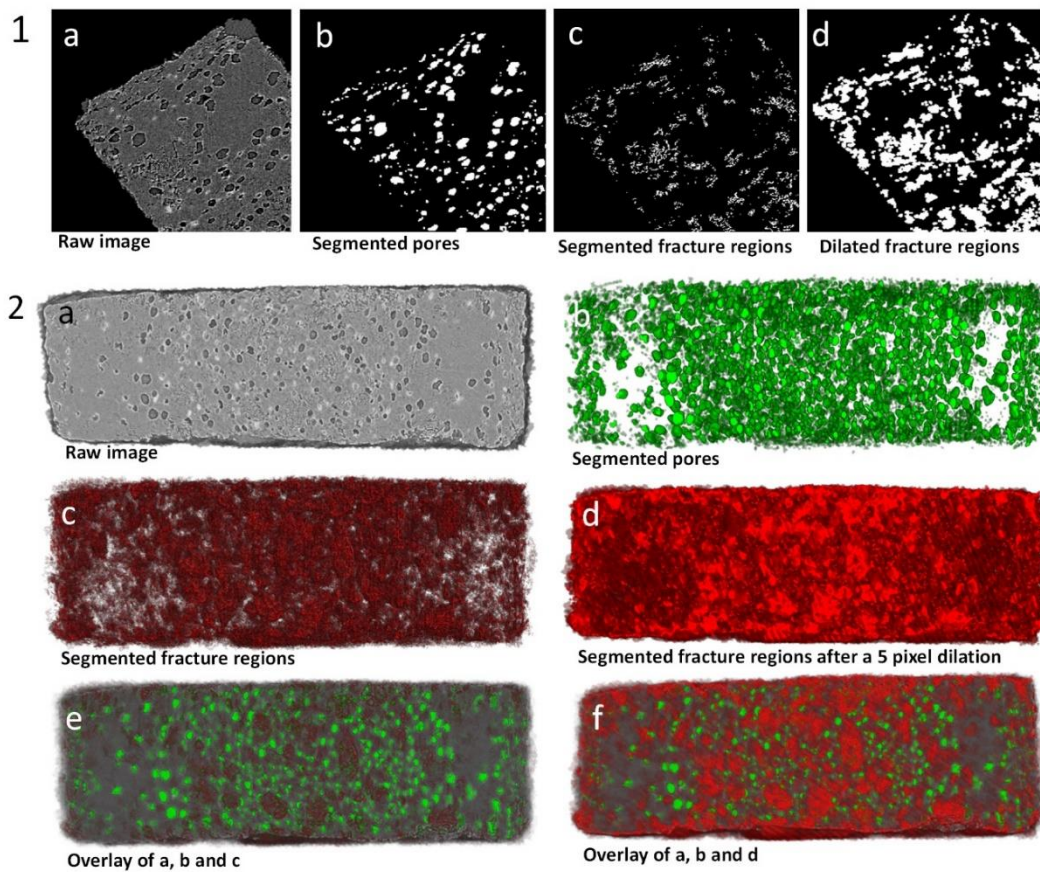
C 3. Loading plot of the PCA results showing that the principal component 1 (PC1) describes the broad amorphous shoulder with peak maxima at  $12\text{cm}^{-1}$ , while the principal component 2 (PC2) mainly captures the API's crystalline lattice vibration modes at  $32, 51, 85\text{ cm}^{-1}$ .



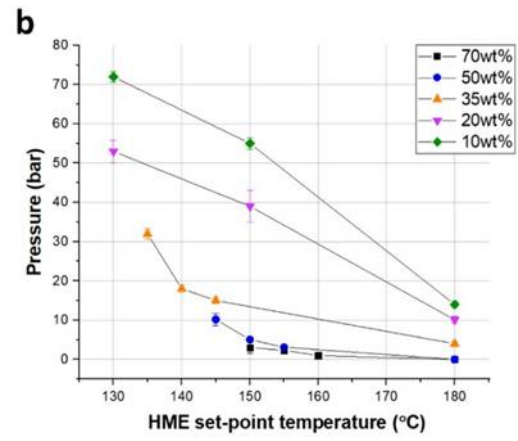
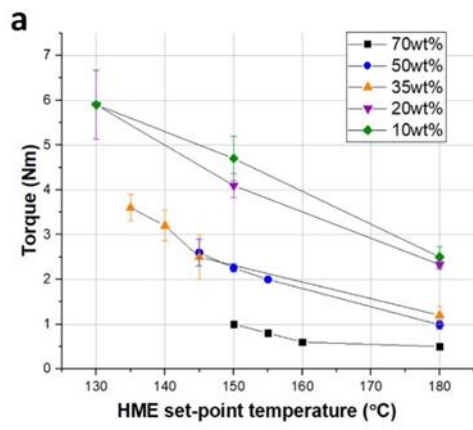
C 4. THz-Raman spectral data and PCA outputs of a) 10wt%, b) 20wt%, c) 35wt% and d) 70wt% drug loading systems extruded at different temperatures. The black arrow denotes the API crystallinity onset temperature. For the 10wt% and 20wt% systems there was no crystalline API detected at any extruding temperatures



C 5. XRD and DSC analysis of the a) 10wt%, b) 20wt%, c) 35wt% and d) 70wt% drug loading systems extruded at different temperatures.



C 6. Image processing sequence for the segmentation of the API-rich crystalline clusters in (1) 2D and (2) 3D of the 6-months aged 50wt% drug-loading system.



C 7. Processing torque (a) and pressure (b) values at all HME experimental conditions. The HME device has a maximum torque and pressure of 12 Nm and 100 bar respectively.

C 8. Statistical analysis of the impact of processing temperature on porosity.

<b>Welch ANOVA Test <sup>a</sup></b>				
Drug loading (wt%)	Compared levels <sup>b</sup>	F-value	P-value	Significantly different
10	130, 150, 180	394.91	<0.001	Yes
20	130, 150, 180	27.54	<0.001	Yes
35	135, 140, 145, 180	226.15	<0.001	Yes
50	145, 150, 155, 180	2638.69	<0.001	Yes

<sup>a</sup> Impact of processing temperature assessed per drug loading.

<sup>b</sup> Compared levels refer to HME processing temperature (°C)

C 9. Games-Howell pairwise statistical analysis of the impact of processing temperature on porosity.

<b>Games-Howell Pairwise Comparison</b>				
Drug loading (wt%)	Compared levels	T-value	P-value	Significantly different
10	180°C-150°C	-0.14	0.989	<b>No</b>
	150°C-130°C	-18.24	<0.001	Yes
	180°C-130°C	-27.14	<0.001	Yes
20	180°C-150°C	-2.38	0.045	Yes
	150°C-130°C	-7.42	<0.001	Yes
	180°C-130°C	-5.48	<0.001	Yes
35	180°C-145°C	10.13	<0.001	Yes
	145°C-140°C	-18.40	<0.001	Yes
	140°C-135°C	5.29	<0.001	Yes
	135°C-180°C	-18.22	<0.001	Yes
	180°C-140°C	-18.40	<0.001	Yes
	145°C-135°C	-17.36	<0.001	Yes
50	180°C-155°C	-51.17	<0.001	Yes
	155°C-150°C	-10.60	<0.001	Yes
	150°C-145°C	20.07	<0.001	Yes
	180°C-145°C	-58.96	<0.001	Yes
	145°C-155°C	4.75	<0.001	Yes
	180°C-150°C	-85.31	<0.001	Yes

C 10. Impact of drug loading on porosity: Welch ANOVA statistical analysis.

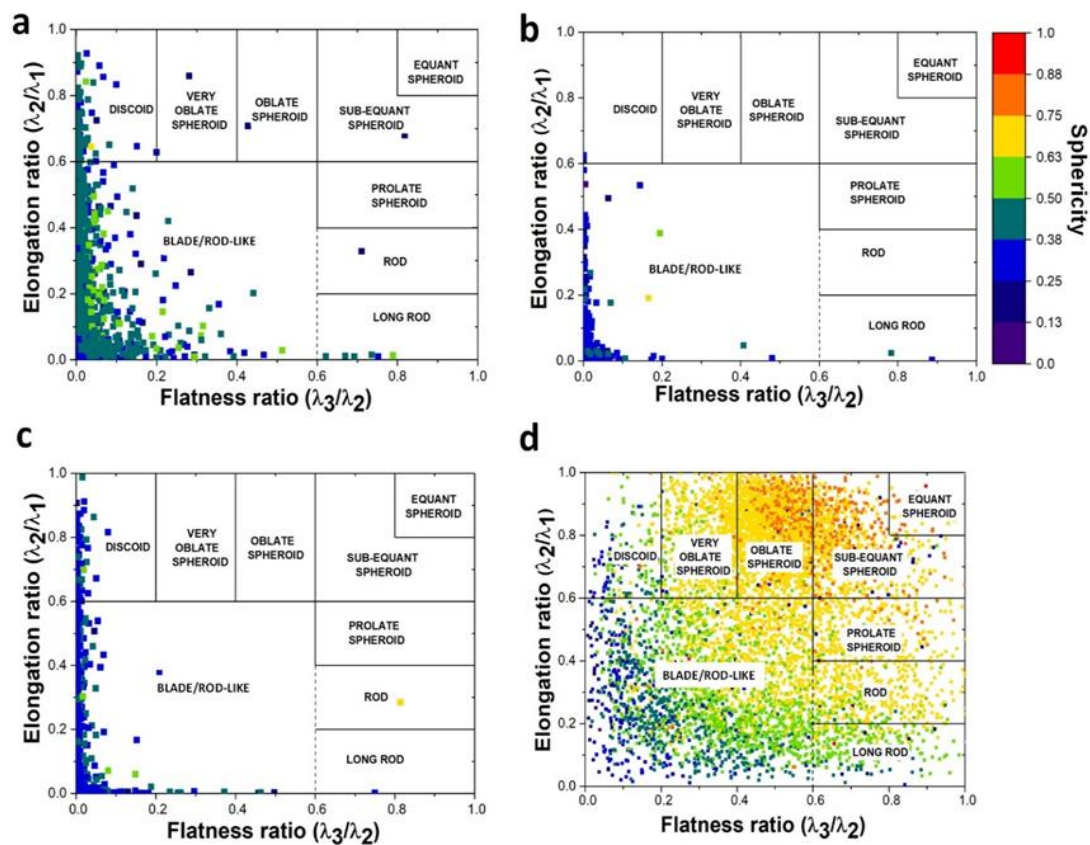
<b>Welch ANOVA Test<sup>a</sup></b>				
Processing regime	Compared levels <sup>b</sup>	F-value	P-value	Significantly different
Melting	10, 20, 35 and 50	6331.80	<0.001	Yes
Dissolution	10, 20, 35 and 50	310.35	<0.001	Yes
Suspension	35 and 50	1653.55	<0.001	Yes

<sup>a</sup> Impact of drug loading assessed per processing regime.

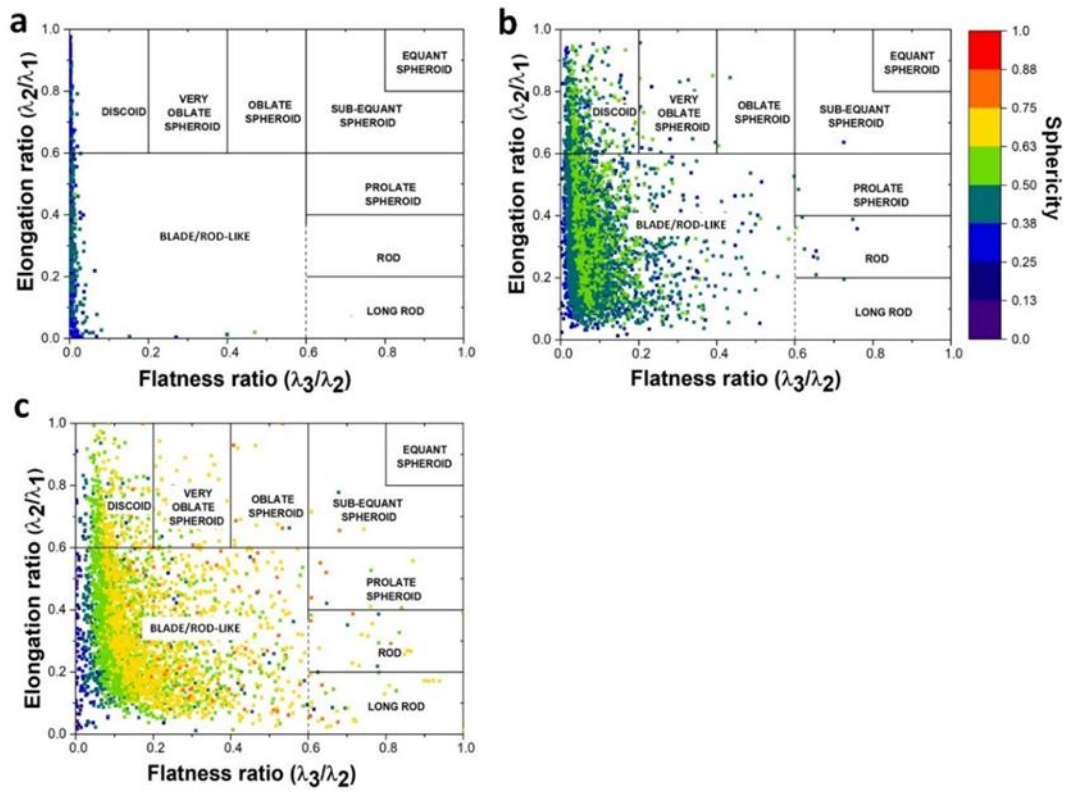
<sup>b</sup> Compared levels refers to drug loading (wt%).

C 11. Impact of porosity quantification method on total porosity: Welch ANOVA statistical analysis.

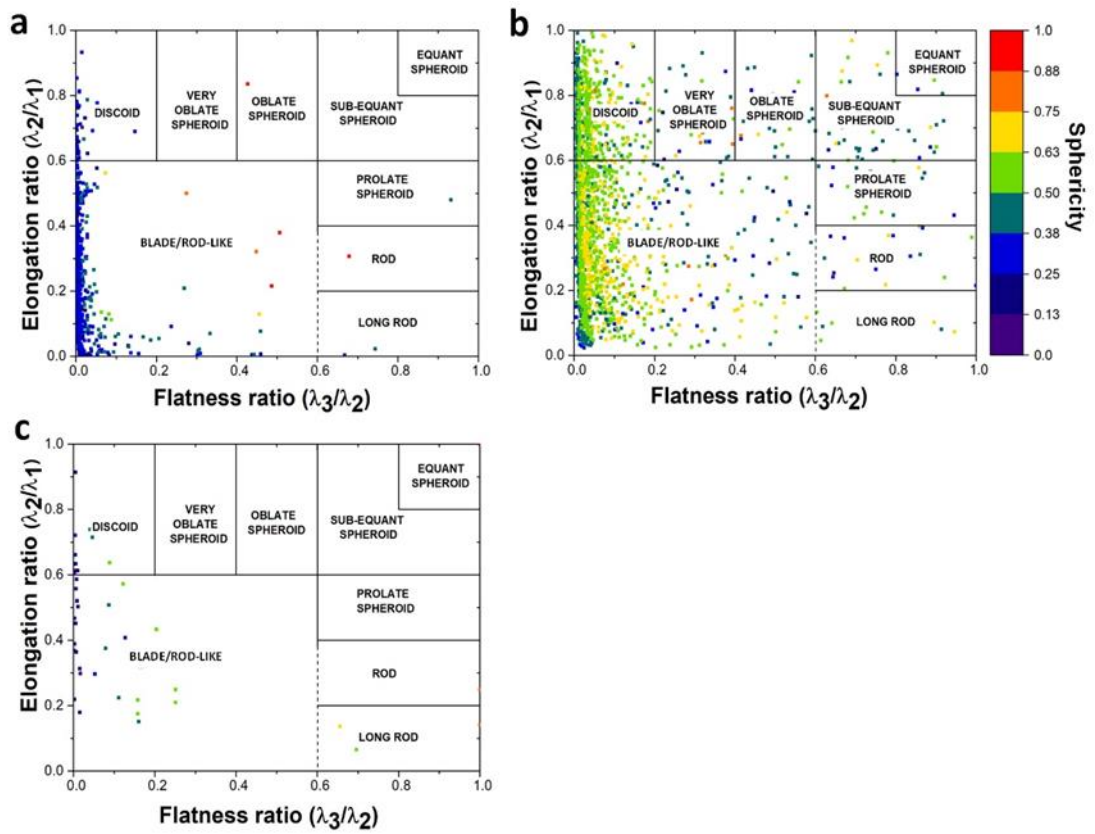
<b>Welch ANOVA Test</b>				
Drug loading (wt%)	Compared levels	F-value	P-value	Significantly different
10	2D and 3D	1.71	0.320	No
20	2D and 3D	0.03	0.877	No
35	2D and 3D	0.52	0.510	No
50	2D and 3D	<0.001	0.997	No



C 12. Shape analysis of the 35wt% drug loading systems extruded at a) 180°C, b) 145°C, c) 140°C and d) 135°C.

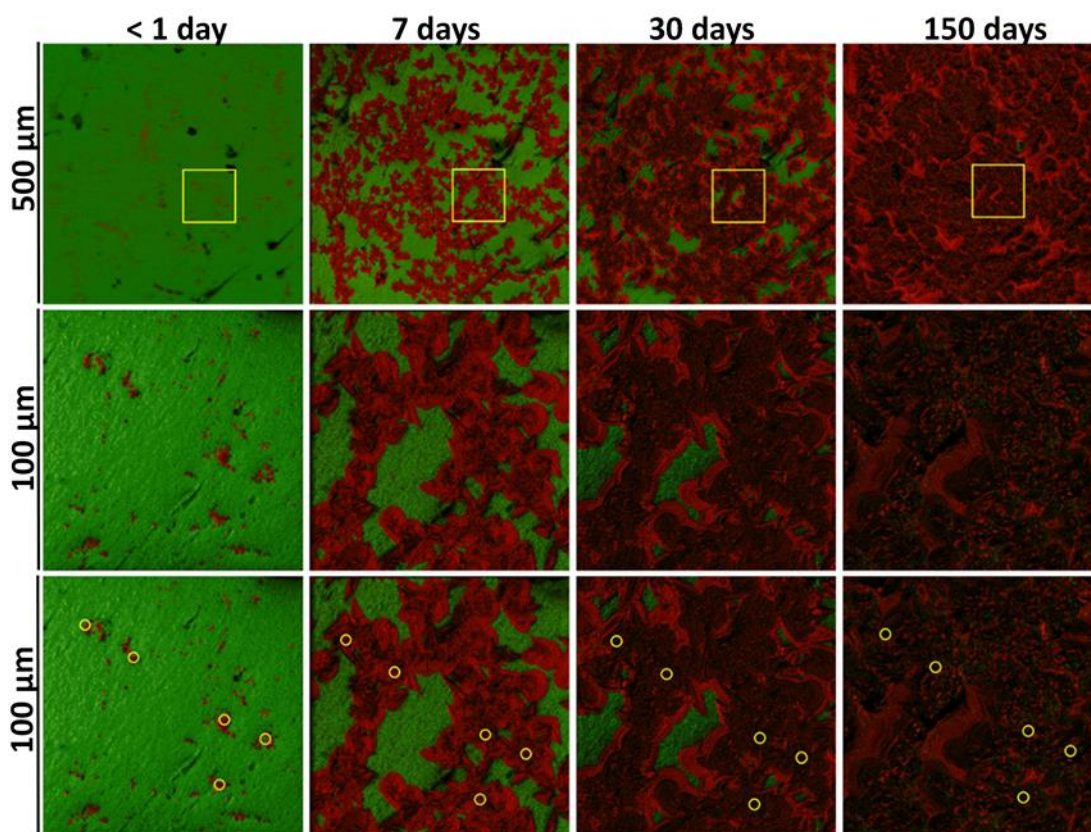


C 13. Shape analysis of the 20wt% drug loading systems extruded at a) 180°C, b) 150°C and c) 130°C.

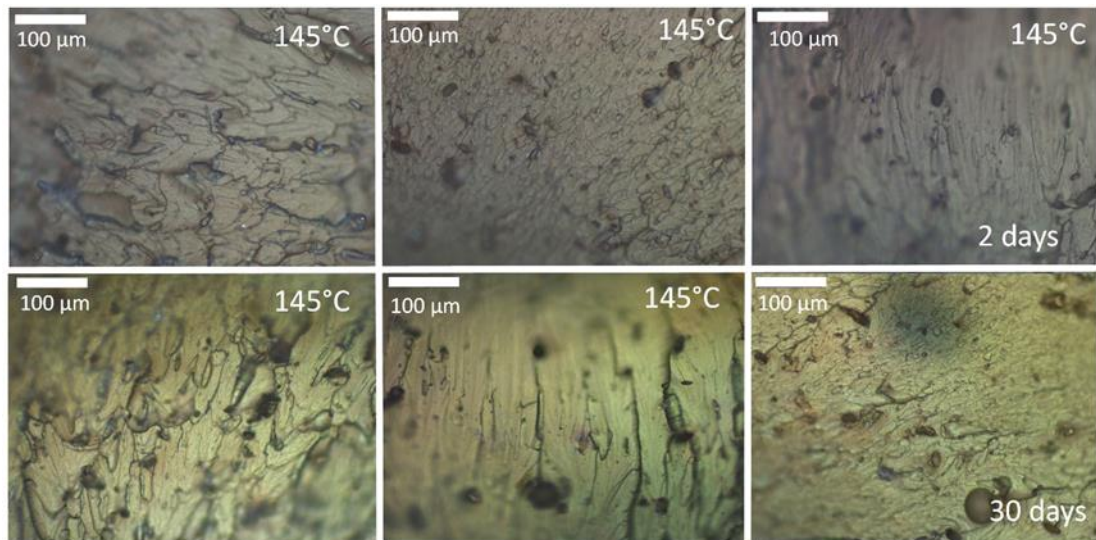


C 14. Shape analysis of the 10wt% drug loading systems extruded at a) 180°C, b) 150°C and c) 130°C.

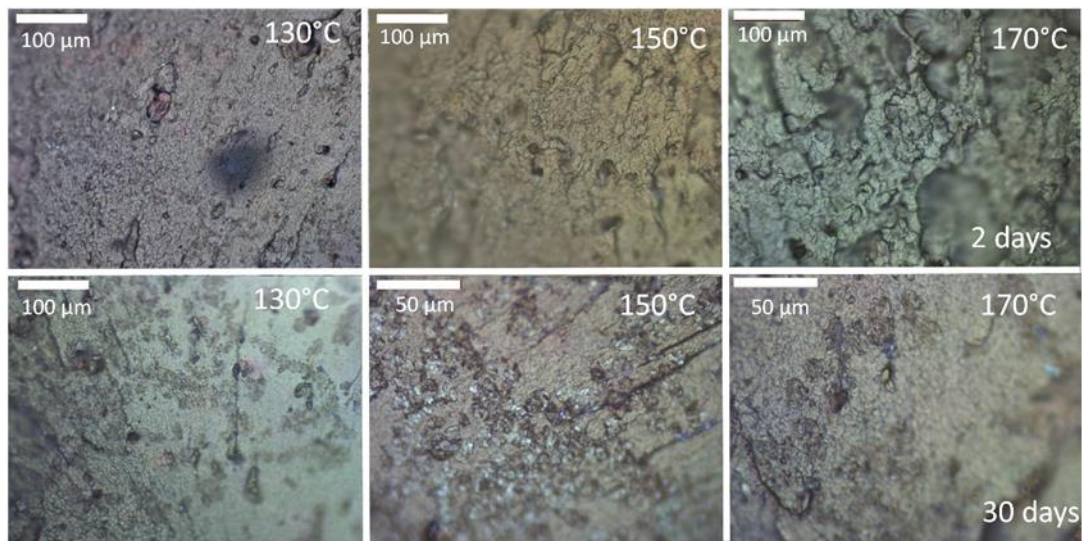
## APPENDIX D – Additional data for Chapter 5



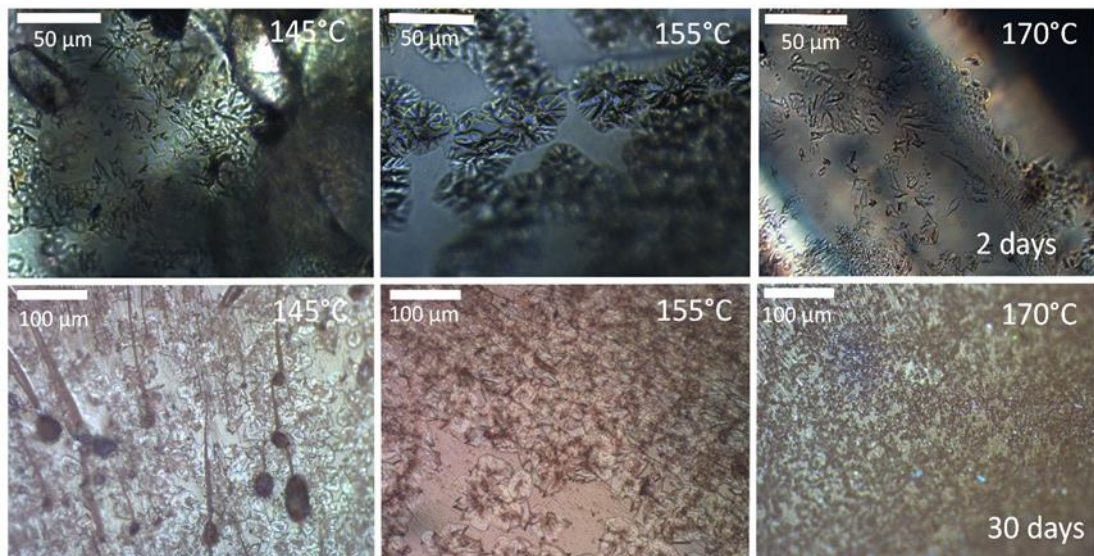
D 1. ToF-SIMS images of the 35wt% drug loading system extruded at 150°C acquired over a period of 150 days. The yellow circles denote the initial drug-rich clusters that constitute active nucleation sites for surface crystallisation upon ageing.



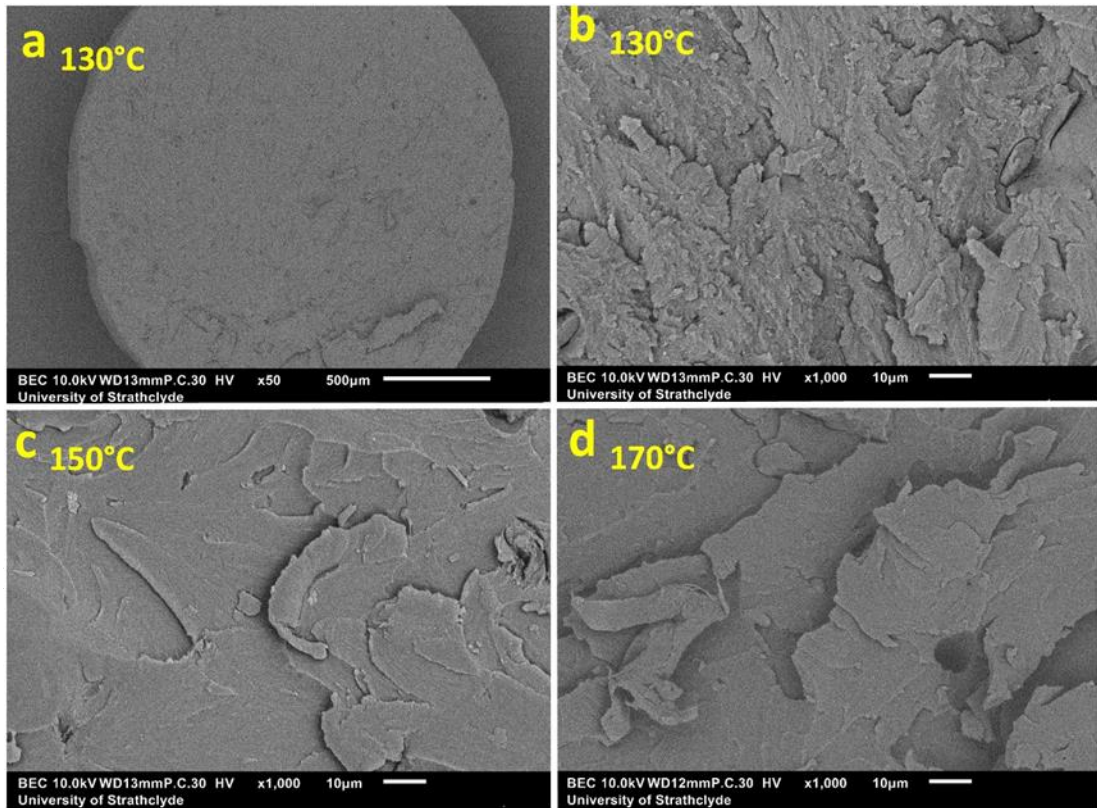
D 3. Optical microscopy images acquired at 2 and 30 days of storage for the 10wt% drug loading system. Despite formation of sharkskin defects there is no evidence of surface crystallisation events.



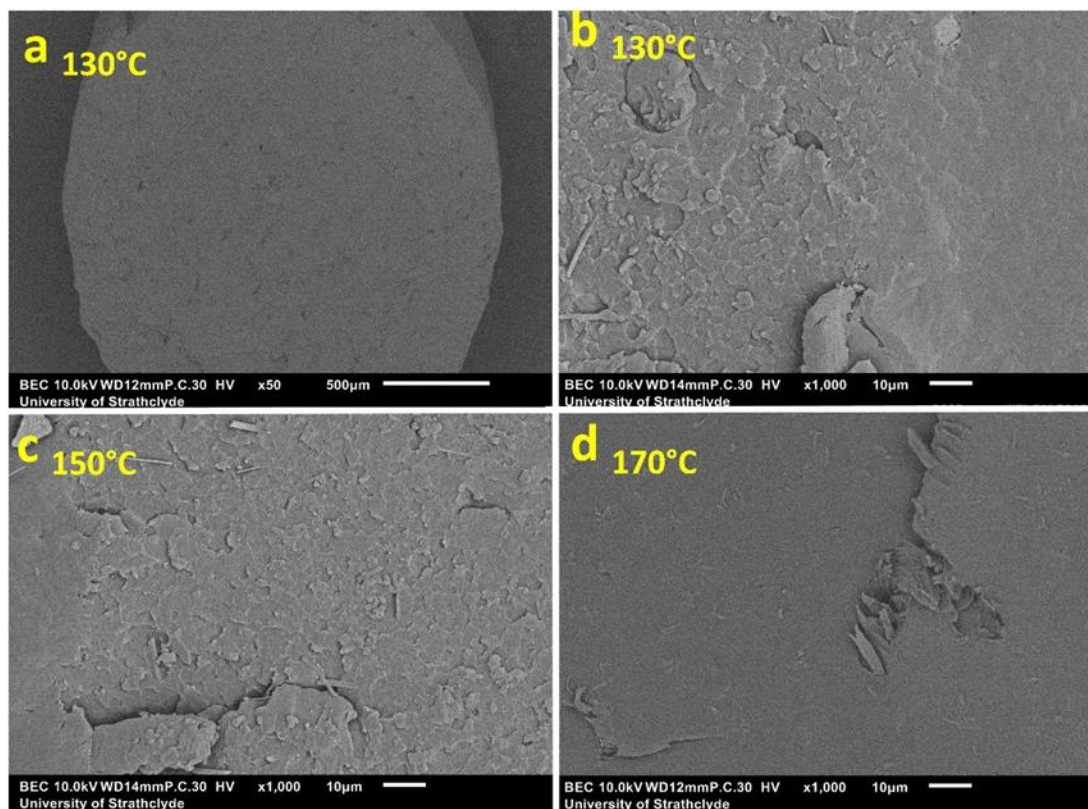
D 2. Optical microscopy images acquired at 2 and 30 days of storage for the 20wt% drug loading system displaying the appearance of birefringent circular defects that are congruent with surface crystallisation at 30days.



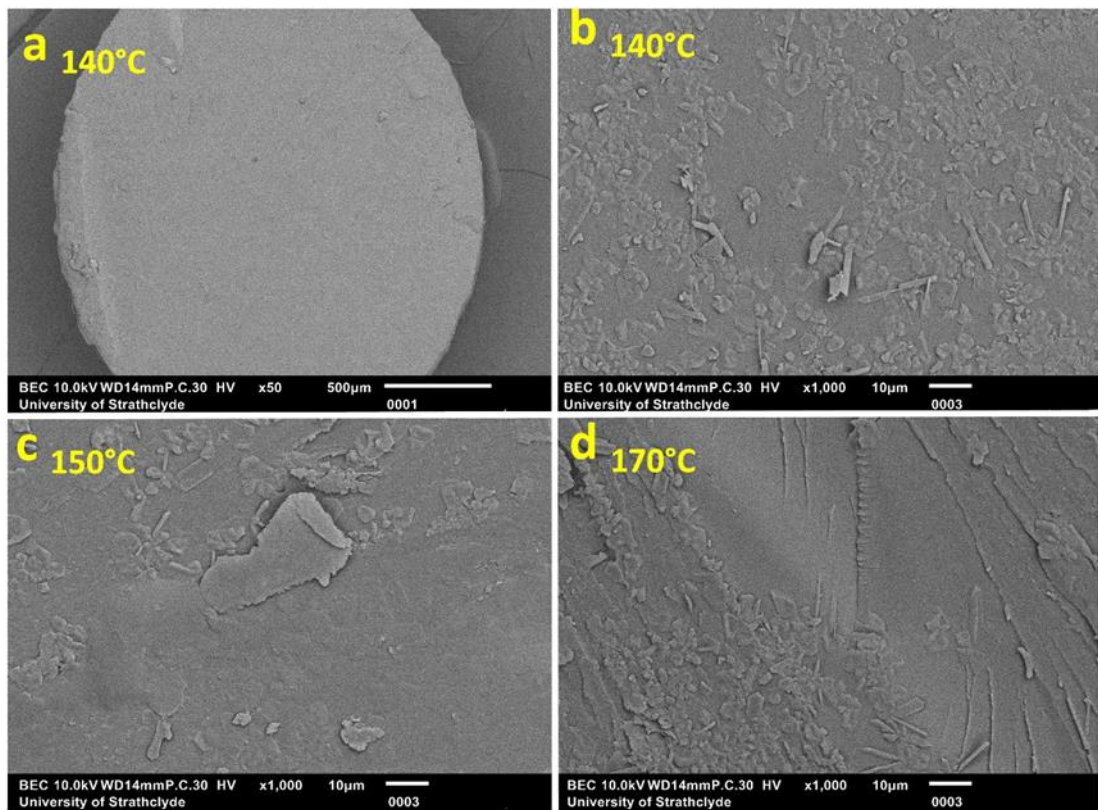
D 4. Optical microscopy images acquired at 2 and 30 days of storage for the 35wt% drug loading system displaying the appearance of birefringent circular defects that are congruent with surface crystallisation at 30days.



D 6. SEM images of the 10wt% system processed at 145°C after 30 days of storage. The yellow arrows point to the circular terraced growth forms and black one to the plate-like crystallites

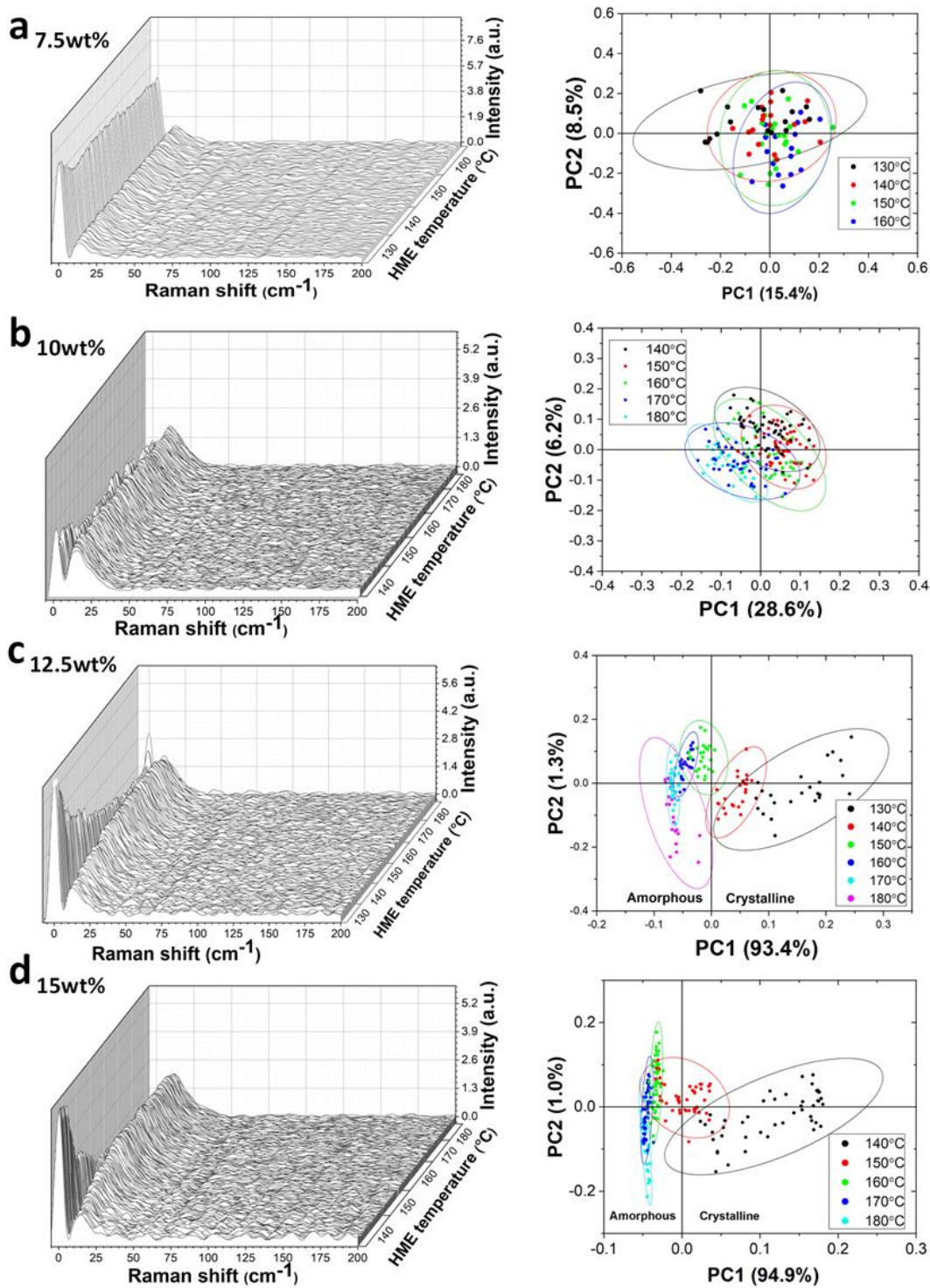


D 7. SEM images of the 20wt% system processed at 145°C after 30 days of storage. The yellow arrows point to the circular terraced growth forms and black one to the plate-like crystallites

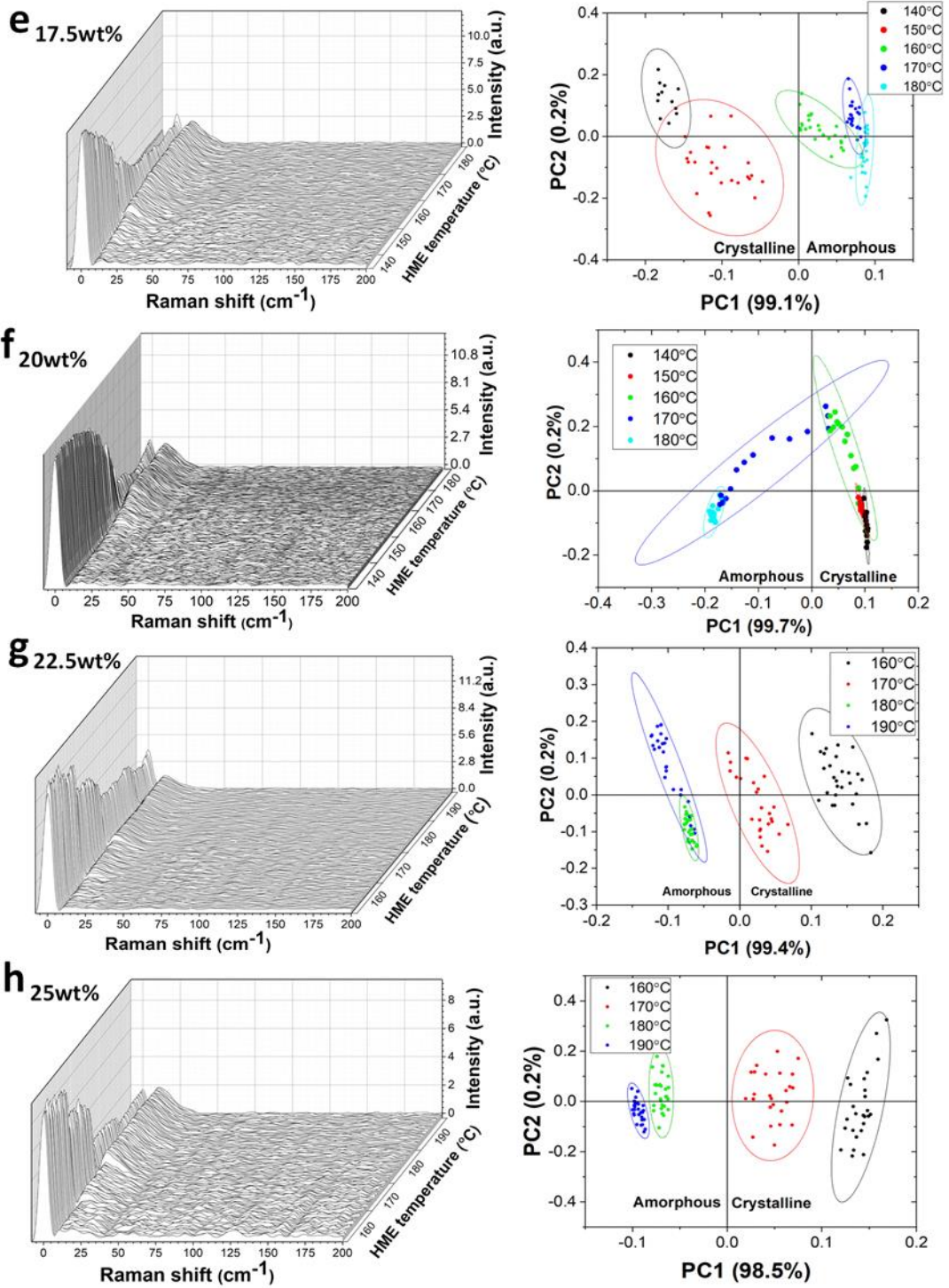


D 8. SEM images of the 35wt% system processed at 145°C after 30 days of storage. The yellow arrows point to the circular terraced growth forms and black one to the plate-like crystallites

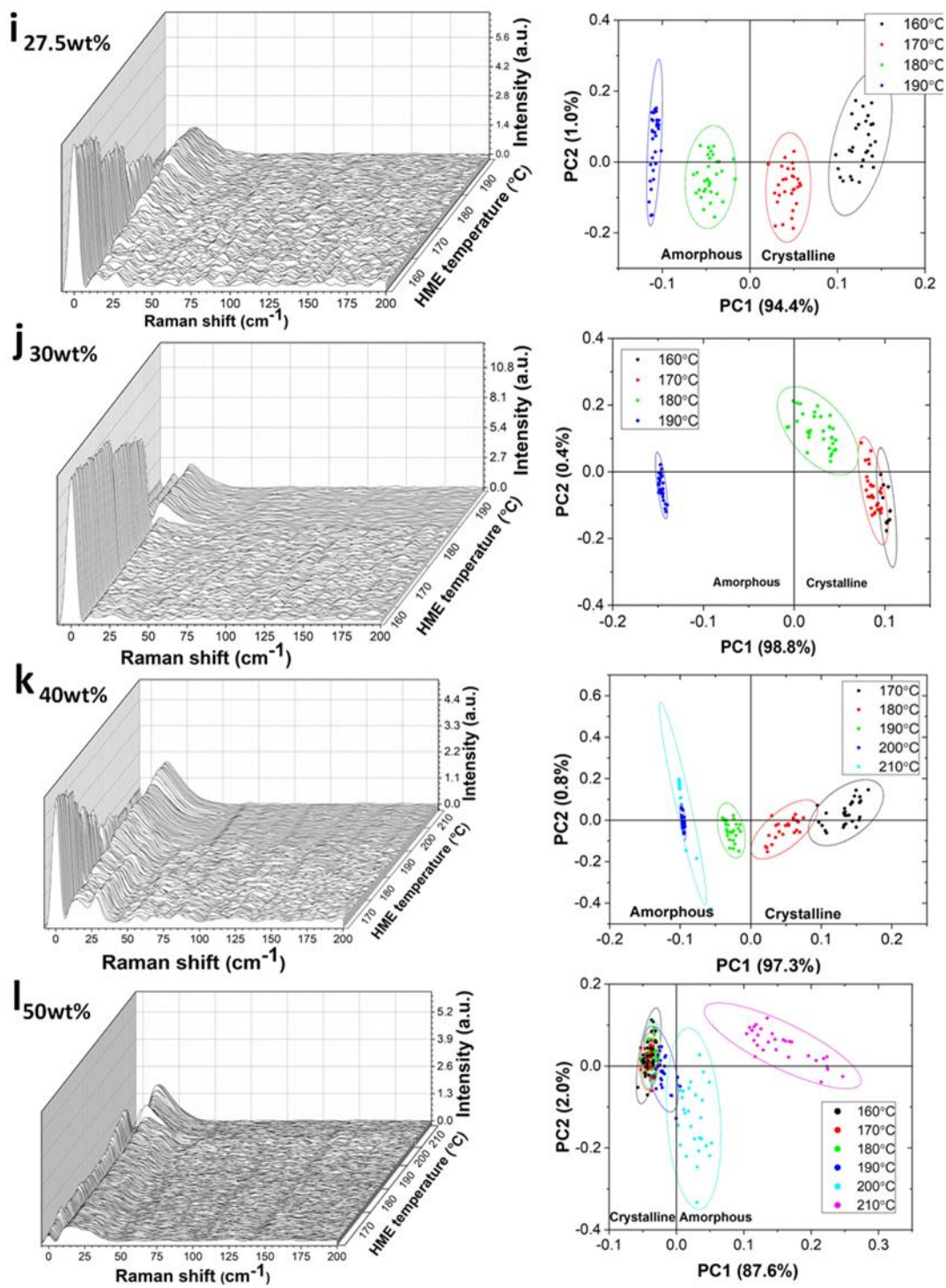
## APPENDIX E – Additional data for Chapter 6



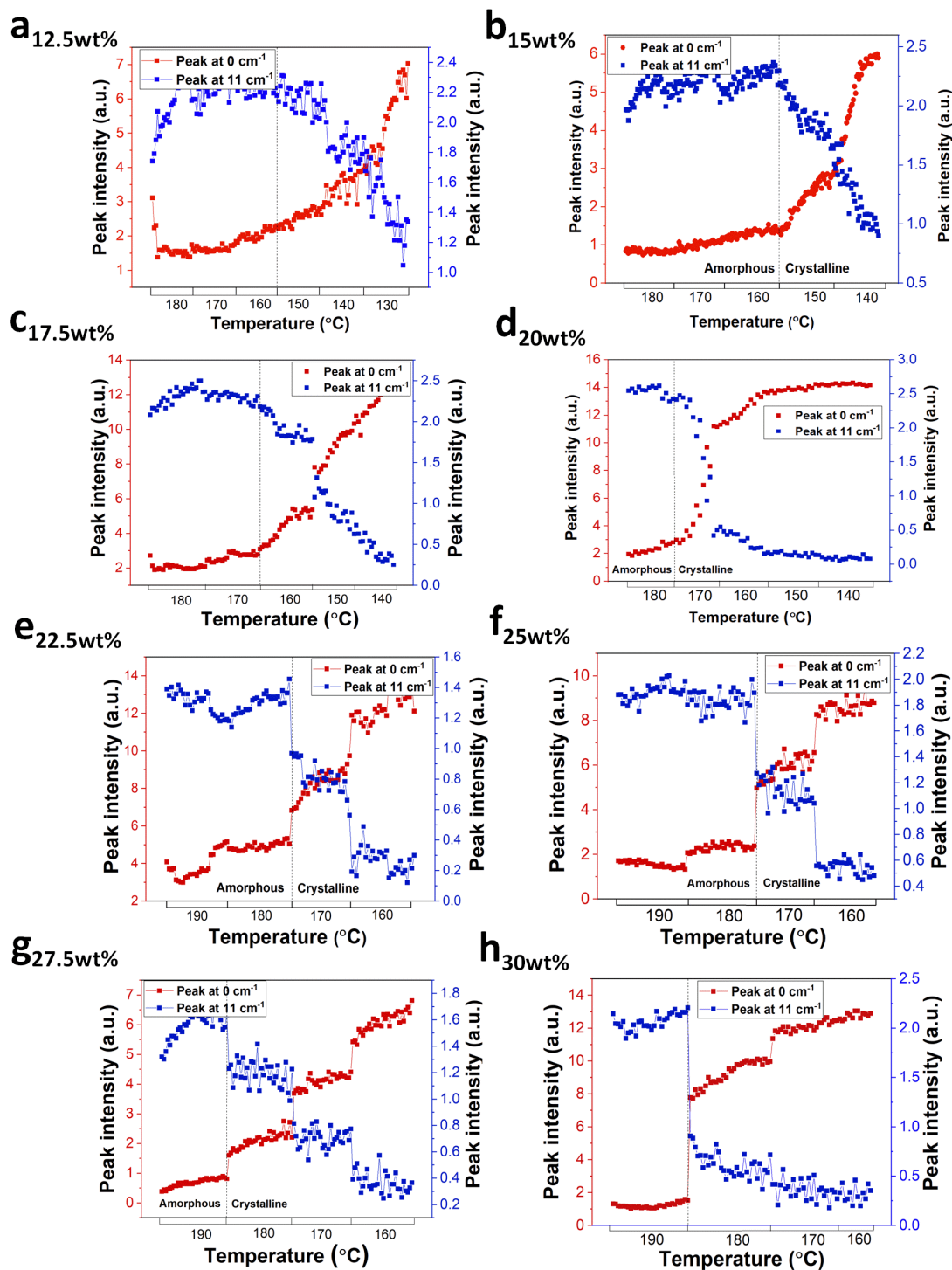
E 1. LFR spectra with respective PCA score plot from 7.5wt% to 15wt% drug loadings.



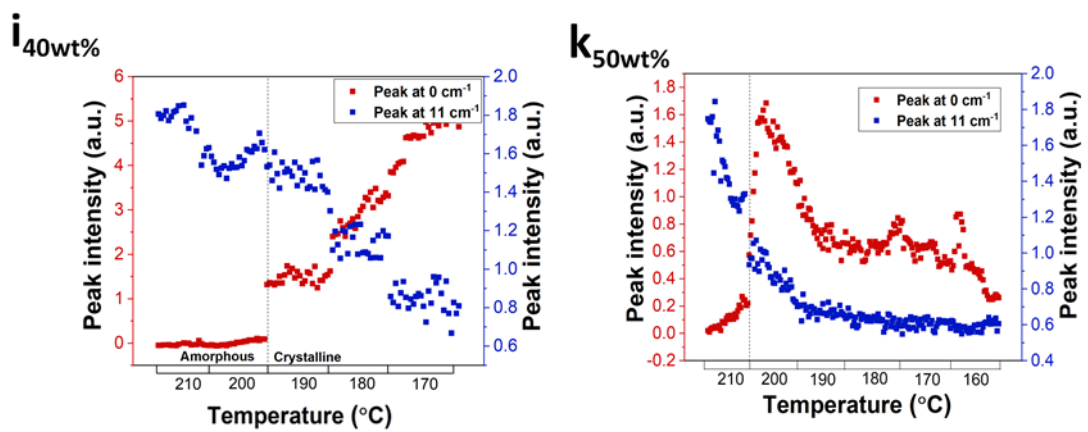
E 2. LFR spectra with respective PCA score plot from 17.5wt% to 25wt% drug loadings.



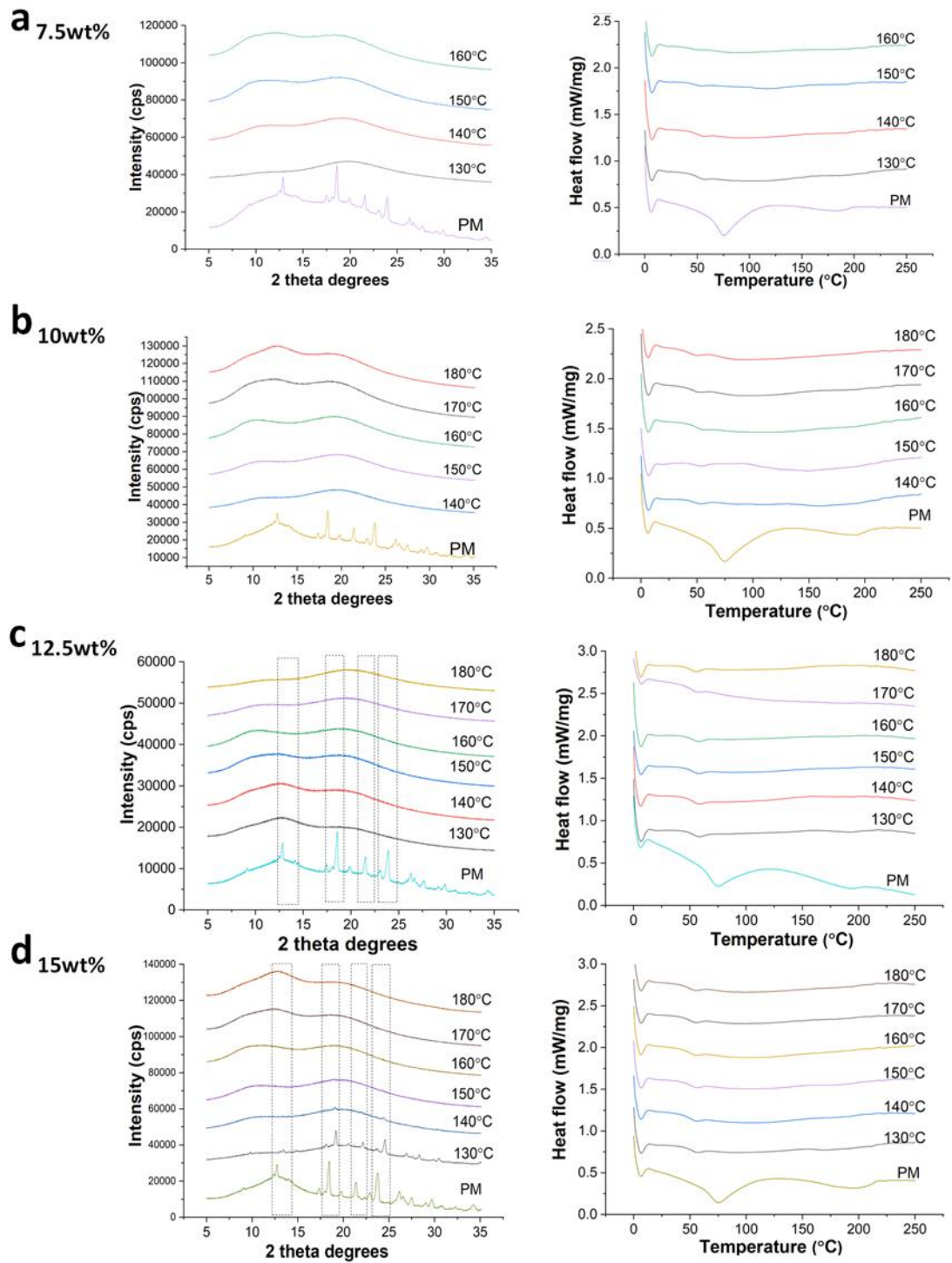
E 3. LFR spectra with respective PCA score plot from 27.5wt% to 50wt% drug loadings.



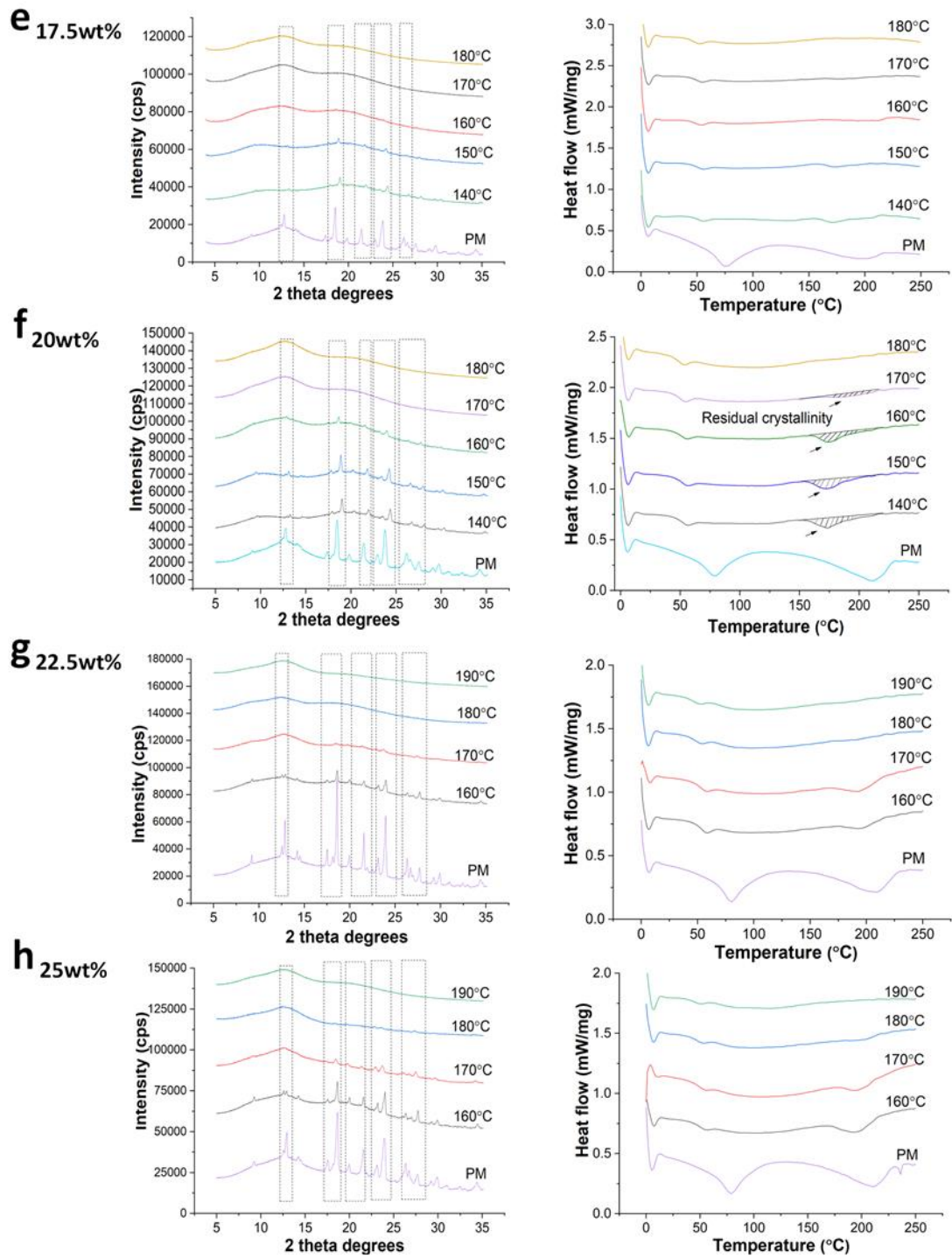
E 4. Rayleigh and Stokes peak intensity variation from 12.5wt% to 30wt% drug loading



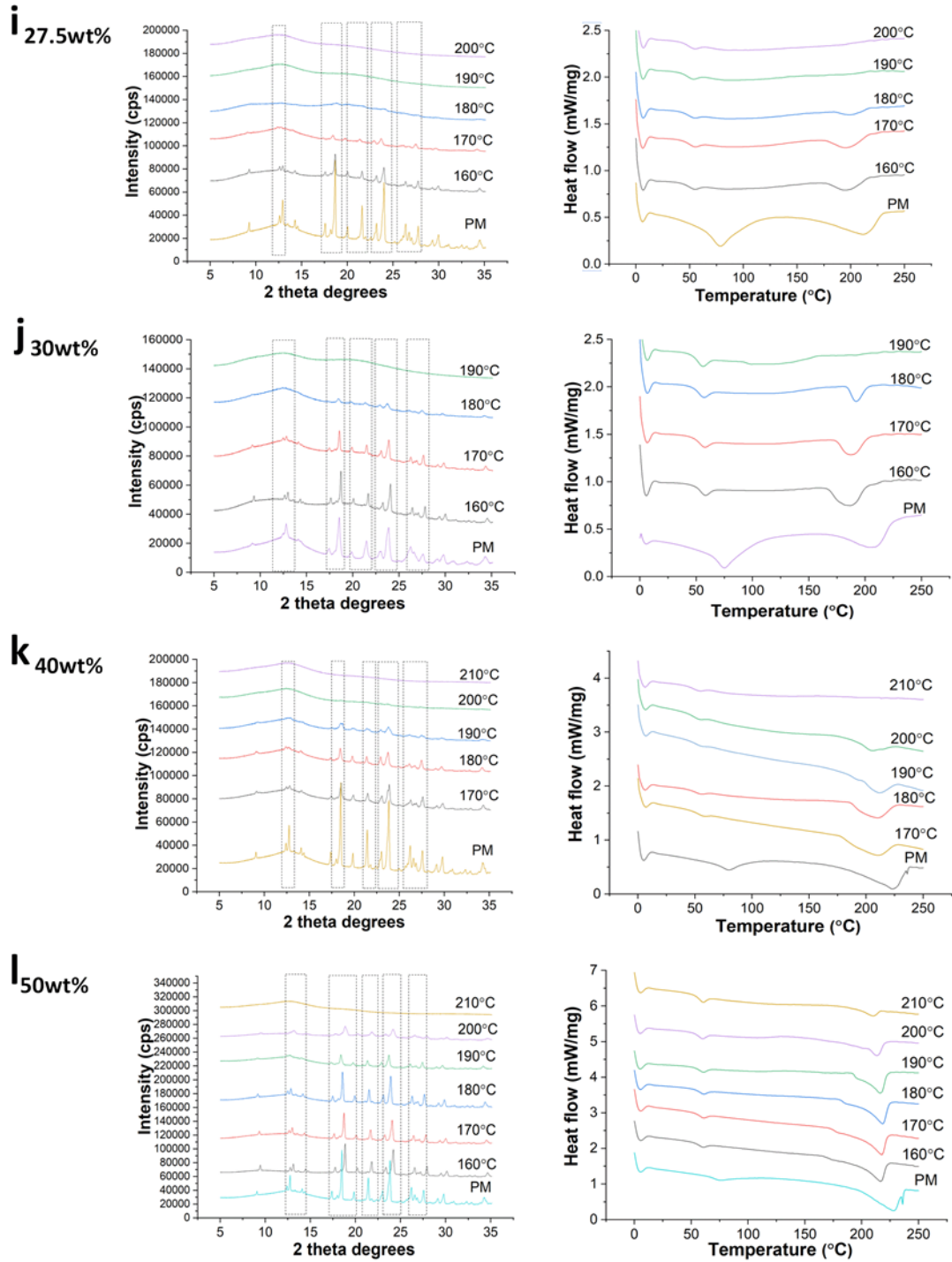
E 5. Rayleigh and Stokes peak intensity variation at 40wt% and 50wt% drug loading



E 6. XRD and DSC analysis of extrudates produced at variable temperatures from 7.5wt% to 15wt% drug loading.



E 7. XRD and DSC analysis of extrudates produced at variable temperatures from 17.5wt% to 25wt% drug loading.



E 8. XRD and DSC analysis of extrudates produced at variable temperatures from 27.5wt% to 50wt% drug loading.